3

Trace Element Geochemistry of Oceanic Peridotites and Silicate Melt Inclusions: Implications for Mantle Melting and Ocean Ridge Magmagenesis

by

KEVIN TODD MICHAEL JOHNSON

B.S., The Pennsylvania State University, 1977
M.S., University of Hawai'i, 1983

SUBMITTED IN PARTIAL FULFILLMENT OF THE
REQUIREMENTS FOR THE DEGREE OF
DOCTOR OF PHILOSOPHY

at the
MASSACHUSETTS INSTITUTE OF TECHNOLOGY
and the
WOODS HOLE OCEANOGRAPHIC INSTITUTION

June 15, 1990

Signature of the author_____
Joint Program in Oceanography, Massachusetts Institute of Technology and Woods Hole Oceanographic Institution and Department of Earth, Atmospheric, and Planetary Sciences, Massachusetts Institute of Technology, June, 1990.

Certified by_____
Henry J. B. Dick, Thesis Supervisor

Accepted by_____
Chairman, Joint Committee for Marine Geology and Geophysics, Massachusetts Institute of Technology/Woods Hole Oceanographic Institution.

Trace Element Geochemistry of Oceanic Peridotites and Silicate Melt Inclusions: Implications for Mantle Melting and Ocean Ridge Magmagenesis

by

Kevin Todd Michael Johnson

Submitted to the Department of Earth, Atmospheric, and Planetary Sciences
Massachusetts Institute of Technology
and
the Department of Geology and Geophysics
Woods Hole Oceanographic Institution
on June 15, 1990
in partial fulfillment of the requirements
for the degree of Doctor of Philosophy

ABSTRACT

The mantle melting process is fundamental to basalt genesis and crustal accretion at mid-ocean ridges. It is believed that melts ascend more rapidly than the surrounding mantle, implying a process similar to fractional melting may be occurring, but geochemical evidence for this has been lacking. Furthermore, crustal accretion is thought to be episodic at slow spreading ridges, but sampling programs that can test this temporal variability are virtually nonexistent. This dissertation examines the trace element compositions of abyssal peridotites and discusses how they preserve details of the melting process that are not recognizable in mid-ocean ridge basalts. The results support fractional melting as the dominant melting process in the sub-ridge upper mantle. Evidence is also presented supporting non-steady state mantle melting at the Atlantis II Fracture Zone cutting the very slow spreading Southwest Indian Ridge.

Trace element compositions of peridotite clinopyroxenes from fracture zones along the American-Antarctic and Southwest Indian Ridges vary as a function of proximity to hotspots. The results presented in Chapter 2 are consistent with higher degrees of melting and greater incompatible element depletion in the upper mantle near hotspots. All peridotites studied are consistent with being residues of fractional melting and inconsistent with batch melting. Some samples recovered near hotspots appear to have begun melting in the garnet stability field, deeper than samples recovered away from hotspots. Most samples show pronounced negative Zr and Ti anomalies, which increase with increasing incompatible element depletion (increased melting), on extended rare earth (spider) diagrams.

The results of Chapter 2 indicated the importance of accurately knowing trace element partition coefficients between clinopyroxene and liquid. It was found that existing partitioning studies report either rare earth elements, Ti, or Zr, but not all elements together. Thus, there is ambiguity about relative partition coefficients for these elements. Accurate knowledge of partitioning is important in understanding the formation of negative Zr and Ti anomalies observed in peridotite clinopyroxenes as well as in constructing realistic melting

models for peridotites. To that end, Chapter 3 reports the results of a clinopyroxene/basaltic liquid trace element partitioning study carried out on natural dredged basalts and experimental charges of mid-ocean ridge basalts. It was found that there are small negative anomalies in the partiton coefficients of Zr and Ti relative to adjacently plotted rare earth elements on spider diagrams.

Fractional melting implies that small parcels of refractory (e.g., high Mg/[Mg+Fe]), incompatible element depleted melts must exist somewhere in the ascending body of melt. Since mixing, wall rock reaction, and fractional crystallization probably alter the compositions of silicate melts extensively on their way from source to surface, representatives of these refractory fractional melts will rarely be erupted as flows on the seafloor. However, some refractory silicate melt inclusions possess compositional characteristics akin to those expected in fractional melts, i.e. low incompatible element concentrations and fractionated trace element ratios. Chapter 4 is a study of refractory melt inclusions from a variety of tectonic settings. The inclusions were obtained from Dr. A. V. Sobolev of the Vernadsky Institute of Geochemistry, Soviet Academy of Sciences, Moscow. They are not ideally suited for studying mid-ocean ridge processes, as only a few of the inclusions are from this environment, but in general, the inclusions show more refractory, incompatible element depleted compositions than their host lavas. Furthermore, the suite of inclusions in different mineral phases contained in a single N-type mid-ocean ridge basalt show variable trace element characteristics indicating unrelated sources for some inclusions. The results of the study do not strongly endorse the fractional melting hypothesis, but some support is suggested by trace element depletions and fractionations warranting a more thorough study of a suite of inclusions.

Finally, the along-ridge major and trace element variability in peridotites observed previously and in Chapter 2 is compared to the variability found in a single fracture zone. The high sampling density at the Atlantis II Fracture Zone on the Southwest Indian Ridge, coupled with its great distance from a hotspot make it a good subject for a baseline study. It was found that the compositional variability observed in peridotites from the Atlantis II Fracture Zone covers nearly the whole range of compositions found along the American-Antarctic and Southwest Indian Ridges in Chapter 2. However, there are systematics to this wide range, suggesting different processes may control the depletions. On the eastern side of the transform, a compositional gradient is observed from the center of the eastern wall to the northern ridge-transform intersection. Peridotites on this side have become gradually more depleted in incompatible elements and modal clinopyroxene over at least the last 10-11 million years. Samples from the western side of the transform are, in general, more depleted than those from the eastern side and show some indication of a compositional gradient as well, although sampling is less dense. Basalts from the western side are clearly different in iron composition and degree of rare earth element fractionation. These differences are consistent with higher pressure, higher degrees of melting producing lavas on the western side. It is believed that the long wavelength chemical variations corresponding to hotspot proximity described in Chapter 2 result from regional thermal conditions in the upper mantle imposed, in large part, by the hotspots. On the other hand, the short wavelength variability on a fracture zone or spreading cell scale may result from episodic mantle upwelling and magma production due to non-steady state accretion at very slow spreading ridges.

Thesis Supervisor: Dr. Henry J. B. Dick
Associate Scientist, W.H.O.I.

ACKNOWLEDGEMENTS

First, I would like to thank all of my committee members, Henry Dick, Nobu Shimizu, Fred Frey, Bill Bryan, Stan Hart, and Hans Schouten for providing both criticism and encouragement throughout my years at M.I.T. and W.H.O.I. Hans, besides being a wonderful friend, was a thesis defense chairman without peer, and his skills both as organizer and M.C. will never be questioned. Fred's guidance in learning the foundations of trace element geochemistry and the use of trace elements in modeling igneous petrogenesis was integral to the successful completion of this thesis. Bill's insights into the workings of mid-ocean ridge systems and his delivery of his knowledge in a scientific vernacular that he was instrumental in developing through the years was both enjoyable and illuminating. Stan's vast knowledge and insatiable curiosity about all aspects of earth sciences, combined with his clarity of expression made him a highly valued member of the committee. Special thanks to Nobu who taught me how to use, understand, and appreciate the ion microprobe, and who nurtured me beyond the stage of "black-box" data acquisition on this unique and powerful tool. Nobu constantly took petrological and geochemical conventional wisdom to the mat, a quality I find inspiring and admirable. And very special, warm thanks to my advisor, mentor, and friend, Henry Dick, who provided the most stimulating, thought provoking, supportive, and enjoyable working environment I could have hoped for. Henry's style is legendary, but he has mellowed like a hearty Bordeaux -- still plenty of substance, but the edges have smoothed. So, like this fine wine, which we have enjoyed on a number of occasions at his numerous also-legendary feasts, Henry will undoubtedly continue to improve with time, and I only regret leaving such a dynamic place of ideas and constant evolution. However, I know that I will always be a part of W.H.O.I. and will eagerly return whenever I can.

Some dear friends have, in no small way, helped me with ideas and good times through the last few years on the road to the Ph.D. They are too numerous to name, but include Peter Meyer, Peter Kelemen, John and Joann Sinton, Mike and Catriona Purdy, Beecher and Chris Wooding, Kathy Gillis, Rob and Cindy Yonover, Tanya Furman, Margaret and Jacek Sulanowski, and Linda Angeloni. I must also mention my old buddies Rich Strucker and Rich Franko whose enduring friendship will always be a spiritual cornerstone in my life. Warm thanks are also extended to Jake Peirson, Abbie Jackson, and Mary Athanis of the Joint Program Education Office for their help.

Last, but most important to me, is the recognition of my family's support over the many years I have spent pursuing, albeit along a convoluted path, my dreams wherever in the world that took me. My parents, Eunice and Thomas, set examples of excellence that I chased after for all I was worth. They are wonderfully complete role models who taught me the importance of setting high standards for oneself. I dedicate this thesis to Eunice, my mother, who has done so much for so many, and has given me more than she probably realizes. Finally, to Laura, my wife and dearest friend, we have both been striving at the same time for the same goal. Fortunately for me, we glanced away from it long enough to find each other and now to create new goals for our lives together. I've never been happier than in these last eventful three months, and it's all because of you.

Biographical Note
Kevin Todd Michael Johnson

EDUCATION

M.S. Marine Geology and Petrology, University of Hawai'i, 1983

B.S. Geology/Marine Sciences; Philosophy, The Pennsylvania State University, June, 1977.

PROFESSIONAL EXPERIENCE

February, 1978 - June, 1980, Peace Corps volunteer; Hydrogeologist and water resources specialist, Dept. of Public Works, Apia, Western Samoa.

January, 1981 - August, 1981, Hydrogeologist, U. S. Geological Survey, Anchorage, Alaska.

October, 1983 - April, 1985, Research Student, Department of Geology and Mineralogy, Hokkaido University, Sapporo, Japan, and Ocean Research Institute, University of Tokyo, Tokyo, Japan. Monbusho Scholarship from Japanese Ministry of Science, Culture, and Education.

AWARDS AND FELLOWSHIPS

1973 - National Merit Scholarship, Honorable Mention.

1981-1983 - East-West Center Graduate Student Fellowship, Honolulu, Hawai'i.

1983-1985 - Monbusho Research Scholarship, Japan Ministry of Science, Education, and Culture, Hokkaido University.

1987-1988 - Woods Hole Oceanographic Institution Ocean Ventures Fund - "Physicochemical Processes of Mantle Melting."

PUBLICATIONS

1985:

Johnson, K. T. M., Major, trace, and rare earth element abundances in boninitic lavas from the Ogasawara forearc,*Journal of Faculty of Science, Hokkaido University,* series IV, v. 21, pp. 453-463.

Johnson, K. T. M. and Y. Nakamura, Island arc tholeiite series rocks from Palau: major, trace, and rare earth elements, Report of the R/V *Hakuho Maru* cruise KH84-1, U. of Tokyo, pp. 298-305.

Katsui, Y., H. Igaraki, K. Johnson, N. Gouchi, and T. Ikeda, Landslide features and volcanic hazards of the Shiretoko Peninsula, in "Environmental Studies of the Shiretoko Peninsula", Dept. of Natural Resources, Hokkaido Prefecural Government (in Japanese).

Johnson, C.J., A. L. Clark, J. M. Otto, K. T. M. Johnson, D. K. Pak, and C. L. Morgan, Resource Assessment of Cobalt-rich Ferromanganese Crusts in the Hawaiian Archipelago, Report to the Federal Task Force on Manganese Crust Mining in the Hawaiian Exclusive Economic Zone, East-West Center, Honolulu, Hawai'i, 135 p.

Sinton, J. M., K. T. M. Johnson, and R. C. Price, Petrology and geochemistry of volcanic rocks from the Northern Melanesian Borderland, in T. M. Brocher, ed., *Geological Investigations of the Northern Melanesian Borderland,* Circum-Pacific Council for Energy and Mineral Resources Earth Science Series, v.3, 34-64.

1986:

Johnson, K. T. M., J. M. Sinton, and R. C. Price, Petrology of seamounts northwest of Samoa and their relation to Samoan volcanism, *Bulletin of Volcanology, 48,* 225-235.

1988:

Sinton, J. M., R. C. Price, K. T. M. Johnson, H. Staudigel, and A. Zindler, Petrology and geochemistry of submarine lavas from the Lau and North Fiji Basins, in L. Kroenke, ed., Circum-Pacific Council for Energy and Mineral Resources Earth Science Series, in press.

1989:

Johnson, K. T. M. and J. M. Sinton, Petrology, tectonic setting, and the formation of back-arc basin basalts in the North Fiji Basin, *Geol. Jahrbuch*, in press.

1990:

Johnson, K. T. M., H. J. B. Dick, and N. Shimizu, Melting in the Oceanic Upper Mantle: an Ion Microprobe Study of Diopsides in Abyssal Peridotites, *Journal of Geophysical Research, 95,* 2661-2678.

Kelemen, P. B., K. T. M. Johnson, R. J. Kinzler and A. J. Irving, High field strength element depletions in arc basalts due to mantle-magma interaction, *Nature, 345*, 521-524.

TABLE OF CONTENTS

CHAPTER 1. INTRODUCTION

The melting process that creates mid-ocean ridge basalt (MORB) from the sub-oceanic upper mantle has been the focus of much attention over the years. Unfortunately, observing the mantle in the act of melting is not possible, so inferences must come from a variety of sources including material experiments and fluid dynamic theory [e.g., *Beere*, 1975;*Waff and Bulau*, 1979;*Whitehead et al.*, 1984; *Cooper and Kohlstedt*, 1986; *Scott and Stevenson*, 1989], geophysical remote sensing [e.g., *Girardin and Poupinet*, 1974; *Forsyth*, 1977; *Rowlett and Forsyth*, 1979; *Kuo and Forsyth*, 1988; *Lin et al.*, 1990; *Kong*, 1990], studies of mid-ocean ridge basalt compositions [*Langmuir et al.*, 1977; *Dick et al.*, 1984, *McKenzie*, 1985; *Klein and Langmuir*, 1987], and studies of abyssal peridotite compositions [*Dick et al.*, 1984; *Michael and Bonatti*, 1985; *Johnson et al.*, 1990]. Although this assortment of disciplinary approaches does not always arrive at the same conclusions about the sub-oceanic mantle melting process, a convergence of results has been occurring in recent years.

Although it is possible to infer the presence or absence of melt in the upper mantle based on seismic and electrical conductivity data, the difference between 1 volume% and 10 volume% liquid cannot be resolved [*Shankland and Waff*, 1977; *Mavko*, 1980]. Physical evidence of trapped liquid, e.g. cumulate pods and veins in peridotites, does not provide much insight into the practical minimum porosity of that sample while it was melting deeper in the ascending sub-ridge mantle system. Recent efforts utilizing fluid dynamic experiments and theory have been quite successful in providing information about the way melts and mantle rocks should behave in an ascending two-phase system [*Whitehead et al.*, 1984; *Phipps-Morgan*, 1987; *Scott and Stevenson*, 1989]. However, these techniques are limited by uncertainties about physical properties such as viscosity contrasts between liquid and residual mantle. Of course, all of these methods have significantly contributed to our present state of understanding about the melting process in the sub-oceanic mantle. In this

thesis, I have approached the problem of sub-ocean ridge mantle melting from a geochemical perspective.

Chapter 2 examines the chemical compositions of clinopyroxenes in oceanic peridotites dredged from fracture zones along the American-Antarctic and Southwest Indian Ridges. Chemical data were collected from individual diopside grains in oceanic harzburgites and lherzolites using a Cameca IMS-3f ion microprobe and JEOL electron microprobe. This unique data base is used to describe lateral variations in upper mantle compositions and to describe for the first time the extremely depleted incompatible trace element compositions of residual oceanic peridotites. From these observations, a model for oceanic mantle melting is constructed that calls for a process approximating fractional fusion to explain the observed residual compositions. For the remainder of this thesis, fractional melting is distinguished from perfect fractional melting or fusion. The former is used to denote the process that is argued to occur in nature in which very small percentages of melt are efficiently removed from the residue. The latter is a theoretical end-member of the melting spectrum in which infinitesimal melt fractions are instantaneously removed from the residue; this can never occur in nature because in order for melt to segregate, interconnection of melt pathways must be achieved, and this only happens at a finite matrix porosity [e.g. *Waff and Bulau*, 1979; *Cooper and Kohlstedt*, 1986]. It is also shown in Chapter 2 that the majority of ocean ridge basalts can be modeled as integrated fractional melts from this process. Another observation in Chapter 2 is that nearly all of the clinopyroxenes exhibited negative Zr and Ti anomalies when plotted with rare earth elements in spider diagrams, but mid-ocean ridge basalts generally show only small negative Ti anomalies and often show positive Zr anomalies.

To investigate whether these anomalies in the residual clinopyroxene could be created by the melting process alone, partitioning of Zr and Ti relative to the rare earth elements must be accurately known. Available compilations of clinopyroxene/liquid partition coefficients from the literature provide partitioning information for one group of elements

or the other, but not both groups together determined from the same samples. Furthermore, there is no consensus about clinopyroxene/liquid rare earth element partition coefficients. Since the melting model in Chapter 2 relies on accurate knowledge of these values, a study was undertaken to determine Zr, Ti and rare earth element partitioning between clinopyroxene and basaltic liquid in the same samples. The results of this study are presented in Chapter 3.

An implied consequence of the fractional melting model is that fractional melt increments must exist beneath the ridge. If these melt fractions are homogenized on their ascent to the surface and then erupted as mid-ocean ridge basalts, as inferred in Chapter 2, then extrusive representatives of the melt fractions are probably very scarce. However, refractory silicate melt inclusions that differ in composition from the mid-ocean ridge basalts that carry their host phenocrysts have been offered as evidence of magma mixing [e.g. *Donaldson and Brown*, 1977; *Dungan and Rhodes*, 1978]. Hence, it was thought that investigating the trace element compositions of refractory silicate melt inclusions might provide insight into the fractional melting process. If fractional melts are trapped before extensive mixing with other melts prior to eruption, then they should preserve some of the source characteristics from which they came. Specific characteristics should include incompatible element depletions (e.g., high Ti/Zr and negative Zr and Ti anomalies) and higher Mg/(Mg+Fe) than N-type MORB.

A collection of refractory silicate melt inclusions was studied in collaboration with A. V. Sobolev of the Vernadsky Institute of Geochemistry, Soviet Academy of Sciences, and Chapter 4 comprises the results. The inclusion collection was not ideally suited for a study of mid-ocean ridge magmatism, as the samples were collected from a variety of tectonic settings, mostly active margins; the purpose of the Soviet study was to document the petrogenesis of refractory melts, emphasizing boninites and komatiites. Thus, only one suite of mid-ocean ridge submarine basalt inclusions and some inclusions from Iceland

were available, along with the active margin samples. All results are presented and discussed in light of their specific settings.

Chapter 5 is a detailed study of peridotite compositions from the Atlantis II Fracture Zone. The purpose of this study was to document the compositional variability in residual peridotites from a single, non-hotspot related fracture zone so that the variations in Chapter 2 could be better understood. The dredging density and peridotite recovery in this fracture zone is greater than any other globally, and it offers the opportunity to map variations in mantle compositional as a function of time along lithospheric flow lines. It was discovered that the variability in this one hotspot-distant fracture zone spans nearly the entire range reported in Chapter 2. However, extremely depleted samples are few, and the mean composition (sampling bias notwithstanding) for the entire fracture zone is in the range of average peridotites in Chapter 2. Another result of the detailed sampling is the identification of a pronounced peridotite compositional gradient on the eastern wall of the transform. This gradient is consistent with an increasing degree of mantle melting over the past 10-11 my. Variation is also suggested in samples from the western wall, although sparser sample recovery makes this assertion tenuous at present.

Finally, Chapter 6 brings together the main results from the previous chapters and current ideas of mid-ocean ridge spreading processes. Melt generation at slow spreading ridges is viewed as episodic, adding a "temporal segmentation" component to the already well-documented along-axis spatial segmentation of ridges. Regional thermal conditions may dictate the time-averaged long-wavelength chemical characteristics of the residual upper mantle, while localized tectonic events, such as episodic spreading and enhanced decompression melting, may control shorter-wavelength variability.

REFERENCES

Beeré, W., A unifying theory of the stability of penetrating liquid phases and sintering pores, *Acta Metall., 23*, 131-138, 1975.

Cooper, R. F., and D. L. Kohlstedt, Rheology and structure of olivine-basalt partial melts, *J. Geophys. Res., 91*, 9315-9323, 1986.

Dick, H. J. B., R. L. Fisher, and W. B. Bryan, Mineralogic variability of the uppermost mantle along mid-ocean ridges, *Earth Planet. Sci. Lett., 69,* 88-106, 1984.

Donaldson, C. H., and R. W. Brown, Refractory megacrysts and magnesium-rich melt inclusions within spinel in oceanic tholeiites: indicators of magma mixing and parental magma composition, *Earth Planet. Sci. Lett., 37,* 81-89, 1977.

Dungan, M. A. and J. M. Rhodes, Residual glasses and melt inclusions in basalts from DSDP legs 45 and 46: Evidence for magma mixing, *Contrib. Mineral. Petrol., 67*, 417-431, 1978.

Forsyth, D. W., The evolution of the upper mantle beneath mid-ocean ridges, *Tectonophysics, 38*, 89-118, 1977.

Girardin, N., and G. Poupinet, Teleseismic S travel-time delay for Mid-Atlantic Ridge earthquakes, *Phys. Earth Planet. Inter., 9*, 306-313, 1974.

Johnson, K. T. M., H. J. B. Dick, and N. Shimizu, Melting in the oceanic upper mantle: an ion microprobe study of diopsides in abyssal peridotites, *J. Geophys. Res., 95*, 2661-2678, 1990.

Klein, E. M., and C. H. Langmuir, Global Correlations of ocean ridge basalt chemistry with axial depth and crustal thickness, *J. Geophys. Res., 92,* 8089-8115, 1987.

Kong, L. S. L., Variations in Structure and Tectonics along the Mid-Atlantic Ridge, 23°N and 26°N, Ph.D. Thesis, M.I.T./W.H.O.I., 1990.

Kuo, B.-Y., and D. W. Forsyth, Gravity anomalies of the ridge-transform system in the South Atlantic between 31 and 34.5°S: Upwelling centers and variations in crustal thickness, *Marine Geophys. Res., 10*, 205-232, 1988.

Langmuir, C. H., J. F. Bender, A. E. Bence, G. N. Hanson, and S. R. Taylor, Petrogenesis of basalts from the FAMOUS area: Mid-Atlantic Ridge, *Earth Planet. Sci. Lett., 36*, 133-156, 1977.

Lin, J., G. M. Purdy, H. Schouten, J.-C. Sempere, and C. Zervas, Evidence from gravity data for focused magmatic accretion along the Mid-Atlantic Ridge, *Nature, 344*, 627-632, 1990.

Mavko, G. M., Velocity and attenuation in partially molten rocks, *J. Geophys. Res., 85,* 5173-5189, 1980.

McKenzie, D., ^{230}Th-^{238}U disequilibrium and the melting processes beneath ridge axes, *Earth Planet. Sci. Lett., 72*, 149-157, 1985.

Michael, P. J., and E. Bonatti, Peridotite composition from the North Atlantic: Regional and tectonic variations and implications for partial melting, *Earth Planet. Sci. Lett., 73*, 91-104, 1985.

Phipps-Morgan, J., Melt migration beneath mid-ocean ridge spreading centers, *Geophys. Res. Lett., 14*, 1238-1241,1987.

Rowlett, H., and D. Forsyth, Teleseismic P-wave delay times in a major oceanic fracture zone, *Geophys. Res. Lett., 6*, 273-276, 1979.

Scott, D. R., and D. J. Stevenson, A self-consistent model of melting, magma migration and buoyancy-driven circulation beneath mid-ocean ridges, *J. Geophys. Res., 94,* 2973-2988, 1989.

Shankland, T. J., and H. S. Waff, Partial melting and electrical conductivity anomalies in the upper mantle, *J. Geophys. Res., 82,* 5409-5417, 1977.

Waff, H. S., and J. R. Bulau, Equilibrium fluid distribution in an ultramafic partial melt under hydrostatic stress conditions, *J. Geophys. Res., 84,* 6109-6114, 1979.

Whitehead, J. A., H. J. B. Dick, and H. Schouten, A mechanism for magmatic accretion under spreading centres, *Nature, 312,* 146-148, 1984.

Chapter 2. Melting in the Oceanic Upper Mantle: An Ion Microprobe Study of Diopsides in Abyssal Peridotites

(appeared in *Journal of Geophysical Research, 95*, 2661-2678, 1990)

Melting in the Oceanic Upper Mantle: An Ion Microprobe Study of Diopsides in Abyssal Peridotites

KEVIN T. M. JOHNSON

MIT/Woods Hole Joint Program in Oceanography, Woods Hole, Massachusetts

HENRY J. B. DICK AND NOBUMICHI SHIMIZU

Woods Hole Oceanographic Institution, Woods Hole, Massachusetts

ABSTRACT

A systematic study of rare earth and other trace elements in discrete diopsides from residual abyssal peridotites sampled from 5000 km of ocean ridge demonstrates that they are the residues of variable degrees of melting in the garnet and spinel peridotite fields. Further, the data clearly demonstrate that the peridotites are the residues of near-fractional melting, not batch melting, and that typical abyssal basalt can evolve from aggregated fractional melts. Ion microprobe analyses of diopsides in abyssal peridotites from fracture zones along the America-Antarctica and Southwest Indian ridges reveal ubiquitous extreme fractionation of rare earth elements (REE) ($[Ce/Yb]_n$=0.002-0.05); depletion of Ti (300-1600 ppm), Zr (0.1-10 ppm), and Sr (0.1-10 ppm); and fractionation of Zr relative to Ti (Ti/Zr=250-4000). Ti and Zr in diopsides decrease with decreasing modal cpx in the peridotites, and samples dredged near hotspots are more depleted in incompatible elements than those dredged away from hotspots, consistent with higher degrees upper mantle melting in the former. All studied samples exhibit marked negative anomalies in Ti and Zr relative to REE. Incompatible element concentrations in peridotite clinopyroxenes are well modeled by repeated melting and segregation in ≤0.1% increments to a total of 5-25% melting, a process very close to Rayleigh (fractional) melting; batch melting of a LREE-depleted source cannot account for the observed trace element concentrations in abyssal peridotites. The shapes of some REE patterns are consistent with variable degrees of melting initiated within the garnet stability field. Trace element concentrations in calculated integrated fractional liquids approximate the composition of primitive ocean floor basalts, consistent with postsegregation aggregation of small increment melts produced over a depth and melting interval.

INTRODUCTION

Extensive geological and petrological evidence supports the contention that mid-ocean ridge basalts (MORB) are the products of decompression melting of a peridotitic mantle [*Green and Ringwood*, 1967; *Bottinga and Allègre*, 1978; *Ahern and Turcotte*, 1979; *Green et al.*, 1979; *le Pichon et al.*, 1982; *McKenzie*, 1984; *McKenzie and Bickle*, 1988], suggesting that the ocean crust should be underlain by a depleted residue of peridotite. Indeed peridotites have been dredged from numerous locations along the world ocean ridge system, and recent detailed mineralogic studies of these mantle peridotites have shown that

they are the products of a large range of melting which increases systematically along the ocean ridges with proximity to postulated mantle hotspots [*Dick et al.*, 1984; *Michael and Bonatti*, 1985]. Moreover, the compositions of spatially associated abyssal basalts show complementary variations consistent with increasing depletion of the melt in magmaphile elements, particularly sodium, with increasing degree of mantle melting [*Dick et al.*, 1984; *Klein and Langmuir*, 1987]. This strongly supports the direct genetic relationship between abyssal peridotites and MORB inferred from plate tectonics and which has been inferred by numerous experimental studies of the basalt-peridotite system [e.g., *Mysen and Kushiro*, 1977; *Presnall et al.*, 1979; *Green et al.,* 1979; *Jaques and Green*, 1980; *Stolper*, 1980; Takahashi and Kushiro, 1983]. However, debate continues over whether mid-ocean ridge basalts sampled from the seafloor are primary melts formed at pressures between 8 and 11 kbar *[Presnall et al.,* 1979; *Takahashi and Kushiro*, 1983; *Fujii and Scarfe*, 1985; *Presnall and Hoover*, 1987] or are derivatives of higher-pressure (15-25 kbar) primary melts formed via polybaric crystal fractionation, mixing, and assimilation [*O'Hara,* 1968; *Green et al.*, 1979; *Stolper*, 1980; *Elthon and Scarfe*, 1984; *Falloon and Green*, 1987, 1988]. Most experimental studies compare compositions of experimentally produced liquids with natural MORB compositions, but studies focusing on the chemical characteristics of abyssal peridotites and their possible relations to MORB are scarce [e.g., *Shimizu and Hart*, 1974; *Dick et al.*, 1984; *Michael and Bonatti*, 1985; *Shibata and Thompson*, 1986; *Johnson et al.*, 1987, 1988]. Defining and interpreting the chemical characteristics of abyssal peridotites, particularly with respect to the key incompatible elements, is therefore critical to understanding the evolution of the oceanic lithosphere.

Gradients in trace elements and isotopes in MORB from the Mid-Atlantic and Southwest Indian Ridge systems proximal to hotspots have been noted by several authors in studies of ocean floor basalts [*Hart et al.*, 1973; *Schilling*, 1975]. Incompatible elements become more enriched and variable in MORB near hotspots, reflecting a heterogeneous mantle source [*leRoex et al.*, 1983; 1989]. *Dick et al.* [1984] showed that abyssal

peridotites and spatially associated basalts recovered from regions along the Mid-Atlantic, American-Antarctic, and Southwest Indian ridges conform to distinct melt extraction trends in several modal mineralogy and major element representations, and that abyssal peridotites recovered closest to hotspots are the most depleted in basaltic components. Hence it is expected that gradients in incompatible trace elements, reflecting greater degrees of melting and depletion near hotspots, should exist in abyssal peridotites in apparent contradiction to what is observed in many ridge basalts, which become enriched in incompatible trace elements approaching hotspots along-strike [*Schilling*, 1975].

The trace element composition of the solid residues of melting is important not only for documenting the chemical composition of the mantle, but for describing the kind of melting which has occurred (e.g., fractional, incremental, dynamic, or batch melting). At low to intermediate degrees of melting, incompatible trace element concentrations in the residual solid phases will record the melting process better than the derived liquid will if the melts are mixed and homogenized in any way en route to the surface. Furthermore, if MORB are produced at a peritectic, then batch and fractional melting will produce melts of very similar major element compositions until a phase is lost.

Conversely, the composition of residual phases will evolve very differently in fractional and batch melting. Trace elements have been used to model melting in alpine peridotites [e.g., *Loubet et al.*, 1975; *Frey et al.*, 1985; *Prinzhofer and Allègre*, 1985] and also in modeling the evolution of derivative liquids in various mid-ocean ridge and oceanic island settings [e.g., *Gast*, 1968; *Langmuir et al.*, 1977; *Minster and Allègre*, 1978; *Hofmann and Feigenson*, 1983; *Bender et al.*, 1984; *Klein and Langmuir*, 1987]. However, because abyssal peridotites are scarce, pervasively serpentinized, and extremely depleted in incompatible elements, detailed geochemical studies of their bulk trace element compositions have heretofore not been undertaken. Compositions of unaltered minerals in the peridotites, however, provide reliable chemical information and can be used with confidence in constraining the magmatic processes affecting the rock as a whole. Since

diopsides contain the highest concentrations of incompatible trace elements in typical oceanic peridotites (olivine + orthopyroxene + clinopyroxene + spinel), we have used the ion microprobe to analyze discrete diopsides in thin sections of serpentinized oceanic peridotites dredged from a 5000-km length of the American-Antarctic and Southwest Indian ridges (Figure 1). This contribution is the first to report incompatible trace element concentrations in abyssal peridotite clinopyroxenes collected by this method and to use these data to constrain melting processes in the mid-ocean ridge upper mantle.

GEOLOGICAL SETTING AND SAMPLES

The abyssal peridotites in this study were dredged from fracture zones cutting the American-Antarctic and Southwest Indian Ridge systems. The American-Antarctic Ridge system extends from the Bouvet triple junction at 54°S, 1°W to the Scotia Arc at 60°S, 24°W, and separates the Antarctic plate to the south from the South American plate to the north (Figure 1). The half-spreading rate of this ridge is ~0.9 cm/yr [*Lawver and Dick*, 1983], lying at the slow end of the spreading rate spectrum for ocean ridges. Samples from the American-Antarctic Ridge dredged from the Vulcan (59°S, 18°W) and Bullard (57.5°S, 7.5°W to 58.5°S, 15.5°W) fracture zones during Leg 5 of the Vulcan expedition of the R/V *Melville* of Scripps Institution of Oceanography are designated Vulc 5-[dredge number]-[sample number].

The Southwest Indian Ridge system extends from the Bouvet triple junction northeastward to the Central Indian Ocean triple junction and separates the African plate to the north from the Antarctic plate to the south. It also has an extremely slow half spreading rate of ~0.86 cm/yr [*Sclater et al.*, 1976] and is characterized by short ridge segments offset by long fracture zones. Bouvet Island (Figure 1), situated in the southwestern rift mountains some 250 km east of the Bouvet triple junction, may be the surface expression of a hotspot [*Morgan*, 1972; *O'Nions and Pankhurst*, 1974]. Marion Island (Figure 1)

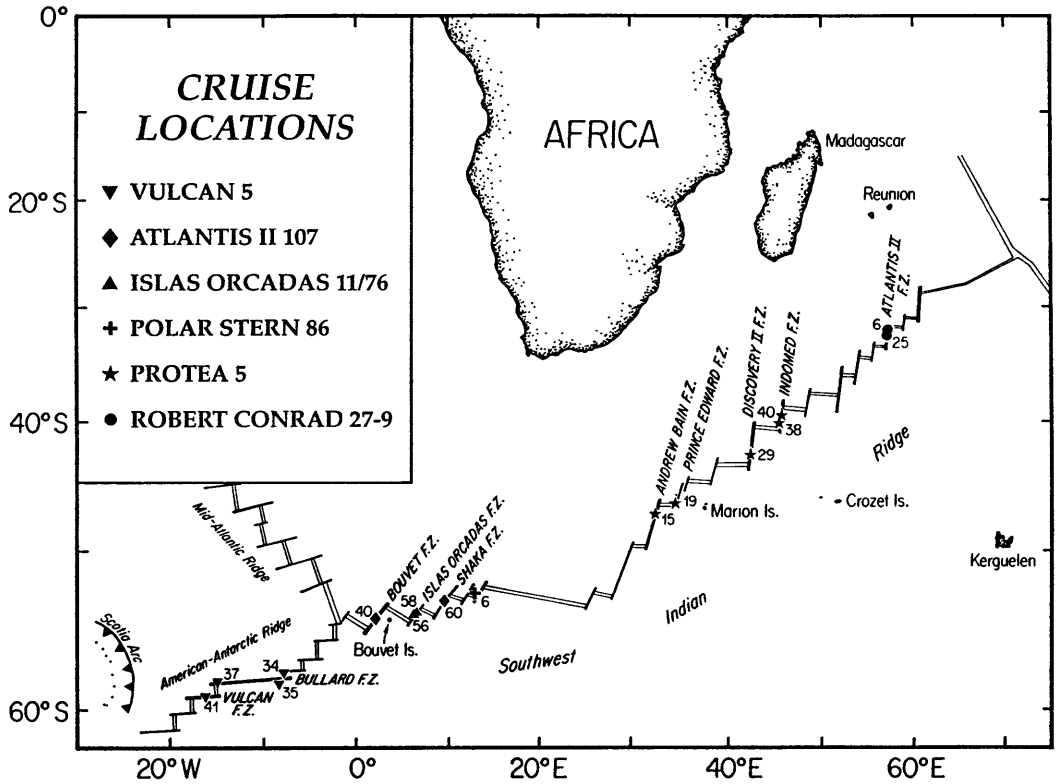

Figure 1. Location map of American-Antarctica Ridge (AAR) and Southwest Indian Ridge (SWIR) showing dredge locations and locations of fracture zones, hotspots, and other features discussed in the text.

may be the surface expression of another hotspot, based on shallow seafloor [*Fisher et al.*, 1987] and a positive residual geoid anomaly [*Rouffosse et al.*, 1981].

Samples from the southern portion of the ridge system are from Bouvet, Islas Orcadas, and Shaka fracture zones and the ridge-transform intersection east of the Shaka Fracture Zone and were dredged during cruise 107, leg 6 of the R/V *Atlantis II*, (AII107), cruise 11/76 of the R/V *Islas Orcadas* (IO11/76), and cruise 86 of the F/S *Polarstern* (PS86). Further to the north, samples were dredged from the Andrew Bain, Prince Edward, Discovery II, Indomed, and Atlantis II fracture zones during leg 5 of the Protea expedition of the R/V *Melville* (Prot 5), and cruise 27, leg 9 of the R/V *Robert Conrad* (RC27-9). All cruise designations are followed by -[dredge number]-[sample number]. Dredge locations and depth ranges are summarized in Table 1.

Abyssal peridotites are recovered in rift mountains and transform faults along the Atlantic and Indian Ocean ridges where the spreading rates are slow to very slow but are rare in dredge hauls from fast spreading ridges (a thorough discussion of their occurrence is given by *Dick* [1989]). Since they are probably emplaced at the base of the crust and faulted or otherwise uplifted to the surface, abyssal peridotites are the top of the mantle section, have experienced the greatest decompression, and likely represent the most extreme residues of the melting process in a given column.

Mineralogy

All samples in this study are plagioclase-free spinel peridotite tectonites with equigranular, protoclastic, or porphyroclastic textures. The primary phases are 65-82% modal forsteritic olivine (Fo_{89-92}), 12-25% enstatite ($Wo_{0.01-0.1}$), 2-12% diopside ($Wo_{0.45-0.5}$, $En_{0.45-0.48}$), and 1-3% Cr-Al spinel. The silicate phases are 20-100% replaced by serpentine or altered to clay minerals (Table 3). However, large parts of pyroxenes are frequently well-preserved and are suitable for chemical microanalysis.

TABLE 1. Dredge Locations and Depths

Cruise and Dredge	Latitude	Longitude	Depth Range, m
Vulcan 5			
34, East Bullard FZ	57°46.9'S	7°40.3'W	3684-3983
35, East Bullard FZ	57°57.0'S	7°48.7'W	2920-3479
37, West Bullard FZ	58°25.8'S	15°39.7'W	3319-4104
41, Vulcan FZ	59°05.2'S	16°48.5'W	3379-4645
Atlantis II 107			
40, Bouvet FZ	54°25.3'S	1°31.7'E	2724-3240
60, Shaka FZ	53°27.3'S	9°10.0'E	4207-5349
Islas Orcadas 11/76			
56, Islas Orcadas FZ	54°05.5'S	6°17.1'E	3650-4390
58, Islas Orcadas FZ	54°04.3'S	6°23.9'E	2960-3580
PolarStern 86			
6, median valley, North wall	52°21.0'S	13°08.0'E	3073-3332
Protea 5			
15, Andrew Bain FZ	47°42.0'S	32°09.5'E	4000-4400
19, Prince Edward FZ	46°30.5'S	33°51.0'E	2700-3900
29, Discovery II FZ	42°41.1'S	41°53.7'E	4400-4600
38, Indomed FZ	39°47.3'S	45°59.3'E	1950-2125
40, Indomed FZ	39°43.1'S	46°17.7'E	2300-2800
Robert Conrad 27-9			
6, Atlantis II FZ	31°55.0'S	57°10.8'E	3500-3930
25, Atlantis II FZ	32°32.5'S	57°03.0'E	4745-5370

Abyssal peridotites often contain plagioclase and hydrothermal alteration products such as chlorite, talc, tremolite, and hornblende occurring both in veins and as discrete reaction products. About a third of all dredged abyssal peridotites contain plagioclase. Only rarely is this phase found in more than trace amounts, though it is locally abundant at a few localities. In most locations, plagioclase is rare, occurring either interstitially to olivine and pyroxene, where it appears to be the product of late impregnation of the peridotite by basaltic melt [*Dick*, 1989] or occurring as exsolution blebs in aluminous pyroxene. It is extremely unlikely that plagioclase occurs as a residual phase (persisted throughout the course of melting) in any of the peridotites we have examined. In any event, samples that include hydrothermal minerals and plagioclase are excluded from this study because of their probable derivative nature.

Clinopyroxenes invariably exhibit some degree of orthopyroxene exsolution. Aside from inhomogeneity introduced by exsolution, grains appear to be unzoned. Based on backscattered electron images, exsolution in analyzed cpx was generally <10%, and exsolved grains were not recalculated to their primary compositions.

ANALYTICAL TECHNIQUES

The reported data are in situ analyses of diopsides and enstatites in thin sections of abyssal peridotites (Table 2). Major element data were collected on a JEOL 733 Superprobe at the Massachusetts Institute of Technology (MIT) using mineral standards and the Bence-Albee correction scheme. Accuracy and precision of major elements are $\pm\leq 1\%$ and minor elements are $\pm\leq 3\%$.

Samples were analyzed for rare earth elements and Ti, Sc, V, Cr, Sr, and Zr using the MIT-Brown-Harvard consortium Cameca IMS-3f ion microprobe at MIT For the major elements and relatively abundant trace elements, such as Sc, Ti, Cr, and V, a primary beam of negatively charged oxygen ions with a current of approximately 0.2 nA and a net energy of 12.55-12.65 keV was focused to a spot 5~8 μm in diameter. Positively charged

TABLE 2. Electron Microprobe Analyses of Pyroxenes in Abyssal Peridotites (wt%)

Sample[1]	SiO_2	TiO_2	Al_2O_3	FeO	MnO	MgO	CaO	Na_2O	Cr_2O_3	Total	Ca	Mg	Fe	Mg#
VULCAN F.Z.														
Vulc5:41-15 (7)	50.46	0.49	8.20	3.01	0.08	14.95	21.09	1.15	0.99	100.41	0.477	0.470	0.053	0.899
Vulc5:41-30 (6)	50.66	0.31	5.68	2.73	0.06	15.76	22.57	0.45	0.99	99.21	0.485	0.470	0.046	0.911
Vulc5:41-30 (6)	54.42	0.09	4.18	6.16	0.06	32.67	1.03	0.01	0.58	99.20	0.020	0.887	0.094	0.904
Vulc5:41-33 (9)	51.50	0.25	5.30	2.75	0.07	16.43	21.86	0.42	0.92	99.50	0.466	0.488	0.046	0.914
Vulc5:41-45 (9)	50.42	0.39	6.40	2.88	0.07	15.67	22.86	0.42	1.05	100.16	0.488	0.465	0.048	0.906
Vulc5:41-45 (3)	54.09	0.09	5.08	6.70	0.11	32.89	0.79	0.00	0.63	100.38	0.015	0.884	0.101	0.897
BULLARD F.Z.														
Vulc5:35-1 (4)	51.40	0.12	4.98	2.71	0.03	16.47	22.33	0.31	1.20	99.55	0.472	0.484	0.045	0.915
BOUVET F.Z.														
AII107:40-4 (7)	51.52	0.04	3.68	2.39	0.10	16.90	23.44	0.10	1.08	99.23	0.481	0.482	0.038	0.927
AII107:40-4 (3)	55.02	0.02	3.24	6.08	0.11	33.42	0.87	0.01	0.78	99.54	0.017	0.892	0.091	0.907
AII107:40-6 (15)	50.99	0.06	4.58	2.58	0.04	17.46	22.85	0.05	1.31	99.93	0.464	0.495	0.041	0.923
AII107:40-6 (5)	55.13	0.05	3.20	5.89	0.15	33.85	1.73	0.00	0.69	100.69	0.032	0.882	0.086	0.911
AII107:40-8 (10)	52.39	0.05	3.39	2.23	0.05	17.11	23.20	0.07	0.93	99.41	0.476	0.488	0.036	0.932
AII107:40-8 (4)	55.43	0.02	3.49	6.04	0.05	33.83	0.81	0.00	0.72	100.38	0.015	0.895	0.090	0.908
AII107:40-11 (6)	51.60	0.06	3.68	2.39	0.05	17.23	22.95	0.08	0.97	99.01	0.470	0.492	0.038	0.928
AII107:40-11 (3)	55.12	0.03	3.07	5.93	0.07	33.37	1.11	0.00	0.61	99.31	0.021	0.890	0.089	0.909
AII107:40-13 (9)	51.38	0.10	4.27	2.35	0.10	16.89	23.99	0.09	1.23	100.38	0.487	0.477	0.038	0.928
AII107:40-13 (5)	55.49	0.07	3.19	6.02	0.12	33.57	1.27	0.01	0.67	100.40	0.024	0.887	0.090	0.908
ISLAS ORCADAS F.Z.														
IO11/76:56-57 (5)	50.68	0.27	5.56	2.15	0.08	15.93	23.22	0.62	0.94	99.42	0.494	0.471	0.036	0.929
IO11/76:56-57 (3)	53.11	0.05	5.98	7.15	0.03	31.73	0.95	0.05	0.70	99.74	0.019	0.871	0.110	0.887
IO11/76:58-18 (6)	50.75	0.22	5.89	2.28	0.05	15.43	23.35	0.51	1.11	99.58	0.501	0.461	0.038	0.923
IO11/76:58-18 (3)	53.90	0.06	5.04	6.25	0.10	32.69	0.89	0.05	0.69	99.67	0.017	0.887	0.095	0.903
IO11/76:58-34 (12)	51.34	0.15	5.80	2.28	0.08	15.41	22.93	0.64	1.06	99.67	0.497	0.465	0.039	0.923
IO11/76:58-34 (3)	53.71	0.02	5.81	6.89	0.17	31.92	0.51	0.00	0.84	99.87	0.010	0.883	0.107	0.892
SHAKA F.Z.														
AII107:60-59 (3)	51.46	0.22	5.47	2.00	0.08	15.44	23.54	0.87	1.08	100.15	0.506	0.461	0.034	0.932
AII107:60-59 (3)	55.00	0.08	3.85	6.09	0.09	33.65	0.59	0.01	0.54	99.89	0.011	0.898	0.091	0.907
AII107:60-61 (6)	50.88	0.20	5.88	2.36	0.05	15.59	22.00	0.84	1.35	99.14	0.483	0.477	0.040	0.922
AII107:60-61 (3)	54.25	0.04	4.34	5.92	0.07	33.46	0.52	0.03	0.75	99.37	0.010	0.901	0.090	0.909
ANDREW BAIN F.Z.														
Prot5:15-90 (6)	50.40	0.20	5.75	2.85	0.07	16.28	22.03	0.33	1.34	99.24	0.470	0.483	0.048	0.910
Prot5:15-90 (3)	53.92	0.06	5.13	6.36	0.10	32.46	1.00	0.01	0.97	100.00	0.020	0.883	0.097	0.900
PRINCE EDWARD F.Z.														
Prot5:19-2 (15)	51.61	0.10	5.62	2.13	0.05	15.53	22.50	1.04	1.22	99.79	0.492	0.472	0.036	0.928
Prot5:19-2 (3)	54.53	0.00	5.07	5.74	0.11	33.12	0.63	0.05	0.82	100.05	0.012	0.900	0.087	0.911
DISCOVERY II F.Z.														
Prot5:29-26 (15)	51.54	0.08	4.02	2.85	0.11	16.90	22.86	0.19	1.12	99.66	0.470	0.484	0.046	0.913
Prot5:29-26 (5)	55.33	0.07	3.35	5.99	0.15	32.54	1.91	0.00	0.84	100.16	0.037	0.873	0.090	0.906
INDOMED F.Z.														
Prot5:38-1 (9)	51.81	0.11	5.27	2.51	0.07	16.34	22.04	0.52	1.17	99.82	0.472	0.487	0.042	0.921
Prot5:39-6 (9)	51.61	0.07	4.37	2.53	0.08	17.29	22.54	0.12	1.28	99.88	0.464	0.496	0.041	0.924
Prot5:40-88 (9)	51.51	0.11	3.94	2.13	0.08	16.31	24.16	0.14	1.42	99.77	0.498	0.468	0.035	0.931
ATLANTIS II F.Z.														
RC27-9:6-3 (6)	51.60	0.20	4.96	2.40	0.05	16.28	22.93	0.34	0.82	99.56	0.484	0.478	0.040	0.923

1 - numbers in parentheses are the number of points making up the average composition.

TABLE 3. Ion Microprobe Analyses of Clinopyroxenes in Abyssal Peridotites (ppm)

Sample[1]	% alter[2]	Mode[3] olivine	opx	cpx	spinel	Sc	Ti	V	Cr	Sr	Zr	Ce	Nd	Sm	Eu	Dy	Er	Yb
VULCAN F.Z.																		
Vulc5:41-13(5)	60	71.8	18.1	8.9	1.2	49	2615	279	5637	5.1	10.6	0.43	1.83	1.22	0.60	2.87	1.87	1.71
Vulc5:41-15(8)	60	63.9	22.7	12.0	1.4	49	2879	297	5925	5.4	11.5	0.50	1.92	1.24	0.57	2.56	1.79	1.61
Vulc5:41-30(3)	40	65.7	27.2	5.8	1.3	53	1979	309	7530	1.0	2.6	0.06	0.71	0.78	0.35	1.94	1.22	1.18
Vulc5:41-33(6)	40	68.1	21.0	9.9	1.0	54	1547	298	6759	2.1	5.0	0.17	0.60	0.70	0.32	1.78	1.14	1.18
Vulc5:41-45(7)	45	68.1	22.3	8.5	1.1	50	1554	355	7928	1.3	1.5	0.04	0.40	0.41	0.20	1.75	1.06	1.10
BULLARD F.Z.																		
Vulc5:34-56(3)	80	74.8	17.1	7.5	0.6	64	796	274	7579	0.6	0.6	0.01	0.08	0.15	0.08	0.87	0.49	0.32
Vulc5:35-1(4)	25	74.4	19.2	6.0	0.4	70	754	300	7158	0.8	0.6	0.02	0.10	0.22	0.11	1.05	0.72	0.54
Vulc5:35-19(2)	30	70.0	22.1	6.9	1.1	56	1893	270	5876	3.1	4.5	0.33	0.61	0.50	0.21	1.71	1.01	0.74
Vulc5:35-22(4)	50	77.4	18.9	3.0	0.7	61	886	295	8150	1.8	0.3	0.01	0.04	0.12	0.07	0.82	0.64	0.57
Vulc5:35-30(8)	40	74.7	20.1	4.3	1.0	54	779	321	8955	3.8	0.3	0.02	0.12	0.17	0.09	1.16	0.79	0.89
Vulc5:37-3(2)	75	82.7	13.9	2.4	0.1	84	1335	367	8275	1.1	3.2	0.05	0.56	0.58	0.30	1.78	0.98	0.78
BOUVET F.Z.																		
AII107:40-6(5)	40	78.2	18.1	3.4	0.3	50	244	342	10227	1.2	0.1	0.01	0.02	0.05	0.02	0.55	0.46	0.57
AII107:40-8(6)	40	77.2	19.6	3.1	0.1	70	363	285	6534	0.7	0.1	0.04	0.13	0.08	0.04	0.48	0.50	0.63
AII107:40-11(9)	65	81.1	15.5	2.9	0.4	54	443	297	8392	0.5	0.1	0.01	0.02	0.05	0.03	0.70	0.57	0.70
AII107:40-13(5)	60	78.7	18.8	2.0	0.5	53	368	291	8519	1.2	0.1	0.01	0.01	0.05	0.03	0.38	0.43	0.46
AII107:40-27(5)	60	80.7	15.5	3.3	0.4	73	326	274	6518	0.8	0.2	0.02	0.04	0.07	0.03	0.52	0.52	0.53
ISLAS ORCADAS F.Z.																		
IO11/76:56-57(4)	25	69.6	24.5	4.3	1.7	73	1608	301	6042	0.6	2.2	0.02	0.48	0.60	0.27	1.79	1.01	1.10
IO11/76:56-10(10)	20	73.4	18.7	7.2	0.7	44	1420	278	6925	0.6	1.4	0.02	0.47	0.48	0.30	2.12	1.57	1.57
IO11/76:56-54(4)	25	69.0	21.7	8.2	1.1	57	1606	276	7793	1.4	2.8	0.06	0.60	0.63	0.34	2.17	1.58	1.49
IO11/76:58-34(4)	25	70.0	25.9	3.5	0.6	52	1113	278	6053	20.2	1.1	1.55	0.60	0.34	0.18	1.46	1.01	0.69
EAST OF SHAKA F.Z.																		
PS86:6-37(3)		66.6	21.9	10.4	1.1	52	2674	293	6829	5.4	11.0	0.87	2.16	1.37	0.56	2.65	1.70	1.67
ANDREW BAIN F.Z.																		
Prot5:15-90(8)	20	70.0	22.0	7.0	1.0	41	1083	290	9462	0.4	0.5	0.02	0.24	0.39	0.18	1.18	0.69	0.74
PRINCE EDWARD F.Z.																		
Prot5:19-2(8)	5	72.9	23.4	3.1	0.6	78	598	258	7433	8.0	2.1	1.02	0.58	0.26	0.12	0.95	0.71	0.62
DISCOVERY II F.Z.																		
Prot5:29-26(6)	40	63.5	28.6	7.0	0.9	74	527	276	7765	1.2	0.9	0.07	0.13	0.13	0.06	0.56	0.51	0.48
INDOMED F.Z.																		
Prot5:38-1(3)	40	69.4	24.8	5.1	0.7	62	567	282	7124	0.6	0.4	0.03	0.12	0.15	0.08	1.02	0.74	0.54
ATLANTIS II F.Z.																		
RC27:9-6-3 (7)	35	67.1	25.6	6.6	0.6	55	1525	305	7051	1.2	2.1	0.04	0.47	0.62	0.33	1.93	1.17	0.78
RC27-9:6-8(8)	35	66.6	25.8	6.6	0.8	47	1702	338	6959	0.6	1.7	0.03	0.57	0.76	0.39	2.67	1.72	1.74
RC27-9:25-142(6)	40	56.1	33.5	9.0	1.5	38	1843	308	7334	1.2	3.1	0.11	0.91	0.92	0.47	2.40	1.50	1.63
Starting bulk mantle composition							1090				7.0	0.92	0.822	0.328	0.129	0.612	0.4	0.4
chondrite normalizing values[4]					5.76	436	56.7	2650	7.91	3.69	0.616	0.457	0.149	0.056	0.245	0.16	0.159	

1 - numbers in parentheses are number of cpx grains analyzed by ion probe in each sample. Each grain analysis is an average of up to three points, depending on grainsize.
2 - reported alteration is mainly serpentinization, but in a few cases includes clay minerals.
3 - Modal analyses done by point counting ~2200-3000 points per thin section.
4 - chondrite normalizing values from *Anders and Ebihara* [1982].

secondary ions were mass analyzed by a double-focusing mass spectrometer with a high-energy offset of -90 eV and an energy bandpass of ±10 eV for a net secondary accelerating voltage of 4400-4420 eV (a technique known as energy filtering used to suppress molecular ion interferences [*Shimizu et al.*, 1978]) and were detected and counted by a 17-stage Allen type electron multiplier in pulse counting mode. For rare earth element (REE), Sr, Zr, and in some cases Ti, a primary beam with 1~2 nA current was focused to a spot of 12-20 μm. Energy filtering of -35 eV for REE and -90 eV for Ti, Sr, and Zr was used with an energy bandpass of ±10 eV. Empirical relationships between secondary ion intensities and concentration (working curves) were used to determine trace element concentrations. Sources of uncertainty include counting error, precision and accuracy of standard analyses used in constructing working curves, acquisition of mass peaks, and magnet drift. Overall accuracy and precision of the data (Table 3) are believed to be ±5~10% for Sc, Ti, Cr, and V; ±10~15% for Sr and Zr; ±10~20% for light REE; and ±10~15% for middle and heavy REE.

RESULTS

Modal clinopyroxene in the studied peridotites ranges from ~2 to ~12 vol % (Table 3) and is correlated with Ti and Zr (Figure 2). Clinopyroxenes are least abundant and most depleted in incompatible elements in peridotites closest to the Bouvet hotspot and have the highest Mg/(Mg+Fe) (Mg #) and among the lowest Ce concentrations (Figure 3), consistent with greater degrees of melting of the shallow mantle in these areas.

Incompatible element concentrations in peridotite clinopyroxenes range from 200 to 3500 ppm Ti, 0.4 to 8.0 ppm Sr, and 0.1 to 14.0 ppm Zr. The lowest incompatible element and highest compatible element concentrations invariably occur in samples nearest the Bouvet hotspot, as illustrated by concentration minima in the incompatible elements titanium, zirconium, dysprosium, and a concentration maximum in the compatible element scandium in clinopyroxene plotted as a function of distance from the Bouvet Hotspot

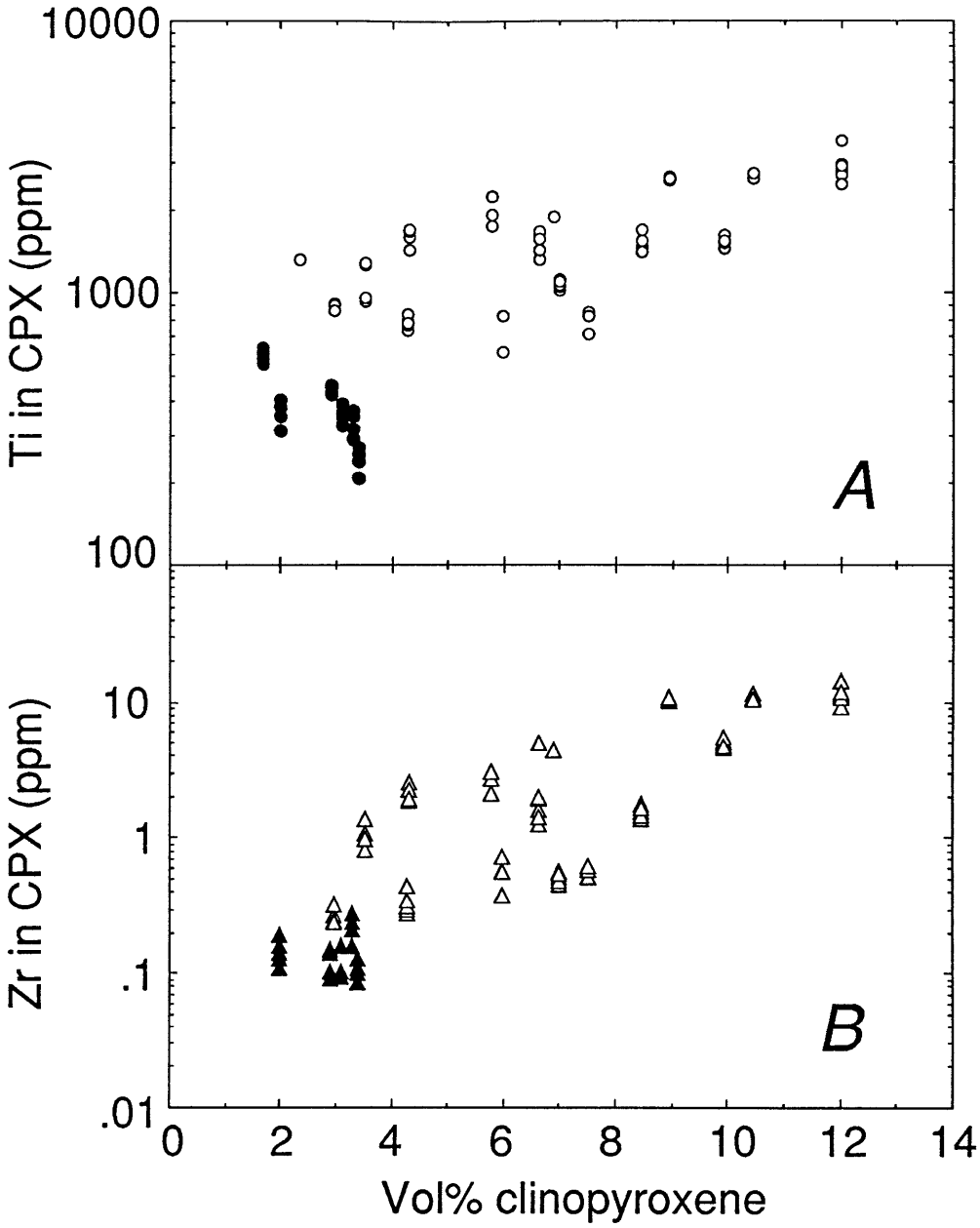

Figure 2. Modal clinopyroxene in peridotite samples plotted versus (a) Ti, and (b) Zr in clinopyroxenes. Individual data points composing the averages reported in Table 3 are plotted. Clustering of points gives an indication of internal sample homogeneity. Solid symbols are those from the Bouvet FZ close to the Bouvet hotspot.

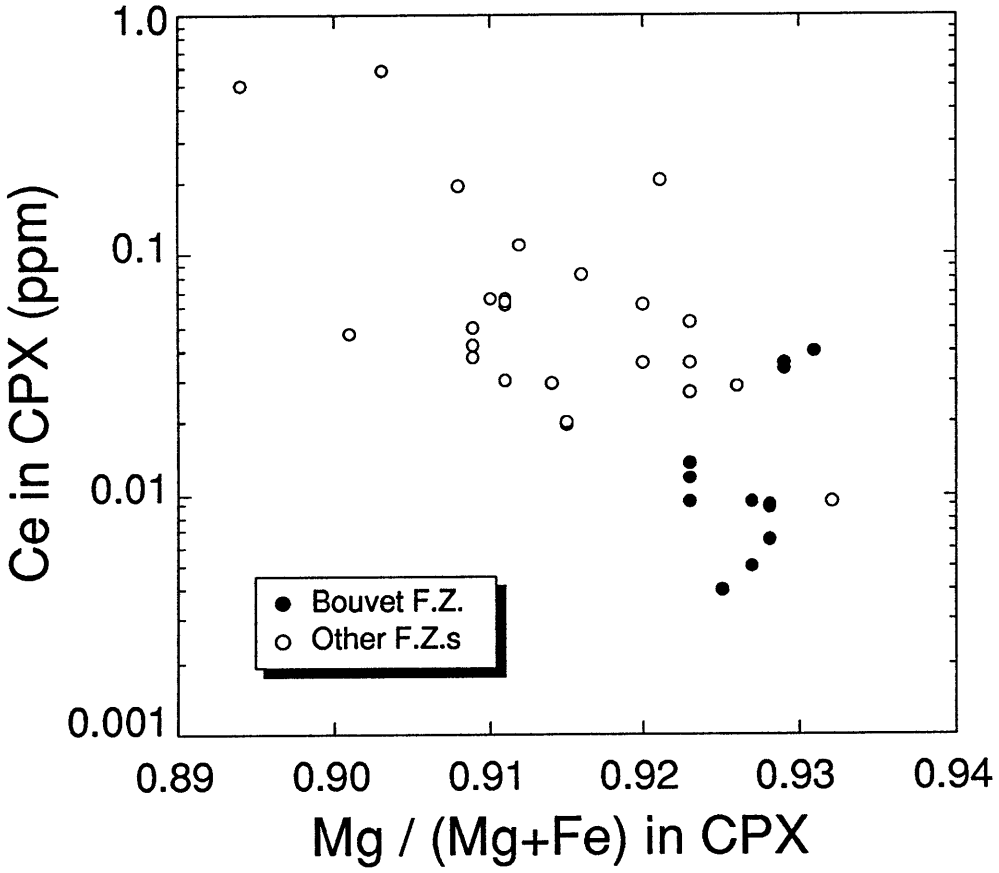

Figure 3. Molar Mg/(Mg+Fe) (Mg #) versus Ce in peridotite clinopyroxenes. Depletion in Ce accompanied by an increase in Mg # is consistent with REE and Ti-Zr data and illustrates the residual nature of the samples and greater incompatible element depletion near the Bouvet hotspot. Solid symbols are data from the Bouvet Fracture Zone.

(Figure 4). Though somewhat fewer data exist for the Marion hotspot region, the same relationship is suggested.

Most clinopyroxene REE patterns in this study are highly fractionated, but they differ between dredge hauls in their overall shape and degree of depletion. All analyzed samples from the Bouvet Fracture Zone near the Bouvet Hotspot exhibit steeply sloping light to middle REE (LREE-MREE) depleted patterns. These patterns are quite similar to those from the Discovery II Fracture Zone peridotites, dredged near the Marion Hotspot (Figure 5).

Clinopyroxenes from nonhotspot peridotites, on the other hand, generally exhibit steeply plunging LREE with flat to humped middle (MREE) to heavy rare earth elements (HREE) quite distinct from Bouvet and Discovery II FZ samples (Figure 6). Also plotted in Figure 6 are shaded fields representing hypothetical liquids in equilibrium with the peridotite clinopyroxenes, calculated using the partition coefficients listed in the appendix, and spatially associated MORB. The field for hypothetical liquids illustrates that most REE concentrations in clinopyroxene are inconsistent with simple clinopyroxene-MORB equilibrium.

Samples Prot 5: 19-2 from the Prince Edward Fracture Zone near the Marion hotspot and IO11/76: 58-34 from the Islas Orcadas Fracture Zone east of the Bouvet hotspot, exhibit LREE inflections in their REE patterns (Figure 7). Other samples from the same fracture zones do not show the same inflections, and we are analyzing other samples from the same dredge hauls to establish the scale of this geochemical anomaly.

High field strength elements (HFSE), Ti and Zr, in peridotite clinopyroxenes are depleted relative to adjacent REE in incompatible element diagrams. These negative anomalies are illustrated by plotting Ti/Ti* versus Zr/Zr* (Figure 8), where Ti and Zr are chondrite normalized concentrations of those elements and Ti* and Zr* are calculated as $(Eu_n+Dy_n)/2$ and $(Nd_n+Sm_n)/2$, respectively [*Salters and Shimizu*, 1988]. Values less than 1.0 indicate negative anomalies, the smaller the value, the larger the anomaly.

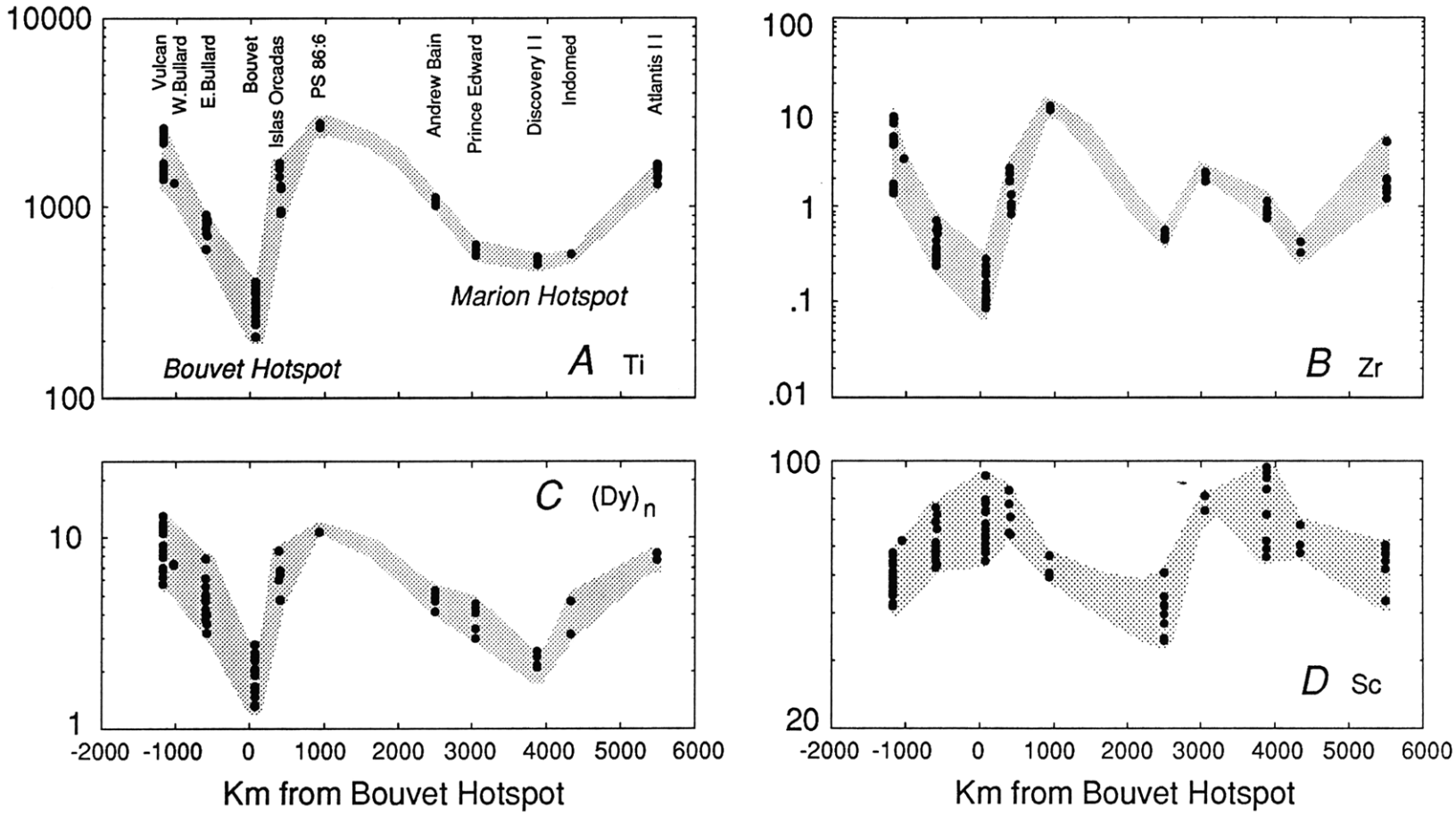

Figure 4. Distance along the AAR and SWIR relative to the Bouvet hotspot versus (a) Ti, (b) Zr, (c) (Dy)n, and (d) Sc in clinopyroxenes. Well-defined minima in incompatible elements Ti, Zr, and (Dy)n and a maximum in the compatible element Sc in the upper mantle diopsides nearest the two hotspots are evident.

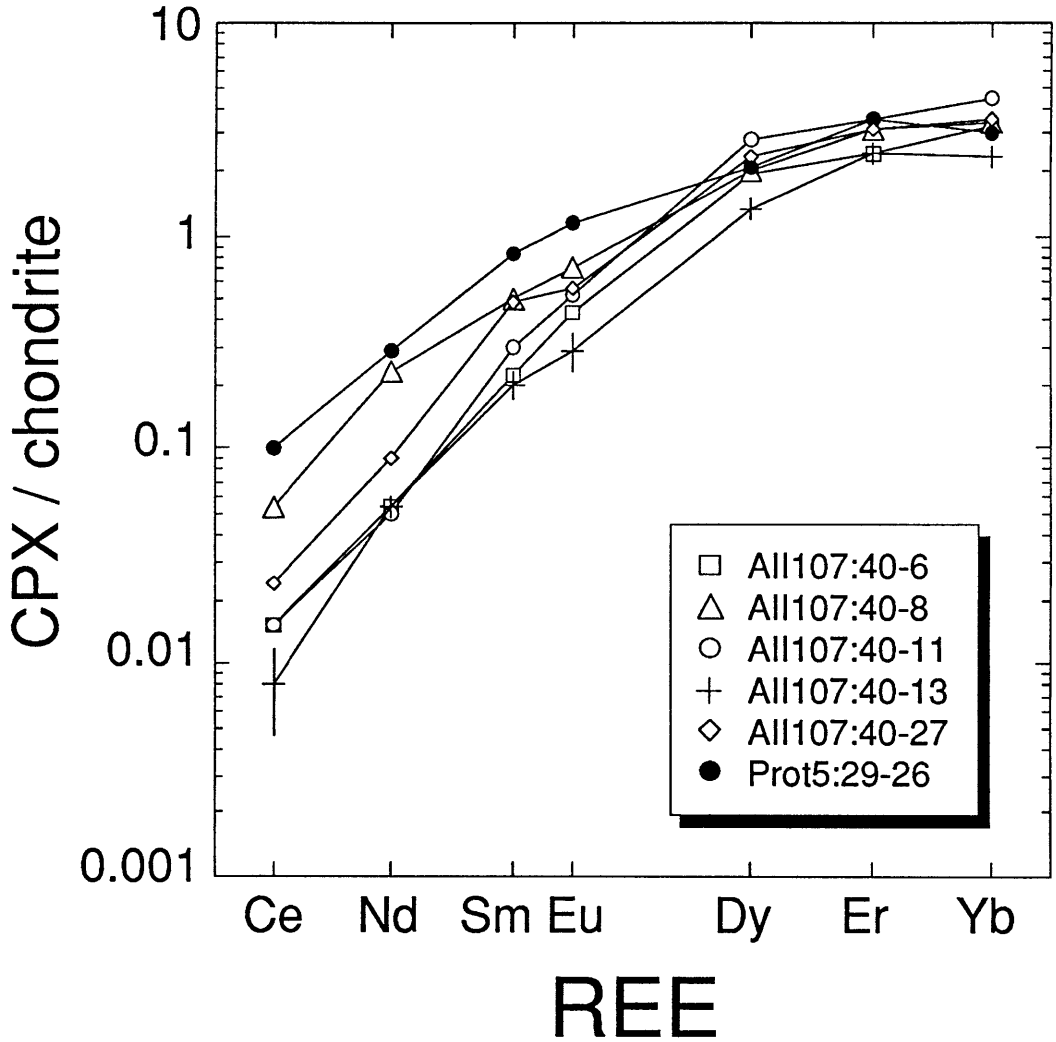

Figure 5. Chondrite-normalized REE concentrations in diopsides from hotspot-proximal peridotites from Bouvet Fracture Zone (AII107) and Discovery II Fracture Zone (Prot 5). REE patterns in both locations have steeply sloping, LREE- depleted patterns unlike those from other sampled locations. Typical error bars are shown on AII107:40-13.

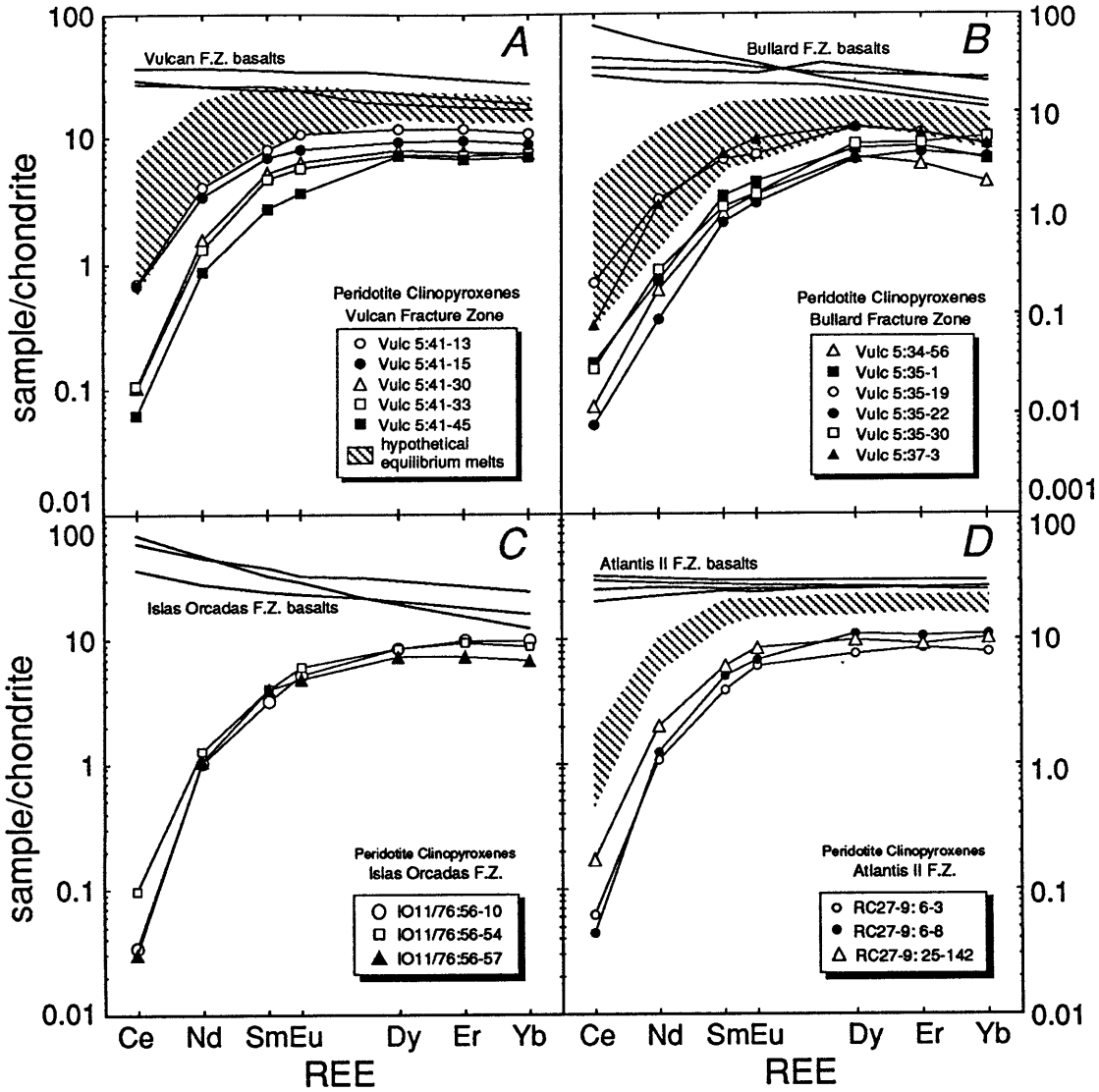

Figure 6. Chondrite-normalized REE concentrations in non-hotspot peridotite clino-pyroxenes. (a) Five samples from a single dredge haul in the Vulcan Fracture Zone on the AAR. Note flat HREE and sharp LREE depletions. (b) Six samples from three dredge hauls in East Bullard FZ (34 and 35) and West Bullard FZ (37). Note pronounced LREE depletions and hump at Dy (see text for detailed discussion). (c) three samples from the Islas Orcadas FZ, and (d) three samples from the Atlantis II FZ. Also shown are REE patterns in spatially associated basalts (data from leRoex et al. [1983, 1985] and K. Johnson, unpublished data, 1989) and fields representing hypothetical melts in equilibrium with the peridotite clinopyroxenes (cross-hatched).

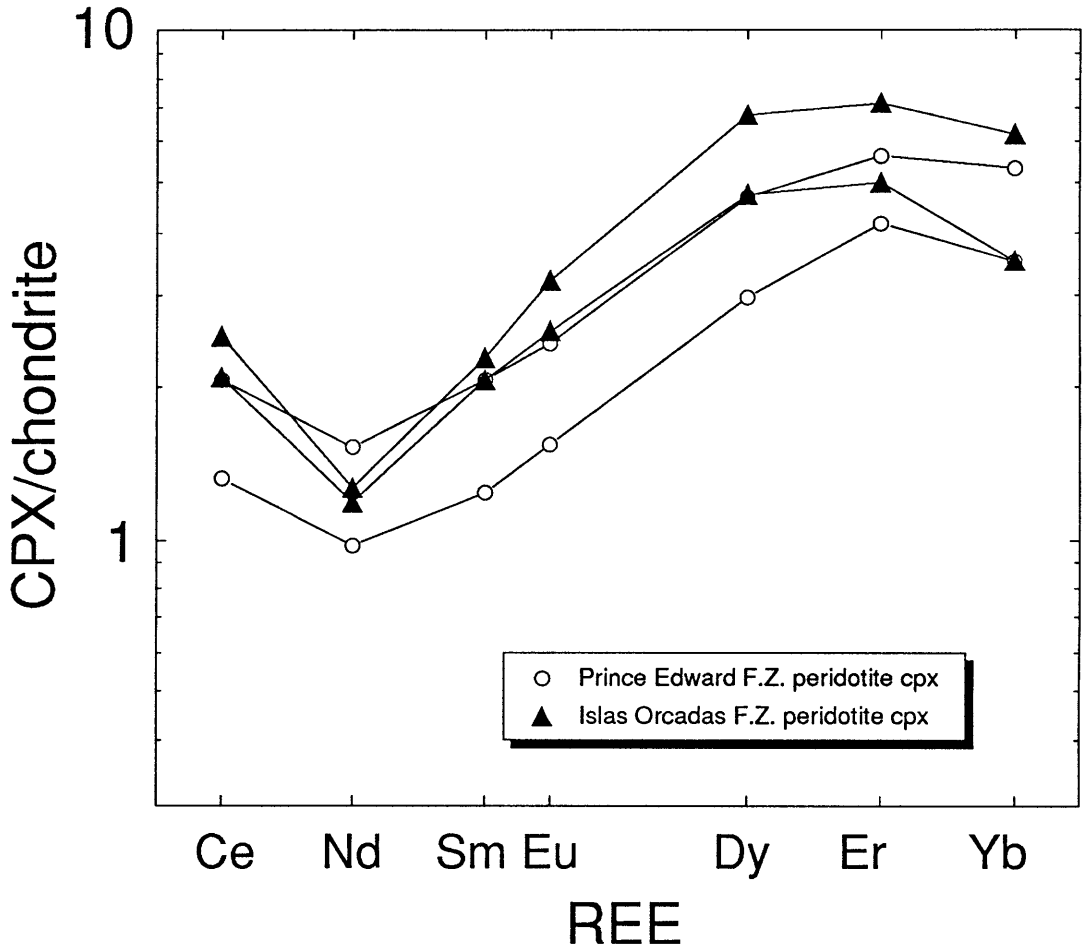

Figure 7. Chondrite-normalized REE concentrations in individual peridotite clinopyrox-enes from Prot 5:19-2 (Prince Edward FZ) and IO11/76:58-34 (Islas Orcadas FZ) showing positive LREE anomalies. Similar inflections were theoretically modeled for early stages of metasomatism of a depleted mantle [Navon and Stolper, 1987].

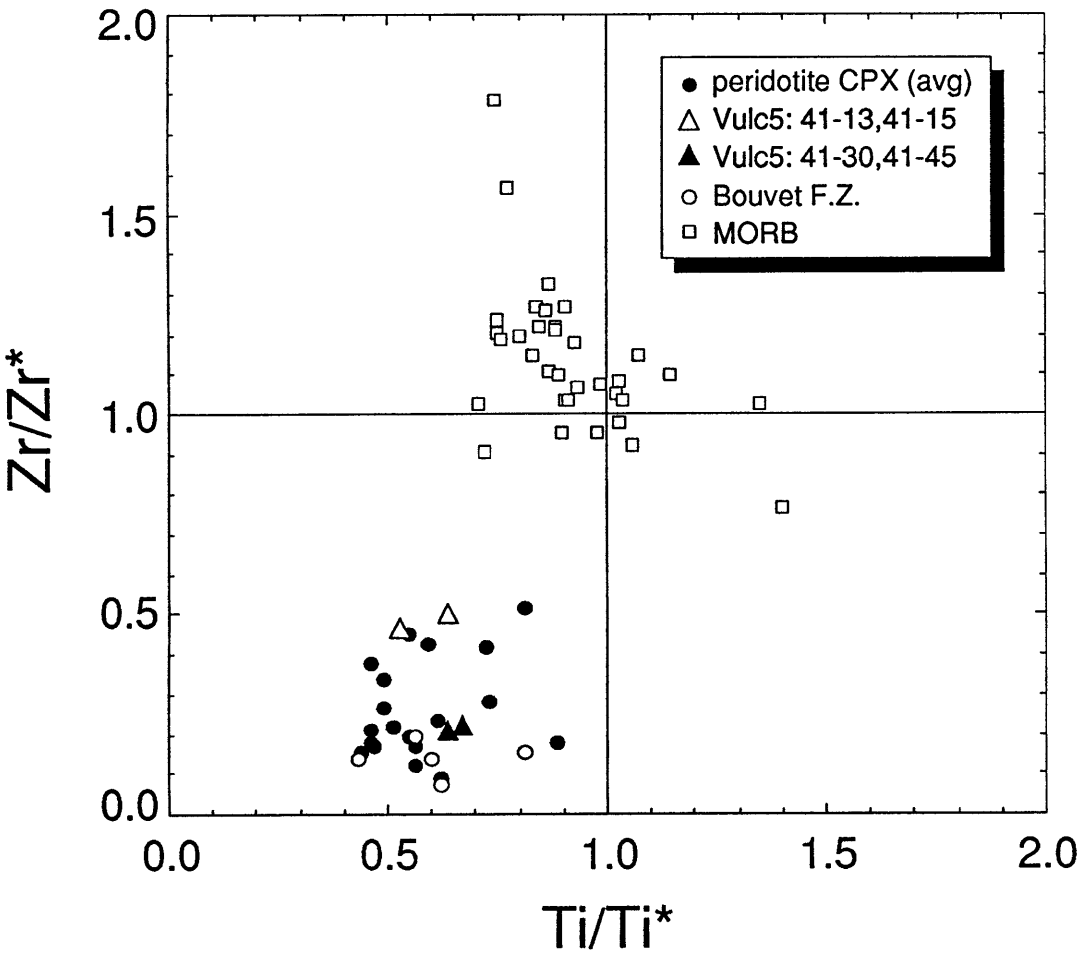

Figure 8. Ti/Ti* versus Zr/Zr* calculated according to the procedure discussed in the text. Data points are sample averages and illustrate the ubiquitous negative HFSE anomalies relative to adjacent REE in clinopyroxenes in a typical incompatible element diagram sequence. Open circles are Bouvet FZ samples and triangles are Vulcan FZ samples. Primitive MORB data from Shibata et al. [1979], Sun et al. [1979], Humphris et al. [1985], and leRoex et al. [1983]. See text for discussion.

Primitive MORB (data from *Shibata et al.* [1979], *Sun et al.* [1979], *le Roex et al.* [1983], and *Humphris et al.* [1985]) cluster around 1.0, rarely exhibiting negative Zr anomalies but often exhibiting negative Ti anomalies (Figure 8). Zr/Zr* in clinopyroxenes from the Bouvet FZ peridotites are among the lowest (open circles in Figure 8), and those in samples from the Vulcan FZ range from relatively small anomalies in the less depleted samples, Vulc5: 41-13 and 41-15 (open triangles), to larger anomalies in the more depleted samples, Vulc5: 41-30 and 41-45 (solid triangles). HFSE depletions in mantle clinopyroxenes from a variety of geologic settings have been described [*Salters and Shimizu*, 1988], and it is now clear that these depletions are pervasive phenomena in the subridge oceanic upper mantle as well. This is an important observation because the major part of their data base is mantle xenoliths for which the provenance and petrogenetic evolution are generally unclear, whereas the geologic and tectonic setting of abyssal peridotites is well constrained.

In summary, the REE, Ti, and Zr data indicate that most of the studied abyssal peridotites could not have been in equilibrium with MORB. Furthermore, if MORB and abyssal peridotites are both descendents of pristine upper mantle lherzolite, they must be related by processes more complicated than simple equilibrium. In order to understand the process producing the extreme depletions of abyssal peridotites and to determine whether this process is capable of producing liquids with MORB compositions, forward melting models were computed.

MELTING MODELS FOR ABYSSAL PERIDOTITES

Melting equations relate incompatible element concentrations in residual solids and derived liquids to the type (e.g. Rayleigh [fractional], incremental, or batch) and degree of melting and can be used to test what type of melting abyssal peridotites have experienced and whether they are related to MORB by this melting process.

Peridotite clinopyroxenes were compared to models calculated from non-modal batch, incremental, and fractional melting equations derived from *Gast* [1968] and *Shaw* [1970, 1977]. In batch melting, solid and liquid fractions remain together throughout the entire melting interval, while in fractional melting infinitesimal increments of melting occur, accompanied by instantaneous segregation of the melt from the solid residue. Conceptually intermediate to these two theoretical end-members is incremental melting in which small, but finite, increments of melting and segregation occur, with a new starting composition employed after each segregation event. Equilibrium partitioning of elements is maintained in all models. Fractional melting depletes the residue in incompatible elements far more effectively than batch melting does and the two processes are easily distinguished in rare earth element diagrams and plots of incompatible elements in the residues [*Gast*, 1968]. Although compositions of infinitesimal fractions of melt produced by fractional melting are quite different from large batches of melt produced by batch melting, liquids produced by the two melting processes are virtually indistinguishable if fractional melts are integrated or aggregated following segregation from the source [*Shaw*, 1970].

Model element abundances in clinopyroxene in the residual solid were calculated to enable direct comparisons with the present data (see appendix for description of method). The partitioning behavior of Ti, Zr, and REE is reasonably well known, and these elements were used in forward modeling calculations. The important input parameters in the models are starting bulk composition, partition coefficients, proportions of minerals in the bulk solid, and those contributing to the liquid. The model starting bulk composition is a LREE-depleted lherzolite (1.5x to 2.5x C1 chondritic [*Loubet et al.*, 1975]), based on Nd and Hf isotope compositions of MORB. The starting bulk composition is listed in Table 3, and all modeling calculations and results are reported in terms of cpx in the residue. Mineral melting proportions were taken to be those comprising peritectic melts in a four-phase peridotite assemblage and calculations were carried to 25% melting, prior to the elimination of cpx in the modeled peridotite assemblages (the Bouvet and Discovery II FZ samples are

modeled differently as discussed below). Starting mineral proportions are listed in the appendix.

Partition Coefficients

Partition coefficients used in the calculations are listed in the Appendix. Most of our chosen partitioning data for clinopyroxene and garnet are from experiments since intensive parameters can be controlled and equilibrium can be assessed. Coefficients were obtained from doped experiments that observe Henry's law behavior [*Grutzeck et al.*, 1974; *McCallum and Charrette*, 1978; *Terakado and Masuda*, 1979; *Nicholls and Harris*, 1980], experiments at natural concentration levels analyzed by isotope dilution, neutron activation, or X ray fluorescence of separated phases [*Shimizu and Kushiro*, 1975; *Fujimaki et al.*, 1984], or by ion or proton microprobes [*Green et al.*, 1989; *Johnson and Kinzler*, 1989]. Partitioning data for other phases in peridotites are taken from *Stosch* [1982], who measured $D_{REE}^{cpx/liq}$ in a large number of mantle xenoliths.

Despite the large number of studies on cpx/liquid partitioning, uncertainties still exist concerning the effects of pressure on partitioning behavior. While some studies report little or no pressure effect on $D_{REE}^{cpx/liq}$ (e.g., *Fujimaki et al.* [1984] and *Colson and Gust* [1989], low-Ca pyroxene), others report an increase in $D_{REE}^{cpx/liq}$ with increasing pressure [e.g., *Green and Pearson*, 1985]. Although moderate to high pressure partition coefficients [*Green and Pearson*, 1985; *Johnson and Kinzler*, 1989] are close to those determined from megacryst/host pairs [e.g., *Irving and Frey*, 1984], the "pressure" effect is unresolved. Partition coefficients used in the calculations are summarized in the appendix.

Model Results and Discussion

Ti and Zr concentrations in peridotite clinopyroxenes and in basalts from nearby ridge segments are plotted in Figures 9*a* and 9*b*, respectively. The wide concentration range and progressive increase in Ti/Zr with decreasing concentrations in the peridotite

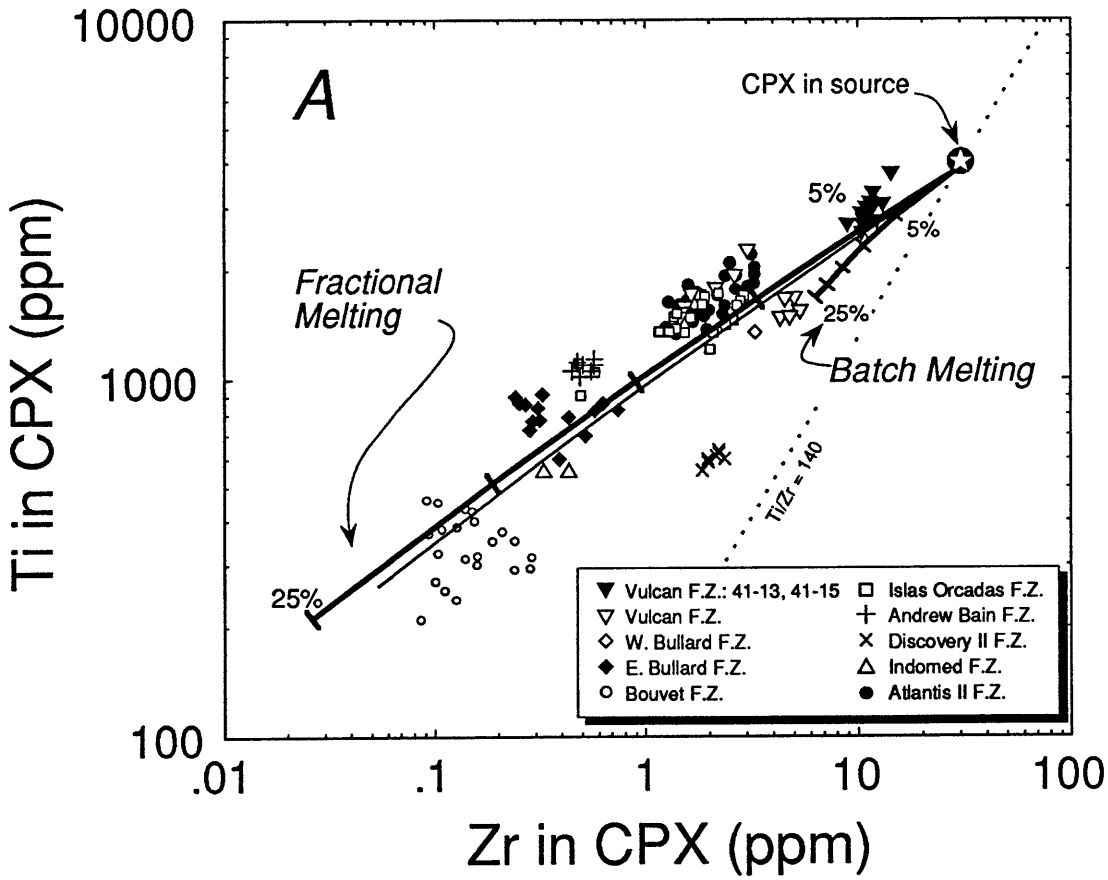

Figure 9a. Ti and Zr concentrations in peridotite clinopyroxenes. Also shown are model melting curves calculated using the procedure discussed in the text and appendix. The fine line subparallel to the fractional melting trend is the model for melting and segregation in 0.1% increments. Clinopyroxene data conform more closely to the model trend for the residue of fractional or incremental melting than to the batch melting trend. Ticks are at 5% intervals and refer to the total degree of partial melting. Also shown is a line for Ti/Zr = 140 to illustrate the efficiency of fractional melting and inefficiency of batch melting and fractional crystallization in changing this ratio.

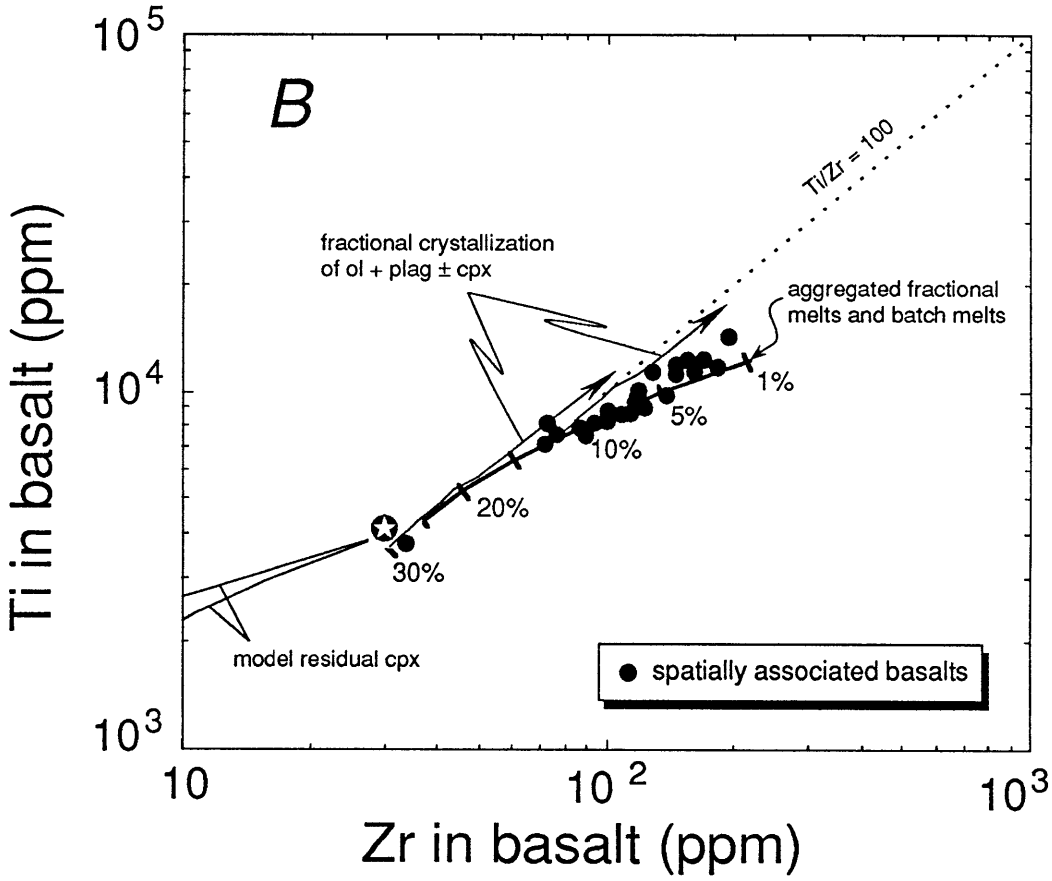

Figure 9b. Ti and Zr concentrations in basalts spatially associated with the studied peridotites. Model liquid curves for integrated or aggregated fractional melts and for fractional crystallization of these melts show that the full range of data can be produced by the combination of fractional melting, aggregation, and fractional crystallization. The curve for batch melts is not shown, but virtually coincides with that for aggregated fractional melts. Also shown is a line for Ti/Zr = 100 which is a near-chondritic value and is relatively constant in MORB. Data from leRoex et al. [1983, 1985].

clinopyroxenes is evident. Spatially associated MORB range from 3500 to 15,000 ppm Ti, 70 to 200 ppm Sr, and 40 to 200 ppm Zr. Assuming cpx/basaltic liquid partition coefficients of 0.35-0.49, 0.1, and 0.14-0.21 for Ti, Sr, and Zr, respectively [*Ray et al.*, 1983; *Fujimaki et al.*, 1984; *Dunn*, 1987; *Tormey et al.*, 1987; *Johnson and Kinzler*, 1989], hypothetical equilibrium liquid concentrations of 550-10,000 ppm Ti (0.09-1.7 wt %), 2.0-60 ppm Sr, and 0.7-100 ppm Zr are implied. Basaltic liquids with compositions near the upper end of these hypothetical ranges occur, but we are not aware of any basaltic liquids recovered from the ocean basins with compositions even approaching the lower end of the ranges.

Also plotted in Figure 9 are model melting curves calculated from the melting equations in the appendix and for melting in 0.1% increments (fine line subparallel to the fractional melting curve). The model starting composition (Table 3) was chosen to be consistent with a light REE depleted chondritic source. It is immediately evident that the broad range in Ti and Zr concentrations in the peridotite clinopyroxenes can not be achieved by batch melting to any reasonable degree (short curve in Figure 9*a*). Ti/Zr ranges from 250 in the least depleted clinopyroxene to 4000 in the most depleted, a change that can be produced by an additional ~18% fractional melting or ~20% incremental melting but cannot be produced by any amount of batch melting, as evidenced by only a minor deviation of the batch melting curve from the starting cpx Ti/Zr ratio of 140. The most depleted samples (Bouvet Fracture Zone) are consistent with a total of 20-25% fractional or incremental melting, the remainder of the samples ranging upward in concentration consistent with lower degrees of melting. This agrees well with the total range in melting predicted using the lever rule and the overall variation of modal mineralogy in these samples by *Dick et al.* [1984] providing model independent confirmation of the result. Samples Vulc 5: 41-13 and 41-15 are more enriched in Ti and Zr than other samples analyzed (Figure 9*a*), and it is not possible to determine whether they have formed by batch or fractional melting using the Ti-Zr model.

However, it will be shown below that REE can better discriminate between melting processes responsible for producing these less depleted compositions.

Melts produced by the above model calculations are compared to ocean floor basalt compositions in the studied areas (Figure 9*b*). The curved line is the integrated fractional melt composition at various degrees of melting. The composition of melts produced by batch melting define a line essentially coincident with the aggregated fractional melt line and are not shown for diagrammatic clarity. Arrows emanating from the melting curve are paths the liquid would follow during fractional crystallization of olivine + plagioclase ± clinopyroxene. Three points can be made from these diagrams: (1) Residual clinopyroxene compositions plot very close to the fractional melting end-member model, (2) Fractional melting, aggregation, and fractional crystallization are capable of producing the array of MORB found in the area where the peridotites were dredged, and (3) if melts are pooled, or otherwise aggregated prior to eruption, then MORB compositions are ineffective in deducing the melting process by which they formed.

Two end-member forward melting models were computed for REE as they were for Ti-Zr. The results are summarized as follows:

1. The extreme fractionation of REE observed in the data was never achieved by any degree of batch melting using reasonable starting compositions, mineral assemblages, or sets of $D_{REE}^{cpx/liq}$ (Figure 10*a*).

2. Fractional melting or incremental melting of very small (≤ 0.1%) increments totaling up to 10% melting in the spinel field alone produce model patterns with flat HREE consistent with data from Vulcan FZ (Figures 10*b* and 10*c*), Islas Orcadas FZ, and Atlantis II FZ (Figure 11). REE in integrated fractional liquids also resemble spatially associated MORB (Figure 10*d*). The results of the fractional and 0.1% incremental models differ only slightly from one another, as expected, and total degrees of melting for the Vulcan FZ samples deduced from REE modeling agree well with the values obtained from Ti-Zr modeling. Samples Vulc5: 41-13 and 41-15 are consistent with ≤5% fractional or

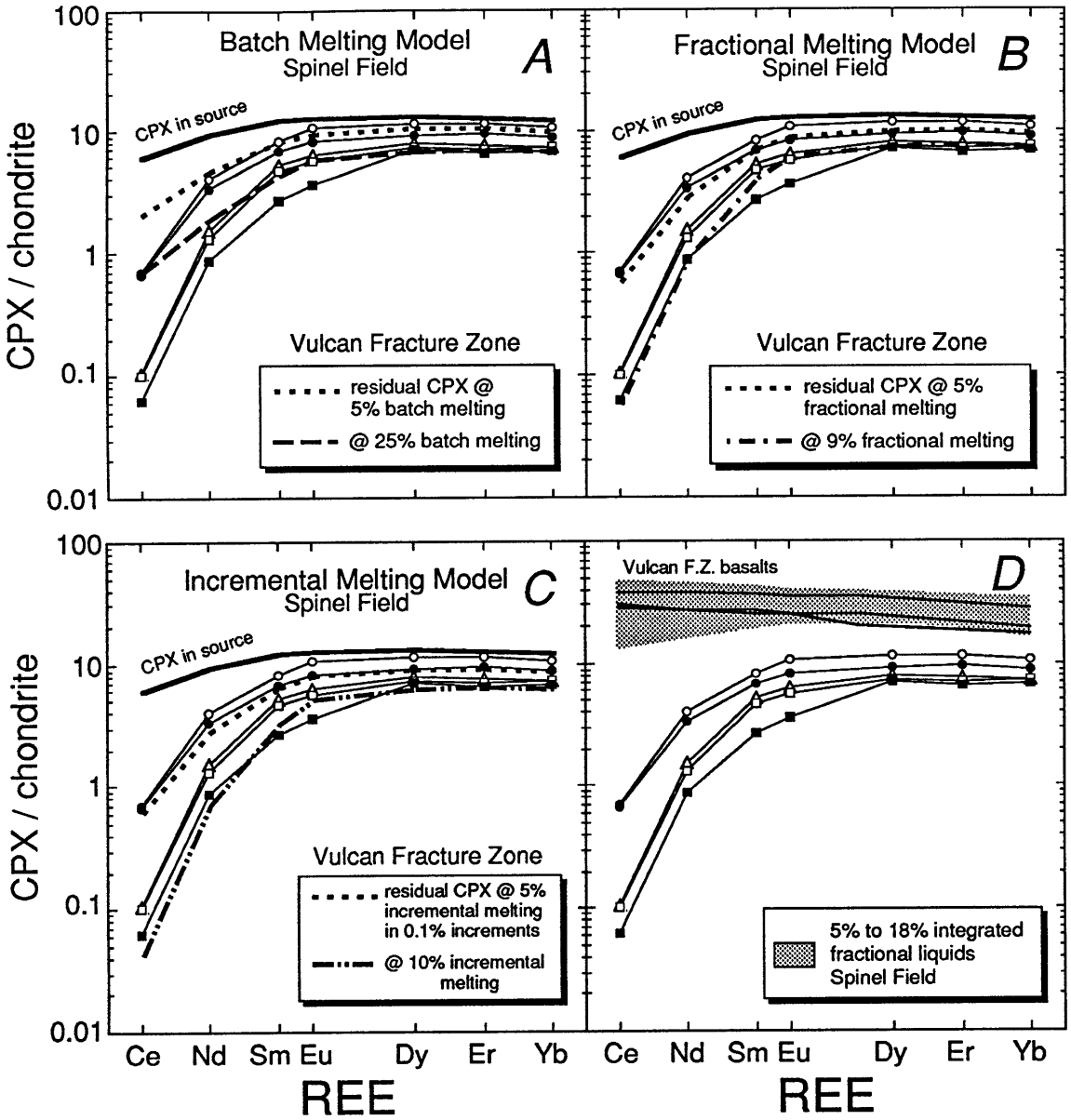

Figure 10. (a) Model batch melting residues of a depleted, 2.5x chondritic source calculated for a spinel peridotite assemblage (dashed lines) compared to REE data from Vulcan FZ peridotite clinopyroxenes showing that LREE depletions in the samples are too extreme to be modeled by batch melting. (b) The same data plotted with model fractional melting residues. (c) Residues formed by repeated melting and segregation of 0.1% melt increments to 5-10% total melting of the same source as in Fig. 10a and 10b show good agreement with peridotite clinopyroxenes. (d) The field for 5-18% integrated fractional liquids plotted with spatially associated basalts (data from leRoex et al. [1985]). Symbols as in Figure 6.

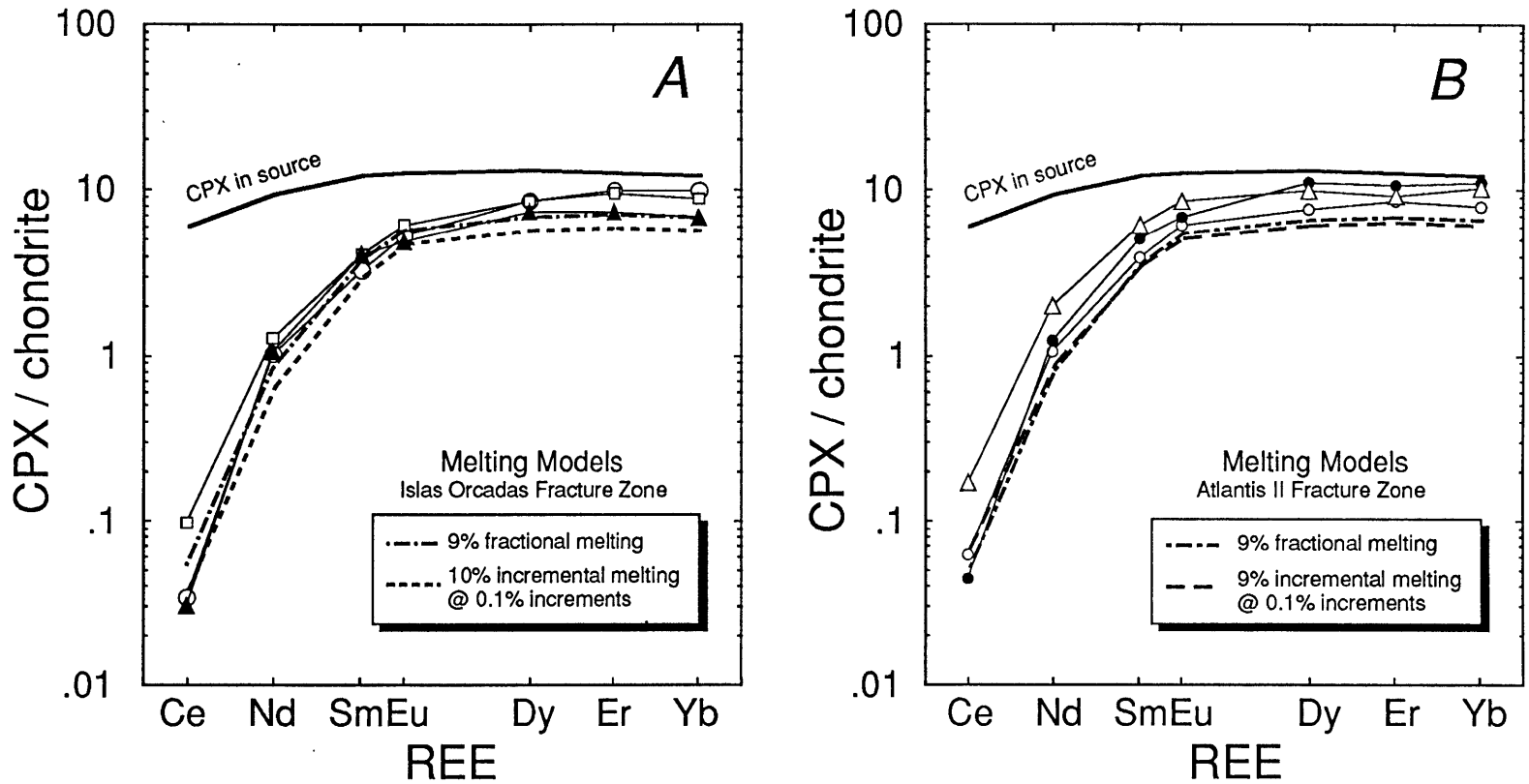

Figure 11. (a) Melting models for samples from the Islas Orcadas FZ calculated as in Figure 10 to illustrate the probable limits of fractional or incremental melting experienced. (b) Melting models for samples from the Atlantis II FZ calculated as in Figure 10 to illustrate the probable limits of fractional or incremental melting experienced. Symbols as in Figure 6.

incremental melting but not with batch melting, eliminating the ambiguity over the melting process noted above in the Ti-Zr modeling results.

3. Samples from Bouvet and Discovery II fracture zones, which are near hotspots, have distinct REE patterns (Figure 5) that are difficult to model by simple melting of four-phase peridotite assemblages. The major difficulty is that although the REE data are fractionated, they are not flat or humped in the MREE to HREE but are steeply inclined from HREE to LREE. Although the unusual patterns might reflect different source compositions from the other studied areas, the similarity of REE patterns in samples from the Bouvet and Discovery II fracture zones, both adjacent to hotspots but separated by several thousand kilometers, implies that the REE traits might be process related. To investigate this possibility, we constructed a multistage model involving the following steps: (1) relatively high degrees of melting in the garnet stability field leaving residual garnet, (2) decompression reaction of garnet to form 2 pyroxenes + spinel, and (3) continued melting in the spinel stability field and granule exsolution of cpx from opx.

If melting in the garnet stability field consumes most of the primary clinopyroxene, and decomposition of the residual garnet due to decompression into the spinel field produces clinopyroxene by the reaction:

$$Mg_2SiO_4\ (Ol) + Ca_{0.75}Mg_{2.25}Al_2Si_3O_{12}\ (Gt) = 2.5MgSiO_3\ (En) + MgAl_2O_4\ (Sp) + 0.75CaMgSi_2O_6\ (Di) \quad (1)$$

Clinopyroxene produced by this reaction would inherit the general shape of the garnet REE pattern, mitigated by interphase partitioning, but further melting of the residual lherzolite in the spinel stability field after recrystallization produces residual cpx with REE patterns that are more fractionated than the data.

Lindsley and Andersen [1983] showed that under cooling conditions similar to those assumed for the upper mantle-crust, orthopyroxene can exsolve up to 9 wt %

clinopyroxene, a figure that is consistent with our observations of exsolution lamellae in some samples. At relatively high temperatures where diffusion is sufficiently rapid, some portion of the exsolution lamellae may coalesce into discrete cpx grains in a process known as "granule exsolution" [*Lindsley and Andersen*, 1983]. Assuming that of the total exsolution in a sample no more than 50% granule exsolution results, a few weight percent of secondary (or tertiary) cpx may be formed. Using this model and the parameters stated in the appendix, we were able to approximate the shape of the hotspot-related peridotite clinopyroxene patterns (Figure 12).

4. REE patterns of clinopyroxenes in samples from the Bullard FZ display humps at the middle to heavy REE (Dy-Er) and cannot be modeled by melting in the spinel stability field alone using the same starting conditions and model parameters as in the Vulcan FZ modeling. However, when garnet lherzolite is used as the starting composition in the early stages of melting, model residual clinopyroxene compositions develop humps at the MREE to HREE (Figure 13). Modeling results show that fractional melting or ≤0.1% melting increments totaling 8-10% in the garnet stability field, followed by an additional 1-10% (total) fractional or incremental melting in the spinel stability field fit the data quite well.

It was found that using garnet in the melting assemblage for the Ti-Zr model did not significantly change the trajectory of the model melting curves, though it did shorten them somewhat. This means that the apparent degree of melting inferred from Figure 9*a* for samples from the Bullard, Bouvet, and Discovery II FZs, which were modeled using garnet, would be slightly higher. However, since we feel that the partiton coefficients for Ti and Zr in garnet are less well known than those for cpx, we decided not to include garnet model curves in Figure 9*a* since no quantitatively definitive improvement of the curves was achieved.

The degree of REE fractionation and development of the MREE hump are functions not only of the partition coefficients used in the model but also of the phase proportions both in the bulk solid and contributing to the melt phase. Variations in depth of melting within the

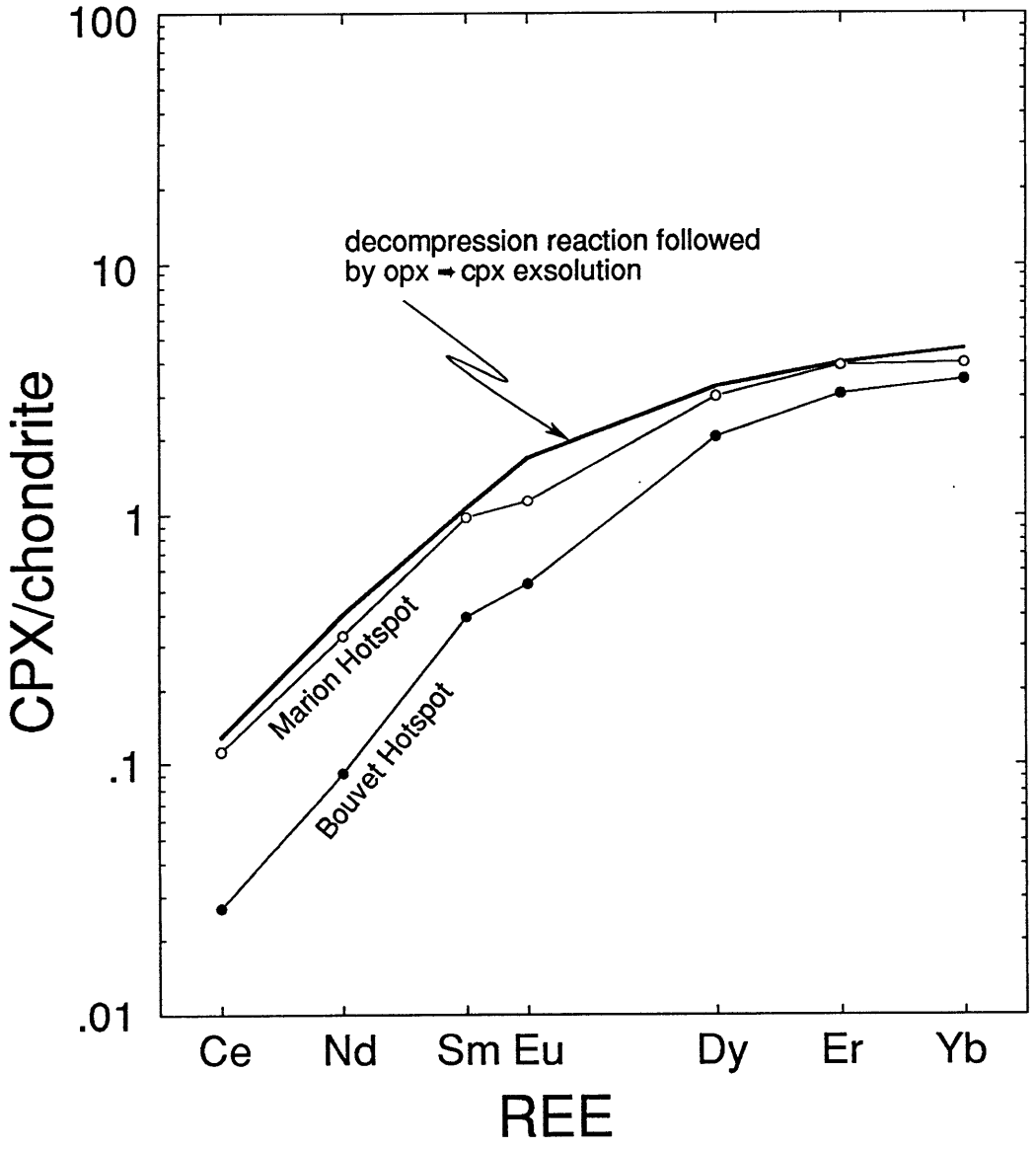

Figure 12. Model to explain the REE patterns observed in Bouvet FZ and Discovery II FZ peridotite clinopyroxenes calculated according to the scheme explained in the text for a multistage melting and exsolution process. Using the starting parameters in the appendix, melting starting in the garnet stability field leaving some residual garnet, followed by the reaction garnet = 2 px + spinel and cpx granule exsolution from opx can produce cpx with the REE pattern shown. The curves are averages of data presented in Figure 5.

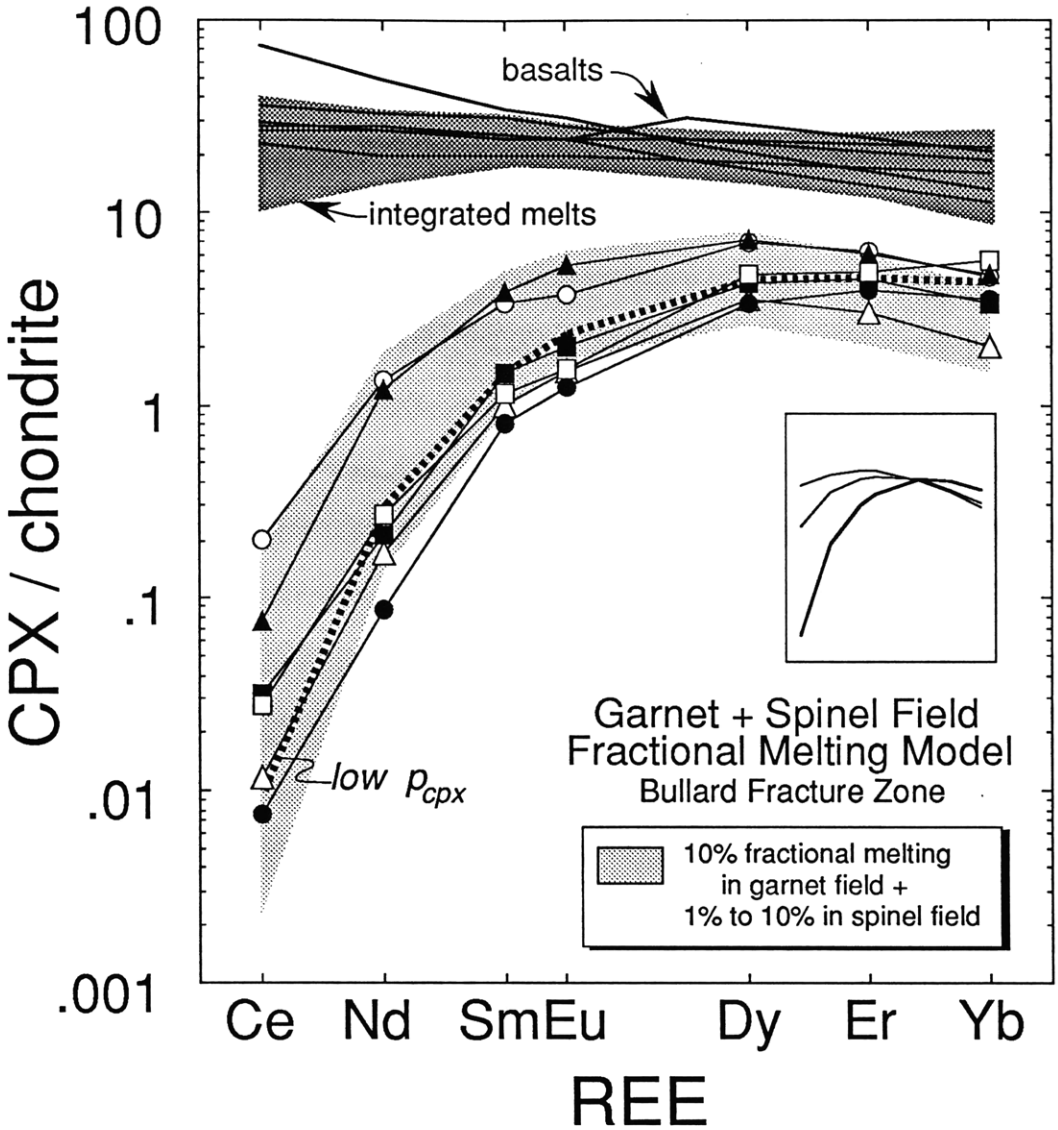

Figure 13. Melting model in which melting in small increments begins in the garnet stability field (up to 10% total melting in the garnet field) and continues up to an additional 10% in the spinel stability field. Data from East and West Bullard FZ peridotite clinopyroxenes (symbols) conform to both the shape (Dy hump) and to the total degree of melting inferred from Ti-Zr model (Figure 9a). Spatially associated basalts [leRoex et al., 1985] and two-stage integrated fractional liquids are also plotted. The dashed line is a residue model calculated using lower pcpx in the melting assemblage (see text for discussion). The inset is a schematic representation of the evolution of the MREE hump in clinopyroxenes with melting from 1% (upper line) to 10% (bolder line) in the presence of garnet as discussed in the text. Symbols as in Figure 6.

garnet stability field will control the position of the garnet-cpx eutectic [*Davis and Shairer*, 1965; *O'Hara and Yoder*, 1967] and consequently control the proportions of phases entering the melt (p_α). We used two different melting phase proportions in our models to determine the effect this has on clinopyroxene patterns and the result is shown in Figure 13. Model REE patterns calculated with p_{cpx}:p_{garnet} = 0.44:0.50 (higher pressures) develop more pronounced MREE humps at similar degrees of melting than patterns produced by p_{cpx}:p_{garnet} = 0.25:0.5 (lower pressures). The lightly stippled field in Figure 13 is calculated using p_{cpx}:p_{garnet} = 0.44:0.50 and the heavy, dashed line is calculated with p_{cpx}:p_{garnet} = 0.25:0.5. Integrated fractional liquids define a composition range encompassing spatially associated MORB from the Bullard Fracture Zone (Figure 13).

DISCUSSION

Correlation between peridotite major element compositions and proximity to hotspots has recently been demonstrated [*Dick et al.*,1984; *Dick*, 1989]. Peridotites dredged from closest proximity to hotspots on the Southwest Indian and Mid-Atlantic ridges have higher modal olivine, higher Cr/(Cr+Al) in spinel, higher Mg # and lower Al_2O_3 in enstatite, and lower Na_2O in diopside compared to those dredged away from hotspots [*Dick et al.*, 1984; *Dick*, 1989]. The same relationship is reflected in the abundances of incompatible trace elements in clinopyroxenes (Figure 4) and in the inverse correlation between Mg # and Ce in cpx (Figure 3).

These observations are consistent with higher degrees of melting in the upper mantle nearest to hotspots. Thus it follows that chemically and isotopically enriched basalts erupted at mid-ocean ridges near hotspots [*Hart et al.*, 1973; *Schilling et al.*, 1983; *leRoex et al.*, 1983] are not related in a simple way to the spatially associated, highly depleted subridge upper mantle. While enriched basalts erupted near hotspot-ridge intersections may be produced by melting a heterogeneous mantle composed of incompatible element-depleted and -enriched components [*leRoex et al.*, 1983], it appears that the hotspot-

proximal peridotites in the present data set represent the depleted component and have experienced the highest degrees of melting and depletion because of the hotspot influence. If hotspots impose higher ambient temperatures on the mantle, then melting would be more extensive and would begin deeper. This is consistent with the interpretation of modeling results that Bouvet FZ and Discovery II FZ peridotites experienced some melting in the garnet stability field. Some samples away from hotspots are consistent with melting in the spinel field alone since a slightly lower mantle temperature will result in initiation of melting at lower pressure, i.e., in the spinel stability field [*O'Hara et al.*, 1971; *McKenzie and Bickle*, 1988].

The influence of garnet in the melting assemblage is not restricted to hotspot areas. Based on modeling results and on the observed shape of REE patterns in Vulc 5: 34-56, 35-1, 35-19,and 37-3 from the Bullard FZ and on modeling results, melting in these samples commenced in the garnet stability field and continued into the spinel field up to ~17% total melting. Theoretical models for subridge melting and studies of alpine massifs also conclude that melting commences in the garnet field and does not exceed 25% [*Loubet et al.*, 1975; *Ahern and Turcotte*, 1979; *McKenzie*, 1984; *Nicolas*, 1986; *McKenzie and Bickle*, 1988]. Additional convincing support for the involvement of garnet in mid-ocean ridge basalt petrogenesis comes from a recent study of Hf and Nd isotopes in MORB [*Salters and Hart,* 1989] which concluded that the observed isotopic covariations are consistent with garnet in the source of ocean ridge basalts.

Of the samples that have experienced >15% melting based on Ti-Zr modeling, all but one are modeled by early melting in the garnet stability field. This implies that if total melting is >15% in a sample, then melting began in the garnet stability field. This has important thermal implications in light of recent theoretical models for melt generation at spreading centers [*McKenzie and Bickle*, 1988]. For melting to begin in the garnet stability field in the thermal environment proposed by *McKenzie and Bickle* [1988], the potential temperature of the mantle must be ~50°C hotter than the 1280°C they predict. Enhanced

melting starting in the garnet field in the hotspot related samples may be explained by higher temperatures, but deeper melting away from hotspots may call for a different explanation. The model of *McKenzie and Bickle* [1988] would change if fractional, rather than batch, melting equations were used since the mantle solidus would increase with each fraction of melt extracted; *McKenzie and Bickle* [1988] themselves believe that batch melting is unrealistic. A more realistic model requires knowledge of latent heats of fusion at different pressures, the oceanic geothermal gradient, and changes in the mantle solidus with degree of depletion and fractional melt extraction. Since all of their assumptions of such parameters are based on available experimental petrology data, which are essentially batch melt compositions, a more realistic theoretical fractional or incremental melting model cannot be constructed at this time.

If melting beneath fracture zones is subdued relative to melting beneath ridge centers [*Fox et al.*, 1980; *Phipps Morgan and Forsyth*, 1988], then it is expected that the high degrees of melting we infer for hotspot-proximal peridotites sampled in fracture zones would be even higher beneath the ridge axis. It should also be noted that *Phipps Morgan and Forsyth* [1988] predicted on the basis of numerical experiments that melting should commence at deeper levels beneath fracture zones than beneath ridge centers. Our assertion that garnet was involved in the early melting history of some fracture zone abyssal peridotites lends support to their hypothesis, although we cannot at this point comment on the depths of melting at ridge centers.

LREE-enriched melts from an enriched component of the upper mantle or from melting in the garnet stability field might be responsible for the unusual REE and Sr abundances in IO11/76: 58-34 and Prot 5: 19-2 (Figure 7). The LREE inflections in these samples are probably not primary since they do not resemble the partitioning behavior of REE in any phase present in the samples. However, they could be evidence for a limited extent of interaction between the depleted peridotite and a LREE-enriched liquid. Worth noting is the similarity of our observed patterns in these samples and those predicted by *Navon and*

Stolper [1987, Figure 4] for residual mantle undergoing metasomatism by incompatible element enriched melts. The fact that two separate volumes of mantle show nearly identical LREE anomalies implies that the process may be common under ocean ridges.

The mechanism creating negative HFSE anomalies in peridotite clinopyroxenes, but not in MORB, remains a puzzle. As *Salters and Shimizu* [1988] noted, basalts carrying many of the intraplate xenoliths do not show corresponding HFSE depletions, a characteristic observed and heretofore associated only with magmas formed above subduction zones in continental and island arcs. Most published cpx/liquid partition coefficients for REE, Ti and Zr do not exhibit negative Ti and Zr anomalies relative to adjacent REE in an incompatible element diagram sequence. Thus, if the source composition does not have HFSE anomalies, and if no phase in the residual assemblage preferentially partitions both Ti and Zr into its structure over REE, then melting will not produce negative HFSE anomalies in clinopyroxene and flat patterns in the derived liquids. The fact that samples from the Bouvet FZ, which are the most depleted in incompatible elements, also exhibit the largest negative HFSE anomalies, and that anomalies in less depleted samples from the Vulcan FZ (Vulc5: 41-13 and 41-15) are smaller than those in more depleted samples (Vulc5: 41-30 and 41-45; Figure 8) are both significant. Taken together, these observations imply that the anomalies grow with increasing degrees of melting, which in turn implies that $D_{Zr}^{cpx/liq}$ is lower than adjacent D_{REE}. Inspection of the melting equations in the appendix shows that a negative Zr anomaly of the observed magnitude can arise by decreasing P_{Zr} or D_{o}^{Zr}. This change can be effected by decreasing $D_{Zr}^{cpx/liq}$ from the "nonanomalous" value of 0.20 to a value of 0.17, a change well within the range of reported $D_{Zr}^{cpx/liq}$. Figure 8 also illustrates that Ti/Ti* does not decrease with increased melting and that most MORB have Zr/Zr* > 1.0 and Ti/Ti* < 1.0. This implies that Ti and Zr do not behave identically as is often assumed in discussions of HFSE. However, a model that accounts for the characteristic incompatible element patterns of both peridotite clinopyroxenes and MORB requires a better understanding of MORB source

characteristics, of the partitioning of elements at different pressures in the upper mantle, and of the reactions between migrating melts and residues.

REE and Ti-Zr concentrations taken separately are consistent with a model of repeated melting and segregation of ≤0.1% increments, totaling from 5-25% melting, of a LREE-depleted (chondrite-normalized) source. Thus it appears that the melting process in nature approaches fractional fusion. Models that utilized increments of batch melting greater than 0.1% failed due to their inability to fractionate REE sufficiently to reproduce the data. Given uncertainties in the data and in the starting model parameters, melt increments may range from «0.1% to as much as 0.3%. Retention of «0.1% melt in the residue can occur (e.g., dynamic melting of *Langmuir et al.* [1977]), but greater amounts of retained melt will flatten the REE patterns and increase the incompatible element concentrations of residual peridotite clinopyroxenes. Because segregation occurs after ~0.1% melting in the present suite of samples, significant constraints are placed on the dynamic melting mechanism, and the implication is that melt removal is both rapid and efficient in the mid-ocean ridge upper mantle. Thus the results of this study can be used to constrain boundary conditions for theoretical geodynamical models of melt segregation, migration, and permeable flow in the subridge asthenosphere. The modeling results do not preclude the possibility that extensive degrees of melting occur at cusps corresponding to the garnet-spinel and spinel-plagioclase transitions in the peridotite solidus [*Presnall et al.*, 1979]. However, if melting does occur at a cusp in the solidus, the mechanisms controlling melt extraction and segregation from the residue must be fully operative to enable efficient melt removal.

Support for the fractional or small increment of melting model also comes from theoretical and experimental studies, field work in alpine massifs, and seismic studies of slow spreading ridges that indicate the amount of melt present in any portion of the subridge upper mantle is small and probably does not exceed 1-3% [*Beeré*, 1975; *Nisbet and Fowler*, 1978; *Ahern and Turcotte*, 1979; *Waff and Bulau*, 1979; *McKenzie*, 1984, 1985*a* and *b*; *Richter and McKenzie*, 1984; *Prinzhofer and Allègre*, 1985; *Nicolas*, 1986].

Further support comes from the depleted major element compositions of residual abyssal peridotites, which generally contain less than 1% primitive basaltic component. As these peridotites have undergone up to 25% melting, this demonstrates that melt removal is generally greater than 95% efficient in the shallow mantle [*Dick*, 1989], suggesting that little melt can be held in mantle peridotites during melting.

The observation that most oceanic peridotites retain primary diopside [*Dick and Fisher*, 1984] further supports the near-fractional melting model. Melting in the spinel stability field removes a cpx-rich liquid from the system leaving an increasingly olivine-opx-rich residue. Olivine has a higher enthalpy of fusion than do pyroxenes [*Robie et al.*, 1979], so removing diopside + pyroxene-rich liquid from the bulk system increases the heat required for melting to proceed from the four-phase (lherzolite) to the three-phase (cpx-free harzburgite) assemblage. This represents an effective thermodynamic barrier to melting beyond the cpx-out point if the liquid is efficiently removed. Interestingly, the only samples that might have moved from the four-phase to the three-phase field by loss of cpx are those from near the hotspots. This may be caused either by higher temperatures associated with hotspots or by possible lowering of solidus temperatures by water at hotspots [*Schilling et al.*, 1983]. This situation compares with alpine peridotite genesis wherein cpx-free harzburgites are evidence of enhanced, probably hydrous, melting [*Dick*, 1977; *Dick and Fisher*, 1984].

It might be expected that extremely depleted late stage fractional melts should rarely be sampled on the ridge system. No voluminous outpourings of such melts are expected and indeed none have been found, but extremely depleted Mg-rich silicate melt inclusions have been found in olivine and plagioclase xenocrysts in MORB from the Galapagos spreading center [*Yonover*, 1989], and from various locations on the Mid-Atlantic Ridge and Iceland [*Sobolev and Dmitriev*, 1989; K. Johnson, manuscript in preparation, 1990]. Ongoing examination of melt inclusions from the Mid-Atlantic Ridge, the American-Antartica Ridge, and the Southwest Indian Ridge should provide additional data to address this question.

Compatible major elements in basaltic melts are buffered by the major peridotite phases and will show little variation as they emerge from the top of the melting column [*Richter*, 1986; *Navon and Stolper*, 1987; *Dick*, 1989]. This, in conjunction with aggregation and mixing of melts in a magma chamber, will obfuscate the melting process recorded in basalts making fractional melting and melt integration difficult to distinguish from batch melting when looking at basalt compositions. Therefore the liquids erupted at the surface as MORB are weighted averages of melts produced over the melting interval and do not show a simple batch melting relationship to the latest stage residues of melting sampled as abyssal peridotites.

CONCLUSIONS

Several important conclusions can be made in this study.

1. Both major and incompatible trace elements in abyssal peridotites reflect greater degrees of melting in the upper mantle near the Bouvet and Marion hotspots. Furthermore, pronounced chemical gradients in the upper mantle approaching hotspots are manifested in peridotite clinopyroxene compositions.

2. Negative anomalies in Zr and Ti (HFSE anomalies) are observed in abyssal peridotite clinopyroxenes. The Zr anomalies are greatest near the Bouvet hotspot and appear to increase with increasing depletion of the samples, or with increasing degree of melting. Ti anomalies do not exhibit this systematic behavior. Thus partition coefficients for Zr in cpx may be lower than adjacent elements in incompatible element diagrams (spidergrams). However, processes relating the observed negative Zr anomalies in peridotite cpx to positive anomalies in MORB are still not clear.

3. Ti, Zr, and REE concentrations in abyssal peridotite cpx are best modeled by fractional melting or by melting and segregation in $\leq 0.1\%$ increments. Some REE patterns are consistent with melting in the spinel stability field alone (Vulcan FZ, Atlantis II FZ), others are consistent with varying degrees of melting beginning in the garnet stability field

and continuing into the spinel field (Bullard FZ), while those near hotspots (Bouvet and Discovery II FZs) are consistent with melting and recrystallization of a garnet-bearing assemblage and subsequent granule exsolution of clinopyroxene from orthopyroxene. Near-fractional melting and melting beginning in the garnet stability field place constraints on models for MORB generation and theoretically based concepts of melt segregation and subridge thermal structure.

4. The melting model is consistent with theoretical, experimental, geophysical, and on-land observations stating that only very small fractions of melt are needed before segregation can commence and that essentially no trapped liquid remains in the residue after segregation and compaction [*Ahern and Turcotte*, 1978; *McKenzie*, 1984; *Nicolas*, 1986; *McKenzie and Bickle*, 1988; *Dick*, 1989].

The implications of this study are that "common" MORB is evolved from a weighted aggregate of very small increments of melting produced over a depth range often beginning in the garnet stability field.

APPENDIX

Basic melting equations derived by *Gast* [1968] and *Shaw* [1970] are recast to describe the change in concentration of an element in cpx with melting.

Assumptions:

A. $D_i\alpha = \frac{C_i\alpha}{C_i l} \equiv \frac{\text{concentration of element } i \text{ in phase } \alpha}{\text{concentration of element } i \text{ in liquid}} \equiv \text{const}$

B. $D_i\alpha/\text{cpx} = \frac{C_i\alpha}{C_i\text{cpx}} \equiv \frac{\text{concentration of element } i \text{ in phase } \alpha}{\text{concentration of element } i \text{ in cpx}} \equiv \text{const}$

C. $X_{o,\alpha} \equiv$ initial weight fraction of phase α

D. $C_i{}^s \equiv$ concentration of i in bulk solid;
$C_i{}^l \equiv$ concentration of i in liquid;
$C_i{}^o \equiv$ concentration of i in original bulk solid

E. F is degree of melting.

F. nonmodal melting of prescribed mineral proportions

$D_i{}^o = \Sigma D_i\alpha X_{o,\alpha} \equiv$ initial bulk solid partition coefficient of element i. (A1)

$P = \Sigma D_i\alpha p_\alpha \equiv$ weighted partition coefficient of liquid; $p\alpha$ = proportion of mineral phase entering liquid. (A2)

$D_i = \Sigma D_i\alpha X_\alpha = (D_i{}^o - PF) / (1 - F) \equiv$ bulk solid partition coefficient of element i at F percent melting. (A3)

G. Equilibrium maintained between all phases.

H. All garnet remaining after melting in the garnet stability field reacts to form 2.5 enstatite + 0.75 diopside + 1.0 spinel upon ascent into the spinel stability field

Given:

Fractional Melting

$$\frac{C_i^s}{C_i^o} = \left[\frac{1}{1 - F}\right]\left[1 - \frac{PF}{D_i^o}\right]^{\frac{1}{P}}$$

Equilibrium Batch Melting

$$\frac{C_i^s}{C_i^o} = \left[\frac{D_i^o - PF}{1 - F}\right]\left[\frac{1}{D_i^o + F\ (1 - P\ )}\right]$$

and knowing that $\frac{C_i{}^s}{C_i{}^o}$ can also be expressed as

$$\frac{(X_{ol}C_i{}^{ol} + X_{opx}C_i{}^{opx} + X_{cpx}C_i{}^{cpx} + X_{sp}C_i{}^{sp})}{(X_{o,ol}C_i{}^{o,ol} + X_{o,opx}C_i{}^{o,opx} + X_{o,cpx}C_i{}^{o,cpx} + X_{o,sp}C_i{}^{o,sp})}$$

which can be rewritten (by introducing $C_i^{\,l}$ and $C_i^{\,o,l}$, assuming $X_{ol}C_i^{ol} = X_{ol}\frac{C_i^{ol}}{C_i^{\,l}} \cdot \frac{C_i^{\,l}}{C_i^{cpx}} \cdot C_i^{\,cpx}$, etc., and then pulling out $C_i^{\,cpx}$ and $C_i^{\,o,cpx}$) as

$$\left[\frac{\dfrac{C_i^{cpx} \cdot C_i^{l}}{C_i^{cpx}}}{\dfrac{C_i^{o,cpx} \cdot C_i^{o,l}}{C_i^{o,cpx}}}\right] \times$$

$$\frac{\left(X_{ol}\dfrac{C_i^{ol}}{C_i^{\,l}} + X_{opx}\dfrac{C_i^{opx}}{C_i^{\,l}} + X_{cpx}\dfrac{C_i^{cpx}}{C_i^{\,l}} + X_{sp}\dfrac{C_i^{sp}}{C_i^{\,l}}\right)}{\left(X_{o,ol}\dfrac{C_i^{o,ol}}{C_i^{o,l}} + X_{o,opx}\dfrac{C_i^{o,opx}}{C_i^{o,l}} + X_{o,cpx}\dfrac{C_i^{o,cpx}}{C_i^{o,l}} + X_{o,sp}\dfrac{C_i^{o,sp}}{C_i^{o,l}}\right)}$$

the numerator and denominator of the second term are D_i and D_i^o, respectively, so that

$$\frac{C_i^s}{C_i^o} = \frac{C_i^{cpx}}{C_i^{o,cpx}} \cdot \left[\frac{\dfrac{C_i^{\,l}}{C_i^{cpx}}}{\dfrac{C_i^{\,o,l}}{C_i^{\,o,cpx}}}\right] \cdot \frac{D_i}{D_i^o}$$

Applying assumption A above yields

$$\frac{C_i^{\,s}}{C_i^{\,o}} = \frac{C_i^{\,cpx}}{C_i^{\,o,cpx}} \cdot \frac{D_i}{D_i^o}$$

and then equating this with expressions for fractional and batch melting from *Shaw* [1970], we get

fractional

$$\frac{C_i^s}{C_i^o} = \frac{C_i^{cpx}}{C_i^{o,cpx}} \cdot \frac{D_i}{D_i^o} = \left[\frac{1}{1-F}\right]\left[1 - \frac{PF}{D_i^o}\right]^{\frac{1}{P}}$$

batch

$$\frac{C_i^s}{C_i^o} = \frac{C_i^{cpx}}{C_i^{o,cpx}} \cdot \frac{D_i}{D_i^o} = \left[\frac{D_i^o - PF}{1-F}\right]\left[\frac{1}{D_i^o + F\ (1-P\ )}\right]$$

D_i is given in assumption (A3) above (*Shaw* [1970], equation 12), and by substitution the whole rock equations can be rewritten in terms of $C_i^{\,cpx}/C_i^{o,cpx}$ or $C_i^{\,cpx}/C_i^{\,o}$

Fractional melting

$$\frac{C_i^{cpx}}{C_i^{o,cpx}} = \left[1 - \frac{PF}{D_i^o}\right]^{\left(\frac{1}{P} - 1\right)} \tag{A4}$$

or

$$\frac{C_i^{cpx}}{C_i^o} = \left[1 - \frac{PF}{D_i^o}\right]^{\frac{1}{P}} \cdot \left[\frac{D_i^{cpx/l}}{D_i^o - PF}\right] \tag{A5}$$

Batch melting

$$\frac{C_i^{cpx}}{C_i^{o,cpx}} = \left[\frac{D_i^o}{D_i^o + F\,(1 - P)}\right] \tag{A6}$$

or

$$\frac{C_i^{cpx}}{C_i^o} = \left[\frac{D_i^{cpx/l}}{D_i^o + F\,(1 - P)}\right] \tag{A7}$$

TABLE A1. Crystal/Liquid Partition Coefficients Used in Models

	Olivine	Clinopyroxene	Orthopyroxene	Garnet	Spinel	Plagioclase
Ti	0.02	0.44	0.10	0.6	0.10	0.01
Zr	0.01	0.20	0.05	0.5	0.05	0.01
Ce	0.001	0.10	0.005	0.008	0.0005	
Nd	0.002	0.19	0.01	0.057	0.0008	
Sm	0.003	0.30	0.02	0.217	0.0009	
Eu	0.003	0.42	0.03	0.45	0.0009	
Dy	0.012	0.50	0.045	2.0	0.0015	
Er	0.025	0.51	0.06	3.5	0.003	
Yb	0.059	0.50	0.075	7.0	0.0045	

Sources of data: Clinopyroxene: REE, *Irving and Frey* [1984], *Green and Pearson* [1985], *Johnson and Kinzler* [1989]. Ti, Zr, *McCallum and Charrette* [1978], *Fujimaki et al.* [1984], *Dunn* [1987], *Tormey et al.* [1987], *Johnson and Kinzler* [1989]. Olivine, opx: REE, *Stosch* [1982], combined with cpx partition coefficients. Ti, Zr, *Fujimaki et al.* [1984]. Spinel: REE, *Stosch* [1982], combined with cpx partition coefficients. Ti, Zr, K. Johnson, Ti calculated from electron probe data; Zr estimated from secondary ion counts relative to cpx. Garnet: REE, *Shimizu and Kushiro* [1975], *Nicholls and Harris* [1980], *Fujimaki et al.* [1984]. Ti, Zr, *Fujimaki et al.* [1984], *Green et al.* [1989]. Plagioclase: Zr - *Fujimaki et al.* [1984].

TABLE A2. Phase Proportions Used in the Models

Phase	Starting mode (Vol %)	Melt mode (Vol%)
olivine	0.55	0.10
opx	0.25	0.20
cpx	0.18	0.68
spinel	0.02	0.02
High p_{cpx}		
olivine	0.55	0.03
opx	0.20	0.03
cpx	0.15	0.44
garnet	0.10	0.50
Low p_{cpx}		
olivine	0.55	0.13
opx	0.20	0.12
cpx	0.15	0.25
garnet	0.10	0.50

REFERENCES

Ahern, J. L., and D. L. Turcotte, Magma migration beneath an ocean ridge, *Earth Planet. Sci. Lett., 45*, 115-122, 1979.

Anders, E., and M. Ebihara, Solar-system abundances of the elements, *Geochim. Cosmochim. Acta, 46*, 2363-2380, 1982.

Beeré, W., A unifying theory of the stability of penetrating liquid phases and sintering pores, *Acta Metall., 23,* 131-138, 1975.

Bender, J. F., C. H. Langmuir, and G. N. Hanson, Petrogenesis of basalt glasses from the Tamayo region, East Pacific Rise, *J. Petrol., 25,* 213-254, 1984.

Bottinga, Y., and C. J. Allègre, Partial melting under spreading ridges, *Philos. Trans. R. Soc. London, Ser. A., 288*, 501-525, 1978.

Colson, R. O., and D. Gust, Effects of pressure on partitioning of trace elements between low-Ca pyroxene and melt, *Am. Mineral., 74,* 31-36, 1989.

Davis, B. T. C., and J. F. Shairer, Melting relations in the join diopside-forsterite-pyrope at 40 kbars and at one atmosphere, *Yearbook Carnegie Inst. Washington, 64*, 123-126, 1965.

Dick, H. J. B., Partial melting in the Josephine Peridotite, I, the effect on mineral composition and its consequence for geobarometry and geothermometry, *Am. J. Sci., 277*, 801-832, 1977.

Dick, H. J. B., Abyssal peridotites, very-slow spreading ridges and ocean ridge magmatism, in *Magmatism in the Ocean Basins,* edited by A. D. Saunders and M. J. Norry, pp. 71-105, Geol. Soc. London Spec. Pub. No. 42, 1989.

Dick, H. J. B. and R. L. Fisher, Mineralogic studies of the residues of mantle melting: abyssal and alpine-type peridotites, in *Kimberlites II: The Mantle and Crust Relationships,* edited by J. Kornprobst, pp. 295-308, Elsevier, New York, 1984.

Dick, H. J. B., R. L. Fisher, and W. B. Bryan, Mineralogic variability of the uppermost mantle along mid-ocean ridges, *Earth Planet. Sci. Lett., 69,* 88-106, 1984.

Dunn, T., Partitioning of Hf, Lu, Ti, and Mn between olivine, clinopyroxene and basaltic liquid, *Contrib. Mineral. Petrol., 96*, 476-484, 1987.

Elthon, D., and C. M. Scarfe, High-pressure phase equilibria of a high-magnesia basalt and the genesis of primary oceanic basalts, *Am. Mineral., 69*, 1-15, 1984.

Falloon, T. J., and D. H. Green, Anhydrous partial melting of MORB pyrolite and other peridotite compositions at 10 kbar: implications for the origin of primitive MORB glasses, *Mineral. and Petrol., 37,* 181-219, 1987.

Falloon, T. J., and D. H. Green, Anhydrous partial melting of a fertile and depleted peridotite from 2 to 30 kb and application to basalt petrogenesis, *J. Petrol., 29,* 1257-1282, 1988.

Fisher, R. L., H. J. B. Dick, J. H. Natland, and P. S. Meyer, Mafic/ultramafic suites of the slowly spreading Southwest Indian Ridge: Protea exploration of the Antarctic plate boundary, 24°E-47°E, 1984, *Ofioliti, 11*, 147-178, 1987.

Fox, P. J., R. S. Detrick, and G. M. Purdy, Evidence for crustal thinning near fracture zones: implications for ophiolites, in *Ophiolites, Proceedings International Ophiolite Symposium, Cyprus, 1979*, edited by A. Panayiotou, pp. 161-168, Ministry of Agriculture and Natural Resources, Nicosia, Cyprus, 1980.

Frey, F. A., C. J. Suen, and H. W. Stockman, The Ronda high temperature peridotite: Geochemistry and petrogenesis, *Geochim. Cosmochim. Acta, 49*, 2469-2491, 1985.

Fujii, T., and C. M. Scarfe, Compositions of liquids coexisting with spinel lherzolite at 10 kbar and the genesis of MORBs, *Contrib. Mineral. Petrol., 90*, 18-28, 1985.

Fujimaki., H., M. Tatsumoto, and K. Aoki, Partition coefficients of Hf, Zr, and REE between phenocrysts and groundmass, *Proc. Lunar Planet. Sci. Conf., 14th, Part 2, J. Geophys. Res., 89,* suppl., B662-B672, 1984.

Gast, P. W., Trace element fractionation and the origin of tholeiitic and alkaline magma types, *Geochim. Cosmochim. Acta, 32*, 1057-1086, 1968.

Green, D. H., and A. E. Ringwood, The genesis of basaltic magmas, *Contrib. Mineral. Petrol., 15*, 103-190, 1967.

Green, D. H., W. O. Hibberson, and A. L. Jaques, Petrogenesis of mid-ocean ridge basalts, in *The Earth:Its Origin, Structure, and Evolution*, edited by M. W. McElhinney, pp. 265-299, Academic Press, San Diego, Calif., 1979.

Green, T. H., and N. J. Pearson, Rare earth element partitioning between clinopyroxene and silicate liquid at moderate to high pressure, *Contrib. Mineral. Petrol., 91*, 24-36, 1985.

Green, T. H., S. H. Sie, C. G. Ryan, and D. R. Cousens, Proton microprobe-determined partitioning of Nb, Ta, Zr, Sr, and Y between garnet, clinopyroxene and basaltic magma at high pressure and temperature, *Chem. Geol., 74,* 201-216, 1989.

Grutzeck, M., S. Kridelbaugh, and D. Weill, The distribution of Sr and REE between diopside and silicate liquid, *Geophys. Res. Lett., 1,* 273-275, 1974.

Hart, S. R., J.-G. Schilling, and J. L. Powell, Basalts from Iceland and along the Reykjanes Ridge: Sr isotope geochemistry, *Nature Phys. Sci., 246,* 104, 1973.

Hofmann, A. W., and M. D. Feigenson, Case studies on the origin of basalt, I, Theory and reassessment of Grenada basalts, *Contrib. Mineral. Petrol., 84,* 382-389, 1983.

Humphris, S. E., G. Thompson, J.-G. Schilling, and R. H. Kingsley, Petrological and geochemical variations along the Mid-Atlantic Ridge between 46°S and 32°S: Influence of the Tristan da Cunha mantle plume, *Geochim. Cosmochim. Acta, 49,* 1445-1464, 1985.

Irving, A. J. and F. A. Frey, Trace element abundances in megacrysts and their host basalts: Constraints on partition coefficients and megacryst genesis, *Geochim. Cosmochim. Acta, 48*, 1201-1221, 1984.

Jaques, A. L., and D. H. Green, Anhydrous melting of peridotite at 0-15 kbar pressure and the genesis of tholeiitic basalts, *Contrib. Mineral. Petrol., 73*, 287-310, 1980.

Johnson, K. T. M., and R. J. Kinzler, Partitioning of REE, Ti, Zr, Hf, and Nb between clinopyroxene and basaltic liquid: An ion microprobe study, *Eos Trans. AGU, 70,* 1388, 1989.

Johnson, K. T. M., H. J. B. Dick, and N. Shimizu, Rare earth element composition of discrete diopsides from the oceanic upper mantle: Implications for MORB genesis and processes of exotic melt infiltration, *Eos Trans. AGU, 68*, 1541, 1987.

Johnson, K. T. M., H. J. B. Dick, and N. Shimizu, Trace element composition of diopsides in abyssal peridotites: Implications for generation of mid-ocean ridge basalts, *Eos Trans. AGU, 69,* 1516, 1988.

Kay, R. W., N. J. Hubbard, and P. W. Gast, Chemical characteristics and origin of ocean ridge volcanic rocks, *J. Geophys. Res., 75*, 1585-1613, 1970.

Klein, E. M., and C. H. Langmuir, Global Correlations of ocean ridge basalt chemistry with axial depth and crustal thickness, *J. Geophys. Res., 92,* 8089-8115, 1987.

Langmuir, C. H., J. F. Bender, A. E. Bence, G. N. Hanson, and S. R. Taylor, Petrogenesis of basalts from the FAMOUS area: Mid-Atlantic Ridge, *Earth Planet. Sci. Lett., 36*, 133-156, 1977.

Lawver, L. A., and H. J. B. Dick, The American-Antarctic Ridge, J. *Geophys. Res., 88,* 8193-8202, 1983.

le Pichon, X., J. Angelier, and J. C. Sibuet, Plate boundaries and extensional tectonics, *Tectonophysics, 81*, 239-256, 1982.

leRoex, A. P., H. J. B. Dick, A. J. Erlank, A. M. Reid, F. A. Frey, and S. R. Hart, Geochemistry, mineralogy, and petrogenesis, of lavas erupted along the Southwest Indian Ridge between the Bouvet triple junction and 11 degrees east, *J. Petrol., 24,* 267-318, 1983.

leRoex, A. P., H. J. B. Dick, and R. L. Fisher, Petrology and geochemistry of MORB from 25°E to 46°E along the Southwest Indian Ridge: Evidence for contrasting styles of mantle enrichment, *J. Petrol., 30,* 947-986, 1989.

Lindsley, D. H. and D. J. Andersen, A two-pyroxene thermometer, *Proc. Lunar Planet. Sci. Conf., 13th, Part 2, J. Geophys. Res., 88*, suppl., A887-A906, 1983.

Loubet, M., N. Shimizu, and C. J. Allègre, Rare earth elements in alpine peridotites, *Contrib. Mineral. Petrol., 53*, 1-12, 1975.

McCallum, I. S., and M. P. Charette, Zr and Nb partition coefficients: implications for the genesis of mare basalts, KREEP, and sea floor basalts, *Geochim. Cosmochim. Acta, 42*, 859-869, 1978.

McKenzie, D., The generation and compaction of partially molten rock, *J. Petrol., 25*, 713-765, 1984.

McKenzie, D., 230Th-238U disequilibrium and the melting processes beneath ridge axes, *Earth Planet. Sci. Lett., 72*, 149-157, 1985*a*.

McKenzie, D., The extraction of magma from the crust and mantle, *Earth Planet. Sci. Lett., 74,* 81-91, 1985*b*.

McKenzie, D., and M. J. Bickle, The volume and composition of melt generated by extension of the lithosphere, *J. Petrol., 29,* 625-679, 1988.

Michael, P. J., and E. Bonatti, Peridotite composition from the North Atlantic: Regional and tectonic variations and implications for partial melting, *Earth Planet. Sci. Lett., 73*, 91-104, 1985.

Minster, J. F., and C. J. Allègre, Systematic use of trace elements in igneous processes, III, Inverse problem of batch partial melting in volcanic suites, *Contrib. Mineral. Petrol., 68*, 37-52, 1978.

Morgan, W. J., Deep mantle convection plumes and plate motions, *Am. Assoc. Pet. Geol. Bull., 56*, 203-213, 1972.

Mysen, B. O., and I. Kushiro, Compositional variations of co-existing phases with degree of melting of peridotite in the upper mantle, *Am. Mineral., 62,* 843-865, 1977.

Navon, O., and E. Stolper, Geochemical consequences of melt percolation: The upper mantle as a chromatographic column, *J. Geol., 95,* 285-308, 1987.

Nicholls, I. A., and K. L. Harris, Experimental rare earth element partition coefficients for garnet, clinopyroxene, and amphibole coexisting with andesitic and baslatic liquids, *Geochim. Cosmochim. Acta, 44,* 287-308, 1980.

Nicolas, A., A melt extraction model based on structural studies in mantle peridotites, *J. Petrol., 27,* 999-1022, 1986.

Nisbet, E. G., and C. M. R. Fowler, The Mid-Atlantic Ridge at 37° and 45°N: Some geophysical and petrological constraints, *Geophys. J. R. Astron. Soc., 54,* 631-660, 1978.

O'Hara, M. J., Are ocean floor basalts primary magma?, *Nature, 220,* 683-686, 1968.

O'Hara, M. J., and H. S. Yoder, Jr., Formation and fractionation of basic magmas at high pressures, *Scott. J. Geol., 3*, 67-117, 1967.

O'Hara, M. J., S. W. Richardson, and G. Wilson, Garnet-peridotite stability and occurrence in the crust and mantle, *Contrib. Mineral. Petrol., 32*, 48-68, 1971.

O'Nions, R. K., and R. J. Pankhurst, Petrogenetic significance of isotope and trace element variations in volcanics from the Mid-Atlantic, *J. Petrol., 15,* 603-634, 1974.

Phipps Morgan, J., and D. W. Forsyth, Three-dimensional flow and temperature perturbations due to a transform offset: Effects on Oceanic crustal and upper mantle structure, *J. Geophys. Res., 93*, 2955-2966, 1988.

Presnall, D. C., and J. D. Hoover, High pressure phase equilibrium constraints on the origin of mid-ocean ridge basalts, *Magmatic Processes: Physicochemical Principles*, edited by B. O. Mysen, pp. 75-89, Spec. Publ., The Geochem. Soc., 1, 1987.

Presnall, D. C., J. R. Dixon, T. H. O'Donnell, and S. A. Dixon, Generation of mid-ocean ridge tholeiites, *J. Petrol., 20*, 3-35, 1979.

Prinzhofer, A., and C. J. Allègre, Residual peridotites and the mechanisms of partial melting, *Earth Planet. Sci. Lett., 74*, 251-265, 1985.

Ray, G. L., N. Shimizu, and S. R. Hart, An ion microprobe study of the partitioning of trace elements between clinopyroxene and liquid in the system diopside-albite-anorthite, *Geochim. Cosmochim. Acta, 47*, 2131-2140, 1983.

Richter, F. M., Simple models for trace element fractionation during melt segregation, *Earth Planet. Sci. Lett., 77*, 333-344,1986.

Richter, F. M., and D. McKenzie, Dynamical models for melt segregation from a deformable matrix, *J. Geol., 92*, 729-740, 1984.

Robie, R. A., B. S. Hemingway, and J. R. Fisher, Thermodynamic properties of minerals and related substances at 298.15 K and 1 bar (105 pascals) pressure and at higher temperatures, *U.S. Geol. Surv. Bull., 1452*, 456 pp., 1979.

Rouffosse, M., B. Parsons, D. McKenzie, and T. Watts, Geoid and depth anomalies in the Indian Ocean, *Eos Trans. AGU, 62*, 389, 1981.

Salters, V. J. M., and S. R. Hart, The Hf-paradox and the role of garnet in the source of mid-ocean ridge basalts, *Nature, 342*, 420-422, 1989.

Salters, V. J. M., and N. Shimizu, World-wide occurrence of HFSE-depleted mantle, *Geochim. Cosmochim. Acta, 52*, 2177-2182, 1988.

Schilling, J.-G., Rare earth variations across 'normal' segments of the Reykjanes Ridge, 60°-53°N, Mid-Atlantic Ridge, 29°S, and East Pacific Rise, 2°-19°S, and evidence on the composition of the underlying low-velocity layer, *J. Geophys. Res., 80*, 1459-1473, 1975.

Schilling, J.-G., M. Zajac, R. Evans, T. Johnston, W. White, J. D. Devine, and R. Kingsley, Petrologic and geochemical variations along the Mid-Atlantic Ridge from 29°N to 73°N, *Am. J. Sci., 283*, 510-586, 1983.

Sclater, J. G., C. Bowin, R. Hey, H. Haskins, J. Peirce, J. Phillips, and C. Tapscott, The Bouvet Triple Junction, J. *Geophys. Res., 81,* 1857-1869, 1976.

Shaw, D. M., Trace element fractionation during anatexis, *Geochim. Cosmochim. Acta, 34*, 237-243, 1970.

Shaw, D. M., Trace element behaviour during anatexis, Proceedings of Chapman Conference, Partial Melting in the Earth's Upper Mantle, edited by H. J. B Dick, *Bull. Oreg. Dep. Geol. Miner. Ind., 96*, 189-213, 1977.

Shibata, T., and G. Thompson, Peridotites from the Mid-Atlantic Ridge at 43°N and their petrogenetic relation to abyssal tholeiites, *Contrib. Mineral. Petrol., 93*, 144-159, 1986.

Shibata, T., G. Thompson, and F. A. Frey, Tholeiitic and alkali basalts from the Mid-Atlantic Ridge at 43°N, *Contrib. Mineral. Petrol., 70*, 127-141, 1979.

Shimizu, N., and S. R. Hart, Rare earth element concentrations in clinopyroxenes from an ocean-ridge lherzolite, *Year Book Carnegie Inst. Washington, 73*, 964-967, 1974.

Shimizu, N., and I. Kushiro, The partitioning of rare earth elements between garnet and liquid at high pressures: Preliminary experiments, *Geophys. Res. Lett., 2*, 413-416, 1975.

Shimizu, N., M. P. Semet, and C. J. Allègre, Geochemical applications of quantitative ion-microprobe analysis, *Geochim. Cosmochim. Acta, 42,* 1321-1334, 1978.

Sobolev, A. V., and L. V. Dmitriev, Primary melts of tholeiites of oceanic rifts (TOR): Evidence from studies of primitive glasses and melt inclusions in minerals, paper presented at International Geological Congress, Washington, D.C., 1989.

Stolper, E., A phase diagram for mid-ocean ridge basalts: Preliminary results and implications for petrogenesis, *Contrib. Mineral. Petrol., 74,* 13-27, 1980.

Stosch, H.-G., Rare earth element partitioning between minerals from anhydrous spinel peridotite xenoliths, *Geochim. Cosmochim. Acta, 46*, 793-811, 1982.

Sun, S.-S., R. W. Nesbitt, and A. Y. Sharaskin, Geochemical characteristics of mid-ocean ridge basalts, *Earth Planet. Sci. Lett., 44,* 119-138, 1979.

Takahashi, E., and I. Kushiro, Melting of a dry peridotite at high pressures and basalt magma genesis, *Am. Mineral., 68*, 859-879, 1983.

Terakado, Y., and A. Masuda, Experimental study of REE partitioning between diopside and melt under atmospheric pressure, Geochem. J., 13, 121-129, 1979.

Tormey, D. R., T. L. Grove, and W. B. Bryan, Experimental petrology of normal MORB near the Kane Fracture Zone: 22°-25°N, Mid-Atlantic Ridge, *Contrib. Mineral. Petrol., 96*, 121-139, 1987.

Waff, H. S., and J. R. Bulau, Equilibrium fluid distribution in an ultramafic partial melt under hydrostatic stress conditions, *J. Geophys. Res., 84,* 6109-6114, 1979.

Yonover, R., Petrological effects of rift failure at the Galapagos Spreading Center near 95.5°W including analyses of glass inclusions by laser mass spectrometry and ion microprobe, PhD thesis, 193 pp., Univ. of Hawaii, May 1989.

(Received May 16, 1989;
revised October 8, 1989;
accepted October 26, 1989)

Paper number 89JB03398.
0148-0227/90/89JB-03398$05.00

Paper number 89JB03398.

CHAPTER 3. MEASUREMENTS OF CLINOPYROXENE/BASALTIC LIQUID TRACE ELEMENT PARTITION COEFFICIENTS IN NATURAL AND EXPERIMENTAL SAMPLES

CHAPTER 3. MEASUREMENTS OF CLINOPYROXENE/BASALTIC LIQUID TRACE ELEMENT PARTITION COEFFICIENTS IN NATURAL AND EXPERIMENTAL SAMPLES

INTRODUCTION

In order to confidently and accurately model the petrogenetic processes discussed in this thesis, a coherent set of crystal/liquid partition coefficients for Ti, Zr, and REE is needed. By a coherent set, it is meant that partition coefficients for all elements are measured on the same mineral grains (in this study, clinopyroxene) and glassy zones in a given basaltic sample. Previous partition coefficient studies were designed for either rare earth elements (REE) or high field strength elements (HFSE), but not for both groups of elements together. Some studies have focused on rare earth elements [*Schnetzler and Philpotts*, 1970; *Grutzeck et al.*, 1974; *Tanaka and Nishizawa*, 1975; *Terakado and Masuda*, 1979; *Nicholls and Harris*, 1980; *Shimizu*, 1980; *Green and Pearson*, 1985], while others have concentrated on high field strength elements [*McCallum and Charette*, 1978; *Dunn and McCallum*, 1982; *Dunn*, 1987; *Green et al.*, 1989]. To my knowledge, only *Irving and Frey* [1984] and *Fujimaki et al.* [1984] have reported partition coefficients for REE as well as some HFSE from the same samples.

Because the melting models in Chapter 2 refer to processes that occur over a pressure range from 8 to 25 kilobars, understanding the possible effects of pressure on element partitioning is desirable. Thus, a second question I hoped to address in this study was to try to establish whether D_{REE} increase with increasing pressure as suggested by some partitioning studies (summarized by *Green and Pearson*, 1985). Recently, Colson and Gust [1989] studied partitioning of Ca, Al, Sc, and Yb between low-Ca pyroxene and basaltic melt and concluded that pressure did not significantly affect the partitioning of Ca, Sc, or Yb. However, they observed a pronounced increase in D_{Al} with increasing pressure.

In this study, I report results on the partitioning of REE, Ti, and Zr between clinopyroxene and basaltic liquid. Trace element measurements were made using the ion

microprobe on coexisting clinopyroxene and glass in 10 kilobar experiments on three ocean floor basalts, and in glassy rinds of three dredged ocean-floor pillow basalts (hereafter referred to as the "natural samples"). Single element partition coefficients between clinopyroxene and basaltic liquid were calculated based on elemental concentrations in both of these phases. Measurements in this study were at natural, undoped concentration levels.

SAMPLES AND METHODS

Experiments

Glassy rims from ocean-floor basalt pillow lavas from the East Pacific Rise and the Mid-Atlantic Ridge were used as starting material. All experiments were done by Rosamond Kinzler for her Ph.D. research. The purpose of her study was to evaluate phase equilibria and reaction stoichiometry in these samples, and I obtained the "finished products" from her for my study. Natural, phenocryst-poor to -free glasses were finely powdered, then placed in graphite capsules and sealed in platinum jackets. These samples were then placed in the piston-cylinder apparatus, heated above their liquidus, and brought to the temperatures shown in Table 1, where they were held for the times shown. Greater detail on the experimental procedure will be discussed in Kinzler's thesis and for this reason, I will not go into detail about the experimental design, but report the experimental conditions in Table 1 for the two samples used.

TABLE 1. EXPERIMENTAL CONDITIONS

Run no.	Sample	Run duration(h)	P (kb)	T (°C)	% crystals
H70	528-1-1, FAMOUS	14	10	1245	15
H91	AII96-18-1, Kane F.Z.	16	8	1250	2-3

Three of Kinzler's experiments containing liquidus clinopyroxene were examined initially for the partitioning study; run no. H102 contained only clinopyroxene, while the

other two contained clinopyroxene ± plagioclase. Clinopyroxenes in runs no. H70 and H91 were not noticeably zoned when examined by backscatter electron imaging, but those in run no. H102 were markedly sector-zoned. Thus, although clinopyroxene was crystallizing in each of the three runs, chemical equilibrium was not achieved in run no. H102 and it is not used in partition coefficient calculations.

Dredged Samples

Dredged pillow basalts from the Galapagos Ridge and the Manus back-arc basin were selected for study on the basis of small (≤150μ), euhedral clinopyroxene crystals present in the glassy selvedges. The samples are all very fine-grained pillow basalts with microphenocrysts of olivine, plagioclase, and clinopyroxene in the pillow interiors and glassy rinds. Plagioclase - clinopyroxene crystal intergrowths were common. Although strict attainment of equilibrium in nature is difficult to assess due to uncertainties about cooling and crystal growth rate histories of the samples, approach to crystal-liquid equilibrium was evaluated on the basis of texture (well-developed crystal habit, sharply defined crystal faces, lack of zoning) and Fe/Mg crystal/liquid partitioning (discussed later); clinopyroxene grains were chosen for analysis based on their inferred approach to equlibrium with the glass in which they were contained. Figure 1 is a photomicrograph of a clinopyroxene crystal from sample MW8518-29-5 (Manus Basin) illustrating the well-defined crystal faces on one of the analyzed clinopyroxene grains.

Analytical Techniques

Electron and ion microprobe analyses of trace elements in clinopyroxene and glass phases in all samples were carried out following the procedures outlined in Chapters 1 and 2. In all samples, several grains were chosen for analysis based on size and optical and backscatter electron uniformity. The ion beam was placed as close to the edge of the grain as possible without overlapping onto the adjacent glass. Post-analysis microscopic examination of the sample was used to monitor this. Similarly on the glass, the beam was

Figure 1. Photomicrograph of a clinopyroxene grain inferred to be crystallizing from the liquid in sample MW8518-29-5. The euhedral crystal morphology and lack of pronounced chemical zonation were used as selection criteria for partition coefficient measurements. The small, roughly circular spots to the left of the grain are ion beam sputtering craters. 150μ scale bar is shown.

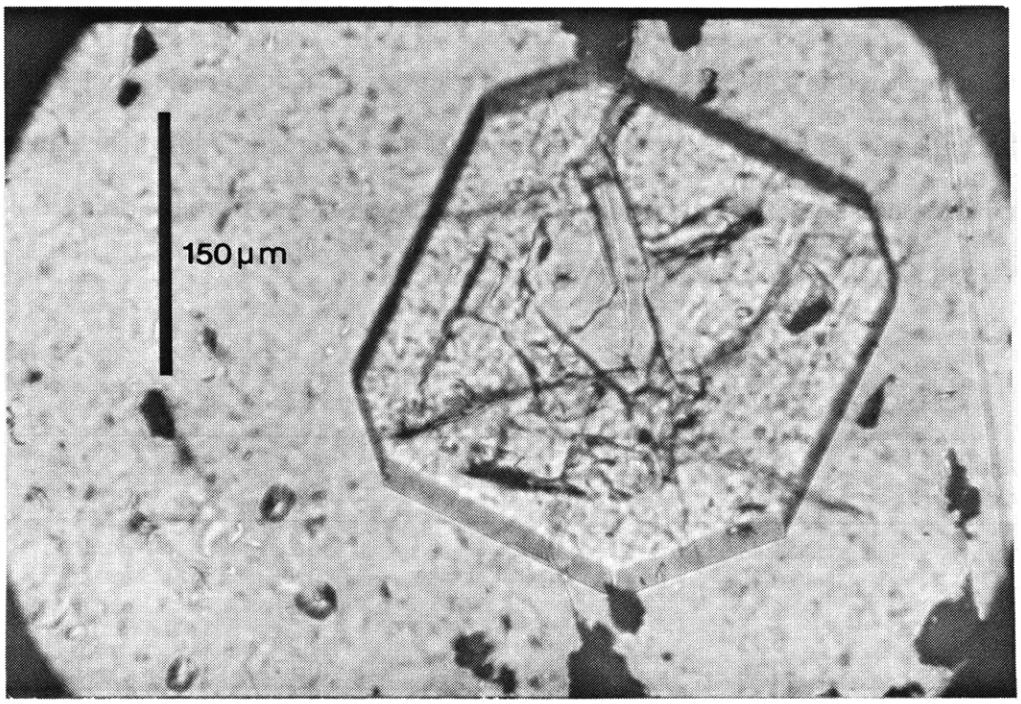
150 µm

placed close to, but not touching, the glass-crystal interface. The beam size in all analyses was ≤ 15μ, which was particularly crucial when analyzing the experimental charges due to the small grain size (generally ≤ 50μ).

RESULTS

Averaged major element analyses of glasses and clinopyroxenes from the experimental samples are reported in Table 2 (data from R. Kinzler, personal communication, 1989), all trace element analyses from the experimental samples are reported in Table 3, and all major and trace element analyses of analyzed glasses and clinopyroxenes from the dredged basalts are reported in Tables 4 and 5, respectively.

TABLE 2. MAJOR ELEMENT ANALYSES OF CLINOPYROXENES AND GLASSES FROM EXPERIMENTAL CHARGES§

Sample Type (#)	H70 cpx(11)	H70 glass(7)	H91 cpx(8)	H91 glass(6)
SiO_2	51.4	48.7	50.2	50.55
TiO_2	0.43	0.87	0.79	1.17
Al_2O_3	6.63	17.3	8.41	16.43
FeO*	5.72	10	5.52	8.01
MnO	0.16	0.17	0.17	0.17
MgO	19.0	8.95	18.5	8.77
CaO	16.1	11.2	15.6	11.08
Na_2O	0.34	2.42	0.43	3.06
K_2O	-	0.13	-	0.09
P_2O_5	-	0.08	-	0.02
Cr_2O_3	0.35	0.1	0.33	0.06
TOTAL	99.93	99.92	99.95	99.41
Mg/(Mg+Fe)	0.86	0.62	0.86	0.66

§ - Electron microprobe data collected by R. Kinzler, M.I.T.
# - number of points analysed and averaged.
* - all Fe analyzed and reported as FeO.

TABLE 3. TRACE ELEMENT CONCENTRATIONS IN EXPERIMENTAL BASALT-CPX PAIRS

H70

	CPX				Glass					
Point*	1	2	3	4	1	2	3	4	avCPX	avGls
Ti	2657	2501	2654		4881	4850	4940		2605 (89)	4890 (46)
Cr	2569	2813	2547		246	247	246		2643(148)	246 (1)
Sr	6	4	6		88	87	88		5 (1)	87 (1)
Zr	11	10	10		50	48	51		10 (1)	50 (2)
Nb	0.6	0.2	0.4		9	10	10		0.4 (0.2)	10 (1)
La	0.5	0.3	0.4	0.5	7	7	7	8	0.4 (0.1)	7 (1)
Ce	1.8	1.4	1.5	2.1	15	14	16	18	1.7 (0.3)	16 (2)
Nd	1.9	2.2	1.7	2.3	9.3	9.4	8.7	11	2.0 (0.3)	9.6 (1.0)
Sm	1.0	0.90	1.0	1.3	3.1	2.6	3.0	3.3	1.1 (0.2)	3.0 (0.3)
Eu	0.2	0.2	0.2	0.2	0.9	0.6	0.9	1.5	0.2 (0)	1.0 (0.4)
Dy	2.5	2.7	2.7	3.1	5.2	5.5	5.6	6.2	2.8 (0.3)	5.6 (0.4)
Er	1.7	2.3	2.2	2.5	3.9	3.9	4.0	4.9	2.2 (0.3)	4.2 (0.5)
Yb	2.2	2.1	2.3	2.8	3.8	3.7	4.0	4.3	2.3 (0.3)	3.9 (0.3)

* - point numbers are separate grains and correspond to CPX-Glass pairs, i.e. CPX 1 pairs with Glass 1. numbers in parentheses in averages columns are standard deviations of the data about the mean.

H91

	CPX			Glass				
Point	1	2	3	1	2	3	avCPX	avGls
Ti	4401	3927	3160	7126	7034	6756	3829 (626)	6972 (193)
Cr	2810	2636	1739	331	307	306	2395 (575)	315 (14)
Sr	7	6	7	137	140	132	7 (1)	136 (4)
Zr	23	21	18	93	93	80	21 (3)	89 (8)
Nb	0.03	0.25	0.30	3.3	3.6	2.9	0.19 (0.14)	3.3 (0.4)
La	0.17	0.30		3.3	4		0.24 (0.09)	4 (0.5)
Ce	0.88	1.5	1.2	9.7	12	11	1.2 (0.3)	11 (1)
Nd	1.5	2.5	2.2	8.0	10	11	2.1 (0.5)	10 (2)
Sm	1.0	1.24	1.6	2.5	3.2	3.2	1.3 (0.3)	3.0 (0.4)
Eu	0.2	0.3	0.3	1.2	1.2	1.4	0.3 (0.1)	1.3 (0.1)
Dy	2.2	3.0	3.2	4.5	5.1	5.4	2.8 (0.5)	5.0 (0.5)
Er	1.5	2.1	2.1	2.7	3.5	3.7	1.9 (0.3)	3.3 (0.5)
Yb	1.5	2.2	2.4	2.5	3.2	3.3	2.0 (0.5)	3.0 (0.4)

TABLE 4. MAJOR ELEMENT CONCENTRATIONS IN NATURAL BASALT-CPX PAIRS

	1557-1		MW8518-29-5		MW8518-31-8	
Type (#pts)	cpx (3)	glass (4)	cpx (3)	glass(6)	cpx (9)	glass (4)
SiO2	51.98(0.54)[1]	50.89(0.21)	51.25(0.46)	52.20(0.12)	52.19(0.64)	51.50(0.25)
TiO2	0.57(0.06)	1.90(0.001)	0.30(0.05)	0.79(0.03)	0.18(0.04)	0.37(0.02)
Al2O3	2.52(0.11)	13.08(0.04)	4.33(0.15)	15.83(0.04)	3.70(0.81)	15.79(0.03)
FeO*	8.90(0.34)	13.17(0.15)	5.25(0.22)	8.03(0.09)	3.84(0.28)	7.51(0.11)
MnO	0.24(0.02)	0.22(0.01)	0.14(0.01)	0.13(0.01)	0.10(0.02)	0.11(0.01)
MgO	17.74(0.38)	6.23(0.04)	17.26(0.18)	6.95(0.09)	18.18(0.45)	8.61(0.05)
CaO	16.75(0.57)	10.48(0.11)	20.44(0.26)	11.57(0.05)	20.82(0.78)	12.94(0.09)
Na2O	0.21(0.01)	2.52(0.02)	0.17(0.01)	2.32(0.09)	0.14(0.00)	1.45(0.04)
K2O	-	0.18(0.002)	-	0.13(0.01)	-	0.06(0.003)
P2O5	-	0.20(0.02)	-	0.10(0.02)	-	0.05(0.01)
Cr2O3	0.11(0.02)	-	0.53(0.04)		1.14(0.15)	-
TOTAL	99.02	98.86	99.67	98.07	100.30	98.41
Mg/(Mg+Fe)[2]	0.78	0.46	0.85	0.61	0.89	0.67

[1] - Numbers in parentheses are standard deviations about the reported means for the number of points analyzed.
[2] - Mg/(Mg+Fe) calculated with all iron as FeO.

TABLE 5. TRACE ELEMENT CONCENTRATIONS IN NATURAL BASALT-CPX PAIRS

MW8518-29-5

	CPX				Glass					
Point*	1	2	3	4	1	2	3	4	avCPX[1]	avGls
Ti	1428	1788	2078		3932	4046	4240		1765(326)	4072(156)
Cr	4060	5056	5068		208	186	238		4728(579)	211(26)
Sr	12	19	11		164	170	175		14(4)	170(6)
Zr	5.4	8.2	8.9		38	40	41		7.5(1.9)	39(2)
Nb	0.11		0.10		0.93	0.93	0.99		0.10(0)	0.95(0.03)
La	0.27		0.27		3.5		3.7	3.5	0.26(0)	3.6(0.1)
Ce	1.1		1.1	0.92	8.4		8.7	8.2	1.0(0.1)	8.4(0.3)
Nd	1.5		1.7	1.4	5.5		6.6	5.6	1.5(0.2)	5.9(0.6)
Sm	0.83		1.0	0.86	1.9		2.0	1.6	0.91(0.09)	1.9(0.2)
Eu	0.3		0.4	0.3	0.7		0.6	0.6	0.3(0.1)	0.6(0.1)
Dy	1.5		1.6	1.3	3.1		3.3	2.8	1.5(0.2)	3.0(0.3)
Er	0.97		1.1	0.88	2.0		2.2	1.9	0.97(0.11)	2.0(0.2)
Yb	0.86		1.1	0.96	2.0		2.1	1.7	0.98(0.12)	2.0(0.2)

* - point numbers are separate grains and correspond to CPX-Glass pairs, i.e. CPX 1 pairs with Glass 1.
[1] - numbers in parentheses in averages columns are standard deviations of the data about the mean.

TABLE 5. CONTINUED

MW8518-31-8

	CPX		Glass			
Point	1	2	1	2	avCPX	avGls
Ti	623		2174		623	2174
Cr	5413		326		5413	326
Sr	5		93		5	93
Zr	1.7		16		1.7	16
Nb	0.12		0.40		0.12	0.40
La	0.19	0.09	1.8	1.4	0.14 (0.07)	1.6 (0.3)
Ce	0.60	0.51	4.5	3.5	0.6 (0.06)	4.0 (0.7)
Nd	0.70	0.75	2.7	2.6	0.7 (0.04)	2.7 (0.1)
Sm	0.33	0.42	1.2	0.93	0.38 (0.06)	1.1 (0.2)
Eu	0.2	0.2	0.3	0.2	0.2 (0)	0.2 (0.1)
Dy	0.72	0.93	1.8	1.7	0.82 (0.15)	1.8 (0.1)
Er	0.47	0.66	1.4	1.3	0.57 (0.13)	1.3 (0.1)
Yb	0.49	0.64	1.4	1.2	0.57 (0.11)	1.3 (0.1)

1557-1

	CPX			Glass				
Point	1	2	3	1	2	3	avCPX	avGls
Ti	3370	3763	3588	11036	10781	10936	3574 (197)	10918 (128)
Cr	1018	2561	1853	71	72	71	1811 (772)	71 (1)
Sr	4	5	6	89	83	88	5 (1)	87 (3.2)
Zr	13	16	15	108	105	108	15 (1.5)	107 (2)
Nb	0.05	0.06	0.03	6.02	5.88	5.95	0.05 (0.02)	5.95 (0.07)
La	0.51	0.50	0.30	5.8	6.1	5.8	0.44 (0.12)	5.9 (0.2)
Ce	1.9	1.8	1.3	15	16	15	1.7 (0.3)	15 (1)
Nd	3.1	2.5	2.2	12	12	11	2.6 (0.5)	12 (1)
Sm	1.8	1.6	1.4	4.2	4.6	4.1	1.6 (0.2)	4.3 (0.3)
Eu	0.7	0.6	0.6	1.3	1.3	1.1	0.6 (0.1)	1.2 (0.1)
Dy	3.9	3.7	3.0	7.3	7.8	7.2	3.5 (0.5)	7.4 (0.3)
Er	2.6	2.3	1.9	4.8	5.1	4.8	2.3 (0.4)	4.9 (0.2)
Yb	2.6	2.6	2.1	5.0	5.2	4.9	2.5 (0.3)	5.0 (0.2)

Exchange Equilibria

Before using the data to derive element partition coefficients, approach to equilibrium must be satisfactorily demonstrated. Besides the criteria based on textural analysis mentioned above, equilibrium was evaluated on the basis of Fe-Mg exchange between coexisting glass - clinopyroxene pairs. This analysis is similar to the well-characterized

Fe/Mg partitioning behavior between olivine and melt studied twenty years ago by *Roeder and Emslie* [1970], except that the behavior in clinopyroxene is less well-determined and may be temperature dependent [*Obata et al.*, 1974].

To arrive at a nominal exchange coefficient, K_d (= $[Fe/Mg]^{cpx} / [Fe/Mg]^{liq}$), for clinopyroxene in equilibrium with silicate melt, I calculated this ratio in experiments in which clinopyroxene was on the liquidus in a basaltic system [*Grove et al.*, 1982; *Grove and Bryan*, 1983; *Tormey et al.*, 1987], and averaged the values. A value of K_d=0.24±0.03 (1σ; n = 28) was calculated, with all iron as FeO. This value agrees very well with high temperature Fe-Mg partitioning between olivine and clinopyroxene pairs in peridotites [*Obata et al.*, 1974] if an olivine K_d of 0.3 is used. Since all of the basalts in this study are inferred to represent similar temperatures, the large temperature dependence identified by *Obata et al.* [1974] does not come into play. It should be noted that the experiments used to derive K_d were done at 1 atmosphere, so caution must be used in comparing these K_d's with $[Fe/Mg]^{cpx} / [Fe/Mg]^{liq}$ of the high pressure experiments used in this study since the effect of pressure on this ratio is not known. Additionally, it should be emphasized that equivalence of sample $[Fe/Mg]^{cpx} / [Fe/Mg]^{liq}$ with "accepted" K_d's does not prove thermodynamic equilibrium, but demonstrates the approach to exchange equilibrium. Calculated average $[Fe/Mg]^{cpx} / [Fe/Mg]^{liq}$ for the studied samples are reported in Table 6. Again, all iron was treated as FeO.

TABLE 6. CALCULATED K_d's

SAMPLE	Kd = $[Fe/Mg]^{cpx} / [Fe/Mg]^{liq}$
H70	0.27
H91	0.33
MW8512-29-5	0.26
MW8512-31-8	0.24
1557-1	0.23

The calculated K_d for experiment H91 is significantly higher than the nominal equilibrium value, while values in the other samples are within the calculated 1σ error of the experimental data used to acquire the nominal value. The high value for sample H91 implies departure from Fe-Mg exchange equilibrium.

Trace Element Partition Coefficients

Based on the data reported in Tables 3 and 5, concentrations of trace elements in the glass versus those in clinopyroxene may be plotted. Single element partition coefficients can then be read from the slope of the line regressed through the data. This has been done for Ce, Nd, Sm, Dy, Er, Yb, Ti, and Zr in Figures 2 through 9. The partition coefficient for Eu was not calculated for two reasons: 1) Significant variations in measured Eu concentrations in the glasses. This variation is believed to be primarily caused by variable interference of BaO and BaOH molecular ions on the measured Eu peaks. The correction algorithm described in Chapter 2, though accounting for BaO, does not account for BaOH. 2) Measured Eu in clinopyroxenes in the experimental charges all contained pronounced negative Eu anomalies (Figure 10).

The negative Eu anomalies in the experimental clinopyroxenes are believed to result from the highly reducing conditions in the experiments arising from the use of graphite capsules. Under reducing conditions, Eu^{2+} is a significant Eu species in basaltic systems [*Philpotts*, 1970]. Because of the larger ionic radius of Eu^{2+} relative to Eu^{3+} in the REE^{3+} valence series, a high proportion of Eu^{2+} leads to lower partition coefficients for Eu between mafic minerals and melt, while increasing Eu partition coefficients between plagioclase and melt [*Drake*, 1975]. The presence of negative Eu anomalies in cpx have been used to estimate the redox conditions of oceanic basalt systems [*Philpotts*, 1970; *Grutzeck et al.*, 1974; *Sun et al.*, 1974; *Weill et al.*, 1974]. Thus, for the purposes of this study, and concomitant modeling chapters, $D_{Eu}^{cpx/liq}$ is interpolated.

Figures 2 through 9. Graphical determination of Cpx/basaltic liquid partition coefficients for (Figure 2) Ce, (3) Nd, (4) Sm, (5) Dy, (6) Er, (7) Yb, (8) Ti, and (9) Zr. Data for the dredged natural basalt samples and experimental sample H70 are the most consistent and are used for determining coefficients. Error bars represent 2σ analytical precision determined from repeated analysis of standards.

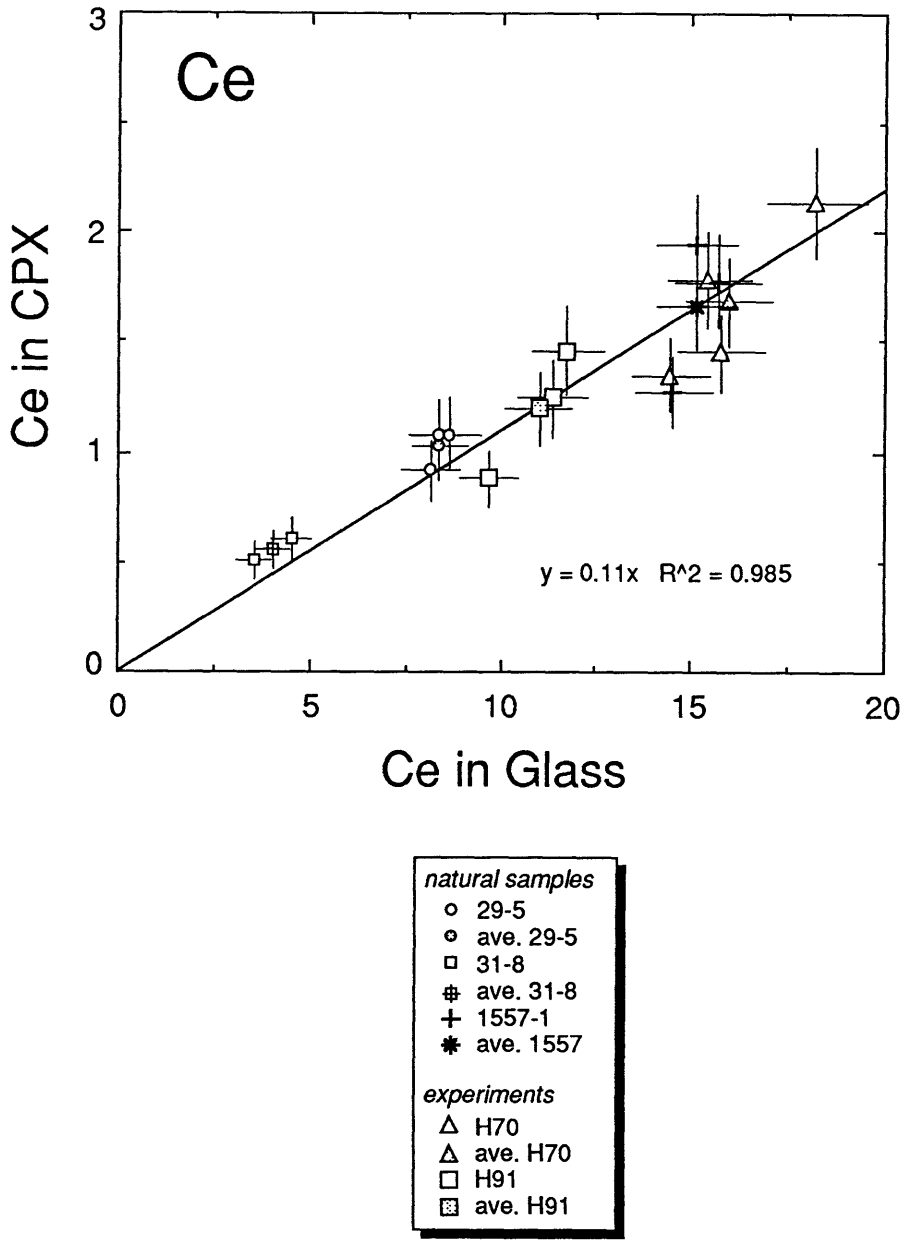
Ce
Ce in CPX
Ce in Glass
y = 0.11x R^2 = 0.985
0
1
2
3
0
5
10
15
20
natural samples
29-5
ave. 29-5
31-8
ave. 31-8
1557-1
ave. 1557
experiments
H70
ave. H70
H91
ave. H91

Figure 2.

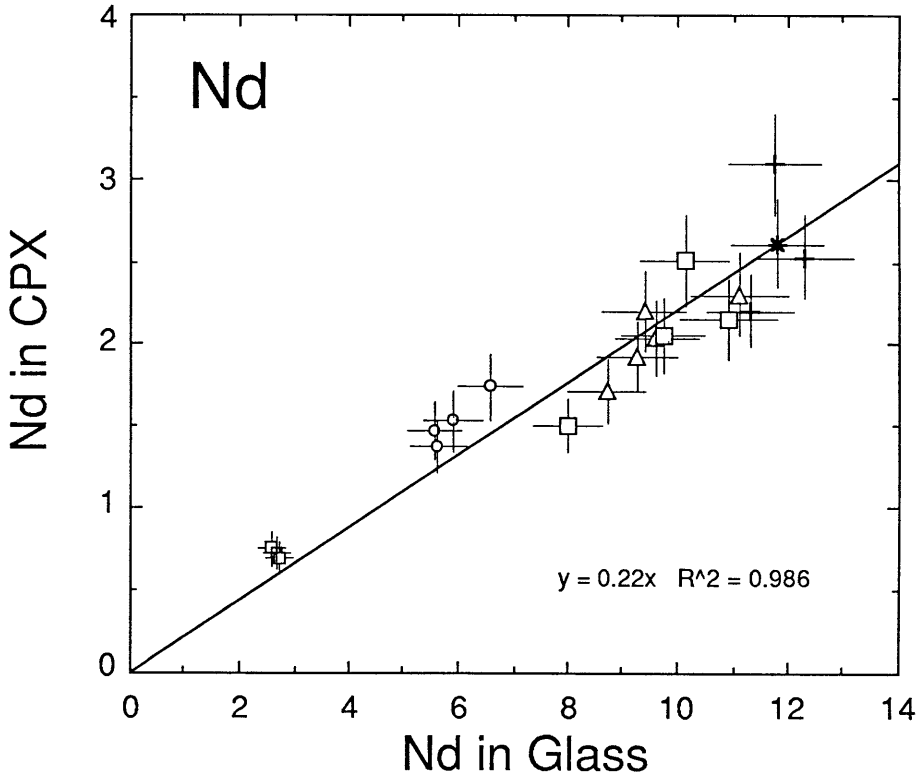

Figure 3.

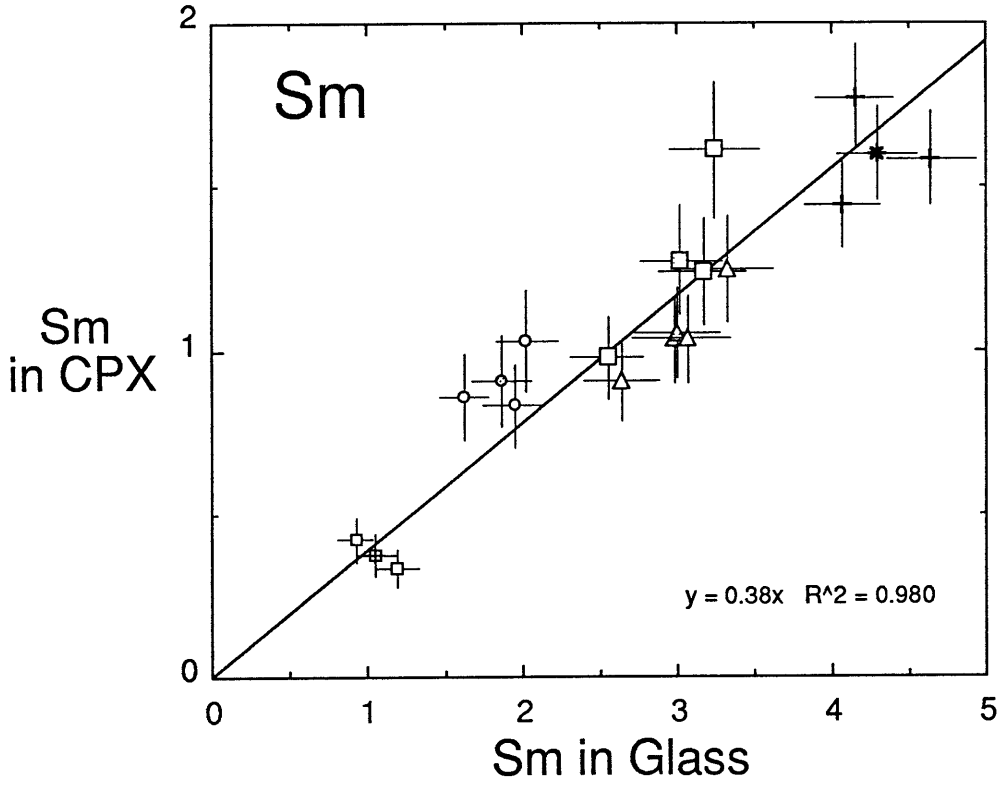

Figure 4.

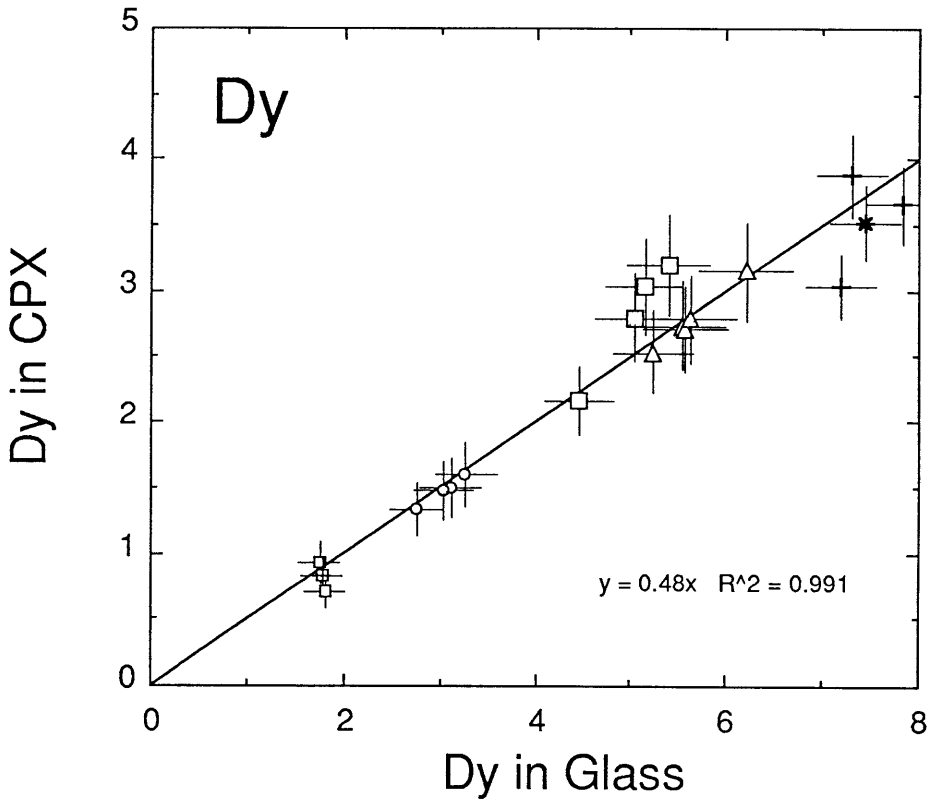

Figure 5.

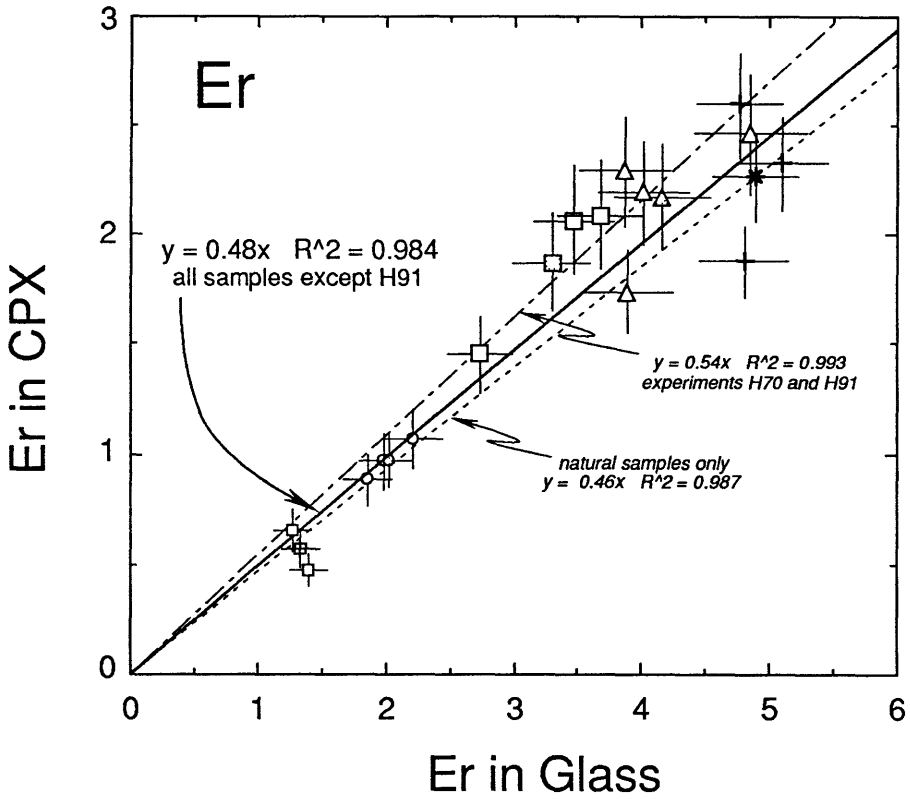
Er
y = 0.48x R^2 = 0.984
all samples except H91
y = 0.54x R^2 = 0.993
experiments H70 and H91
natural samples only
y = 0.46x R^2 = 0.987
Er in CPX
Er in Glass
0
1
2
3
4
5
6

Figure 6.

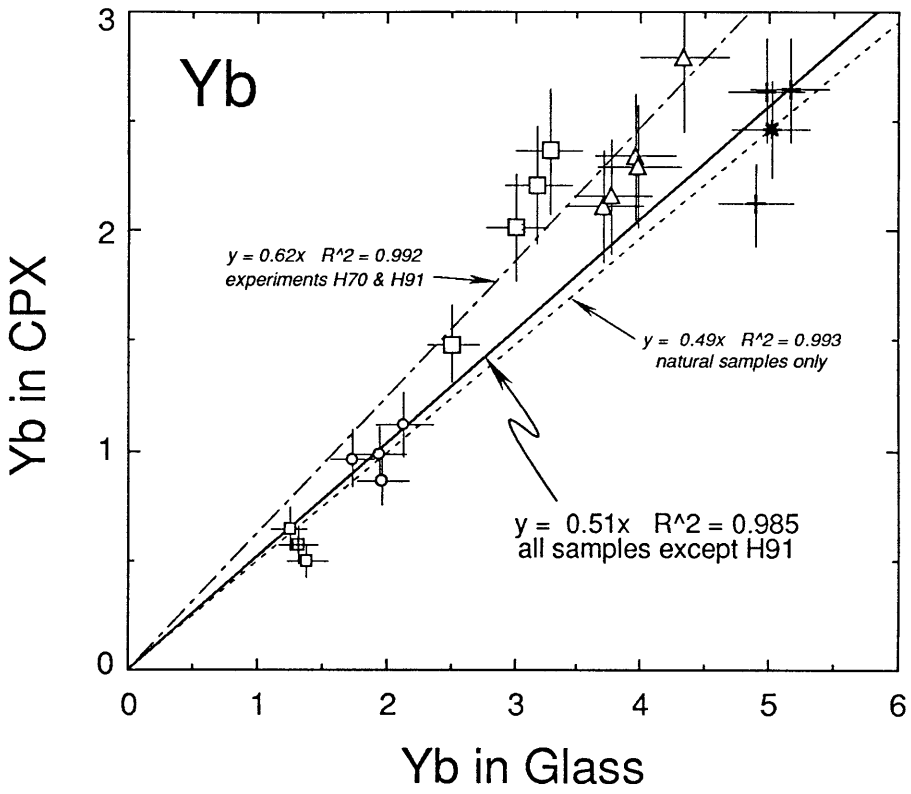
Yb
y = 0.62x R^2 = 0.992
experiments H70 & H91
y = 0.49x R^2 = 0.993
natural samples only
y = 0.51x R^2 = 0.985
all samples except H91
Yb in CPX
Yb in Glass
0
1
2
3
4
5
6

Figure 7.

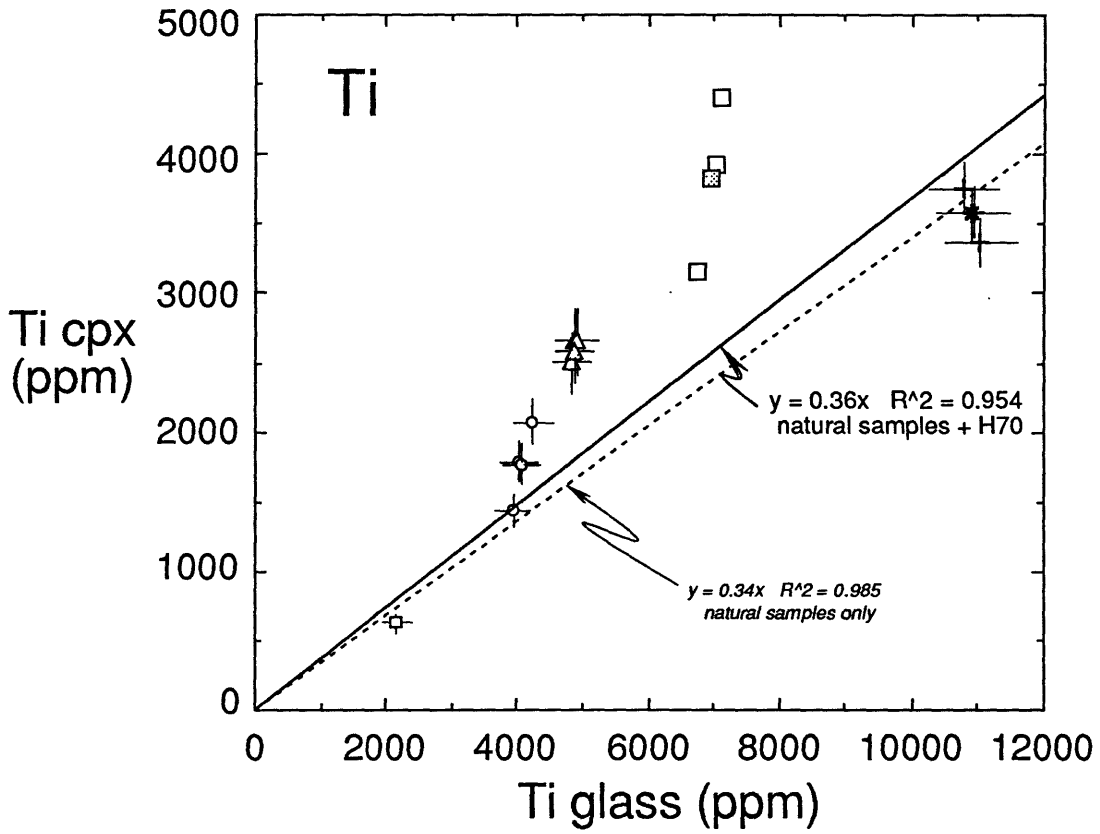
Ti
Ti cpx (ppm)
Ti glass (ppm)
0
1000
2000
3000
4000
5000
0
2000
4000
6000
8000
10000
12000
y = 0.36x R^2 = 0.954
natural samples + H70
y = 0.34x R^2 = 0.985
natural samples only

Figure 8.

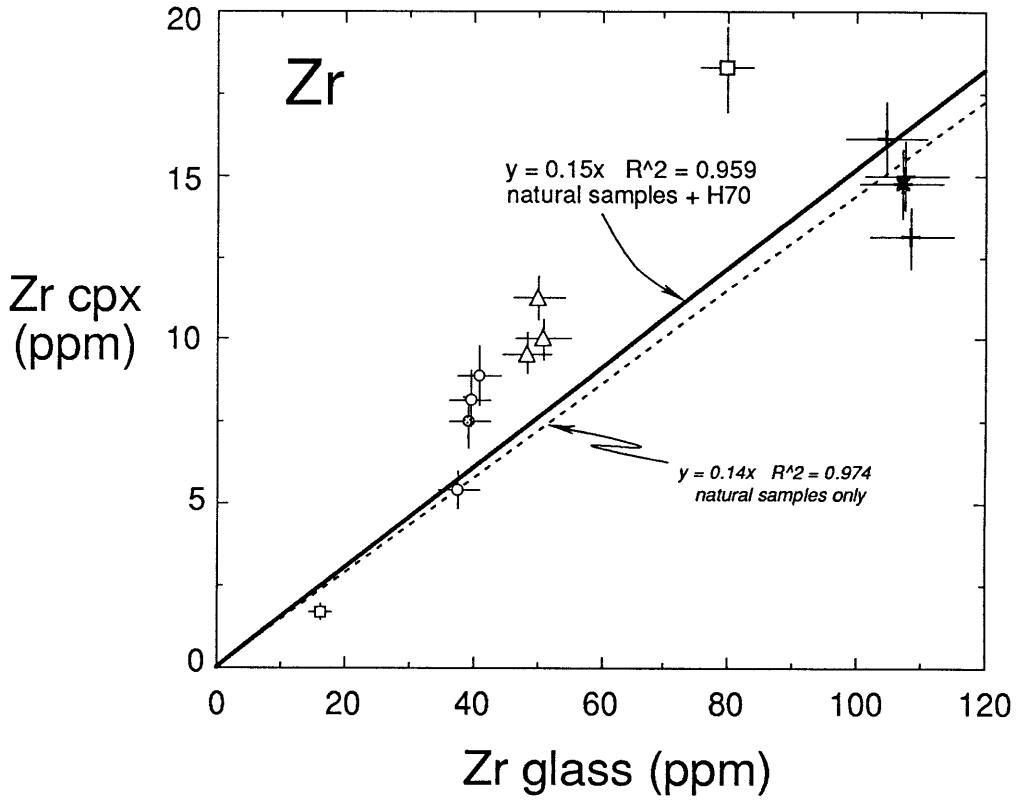
Zr
y = 0.15x R^2 = 0.959
natural samples + H70
y = 0.14x R^2 = 0.974
natural samples only
Zr cpx (ppm)
Zr glass (ppm)
0
5
10
15
20
0
20
40
60
80
100
120

Figure 9.

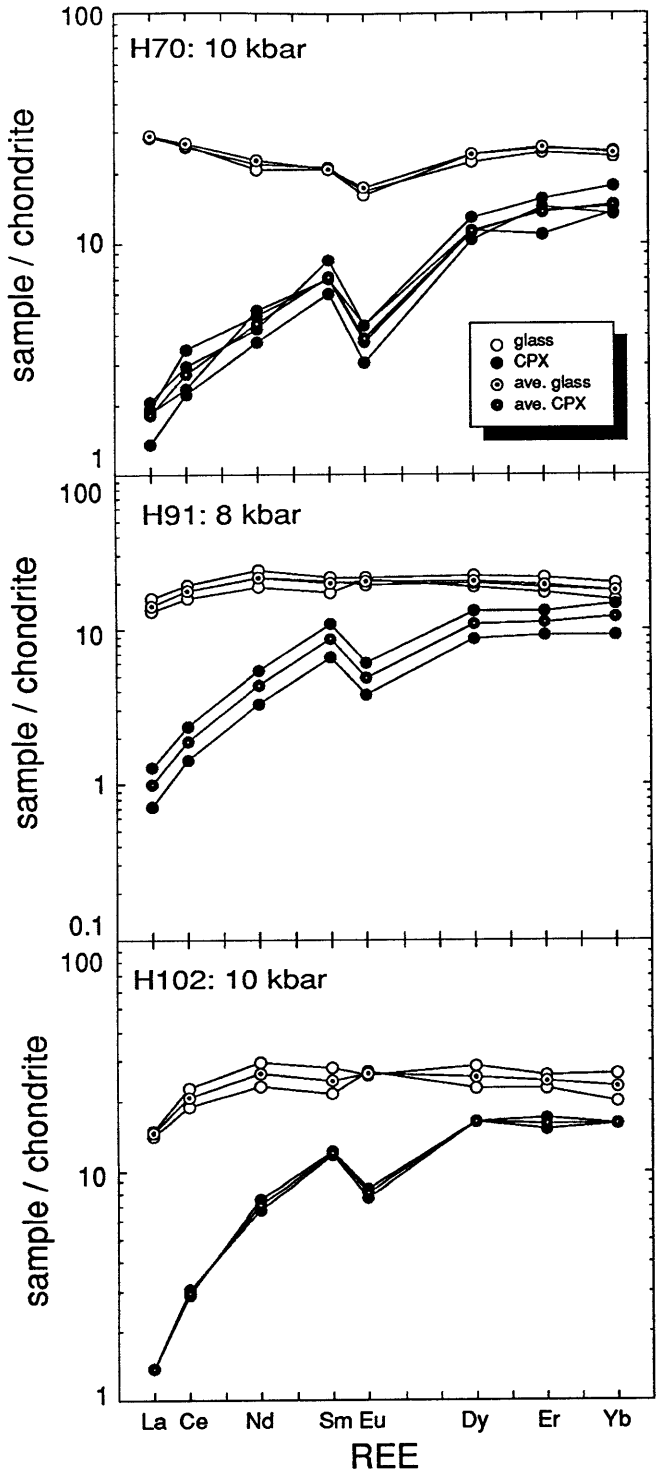

Figure 10. Rare earth element plots of glasses and clinopyroxenes in the experimental charges showing the pronounced negative europium anomalies that exist in the clinopyroxenes. The anomalies are thought to be caused by the high proportion of divalent Eu present in the system as a result of highly reducing conditions that prevailed in the experiments. Since divalent Eu is more incompatible in clinopyroxene than the trivalent Eu species, overall Eu concentrations in cpx are anomalously low.

Rare Earth Elements

Partitioning of the rare earth elements is illustrated in Figures 2-7. $D_{Ce}^{cpx/liq}$, $D_{Nd}^{cpx/liq}$, $D_{Sm}^{cpx/liq}$, $D_{Dy}^{cpx/liq}$, and $D_{Er}^{cpx/liq}$ calculated from both experiments and natural basalts are essentially identical, within analytical error. Some evidence of non-equilibrium in the experimental charges is evidenced by the spread of trace element concentrations in clinopyroxene at a given glass composition. In spite of this, the correlation coefficients of the least-squares linear regression through the data points are all very high. The good correlation of these data contrasts somewhat with the plot for Yb (Figure 7), which shows some deviation from linearity, particularly in experimental sample H91. This sample also has $K_d = 0.33$, which is significantly higher than the calculated mean for this value. Partition coefficients derived by this method are presented in Table 7.

TABLE 7. CLINOPYROXENE/BASALTIC LIQUID PARTITION COEFFICIENTS

Element	$D_{element}^{CPX/liq}$
La*	*0.06*
Ce	0.11
Nd	0.22
Sm	0.38
Dy	0.48
Er	0.48
Yb	0.49
Ti	0.36
Zr	0.15

* - $D_{La}^{CPX/liquid}$ is poorly determined due to insufficient clinopyroxene and glass standards.

High field strength elements

Figures 8 and 9 present the results of analyses for Ti and Zr. Ti concentrations in H91 clinopyroxenes are quite variable, but those in H70 clinopyroxenes plot in a tight cluster on both Ti and Zr plots. It is worth noting that H70 also shows the closest approach to equilibrium K_d values (Table 6) and the consistently good analytical results illustrated in

Figures 8 and 9 may reflect this approach to equilibrium. Conversely, the variable Ti and Zr concentrations displayed by experiment H91 probably reflect chemical disequilibrium.

Rare earth element concentrations in clinopyroxenes in sample H91 do not seem to be as strongly affected by the apparent sample disequilibrium as do Ti and Zr concentrations. Observations on the variable behavior of elements with high z/r^2 (i.e. high field strength elements Ti and Zr; z = ionic charge, r = ionic radius) were recently made in a study of element partitioning between diopside and basaltic melt, while relatively constant behavior of REE was noted in the same samples [*Kuehner et al.*, 1989]. *Shimizu* [1981] also conducted a systematic study of trace element concentrations in a sector-zoned clinopyroxene and found that both compatible and incompatible elements were enriched in the slower-growing prism [100] sector relative to the faster-growing basal [$\bar{1}$11] sector. He demonstrated a positive correlation between the enrichment of elements in the prism sector relative to the basal sector and z/r^2. Thus, high field strength elements show stronger relative enrichments between sectors than do REE, which have lower z/r^2. This may explain why Ti and Zr show more variable concentrations than do the REE in sample H91, although a more thorough time-series experimental study to examine the contrasting behavior of REE and high field strength elements is needed to verify this hypothesis.

Clear correlations in cpx/glass Ti and Zr concentrations are seen in the natural samples and in H70 (Figures 8 and 9). While there is variation within samples, it is generally within analytical precision. The partition coefficients determined by the dredged samples alone in Figures 8 and 9 define a well-constrained minimum value, and range to higher values when calculated along with the experimental samples.

DISCUSSION AND CONCLUSIONS

The REE partition coefficients calculated in this study are higher than those measured at 1 atmosphere by other authors [e.g. *Grutzeck et al.*, 1974; *Terakado and Masuda*, 1979; *McKay et al.*, 1986]. They are in close agreement with measurements made on megacrysts

[*Irving and Frey*, 1984], high pressure experiments [*Dunn*, 1987], and on separated phenocrysts from a tholeiitic basalt [*Fujimaki et al.*, 1984]. They are also similar to values reported by *Shimizu* [1980], and *Tanaka and Nishizawa* [1975], though these studies were done by phase separation of experimental charges and may suffer from both non-equilibrium and inefficient phase separation due to small sample sizes.

Kinetic effects on rare earth element partitioning were addressed in a study by *Terakado and Masuda* [1983] using short duration (<10 hours) experiments. They observed a pronounced increase in partition coefficients for short duration experiments relative to those for longer duration experiments (e.g. *Grutzeck et al.* [1974] allowed their experiments to equilibrate at 1265°C for 100 to 170 hours prior to quenching). *Terakado and Masuda* [1979] concluded that their 12-20 hour experiments attained sufficient equilibrium to validate their measured partition coefficients, based on similarity of their results with those for *Grutzeck et al.* [1974] for similar synthetic, doped compositions at one atmosphere. Since experiments H70 and H91, used in this study, had similar run times and higher temperatures than those of *Terakado and Masuda* [1979], I assume that the experiments reached comparable levels of equilibration. Diffusion rates, and thus equilibration rates, are probably a function of pressure as well as temperature, and this may be one of the causes of observed differences in partition coefficients in low and high pressure experiments. But more thorough experimentation is required to know what role pressure plays in controlling diffusion rates and, in turn, what role this plays in experimental equilibration and in affecting measured partition coefficients. Therefore, the observed differences between the present values and those reported by *Grutzeck et al.* [1974] and *Terakado and Masuda* [1979] are assumed to be real and are assessed on the basis of either pressure or compositional differences.

The partition coefficients obtained at one atmosphere by *Grutzeck et al.* [1974] and*Terakado and Masuda* [1979] are in a synthetic basaltic composition Di_{60-90}-Ab_{5-30}-An_{5-30} and Di_{80}-Fo_{10}-Qz_{10}, whereas the coefficients measured in this study are in natural

basalts. Thus, the lower values they obtained cannot be strictly compared to the higher values obtained in this study. Recent measurements done on doped natural basalt experiments at 10, 15, and 20 kbars by *Dunn* [1987] indicate that the cpx/basaltic liquid partition coefficient for Lu is 0.5 to 0.6, which is in the range of the measured coefficients in this study, and higher than the one atmosphere values. The similarity between the partition coefficients derived from the natural basalts and the experiments in this study does not illuminate the pressure dependence question since little information on equilibration pressure is available for the natural basalts.

Compositional effects may be important in controlling element partitioning, as suggested by several studies. Increasing FeO content in basaltic systems was correlated with increasing cpx-melt partition coefficients [*Schnetzler and Philpotts*, 1970] and since the Di-Ab-An system used in the above-mentioned experimental studies contains no FeO, we may infer that coefficients will be lower in these systems than in natural systems. Related to this are stoichiometric controls on element partitioning [*Takahashi and Irvine*, 1981] and the observed increase in cpx-melt REE partition coefficients with increasing Wo component in the pyroxene [*McKay et al.*, 1986]. Nevertheless, the magnitude of the differences between REE partitioning in synthetic and natural systems is not empirically known with much accuracy, and experiments in synthetic and natural systems under identical physical conditions are needed to better comprehend the controlling factors.

Other models of trace element partitioning define trace elements in terms of component molecules in the crystal lattice [e.g. *Nielsen and Dungan*, 1983; *Nielsen*, 1985]. This approach assumes that the system is composed of network-forming and network-modifying components and attempts to eliminate variations in partition coefficients caused by differences in melt composition. The procedure is most effective when comparing partitioning in samples of very different composition; its effect is minor when comparing compositionally similar samples, as in the present study of basaltic samples. Utilization of these models had no significant effect on the calculated partition coefficients.

A graphical representation of the values from Table 7 is shown in Figure 11. While the REE partitioning pattern is smooth, Zr and Ti define slight negative anomalies in the pattern. It should be emphasized that the range in Ti and Zr partition coefficients measured in this study is larger if experimental sample H91 is included in the calculation. If only the samples that have "equilibrium" K_d values (29-5, 31-8, 1557-1, and H70) are used to derive D_{Ti}, then a value of 0.36 is obtained. If H91 is included in the calculation, a value of 0.41 is derived. Similarly, D_{Zr} is 0.15 if only the samples that have "equilibrium" K_d values are used, and 0.17 if H91 is also used in the calculation. Error bars in Figure 11 primarily represent the propagated analytical uncertainties.

Positive aspects of this study *vis-a-vis* other partitioning studies is that measurements were made on *in situ* grains in glassy margins or experimental charges at natural concentration levels for the REE, Ti, and Zr together. Difficulties still remain, however, in confidently assessing equilibrium in the samples. Furthermore, the question of pressure dependence on REE, Ti and Zr partitioning between clinopyroxene and melt was not resolved. The results obtained in this study are very encouraging in terms of using the ion probe for meaningful partition coefficient determinations. Given the degree of precision of the measurements reported in this study, it would appear that the main hurdle in the quest to rigorously determine partition coefficients is no longer analytical, but experimental.

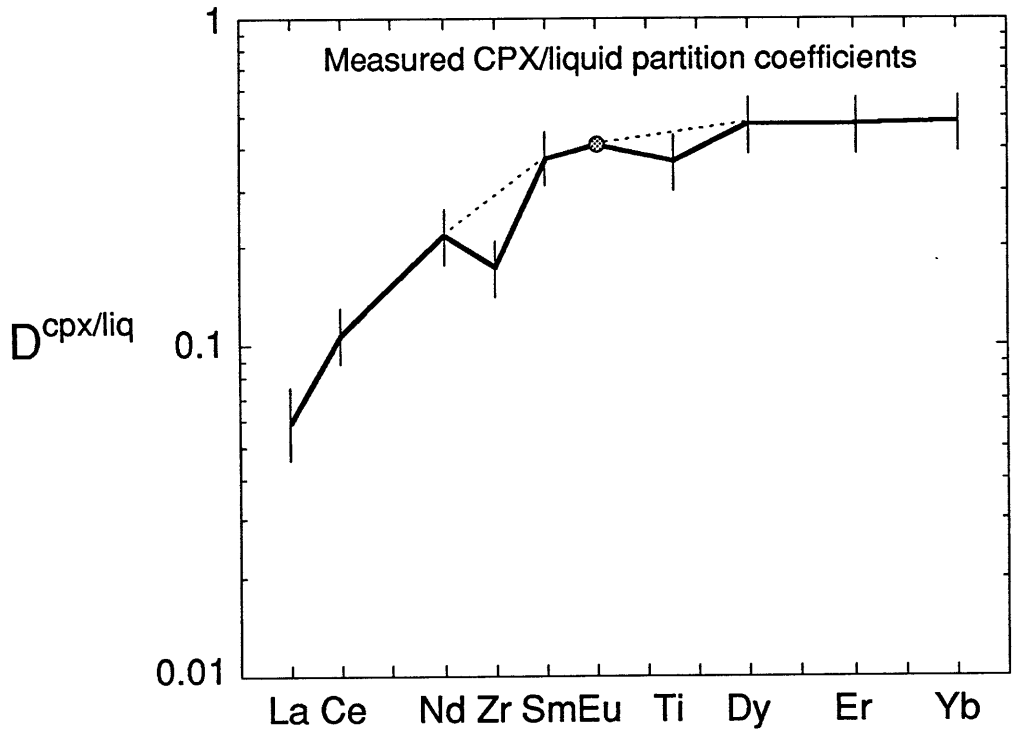

Figure 11. Graphical representation of partitioning data presented in Table 7 showing the typical smooth REE partition coefficient pattern, but also displaying noticeable negative anomalies at Zr and Ti. Dotted lines signify REE pattern without Zr and Ti plotted, and shaded circle indicates that Eu is an interpolated partition coefficient value (see text for explanation). Error bars are estimated analytical uncertainties propagated during the calculations and range from 20% for middle REE and Ti, to 30% for La.

REFERENCES

Colson, R. O., and D. Gust, Effects of pressure on partitioning of trace elements between low-Ca pyroxene and melt, *Am. Mineralogist, 74,* 31-36, 1989.

Drake, M., The oxidation state of europium as an indicator of oxygen fugacity, *Geochim. Cosmochim. Acta, 39*, 55-64, 1975.

Dunn, T. and I. S. McCallum, The partitioning of Zr and Nb between diopside and melts in the system diopside-albite-anorthite, *Geochim. Cosmochim. Acta, 46*, 623-629, 1982.

Dunn, T., Partitioning of Hf, Lu, Ti, and Mn between olivine, clinopyroxene and basaltic liquid, *Contrib. Mineral. Petrol., 96*, 476-484, 1987.

Fujimaki., H., M. Tatsumoto, and K. Aoki, Partition coefficients of Hf, Zr, and REE between phenocrysts and groundmass, *Proc. Lunar Planet. Sci. Conf., 14th, Part 2, J. Geophys. Res., 89,* suppl., B662-B672, 1984.

Green, T. H., and N. J. Pearson, Rare earth element partitioning between clinopyroxene and silicate liquid at moderate to high pressure, *Contrib. Mineral. Petrol., 91*, 24-36, 1985.

Green, T. H., S. H. Sie, C. G. Ryan, and D. R. Cousens, Proton microprobe-determined partitioning of Nb, Ta, Zr, Sr, and Y between garnet, clinopyroxene and basaltic magma at high pressure and temperature, *Chem. Geol., 74,* 201-216, 1989.

Grove, T. L. and W. B. Bryan, Fractionation of pyroxene-phyric MORB at low-pressure: an experimental study, *Contrib. Mineral. Petrol., 84*, 293-309, 1983.

Grove, T. L., D. C. Gerlach, and T. W. Sando, Origin of calc-alkaline series lavas at Medicine Lake Volcano by fractionation, assimilation, and mixing, *Contrib. Mineral. Petrol., 80,* 160-182, 1982.

Grutzeck, M., S. Kridelbaugh, and D. Weill, The distribution of Sr and REE between diopside and silicate liquid, *Geophys. Res. Lett., 1,* 273-275, 1974.

Irving, A. J. and F. A. Frey, Trace element abundances in megacrysts and their host basalts: Constraints on partition coefficients and megacryst genesis, *Geochim. Cosmochim. Acta, 48*, 1201-1221, 1984.

Kuehner, S. M., J. R. Laughlin, L. Grossman, M. L. Johnson, and D. S. Burnett, Determination of trace element mineral/liquid partition coefficients in melilite and diopside by ion and electron microprobe techniques, *Geochim. Cosmochim. Acta, 53,* 3115-3130, 1989.

McCallum, I. S. and M. P. Charette, Zr and Nb partition coefficients: implications for the genesis of mare basalts, KREEP, and sea floor basalts, *Geochim. Cosmochim. Acta, 42,* 859-869, 1978.

McKay, G., J. Wagstaff, and S.-R. Yang, Clinopyroxene REE distribution coefficients for shergottites: the REE content of the Shergotty melt, *Geochim. Cosmochim. Acta, 50,* 927-937, 1986.

Nicholls, I. A., and K. L. Harris, Experimental rare earth element partition coefficients for garnet, clinopyroxene, and amphibole coexisting with andesitic and baslatic liquids, *Geochim. Cosmochim. Acta, 44,* 287-308, 1980.

Nielsen, R. L., A method for the elimination of the compositional dependence of trace element duistribution coefficients, *Geochim. Cosmochim. Acta, 49,* 1775-1779, 1985.

Nielsen, R. L., and M. A. Dungan, Low presure mineral-melt equilibria in natural anhydrous mafic systems, *Contrib. Mineral. Petrol., 84,* 310-326, 1983.

Obata, M., S. Banno, and T. Mori, The iron-magnesium partitioning between naturally occurring coexisting olivine and Ca-rich clinopyroxene: an application of the simple mixture model to olivine solid solution, *Bull. Soc. fr. Minéral. Cristallogr., 97,* 101-107, 1974.

Philpotts, J. A., Redox estimation from a calculation of Eu2+ and Eu3+ concentrations in natural phases, *Earth Planet. Sci. Lett., 9*, 257-268, 1970.

Roeder, P. L. and R. F. Emslie, Olivine-liquid equilibrium, *Contrib. Mineral. Petrol., 29,* 275-289, 1970.

Schnetzler, C. C., and J. A. Philpotts, Partition coefficients of rare earth elements between igneous matrix and rock-forming mineral phenocrysts, *Geochim. Cosmochim. Acta, 34,* 331-340, 1970.

Shimizu, H., Experimental study on rare-earth element partitioning in minerals formed at 20 and 30 kb for basaltic systems, *Geochem. J., 14,* 185-202, 1980.

Shimizu, N., Trace element incorporation into growing augite phenocryst, *Nature, 289,* 575-577, 1981.

Sun, C.-O., R. J. Williams, and S.-S. Sun, Distribution coefficients of Eu and Sr for plagioclase-liquid and clinopyroxene-liquid equilibria in oceanic ridge basalt: an experimental study, *Geochim. Cosmochim. Acta, 38,* 1415-1433, 1974.

Takahashi, E., and T. N. Irvine, Stoichiometric control of crystal/liquid single component partition coefficients, *Geochim. Cosmochim. Acta, 45,* 1181-1185, 1981.

Tanaka, T., and O. Nishizawa, Partitioning of REE, Ba, and Sr between crystal and liquid phases for a natural silicate system at 20 kb pressure, *Geochem. J., 9,* 161-166, 1975.

Terakado, Y., and A. Masuda, Experimental study of REE partitioning between diopside and melt under atmospheric pressure, *Geochem. J., 13,* 121-129, 1979.

Terakado, Y., and A. Masuda, Kinetic effect on rare-earth element partitioning in the diopside-melt system: an experimental observation, *Chem. Geol., 40,* 13-23, 1983.

Tormey, D. R., T. L. Grove, and W. B. Bryan, Experimental petrology of normal MORB near the Kane Fracture Zone: 22°-25°N, Mid-Atlantic Ridge, *Contrib. Mineral. Petrol., 96,* 121-139, 1987.

Weill, D. F., G. A. McKay, S. J. Kridelbaugh, and M. Grutzeck, Modeling the evolution of Sm and Eu abundances during lunar igneous differentiation, *Proc. Lunar Sci. Conf. 5th,* 1337-1352, 1974.

CHAPTER 4. GEOCHEMICAL CHARACTERISTICS OF REFRACTORY SILICATE MELT INCLUSIONS

CHAPTER 4.
GEOCHEMICAL CHARACTERISTICS OF REFRACTORY SILICATE MELT INCLUSIONS

INTRODUCTION

Melting models based on trace element concentrations in abyssal peridotite diopsides [*Johnson et al.*, 1990] and theoretical models based on fluid dynamical considerations and geochemistry [*Ahern and Turcotte*, 1979; *McKenzie*, 1985a and b, 1989] are converging toward the hypothesis that very small melt fractions are mobile and will segregate in the upper mantle. If fractional melting (for simplicity, the term "fractional melting" will be used to denote the natural process in which very small increments [<1%] of melting are separated from the matrix. Perfect fractional fusion is a theoretical, unattainable endmember of the melting spectrum in which melt increments are infinitesimal.) is dominant in the oceanic upper mantle during mid-ocean ridge basalt (MORB) production, then it follows that late-stage, highly depleted, refractory melts must exist somewhere between the point of magma segregation and the region of aggregation and final mixing prior to eruption as MORB. Such melts are a necessary consequence of fractional melting and their recognition is of critical importance in understanding processes of MORB petrogenesis in general, and in evaluating the validity of the fractional melting model in particular. Very small fractions of these late-stage primary melts are probably very small in volume and thus will rarely reach the surface unaffected by mixing, making their existence difficult to directly document. However, minerals growing in a magma occasionally trap small drops of melt on their growing surface or in their skeletal interiors [*Roedder*, 1984] and preserve them, more or less unaffected by external processes except for post-entrapment interaction with the host-phase. Thus, these melt inclusions could be very useful in evaluating the fractional melting process in nature.

Interest in the chemical composition of melt inclusions stems directly from their potential role as windows into the mantle. Refractory melt inclusions with compositions that could be in equilibrium with mantle olivine of Fo_{90-91} have been described [e.g.,

Donaldson and Brown, 1977; *Dungan and Rhodes*, 1978; *Sobolev and Naumov*, 1985; *Falloon and Green*, 1986]. If melting occurs over a depth range, and if minerals crystallize at any given depth(s), then they are theoretically capable of trapping melt anywhere along the ascent path. Thus, primary melt inclusions (*Roedder* [1984] defines "primary" inclusions as those fractions of melt trapped in a growing crystal as a result of some process or mechanism(s) that interrupts the growth of a perfect crystal, such as surface cracks, defects, or non-uniform growth) would record the composition(s) of any liquids in which the host mineral experienced a growth phase. Thus, the working hypothesis for this study is that if subridge melting is nearly fractional, then it is expected that small, primary melt increments will rarely be preserved in the erupted lavas due to post-segregation homogenization [*Anderson*, 1976; *Dungan and Rhodes*, 1978; *Walker et al.*, 1979], but melt inclusions can span the range of compositions segregated from the mantle over the melting interval and often should be closer to primary magma compositions. This leads to the prediction that some melt inclusions will be more refractory and depleted in incompatible elements than most sampled lavas.

In order to utilize melt inclusions to test the above hypothesis, several questions must be addressed: 1) Has post-entrapment host-phase interaction affected the inclusion composition? Even if it has affected absolute concentrations of elements, certain incompatible element ratios will be unaffected and the compositions can be used to infer source characteristics, 2) Can melt inclusions in different mineral phases contained in a single rock sample be related by fractional crystallization or by melting of a common source?, 3) Can mixing of "end-member" compositions account for the observed range in inclusion compositions contained in a single sample?, 4) If the above questions are answered in the negative, to what extent do the inclusion compositions indicate source differences? Based on the results of Chapter 2 [*Johnson et al.*, 1990], expected characteristics of refractory primary melts would include high Ti/Zr (>150), low Ti, Zr, rare earth elements (REE) and other incompatible element concentrations, negative Ti and

Zr anomalies (HFSE anomalies) relative to REE on spider diagrams, and high compatible element concentrations (MgO, Cr).

In this paper, I report major and trace element compositions of silicate melt inclusions from a variety of geographic locations. From these data, I discuss their potential role as indicators of source and primary melt compositions and, in some cases, of the melting process by which they were produced. The samples were collected by Dr. Alexander Sobolev and colleagues at the Vernadsky Institute of Geochemistry, Academy of Sciences, U.S.S.R., and comprise mineral grains which contain one or more silicate melt inclusions ranging from 20-150μm. Because the melt inclusions are so small, all analyses were done by ion microprobe at M.I.T. In Part A of the paper, I focus on lavas formed in the mid-oceanic setting, at a location near the Vema Fracture Zone, Mid-Atlantic Ridge, and on the Reykjanes Peninsula, Iceland. I discuss the relationship between the inclusions, host minerals, and the host glass, and relationships between inclusions in different minerals in the same sample and attempt to understand their evolution via melting, fractional crystallization, and mixing processes. In Part B of the paper, I report the results from a global suite of inclusions which, because of difficulties in receiving associated host-rock material from Moscow, are discussed in terms of their similarities and differences with published analyses of lavas from the respective sampling locations or areas. Samples discussed in this part of the paper are from Kamchatka, Cape Vogel (Papua New Guinea), Tonga, the Troodos ophiolite upper pillow lava sequence in Cyprus, and Iceland.

ANALYTICAL TECHNIQUES

Major element compositions of the melt inclusions and host minerals were determined at the Vernadsky Institute using a wavelength dispersive Cameca electron microprobe. The accelerating voltage was 15kV and the sample currents were 50nA. To avoid volatile loss from the glass, analyses were carried out in scanning mode at a sample temperature of -170°C. Major element compositions are reported in Table 1.

High temperature microthermometry

The individual, hand-picked grains are mounted in epoxy and subjected to microthermometric measurement to determine homogenization temperatures. Homogenization temperatures are defined as the temperature at which the two-phase inclusion (vapor+silicate melt) homogenizes to a single melt phase. It is assumed that the inclusion was trapped as a one phase silicate melt and that with cooling and decompression, a vapor phase exsolved and was trapped in the inclusion cavity along with the remaining silicate liquid as long as it remains intact. By heating the mineral and inclusion and observing the shrinkage of the vapor bubble, the temperature at which the bubble disappears is the homogenization temperature (T_h) and represents a minimum temperature of the system at the time the inclusion was trapped.

The present melt inclusions were studied with a high temperature optical apparatus in high purity He. Sample temperatures were measured by Pt/Pt-10% Rh thermocouples with a reported accuracy of ±5°C [*Sobolev et al.*, 1980]. Temperature control was checked against the melting points of Au and Ag fixed directly to the examined section. The rate of sample heating was varied as a function of the rate of phase transformation in inclusions, and ranged from 5° to 50°C min^{-1}. To fix melting and homogenization temperatures of inclusions, temperatures were held constant for 6-60 minutes. The temperatures reported in Table 1 are homogenization temperatures. The true trapping temperature also requires knowledge of the ambient pressure at the time of trapping. Given the compressibility of silicate melts and the accuracy of the temperature measurements, T_h and T_t are probably the same, within experimental and analytical error [*Roedder*, 1984].

TABLE 1. Major and Trace Element Compositions of Melt Inclusions

Sample Element	649/11 MORB host glass	TOR-2 OLN63 olivine #63	TOR-2 OL N7 olivine #7	TOR-2 PLN17 plag. #17	TOR-2 PLN47 #1 plag.#47,incl.1	TOR-2 PLN47 #2 plag.#47,incl.2	TOR-2 CPX N2 cpx #2
TiO2(ion probe)	1.25	0.75	0.84	0.83	0.73	0.61	1.42
Sc	35.6				30.8	30.1	33.9
Ti	7466	4474	5027	4951	4353	3635	8496
V	233				234	164	278
Cr	393	393	427	405	447	350	477
Sr	123	100	81	111	137	130	124
Zr	79	48	43	44	16	17	90
Nb	2.1	1.8	1.6	1.1	0.44	0.52	1.8
Ti/Zr	95	94	117	112	267	211	94
Ti/Sr	61	45	62	45	32	28	69
Zr/Nb	37	27	26	41	37	33	49
La	2.67	1.49	2.29	1.06	1.50		2.88
Ce	7.91	4.44	6.25	3.69	5.16		9.08
Nd	8.79	4.22	6.12	5.43	4.71		8.81
Sm	3.36	1.31	2.38	2.50	1.83		3.78
Eu	1.27	0.60	0.75	0.60	0.80		1.34
Gd							
Tb							
Dy	5.60	2.28	3.95	3.65	3.49		5.72
Er	3.62	1.55	2.47	2.21	2.05		3.76
Yb	3.65	1.32	2.41	2.32	1.62		3.59
Major Elements							
SiO2	50.05	50.94	49.33	49.73	49.68		51.60
TiO2	1.26	0.93	0.88	0.83	0.71		1.35
Al2O3	16.02	16.94	16.97	16.73	16.36		15.22
FeOt	9.00	7.85	7.13	7.86	8.15		8.79
MnO	0.17	0.15	0.14	0.14	0.13		0.17
MgO	8.35	8.64	9.17	8.52	8.43		7.96
CaO	12.03	11.62	12.38	11.90	11.94		11.84
Na2O	2.40	2.26	2.33	2.92	3.12		2.97
K2O	0.10	0.08	0.05	0.05	0.08		0.08
P2O5							
Total	**99.38**	**99.41**	**98.38**	**98.68**	**98.60**		**99.98**
mg#(FeO=0.95FeOt	0.635	0.674	0.707	0.670	0.660		0.629
Th (°C)		1220	1230	1225	1220		1200
mg # ol or cpx		0.891	0.9				0.878
An plag				0.849	0.846		

TABLE 1. continued

Sample Element	Cape Vogel 41F,L3,Sp3 spinel	Cape Vogel 41F OL N1-H-2 olivine	Cape Vogel 2985 (a) hi-Mg andesite	Cape Vogel 2987 (a) hi-Mg andesite	Tonga 26/2, OLN43 olivine#43	Tonga 26/2, OLN65,#1 olivine#65,incl1	Tonga 26/2, OLN65,#2 olivine#65,incl2	Tonga 26/1 (b) boninite	Troodos KOL-OL N4 olivine	Troodos 8 (c)
TiO2	0.13	0.08	0.46	0.27	0.32	0.34	0.38	0.25	0.22	0.31
Sc										
Ti	784	497	2757	1618	1911	2039	2297	1499	1302	1858
V			165	145						
Cr		2549	664	1615	809	507	672		442	960
Sr	54	32	91	83	133	163	199		8	62
Zr	29	20	36	55	25	35	43		3.4	18.0
Nb	1.5	1.3			5.7	7.3	10.0		0.64	1.00
Ti/Zr	27	25	77	29	76	58	54		385	103
Ti/Sr	15	15	30	19	14	12	12		160	30
Zr/Nb	20	16			4	5	4		5	18
La		0.91	4.80	3.11	7.50	6.93	8.33	3.60	0.33	0.88
Ce	3.84	2.14	9.47	6.48	14.60	13.90	17.62	7.00	0.46	2.22
Nd	1.80	1.05	4.72	2.95	7.59	6.71	9.38	3.50	0.37	1.91
Sm	0.34	0.20	1.13	0.69	1.76	1.37	1.87	0.82	0.40	0.73
Eu	0.42	0.06	0.39	0.23	0.25	0.21	0.17	0.44	0.11	0.27
								1.50		0.96
			0.22	0.13				0.24		0.20
Dy	0.63	0.27			1.58	1.61	1.87	1.50	1.43	1.39
Er	0.26	0.16			1.35	1.06	1.20	1.20	0.90	1.03
Yb	0.24	0.16	0.82	0.52	1.39	1.06	1.32	1.20	1.02	1.04
Major Elements										
SiO2	58.74	57.85	57.80	57.60	51.22		54.06	54.24	52.51	53.80
TiO2	0.15	0.08	0.46	0.27	0.31		0.41	0.25	0.25	0.31
Al2O3	9.14	5.50	11.50	8.50	9.07		10.92	10.82	13.15	11.40
FeO	6.18	7.90	9.46	9.83	7.77		7.39	8.69	6.93	7.47
MnO	0.13	0.10	0.20	0.26	0.11		0.12	0.15	0.14	0.16
MgO	17.02	25.72	12.60	17.10	17.69		12.68	14.10	12.70	12.54
CaO	4.83	2.80	6.00	5.10	8.07		9.10	8.72	12.26	8.73
Na2O	0.85	0.36	1.30	0.60	1.19		1.53	0.53	0.36	1.30
K2O	0.19	0.07	0.40	0.40	0.41		0.49	0.24	0.06	0.15
P2O5	0.03	0.07						0.07		0.02
Total	**98.52**	**100.45**	**99.72**	**99.66**	**95.84**		**96.70**	**97.81**	**98.36**	**95.88**
mg#	0.838	0.859	0.714	0.765	0.810		0.763	0.753	0.775	0.759
T hom (°C)					1330		1255			
mg # ol or cpx					0.92		0.905			
An plag										

a - Cape Vogel whole rock data from Jenner [1981]
b - Tonga forearc whole rock data from Sharaskin et al. [1983]
c - Troodos whole rock data from Cameron et al. [1983]

TABLE 1. continued

Sample Element	Troodos 9 (c)	Troodos 10 (c)	Troodos 24 (d)	Kamchatka DAN-51,OL N8 olivine #8	Kamchatka DAN-51, OLN2' olivine #2'	Kamchatka KB-66, OL5 olivine	Kamchatka KB-9, N6 olivine	Kamchatka KB38,cpx,L1 cpx, incl 1	Kamchatka KB38,cpx,L2 cpx, incl 2	Snaefellsnes OL-110189/1 olivine
TiO2	0.19	0.25	0.24	0.32	0.31	0.44	1.00	0.77	0.72	3.18
Sc										
Ti	1139	1499	1439	1913	1841	2618	6018	4604	4299	19063
V										
Cr	850	800	650	1420	649	363	451	41	53	
Sr	62		38	331	349	768	942	1298	1258	711
Zr	16.0	7.0	38.0	12	12	42	53	65	57	171
Nb	1.00	1.00	<1	0.17	0.22	0.44	7.4	2.0	1.7	50.2
Ti/Zr	71	214	38	158	151	62	113	71	75	111
Ti/Sr	18		38	6	5	3	6	4	3	27
Zr/Nb	16	7		72	56	96	7	33	34	3
La	1.09	0.56	0.55	2.64	2.49		9.14	14.28	11.14	22.79
Ce	2.19	1.15	1.04	4.87	4.99		22.89	28.77	28.71	46.22
Nd	1.02	0.87	0.50	3.78	3.37		16.97	19.30	18.14	23.93
Sm	0.32	0.44	0.26	1.43	1.14		4.38	4.79	4.24	5.53
Eu	0.11	0.18	0.11	0.42	0.40			0.24	0.03	1.87
	0.51	0.82	0.54							
	0.11	0.16	0.13							
Dy	0.93	1.28	1.15	1.86	1.44		2.86	3.81	3.78	4.67
Er	0.75	1.02	1.00	1.21	0.87		1.24	2.48	2.43	2.63
Yb	0.84	1.11	1.06	1.41	0.87		1.59	2.54	2.27	2.55
Major Elements										
SiO2	51.74	49.54	50.19	46.57	44.23	48.56	48.36	49.38	48.67	46.63
TiO2	0.19	0.25	0.24	0.30	0.29	0.56	0.47	0.77	0.74	2.72
Al2O3	12.47	11.95	12.74	9.60	6.36	9.82	7.94	16.48	15.68	15.80
FeO	7.18	7.56	8.21	7.89	11.42	9.62	7.21	9.44	9.72	7.72
MnO	0.14	0.15	0.15	0.12	0.21	0.12	0.16	0.16	0.15	0.12
MgO	12.74	11.02	10.88	20.82	22.96	14.25	23.03	5.06	4.70	9.38
CaO	9.88	10.45	11.11	8.65	9.65	10.62	5.47	10.44	10.07	13.38
Na2O	1.10	0.86	0.83	1.38	0.88	1.82	2.19	2.09	2.64	2.48
K2O	0.39	0.21	0.14	2.07	1.86	2.81	1.97	2.58	2.93	1.12
P2O5	0.01	0.02	0.02	0.21	0.23	0.48	0.36	0.56	0.65	0.61
Total	**95.84**	**92.01**	**94.51**	**97.40**	**97.86**	**98.18**	**96.80**	**96.40**	**95.30**	**99.35**
mg#	0.769	0.732	0.713	0.832	0.790	0.735	0.857	0.501	0.476	0.695
T hom (°C)				1470	1515	1345	1520			1250
mg # ol or cpx				0.906	0.89	0.909	0.909			0.882
An plag										

c - Troodos whole rock data from Cameron et al. [1983]
d - Troodos whole rock data from Cameron [1985]

TABLE 1. continued

Sample Element	Theistareykir OL-150785/2 olivine #2, incl 1	Theistareykir OL-150785/2 olivine #2, incl 2	Theistareykir OL-170485/4 olivine	14134 150787 host glass	Reykjanes Pen. OL 150787/3 olivine	14124 230787 host glass	Reykjanes Pen. OL 230787/1 olivine #1	Reykjanes Pen. OL 230787/3 olivine #3
TiO2	0.51		0.53	0.53	0.49	0.47	0.40	0.45
Sc				42.8		37.7		
Ti	3056		3205	3177	2948	2843	2417	2716
V				207		189		
Cr	2797		365	502	221	517	378	566
Sr	15		53	55	68	67	45	39
Zr	12		20	18	20	17	6.6	11
Nb	0.58		0.50	0.64	1.03	0.51	0.13	0.42
Ti/Zr	251		161	175	147	172	365	246
Ti/Sr	200		60	57	43	42	54	70
Zr/Nb	21		40	28	19	32	51	26
La	0.11	0.14		0.63	1.46	0.73	0.11	0.54
Ce	0.74	0.99		2.18	3.21	2.32	0.52	1.83
Nd	1.83	1.73		2.58	3.45	3.06	0.94	2.58
Sm	1.08	0.83		1.24	1.09	1.59	0.83	1.40
Eu	0.48	0.42		0.49	0.44	0.70	0.27	0.50
Dy	2.52	1.95		3.30	2.55	3.00	1.50	3.46
Er	1.71	1.42		2.26	1.50	2.34	1.02	2.58
Yb	1.66	1.37		2.28	1.91	2.20	0.89	2.56
Major Elements								
SiO2	49.62	49.62	48.83	49.34	50.24	49.00	49.31	48.92
TiO2	0.50	0.50	0.55	0.53	0.52	0.50	0.41	0.53
Al2O3	14.07	14.07	16.24	15.50	15.48	16.12	16.63	15.90
FeO	7.19	7.19	7.19	8.02	6.84	8.16	6.71	6.94
MnO	0.13	0.13	0.14	0.15	0.08	0.17	0.11	0.14
MgO	12.78	12.78	9.73	9.81	9.15	10.27	9.94	11.54
CaO	14.26	14.26	13.81	14.71	15.80	13.90	15.81	14.85
Na2O	1.25	1.25	1.67	1.70	1.64	1.52	1.57	1.75
K2O	0.02	0.02	0.01	0.02	0.06	0.03	0.01	0.02
P2O5								
Total	**99.82**	**99.82**	**98.17**	**99.78**	**99.81**	**99.67**	**100.50**	**100.59**
mg#	0.769	0.769	0.717	0.696	0.715	0.702	0.735	0.757
T hom (°C)	1245	1245	1200		1225		1245	1290
mg # ol or cpx	0.915	0.915	0.885		0.885		0.89	0.907
An plag								

Trace Elements

Trace element concentrations were measured by ion microprobe at M.I.T. Operating conditions were the same as those described in Chapter 2 [*Johnson et al.*, 1990], except that generally smaller beam sizes were used due to the size of the inclusions. Working curves were derived specifically for basaltic glasses using basaltic to rhyodacitic glass standards provided by Dr. John Bender. All glasses were previously analyzed for REE and other trace elements by isotope dilution mass spectrometry (ID) and X-ray fluorescence (XRF) [*Bender et al.*, 1984]. The ion probe working curves were derived by repeated analysis of the standards over a period of $1\frac{1}{2}$ to 2 years and the resulting ion intensities, ratioed to ^{30}Si, were averaged for each standard and plotted versus their absolute elemental concentrations. The least-squares regression fit to the data was then calculated and taken as the calibration, or "working" curve. Two corrections were found to be necessary for constructing the working curves. The first stems from the varying silica contents in the standards and samples. Because standards were chosen to span a wide range of trace element concentrations, high silica rhyodacites were used to constrain the curves at relatively high concentration levels. Since trace element ion intensities are ratioed to silicon, trace element intensity ratios from these high silica samples invariably plotted off of the calibration curve defined by basaltic glasses. By normalizing all of the ratios based on a basaltic silica concentration of 49.5 wt%, this artifact was eliminated and the high silica standards conformed to the basaltic working curves, which became linear in all cases.

The second correction is needed because of the mass overlap of the molecular ions $^{135}Ba^{16}O$ and $^{137}Ba^{16}O$ with ^{151}Eu and ^{153}Eu isotopes. This overlap is generally not a factor in clinopyroxene analyses since Ba is highly incompatible, but in basaltic glasses, Ba is abundant enough to increase the apparent Eu concentrations. Energy filtering at -35v offset was found to be insufficient to remove the BaO interferences, so a theoretical algorithm was introduced to eliminate the effects. The procedure is as follows:

Assumptions:

1. BaO is the only interfering molecular ion
2. BaO isotope abundances are the same as those of Ba
3. $153\# = {}^{153}Eu + {}^{137}Ba^{16}O$; $153\# \equiv$ measured 153 peak
4. $151\# = {}^{151}Eu + {}^{135}Ba^{16}O$; $151\# \equiv$ measured 151 peak
5. ${}^{153}Eu/.522 = {}^{151}Eu/.478 \therefore {}^{151}Eu = 0.915709 * {}^{153}Eu; {}^{153}Eu = 1.09205 * {}^{151}Eu$
6. ${}^{137}Ba/.112 = {}^{135}Ba/.066 \therefore {}^{135}Ba = 0.589286 * {}^{137}Ba; {}^{137}Ba = 1.69697 * {}^{135}Ba$

Combining 3, 4, 5, and 6 we can write

$$151\# = 0.915709 * {}^{153}Eu + 0.58929 * {}^{137}Ba^{16}O$$
$$+ \quad -0.58929 * (153\# = {}^{153}Eu + {}^{137}Ba^{16}O)$$

$$151\# - (0.58929 * 153\#) = (0.915709 * {}^{153}Eu) - (0.58929 * {}^{153}Eu)$$

and then by rewriting, this becomes

$$151\# - (0.58929 * 153\#) = 0.326423 * {}^{153}Eu, \text{ or}$$
$${}^{153}Eu = 3.06351 * 151\# - 1.80528 * 153\#$$

and finally

$$\mathbf{Eu} = \frac{{}^{153}\mathbf{Eu}}{.522}$$

However, this procedure assumes that the only interfering molecular ion species is BaO. Because it is likely that BaOH also interferes with the Eu mass peaks, this procedure meets with only limited success and is necessarily accompanied by lower analytical accuracy and precision for Eu.

Working curves for two representative elements are shown in Figure 1 and working curve values for all of the analyzed elements are given in Table 2. Estimated accuracy and precision for the elements, based on replicate analyses of standards over a two year period, are also indicated by error bars in Figure 1. The working curve for Nb is poorly defined due to the limited range of Nb data in basaltic glasses used to construct the working curve. Thus, Nb concentrations are only believed to be accurate to ± 25%. Figure 2 shows REE measurements on three representative internal standards along with values determined by isotope dilution [*Bender et al.*, 1984].

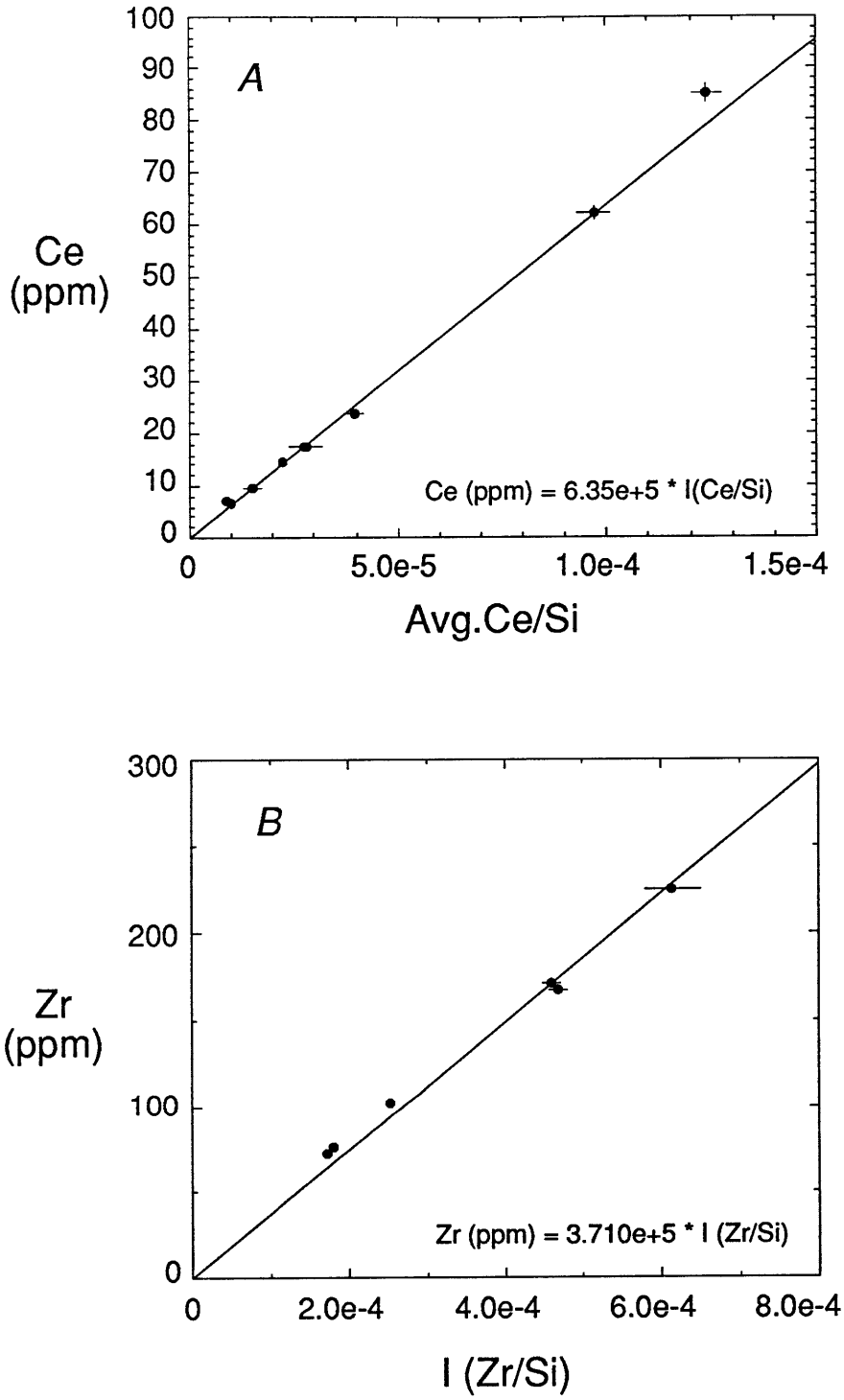

Figure 1. Basaltic glass working curves for (a) Ce and (b) Zr to illustrate the accuracy of the calibration technique. 2σ error bars on the averaged points are determined from repeated analyses of the standards over a two year period.

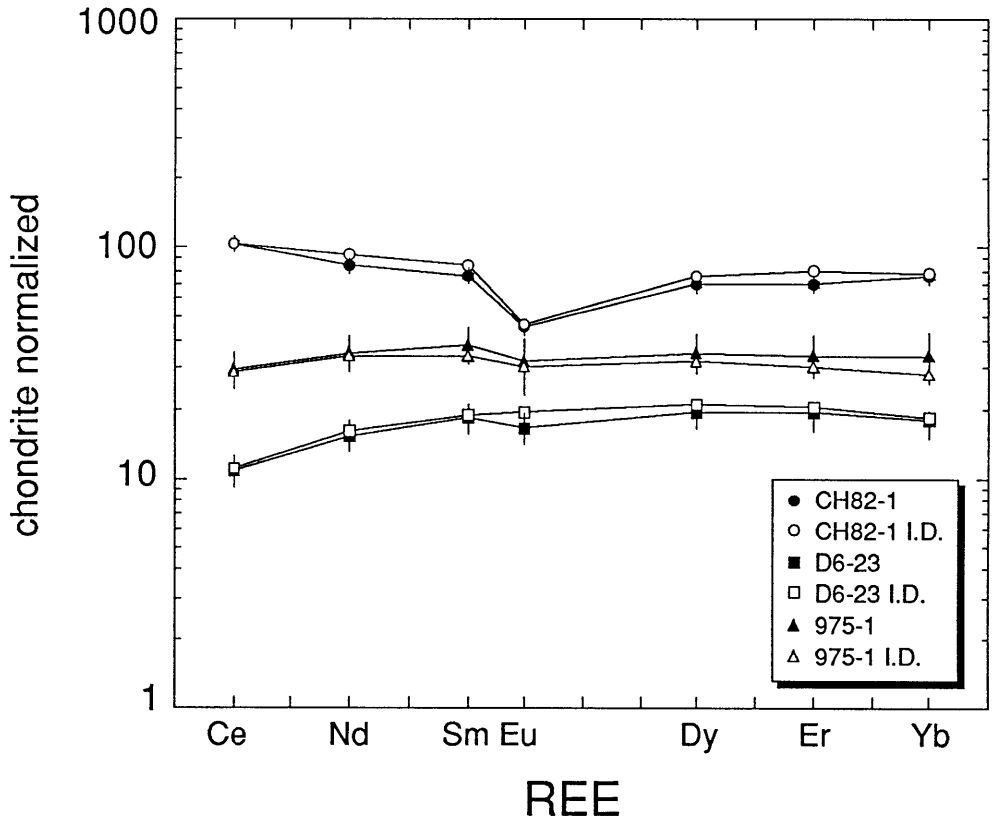

Figure 2. REE analyses of basaltic glasses used as internal standards over the two years of glass working curve development. Solid symbols are ion probe analyses using the derived working curves, and open symbols are isotope dilution analyses of the same samples [Bender et al., 1984; J. Bender, personal communication, 1988]. 2σ error bars, based on repeated ion probe analyses, are also shown.

TABLE 2. BASALTIC GLASS WORKING CURVES

$Sc = 8.3 \times 10^4\ I(^{45}Sc/^{30}Si)$
$Ti = 1.882 \times 10^5\ I(^{47}Ti/^{30}Si)$
$V = 3.18 \times 10^5\ I(^{51}V/^{30}Si)$
$Cr = 3.72 \times 10^5\ I(^{52}Cr/^{30}Si)$
$Sr = 4.03 \times 10^5\ I(^{88}Sr/^{30}Si)$
$Zr = 3.71 \times 10^5\ I(^{90}Zr/^{30}Si)$
$Nb = 7.61 \times 10^5\ I(^{93}Nb/^{30}Si)$
$La \approx 5.8 \times 10^5\ I(^{139}La/^{30}Si)$
$Ce = 6.35 \times 10^5\ I(^{140}Ce/^{30}Si)$
$Nd = 4.8 \times 10^5\ I(^{146}Nd/^{30}Si)$
$Sm = 4.4 \times 10^5\ I(^{147}Sm/^{30}Si)$
$Eu = 4.07 \times 10^5\ I^*$
$Dy = 5.1 \times 10^5\ I(^{163}Dy/^{30}Si)$
$Er = 5.35 \times 10^5\ I(^{167}Er/^{30}Si)$
$Yb = 4.55 \times 10^5\ I(^{174}Yb/^{30}Si)$

* - Eu calculated according to the procedure in the text.

In addition to uncertainties in the Nb working curve, it was observed that Cr concentrations in some of the measured inclusions were unrealistically high. Generally, Cr is abundant enough in basaltic and refratory liquids to provide very good analytical precision, and indeed the aberrantly high numbers are reproducible. However, it is possible that in some of the inclusions high Cr is the result of quench crystallization of spinel or clinopyroxene, of microinclusions of Cr-spinel, or of host-phase incorporation in the analysis. In spinel-hosted inclusions, incorporation of spinel in the analysis is probable given the high measured Cr concentrations (e.g. sample 41FSp3 from Cape Vogel). However, answers are less obvious in other inclusions and care must be taken in interpreting the Cr data because of these sampling uncertainties.

POST-ENTRAPMENT HOST-PHASE INTERACTION

In order make inferences about primary inclusion compositions, the extent of post-entrapment interaction must be evaluated. Ways in which the inclusion composition might be altered after trapping include, crystallization of the host phase on walls of or as quench crystals in the inclusion, diffusive re-equilibration of the host phase and the melt inclusion at different pressures and temperatures than those prevailing at the time of traping, and possible decompression melting of the host phase upon ascent.

An elegant approach to the first problem was presented by *Watson* [1976] in which he employed mineral control lines to determine the original composition of a suite of inclusions trapped in olivine, plagioclase, and augite contained in a basalt from the South Atlantic. He used a ternary plot of CaO, Al_2O_3, and MgO to graphically represent the compositions of the inclusions as well as hypothetical compositions of the mineral phases. Watson argued that crystallization of the host phase on the walls of the inclusion would drive the residual liquid composition away, along control lines, from the point in the ternary where the ideal mineral plotted, and that this was a likely explanation for the radiating pattern of plotted inclusion compositions. Fundamental to the success of this

technique is the validity of Watson's assumption that the inclusions were all trapped at the same time in the different minerals and that the trapped liquid had the same composition in all phases. In this paper, multiple inclusions in a single crystal and/or multiple mineral phases in a single rock sample were not available and therefore control line analysis could not be utilized to determine host-phase crystallization. In some instances, however, post-entrapment crystallization in the inclusion was obvious, even upon microscopic inspection (see Kamchatka and Cape Vogel sections below). While the inclusions constituting the TOR (MORB) suite are appropriate for control line analysis, the condition that the liquids were identical in composition at the time of trapping is not met, as will be discussed below. Thus, in this case *Watson's* [1976] technique cannot be used to identify the effects of post-entrapment crytallization.

Some of *Watson's* [1976] other assumptions are also open to question. First, it is not clear why one should expect that only the host-phase will crystallize on the walls of a multiply-saturated melt inclusion. It is expected that all phases saturated in the liquid should crystallize from such melts, not just the host-phase. It could be argued, perhaps, that the crystal lattice of the host phase along the walls of the inclusion constitutes nucleation sites for the host phase. However, this should not rule out nucleation of other phases as well since it is not required that seeds of the saturated phase be present in order for those phases to nucleate; they can just as easily nucleate on any impurity or imperfection. However, evaluating this possibility requires examination of inclusion walls by a high resolution technique such as scanning electron microscopy, which was not done in this study. Furthermore, conditions for producing glass do not favor significant host-phase crystallization. In order to form glass in the first place, the cooling rate must be high enough to prevent nucleation of mineral phases in the melt. *Uhlmann* [1972] and *Klein and Uhlmann* [1976] reported on the kinetics of glass formation and estimated, based on experiments and transformation kinetic theory, that cooling rates of from ≥ 1°C/hr for pure SiO_2 and ≥ 1°C/sec for lunar soil breccia 70019 were required to prevent nucleation of

crystals. Further counteracting the crystal growth process to some extent is the possibility of host-phase melting as a result of adiabatic decompression. Also, if any crystallization does occur, it will cause release of latent heat, which could arrest further crystal growth in a small inclusion [*Kirkpatrick*, 1976]. Thus, while the possibility of post-entrapment crystallization is not absent (e.g., in KB-9, and Cape Vogel melt inclusion in spinel, see below, and *Watson* [1976]), especially given the small diffusion distances in melt inclusions, it is uncommon in the present suite of samples, except where noted.

Chemical changes in the inclusion could also occur by decompression melting, as noted above, by chemical diffusion as the melt-crystal system re-equilibrate at new pressure-temperature conditions, or by artificially induced re-equilibration of the system or melting of the host crystal due to heating at 1 atmosphere in the microthermometry experiments. Some or all of these processes may commonly occur and be responsible for some of the chemical characteristics reported below (e.g. TOR-PLN47 in the MORB suite).

RESULTS

Extreme care was taken to avoid beam overlap onto the mineral. An independent assessment of the analyses' accuracy was carried out by plotting the Ti contents of the inclusions as determined by both ion and electron microprobes. Ideally, data on this plot should define a slope of one. The results of this comparison are shown in Figure 3. Three points plot significantly off the 1:1 line; TOR OLN63, KB-9 from Kamchatka, and an enriched inclusion from Snaefellsnes, Iceland. Assuming that the electron probe analyses are good, based on its superior optical imaging capabilities, a point above the line could be caused by the ion beam overlapping onto the host mineral causing a dilution of Ti. Another explanation could be that the inclusions are heterogeneous or contain impurities. Inspection of Kamchatka inclusions in olivine reveals a pronounced spinifex quench texture in the glass (Figure 4), meaning that the inclusion is not a homogeneous glass and that differences in beam placement between electron and ion probe analyses could account for

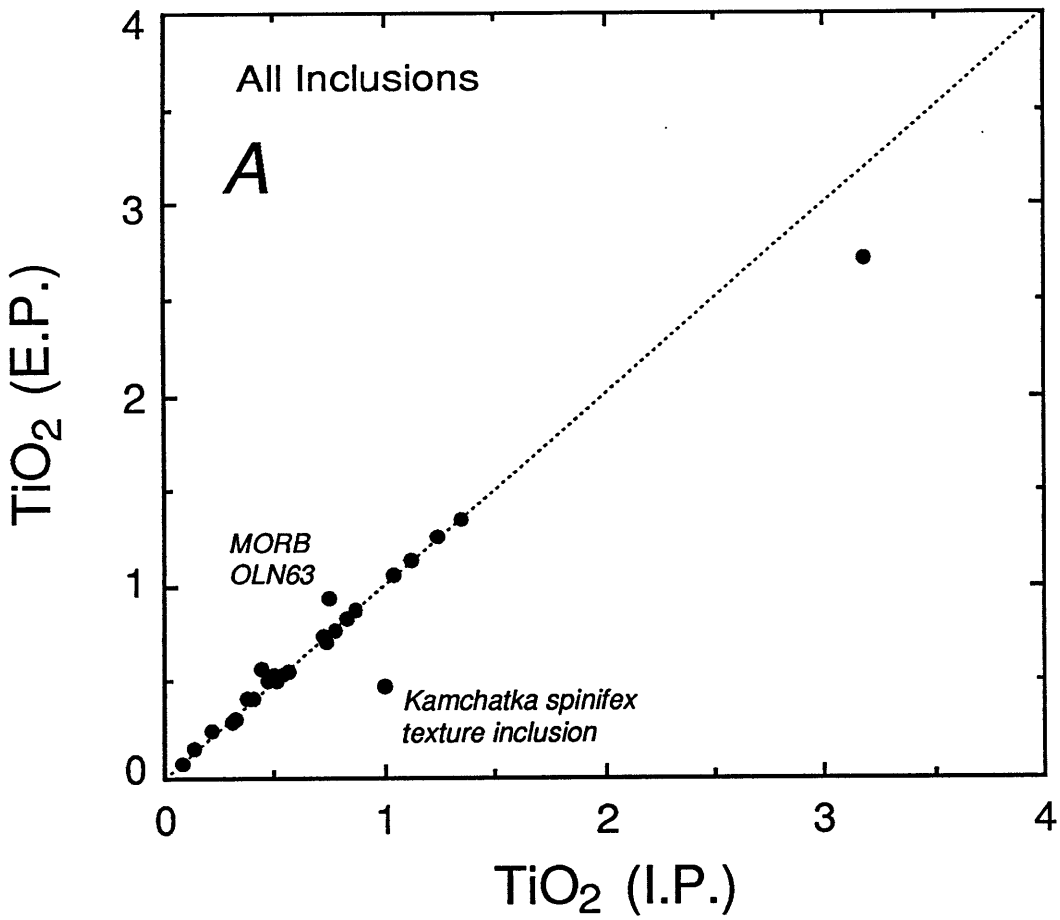

Figure 3. TiO2 analyzed by ion probe versus TiO2 measured by electron probe for (a) all inclusions, (b) TOR (MORB) melt inclusions, and (c) Theistareykir and Reykjanes Peninsula melt inclusions to illustrate the relative accuracy of the measurements. This was used as an internal check for the ion probe analyses.

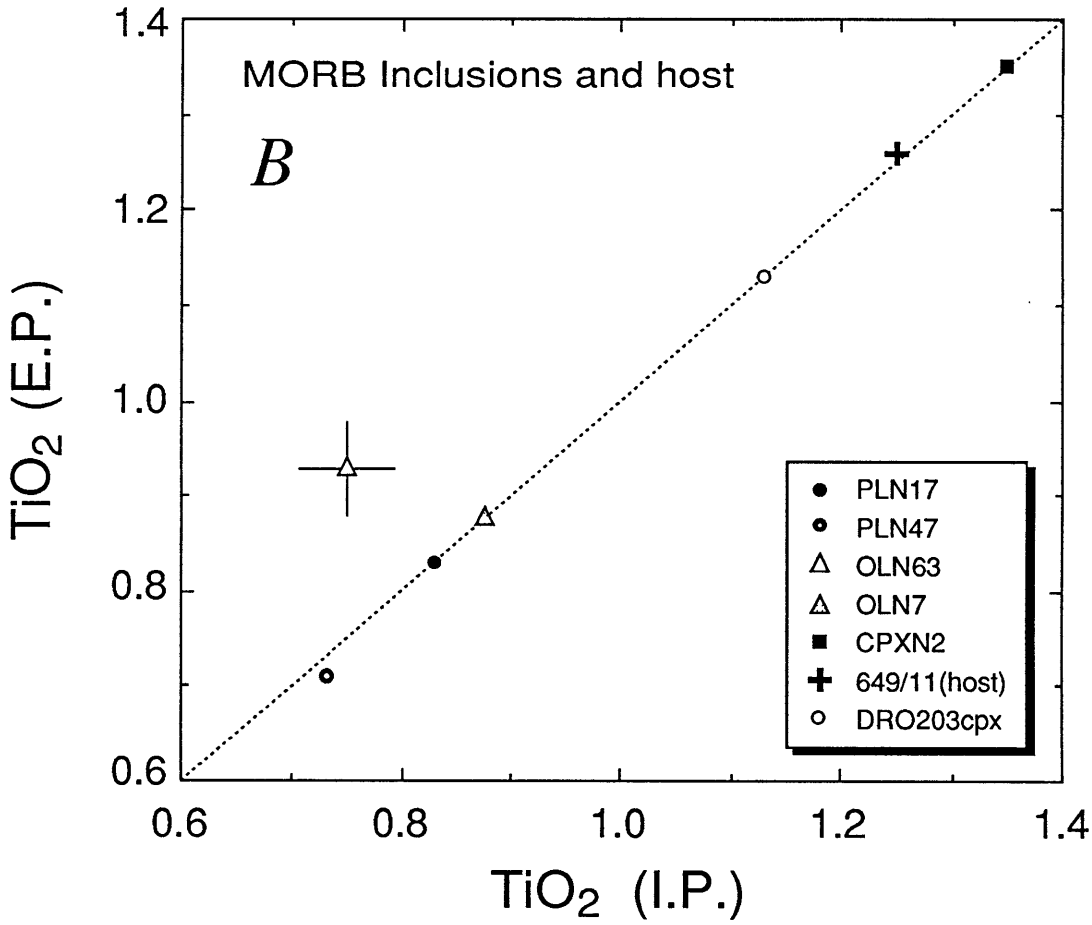
MORB Inclusions and host
B
1.4
1.2
1.0
0.8
0.6
0.6
0.8
1.0
1.2
1.4
TiO2 (E.P.)
TiO2 (I.P.)
PLN17
PLN47
OLN63
OLN7
CPXN2
649/11(host)
DRO203cpx

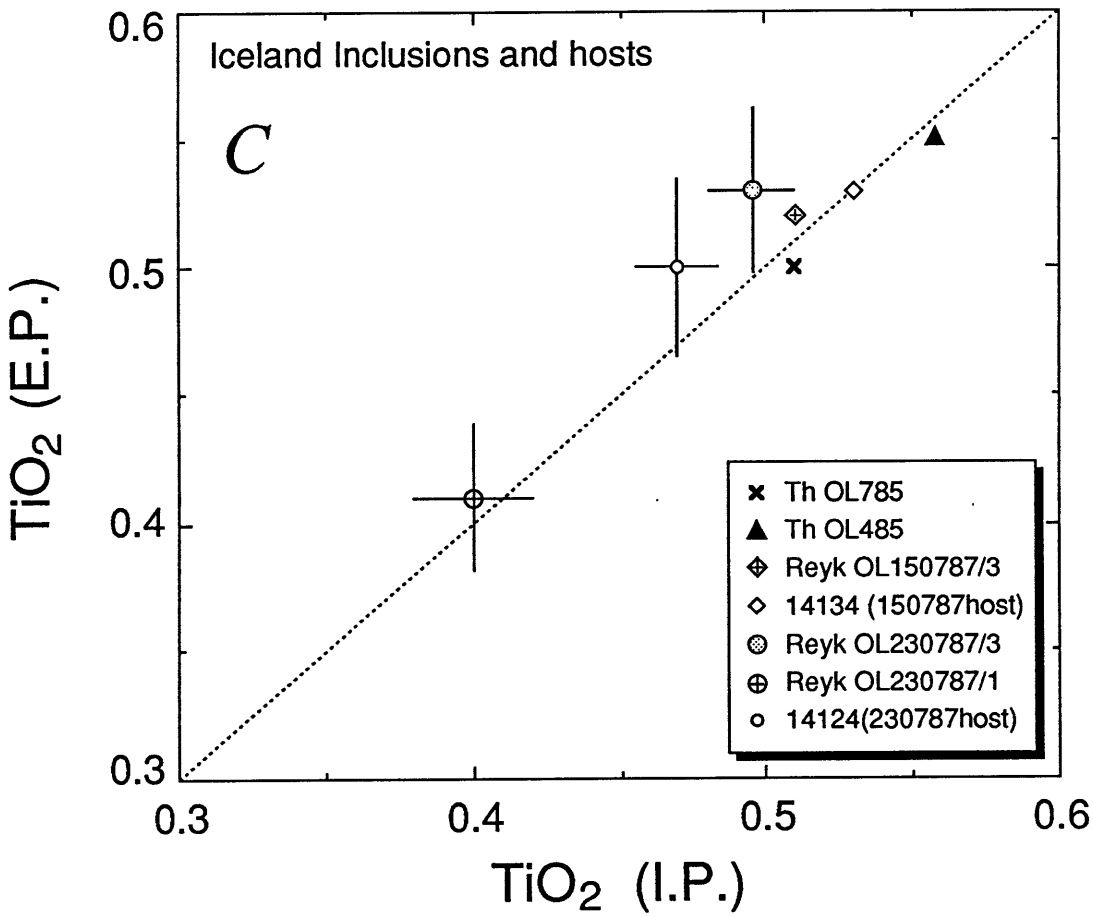
Iceland Inclusions and hosts
C
0.6
0.5
0.4
0.3
0.3
0.4
0.5
0.6
TiO2 (E.P.)
TiO2 (I.P.)
Th OL785
Th OL485
Reyk OL150787/3
14134 (150787host)
Reyk OL230787/3
Reyk OL230787/1
14124(230787host)

Figure 4. Reflected light photomicrograph of spinifex texture in inclusion KB-9 from Kamchatka. The spinifex texture probably results from quench crystallization of olivine (± other phases?) after heating in the homogenization experiment. Thus the analyzed inclusion composition is not a pure liquid composition, but is liquid + crystals. The dark, 10-15μ circular features in the inclusion are sputtered craters from the ion beam. Scale is shown in microns.

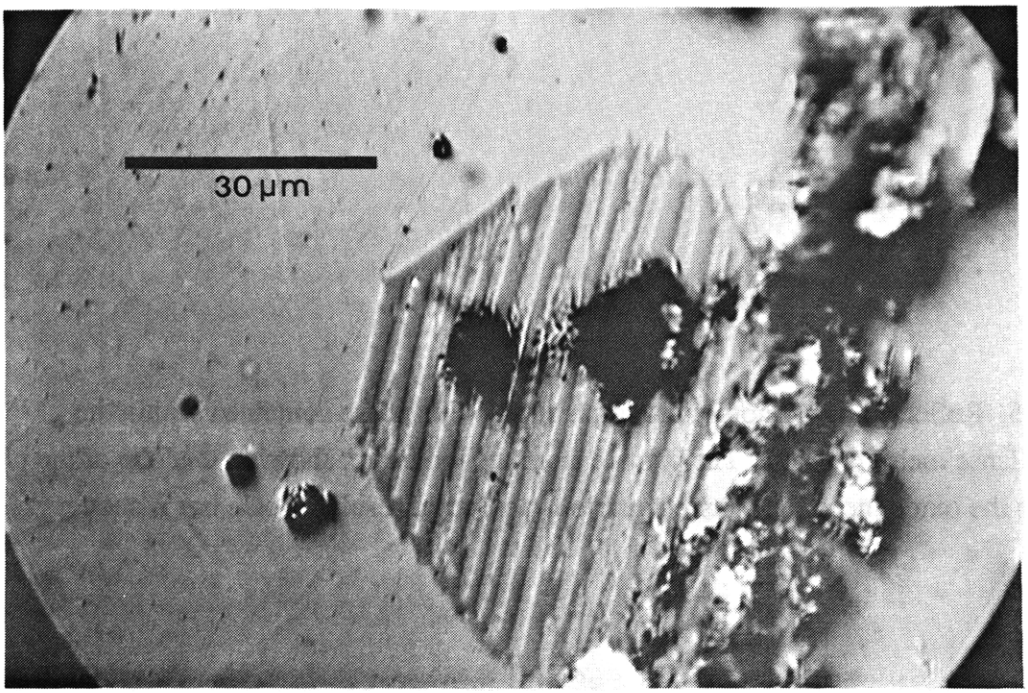
30 µm

Figure 5. Reflected light photomicrograph of an oxide phase contained within the Snaefellsnes melt inclusion. The pits are from the ion beam, showing that one of the pits touches the oxide inclusion causing spurious analytical results. Scale bar is shown.

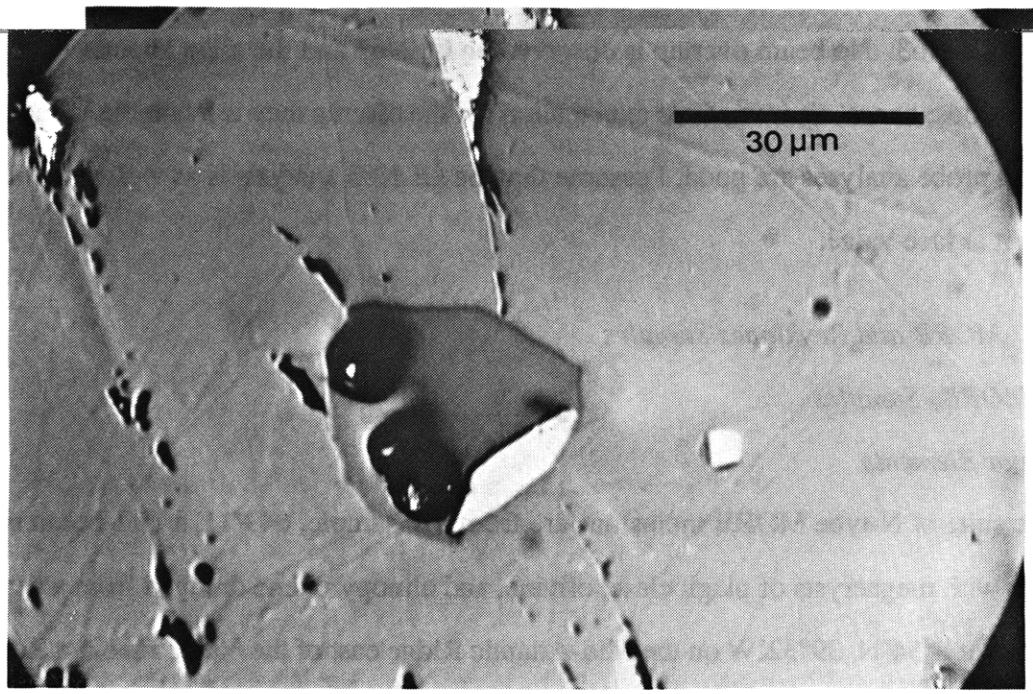
30 µm

compositional disagreement. Similarly, the Snaefellsnes inclusion contains a highly reflective oxide crystal (Figure 5) which, if accidentally touched by the beam, will cause higher measured Ti concentrations if it is titanomagnetite or ilmenite.

Expanded views of the MORB (TOR) data (Figure 3b) and the Reykjanes and Theistareykir, Iceland data (Figure 3c) show that excellent agreement is achieved, except for TOR OLN63. No beam overlap is observed on OLN63 and the glass appears homogeneous; hence, no immediate explanation for the discrepancy is available. Since the other ion probe analyses are good, I assume that the OLN63 analysis is as well and will discuss it at face value.

Part A. MORB and Reykjanes Samples

TOR (MORB) Samples

Major Elements

The suite of N-type MORB inclusions are from one sample, 649/11, a mid-ocean ridge tholeiite with megacrysts of plagioclase, olivine, and clinopyroxene dredged from a depth of 3850m at 8°34'N, 39°32'W on the Mid-Atlantic Ridge east of the Vema Fracture Zone. The inclusions are contained in olivines OLN7 and OLN63, plagioclases PLN17 and PLN47, and clinopyroxene CPXN2, and analyses, in general, agree very well between ion and electron probes (Figure 3b). The samples are prefixed by TOR-2, meaning Type-2 tholeiites of oceanic rifts [*Dmitriev et al.*, 1989]. All of the inclusions are tholeiitic in composition and have Mg# (Mg/[Mg+Fe]) in the range 0.63-0.71. Glass from the pillow rind of the host basalt, 649/11, is very similar in composition to the cpx-hosted inclusion, as will be seen in a variety of different plots. Plagioclase- and olivine-hosted inclusions are more primitive than CPXN2, having higher MgO, Mg#, and lower K_2O, TiO_2, and incompatible trace element concentrations. There is no indication of host-phase crystallization based on mineral control lines in CaO-MgO-Al_2O_3 (Figure 6), but such an indication is not expected for two reasons: 1) Heating of the sample for the

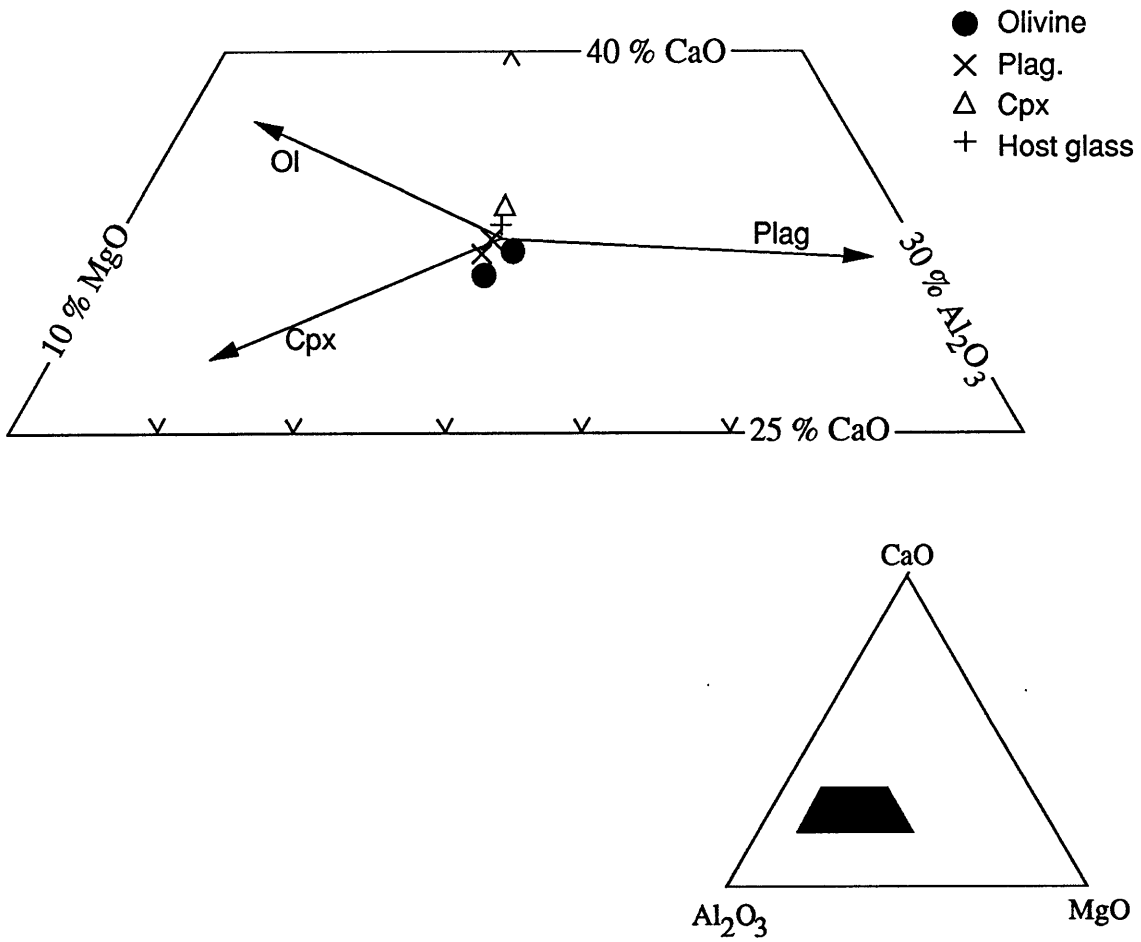

Figure 6. CaO-Al2O3-MgO control line diagram for MORB inclusions used to determine the effects of host-phase post-entrapment crystallization [Watson, 1976]. Crystallization of minerals in this diagram will drive the residual liquid in the direction of the annotated arrows. Crystallization from an identical starting liquid composition trapped as inclusions within all three mineral phases will result in post-interaction inclusion compositions that radiate from a central point. This is not observed on this diagram (see text for discussion).

microthermometry experiment could, in part, reverse the effects of post-entrapment crystallization, 2) As evidence below will show, more than one liquid line of descent is represented by the inclusions.

Equilibrium between host-phases and either inclusions or host glass can be assessed using known relationships between glass Mg#, forsterite contents of olivines, glass Ca/(Ca+Na), and anorthite contents of plagioclases. In order to evaluate whether minerals are in equilibrium with inclusions or with host glass 649/11, two-component K_d's $(Fe/Mg_{mineral}) / (Fe/Mg_{liquid})$ and $[Ca/(Ca+Na)_{plagioclase}] / [Ca/(Ca+Na)_{liquid}]$ were calculated for the samples. Table 3 shows the results of the Fe/Mg calculations for equilibrium between olivine-liquid and clinopyroxene-liquid. Total iron in electron microprobe analyses is reported as FeO, so various ratios of Fe^{2+}:Fe(total) were used in the calculations. It can be seen that equilibrium between mineral and inclusion, based on $K_d = 0.3$ for olivine [*Roeder and Emslie*, 1970; *Takahashi and Kushiro*, 1983] and 0.26 for augite [*Grove and Bryan*, 1983; *Tormey et al.*, 1987], occurs at $Fe^{2+} = \sim 0.85$ Fe(total) for olivine, and at $Fe^{2+} = \sim 0.9$ Fe(total) for cpx. It appears that equilibrium between olivines and host glass 649/11 requires $Fe^{2+} \leq 0.7$ Fe(total), which is far more oxidized than normal MORB [*Christie et al.*, 1986; *Bryndzia et al.*, 1989], whereas equilibrium between cpx and host glass 649/11 is reasonable. That the cpx could be in equilibrium with either the inclusion or the host glass is consistent with late-stage crystallization of cpx from, and entrapment of, the magma close to the time of eruption.

Plagioclase equilibrium can be evaluated in a similar way using an empirical relationship between the anorthite content of plagioclase and Ca/(Ca+Na) of the liquid compiled from experimental data [*Falloon and Green*, 1986]. These parameters are plotted in Figure 7 and it is shown that the inclusions are closer to the empirical equilibrium line with their host-plagioclase than is the host-glass composition. Similar results are obtained using the empirical $K_d = Ca/Na_{plag.} / Ca/Na_{liquid} = 1.2$ at 1 atm. [*Tormey et al.*, 1987].

TABLE 3. Calculated Fe/Mg mineral/liquid K_ds

Sample	FeO = FeOt		FeO = 0.95*FeOt		FeO = 0.90*FeOt	
	K_d (min/incl.)	K_d (min/host)	K_d (min/incl.)	K_d (min/host)	K_d (min/incl.)	K_d (min/host)
Theistareykir OL-150785/2	0.294		0.310		0.327	
Theistareykir OL-170485/2	0.313		0.330		0.348	
Reykjanes Pen. OL-150787/3	0.310	0.283	0.326	0.298	0.344	0.315
Reykjanes Pen. OL-230787/1	0.326	0.277	0.343	0.292	0.363	0.308
Reykjanes Pen. OL-230787/3	0.304	0.230	0.320	0.242	0.338	0.256

	FeO = FeOt		FeO = 0.90*FeOt		FeO = 0.85*FeOt	
	K_d (min/incl.)	K_d (min/host)	K_d (min/incl.)	K_d (min/host)	K_d (min/incl.)	K_d (min/host)
TOR-2 OLN7	0.255	0.184	0.283	0.204	0.300	0.216
TOR-2 OLN63	0.240	0.202	0.267	0.225	0.282	0.238
TOR-2 CPXN2	0.224	0.230	0.249	0.255	0.264	0.270

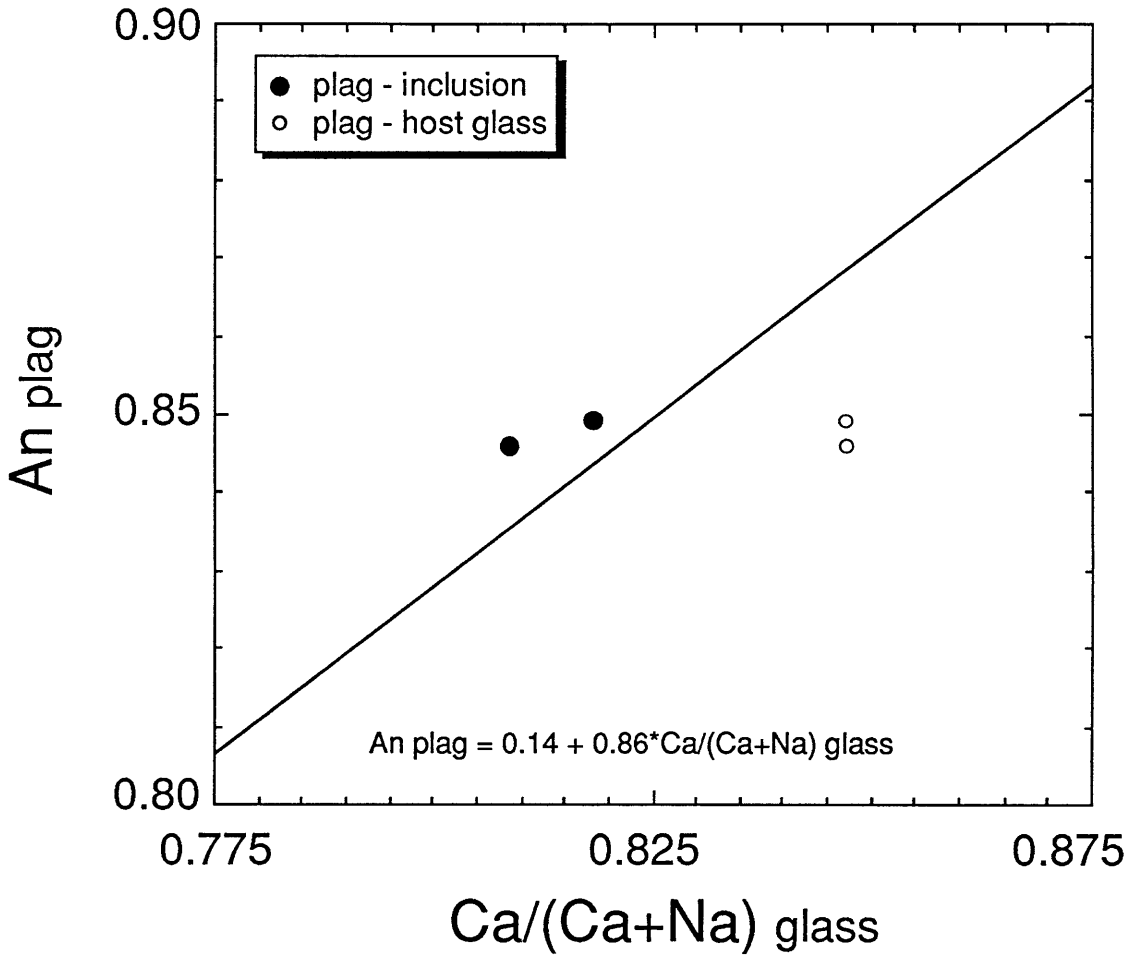

Figure 7. An content of plagioclase PLN17 and PLN47 versus Ca/(Ca+Na) of host glass, 649/11, and inclusions. The diagonal line corresponds to an empirical plagioclase-liquid equilibrium relationship and indicates that plagioclase crystals and their inclusions are close to equilibrium, whereas plagioclase and host glass 649/11 are not. Equation of line is calculated from experimental data reported in Falloon and Green [1986] and Tormey et al. [1987].

Thus, all three mineral phases could have been in equilibrium with their inclusions, but only cpx could have been in equilibrium with the liquid of the host rock at low pressure.

Figure 8 shows the inclusion data projected in the Cpx-Olivine-Silica face of the CMAS tetrahedron using the projection algorithm of *Walker et al.* [1979]. The data were plotted at the redox conditions derived from the above analysis; using more reducing conditions will shift the points slightly to the left in these projections. The inclusion compositions are linearly arrayed from the silica deficient side of the cpx-olivine-plagioclase join (PLN47) subparallel to the cpx-olivine-plagioclase-liquid pseudocotectic surface at <8 kb defined by experiments [*Stolper*, 1980; *Takahashi and Kushiro*, 1983; *Falloon and Green*, 1987, 1988a and b]; only CPXN2 appears to be saturated in clinopyroxene at 1 atmosphere in this projection. Also shown on this diagram are homogenization temperatures and Mg# of the samples. If the inclusions were related by fractional crystallization, the temperature and Mg# should decrease toward the lower right, which is clearly not the case. Relationship by melting of a common source should result in data arrayed perpendicular to the observed trend.

Trace Elements

A striking feature of the trace element compositions is that Zr = 16 ppm in PLN47. Beam overlap onto plagioclase to account for the low Zr is ruled out because Ti is identical in the ion and electron probe analyses and because visual inspection revealed that the beam was within the inclusion. Assuming the inclusion is nearly spherical, beam penetration through the glass to the host phase is also unlikely. Moreover, three analyses of the same inclusion reproduced the same concentrations. Ti/Zr in this sample is 267, more than a factor of two larger than in all other inclusions, including PLN17, and higher than values measured in a suite of inclusions from the Galapagos Ridge [*Yonover*, 1989]. Nb is also depleted in PLN47 at 0.4-0.5 ppm, so that Zr/Nb = 33-37, similar to the other inclusions and 649/11, and typical for N-MORB in general. Sr concentration is not unusual in any of the inclusions, but is slightly higher in the PLN47 (130-137) than in the cpx-hosted (124),

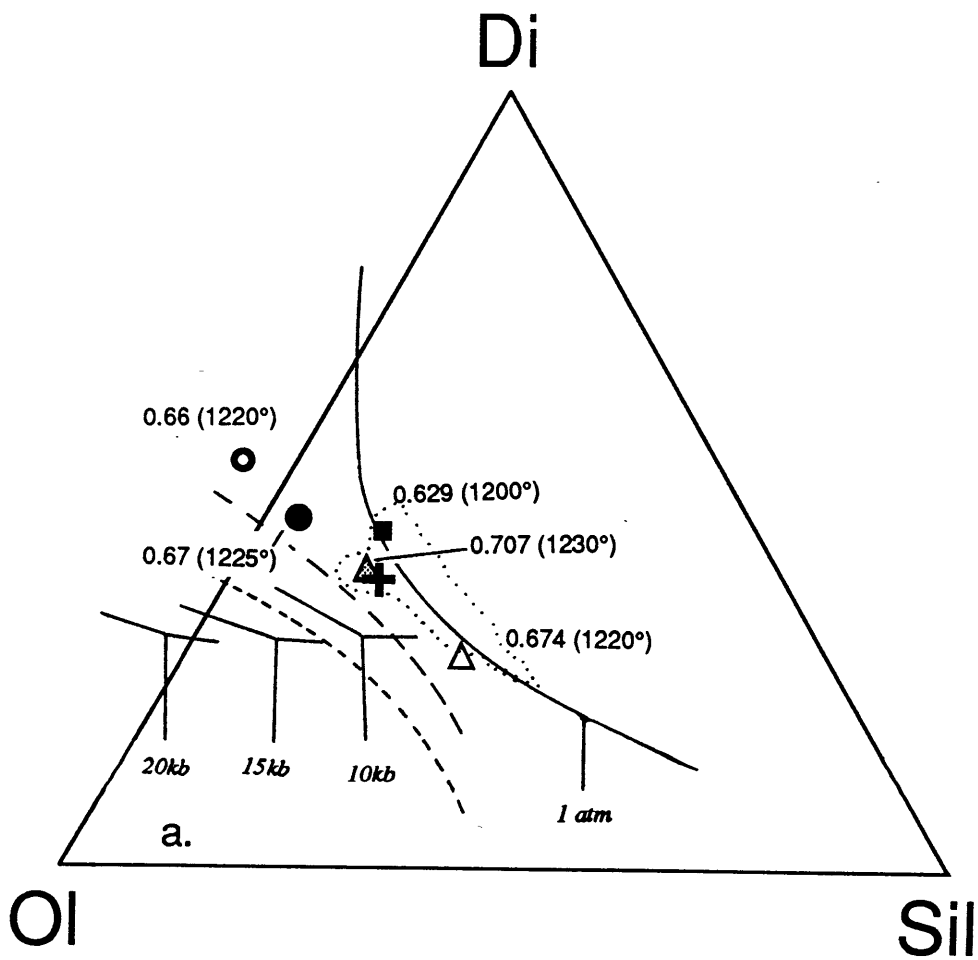

Figure 8. Di-Ol-Sil projection in the CMAS system for MORB inclusions using the projection algorithm of *Walker et al.* [1979]. Labeled pseudocotectics at various pressures are after *Stolper* [1980] and dashed curves are constructed from 8 kbar (long dashes) and 10 kbar (short dashes) melting experiments of *Takahashi and Kushiro* [1983] and *Falloon and Green* [1987, 1988a and b]. Dotted field encloses N-MORB glass compositions in this projection. Annotations adjacent to each data point are Mg# and homogenization temperature of the inclusions.

and olivine-hosted (81-100) inclusions, and in 649/11 (123). However, Cr is also higher in the plagioclase-hosted inclusions than in the olivine-hosted inclusions, suggesting that incorporation of plagioclase in the analysis was not responsible for the high Sr values in PLN47. Conversely, if host-plagioclase dissolved slightly during the microthermometry experiment or decompression of the host phase causing increased Sr in the inclusion, we would also see an increase in Al_2O_3 in the melt inclusion relative to the olivine inclusions. Al_2O_3 is lower in PLN47, arguing for minor plagioclase crystallization from the inclusion during cooling, if anything. At any rate, ratios such as Ti/Zr will remain essentially unchanged by either of these mechanisms and could be used to infer source characteristics or melting processes of the inclusions.

All inclusions have light REE depleted patterns (Figure 9). The lowest absolute abundances are found in OLN63 and the highest are found in CPXN2 and 649/11, which are essentially identical. Inclusions in PLN17, PLN47, and OLN7 have negative Zr anomalies (Figure 10). This feature is not observed in the host glass (649/11), CPXN2, or OLN63, although both CPXN2 and 649/11 have negative Ti anomalies.

Reykjanes Peninsula Inclusions

Major elements

Figure 3c shows the correlation between TiO_2 measured by ion and electron microprobes. The correlation is not as good as that for MORB samples, but is still within analytical uncertainty.

The Reykjanes inclusions are all characterized by high CaO (13.8-15.8 wt%) and MgO (9.15-11.54 wt%), moderate Al_2O_3 (15.5-16.6 wt%), and low TiO_2 (0.4-0.53 wt%); they are described as picritic tholeiites [A. Sobolev, personal communication, 1989]. Host rock glasses have lower Mg#, CaO, CaO/Al_2O_3, and CaO/Na_2O than do their inclusions. Mg# are quite high in all cases, ranging from ~0.7 to 0.76. These liquids could all be in equilibrium with presumed mantle olivines, the forsterite compositions of which coincide

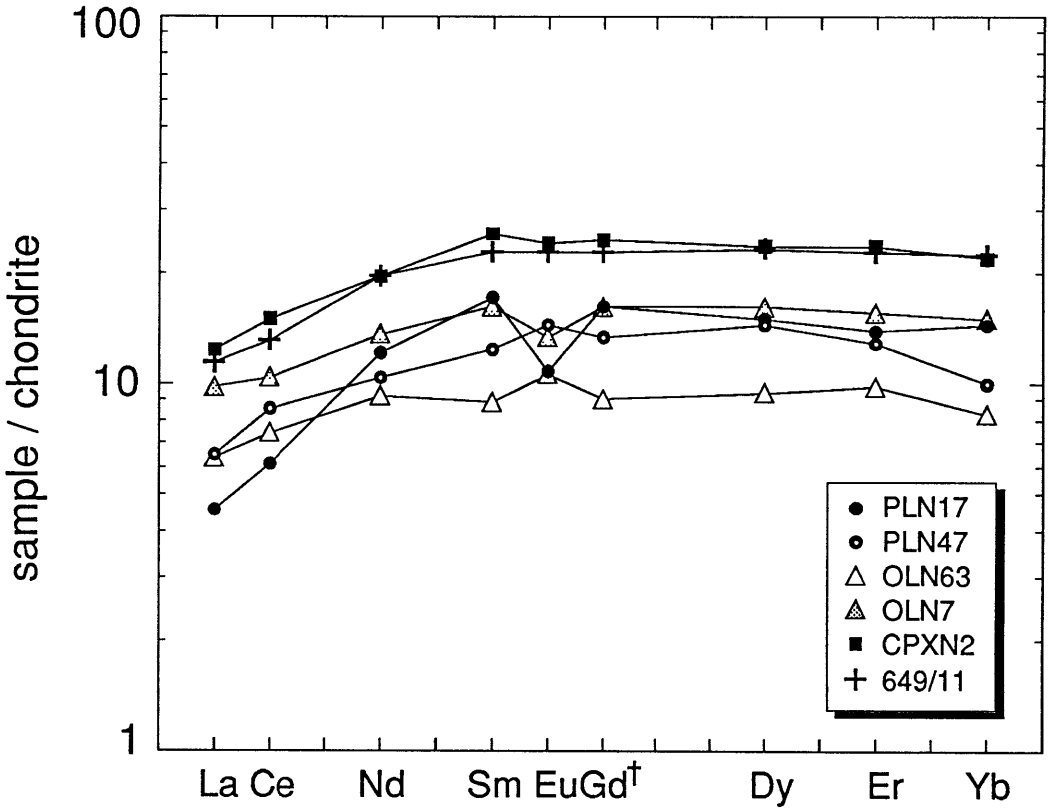

Figure 9. REE diagram for MORB inclusions. Note elevated, nearly identical patterns for CPXN2 and the host glass, 649/11. Apparent fractionation relationship of OLN7 from OLN63 is inconsistent with the projected positions of these samples in Figure 8. In this and subsequent diagrams, Gd† signifies an interpolated value.

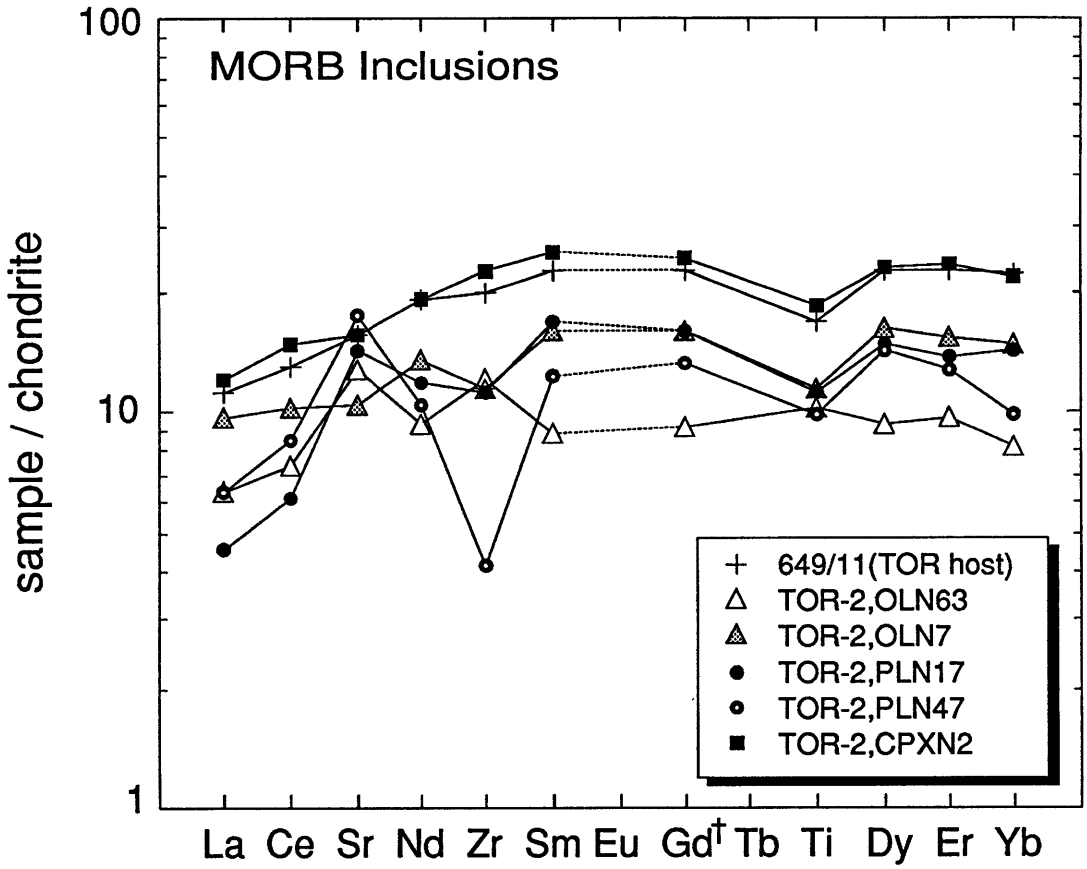

Figure 10. Spider diagram for MORB inclusions. Inclusion CPXN2 and the host glass are again essentially identical with no HFSE anomalies. However, PLN17, PLN47, and OLN7 have pronounced negative HFSE anomalies.

with those of the host olivines. Thus, it is possible that the host olivines could be in equilibrium with their inclusions at very low oxygen fugacities similar to those reported in recent studies on MORB and abyssal peridotites [*Christie et al.*, 1986; *Bryndzia et al.*, 1989], or with the host glasses at slightly higher, but still reasonable, fugacities (Table 3).

The Reykjanes inclusions and two inclusions from Theistareykir are plotted in the projection from plagioclase onto the cpx-olivine-silica plane of the cpx-olivine-plagioclase-silica tetrahedron (Figure 11). The host glass of Reykjanes 150787/3 plots down and to the left of the inclusion which could reflect absorption of olivine into the inclusion. However, the 100% increase in Cr from inclusion to host glass could not be caused by olivine dissolution. It is possible that the inclusion in olivine 150787/3 represents a mixture of liquid end-members plotting in the direction of the arrows in Figure 11 but not represented in the sample suite. Its position in the concave portion of the low pressure pseudocotectic is also consistent with this interpretation.

The host glass of inclusions in Reykjanes olivines 230787/1 and 230787/3 plots down and slightly to the right of the inclusions along the pseudocotectic, and has lower Mg#, CaO, and CaO/Al_2O_3 than do the inclusions. Moreover, TiO_2 and MgO are both higher and CaO is lower in inclusion 230787/3 than in 230787/1. Although MgO, FeO, CaO, and trace element concentrations discussed below are consistent with a genetic relationship between inclusion 230787/3 and host 14124, these elements do not support a simple genetic relationship between inclusion 230787/1 and either host 14124 or inclusion 230787/3.

Trace Elements

As noted above, the Cr concentration in host glass 14134 of inclusion 150787/3 is 502 ppm, compared to 221 ppm in the inclusion and the Sr concentration in 14134 is 55 ppm, compared to 68 ppm in the inclusion. Ti/Zr = 175 in host 14134 and 147 in inclusion 150787/3, while Zr/Nb = 57 in 14134 and 44 in the inclusion.

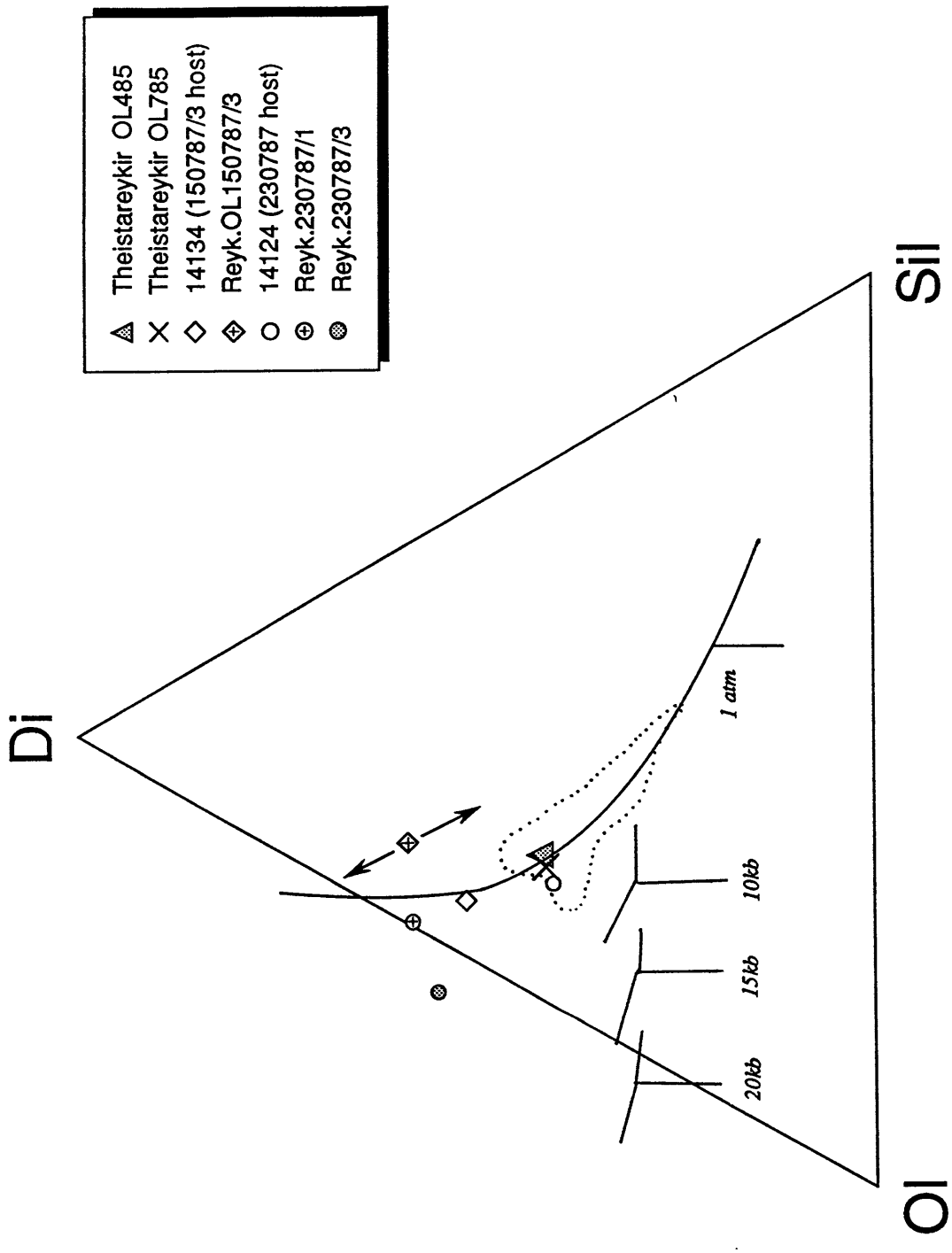

Figure 11. Di-Ol-Sil projection in the CMAS system for Reykjanes and Theistareykir inclusions using the projection algorithm of *Walker et al.* [1979]. Arrows near sample 150787/3 are hypothetical mixing vectors. One atmosphere pseudocotectic is from *Walker et al.* [1979] and high pressure pseudocotectic boundaries are from *Stolper* [1980]. Dotted field encloses N-MORB glass compositions.

Rare earth element patterns for inclusion 150787/3 and host 14134 are quite distinct (Figure 12). The patterns cross between Nd and Sm, the host being more fractionated than the inclusion. The pronounced difference in REE pattern shape between the two argues strongly against a simple derivative relationship either by melting or by fractional crystallization. This is confirmed when taken together with the major elements; it is not possible to relate the inclusions to the host glass by fractionation of olivine, cpx, plagioclase, or chrome spinel. Crossing rare earth patterns have been considered diagnostic of liquids produced by dynamic melting [*Langmuir et al.*, 1977]. Mixing between a depleted and an evolved liquid might also explain the observed major (Figure 11) and rare earth elements (Figure 12).

Cr decreases slightly, and Ti, Sr, Zr, Nb increase slightly from inclusion 230787/3 to host 14124. Likewise, REE patterns are nearly identical in these two samples, the host being slightly less fractionated than the inclusion. Although Ti/Zr differ by ~35%, 20-25% of this difference could be accounted for by compounded analytical error due to low Zr counts. Similarly, Zr/Nb ratios of these two samples are effectively the same, within analytical error. These relationships strongly support a genetic relationship between inclusion 230787/3 and host 14124. Further, the relationships are consistent with the inclusion representing a slightly more depleted melt increment than the host.

Zr and Nb in inclusions 230787/1 and 230787/3 vary antithetically from Sr. Ti/Zr = 365 for inclusion 230787/1, and 246 for inclusion 230787/3. This ratio is rather insensitive to fractional crystallization of olivine, plagioclase and moderate amounts of clinopyroxene, but increases in residues and instantaneous fractional melt increments. Thus, while the observation of lower Al_2O_3 and Sr, and higher MgO, Ti, Zr, and Nb in inclusion 230787/3 relative to inclusion 230787/1 is consistent with fractional crystallization of plagioclase, the observed 50% increase in Ti/Zr and ~100% increase in Zr/Nb could not be produced by this mechanism, even taking into account analytical error. Fractionation of olivine and plagioclase from basaltic melts raises the absolute

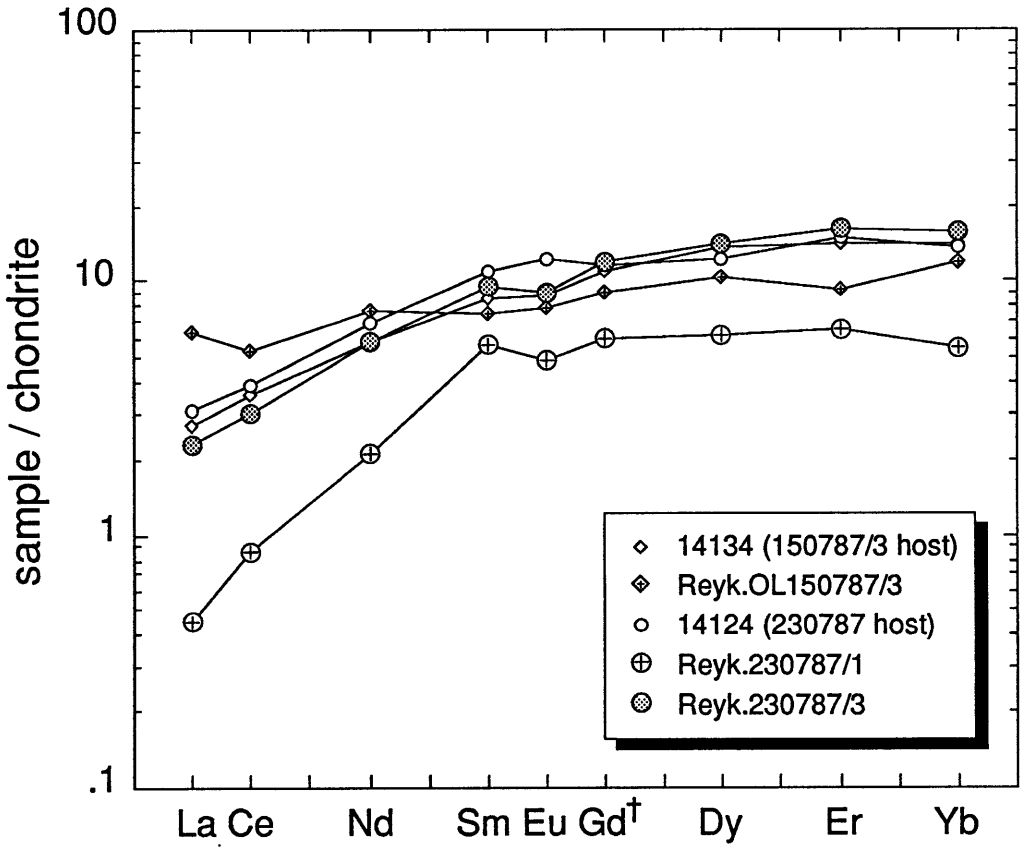

Figure 12. REE diagram for Reykjanes inclusions and host glasses. Note crossing patterns of inclusion 150787/3 and its host glass, 14134. Also, inclusion 230787/3 is essentially identical to its host glass 14124, while inclusion 230787/1 in another olivine grain in the same sample is substantially more depleted.

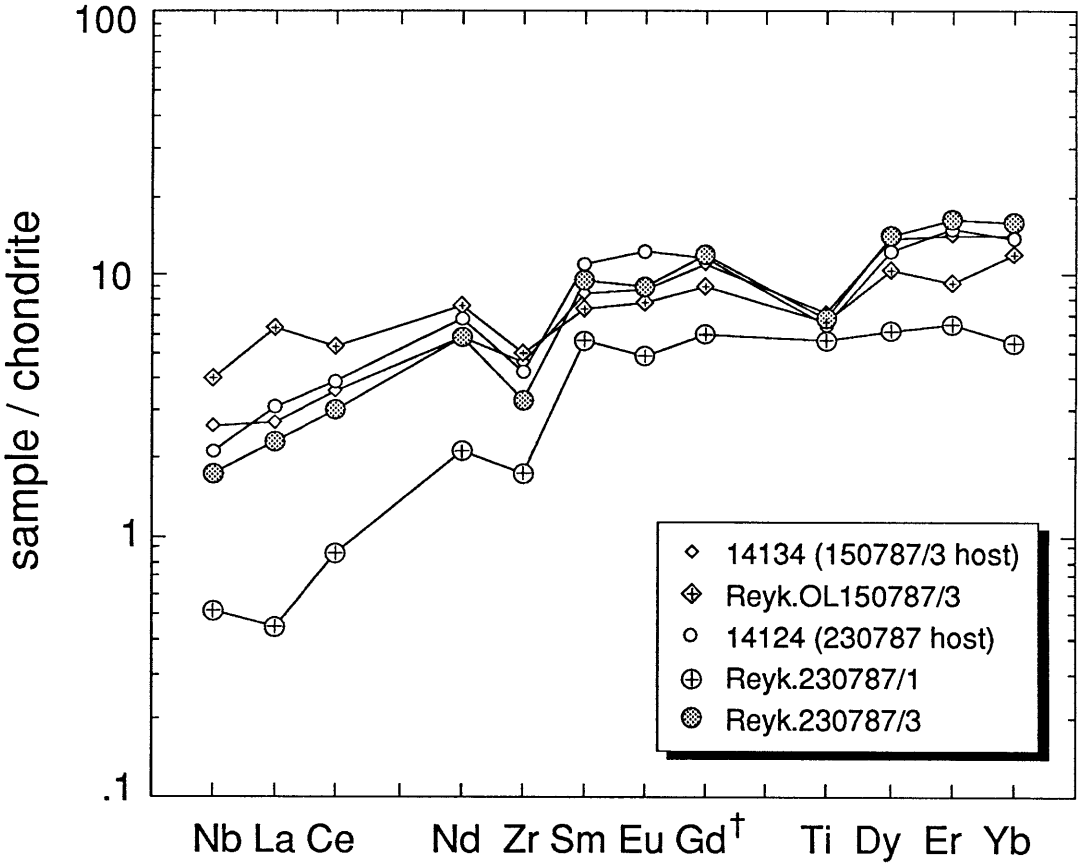

Figure 13. Spider diagram for Reykjanes inclusions and host glasses. Pronounced negative Zr and Ti anomalies are seen in all inclusions and host glasses.

concentrations of REE, but these phases do not significantly fractionate light from heavy REE. Extensive cpx fractionation can affect the light REE to heavy REE ratio, but >75% cpx fractionation is required to account for the difference between 230787/1 ($[La/Yb]_n$ = 0.075) and 230787/3 ($[La/Yb]_n \sim 0.15$) if they are from cogenetic liquids (Figure 12). Increasing degrees of melting of a common source would produce higher Ti/Zr in later melt fractions, but should also produce higher Cr and lower Al_2O_3. This is not observed in the inclusions. Hence, these observations are inconsistent with the two inclusions being related by fractional crystallization of any of the major phases, or by melting. An additional formation model is discussed below along with the MORB samples.

Finally, all of the inclusions and host glasses in this suite exhibit pronounced negative HFSE anomalies (Figure 13).

Part B. Globally Widespread Samples

As stated above, I present these data to illustrate the diversity of the measured melt inclusion compositions, their relationship with associated lava types from the literature, where available, and the capabilities of the analytical technique. Discussion is incorporated into the following Part B sections.

Kamchatka

Kamchatka inclusions come from late Cretaceous ultramafic lavas of Eastern Kamchatka in two different areas. Sample DAN-51 is from the Tumrok Ridge and samples KB-9 and KB-38 are from the Valaginsky Ridge. In terms of major element classification, all of the inclusions are in the shoshonitic series of arc volcanic rocks. Their K_2O/Na_2O ratios range from 0.9 - 2.1, with $K_2O > 1.86$ in all cases and SiO_2 in the range of 44 - 49 wt%. Large variations exist, however, in MgO, CaO, Al_2O_3, P_2O_5, and TiO_2. The two DAN inclusions in olivine have MgO contents of 21 - 23 wt% and Mg# in the range 0.79 - 0.83, whereas the KB group has MgO from 4.7 - 23 wt%, and Mg# 0.48 to 0.86. TiO_2 and Al_2O_3 in the DAN group are low, and CaO is very low for liquids with such high

concentrations of MgO. TiO_2, Al_2O_3, CaO, and FeO/MgO in the KB group are variable and low oxide totals in all samples may be a result of moderate volatile contents.

Invariably, the inclusions in olivines have high MgO, whereas the two inclusions in clinopyroxene (KB38) have low MgO. This suggests olivine influence on the inclusion compositions either by beam overlap, decompression or experimental melting, or olivine crystallization in the inclusions. Beam overlap is ruled out based on microscopic examination of the inclusions after analysis. Decompression or experimental melting are possible, but a similar process would also be expected in clinopyroxene inclusions, raising the CaO concentrations, which is not observed. However, abundant quench crystals are observed in the KB and the DAN inclusions (Figure 4) and, if olivine, could be responsible for the high MgO contents measured.

Trace elements in the two inclusions in DAN-51 are similar to each other. Cr contents are quite high, 649 and 1420 ppm, and reflect the refractory nature of the major elements. The large difference in Cr in these two inclusions from the same rock sample may result from the quench crystals observed in both inclusions. Variable incorporation of these quench crystals in the analysis will cause large variations in compatible element concentrations. Perhaps significantly, the large variations are limited to Cr, Al, and Fe, implying that the interfering quench phase is one which concentrates these elements. However, moderate to low Ca in the inclusions argues against clinopyroxene as the dominant interfering quench phase, while high Mg and Cr could indicate that either olivine or spinel are responsible for the specious results. The predominance of either phase cannot, however, be discerned from available photomicrographs. Sr is also high (330-350 ppm) in the inclusions, and Zr and Nb are quite low, 12 and 0.2 ppm, respectively. This results in Ti/Zr = 151-158 and Zr/Nb = 56-72, both significantly higher than chondritic values (Ti/Zr = 111 and Zr/Nb = 16) indicating significant depletion of the source. REE patterns are slightly light REE enriched, with pronounced negative HFSE anomalies and positive Sr anomalies on a spider diagram (Figure 14). These compositions are similar to

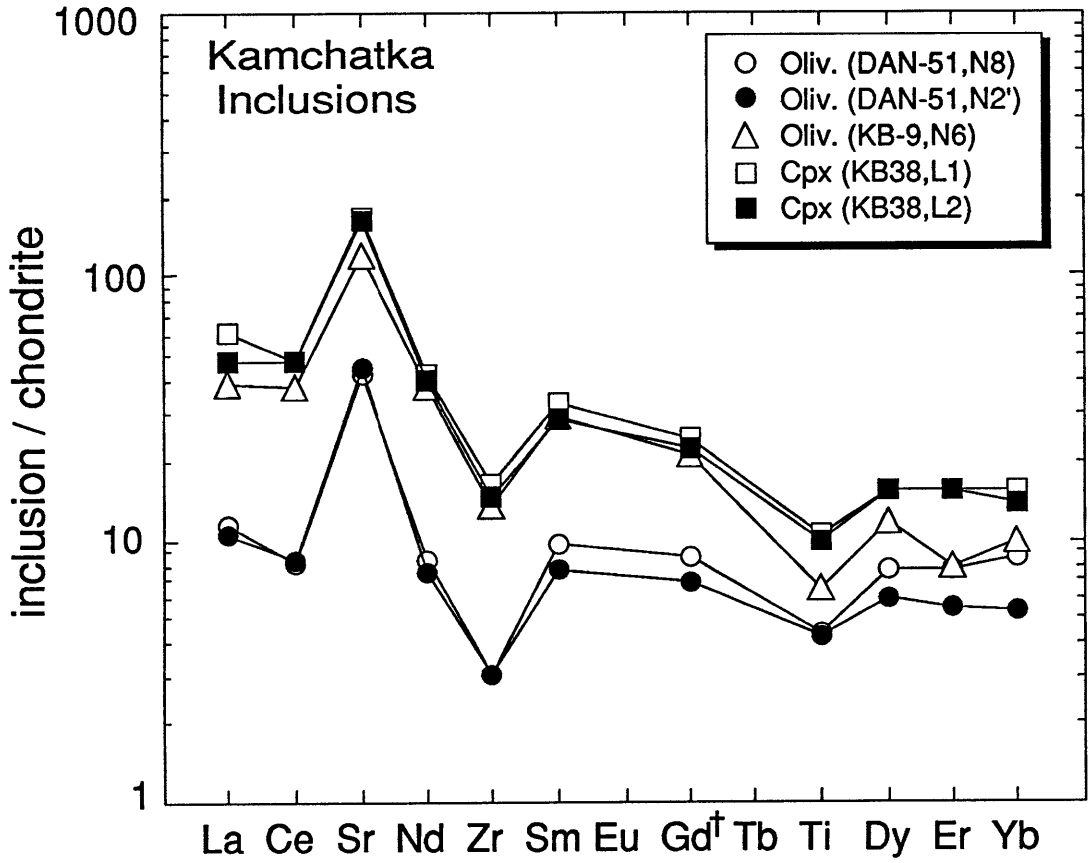

Figure 14. Spider diagram of Kamchatka inclusions.

other arc volcanics in terms of their low HFSE and high Sr. Low CaO in the liquids would appear to indicate the imminent exhaustion of clinopyroxene in the source. This is consistent with conventional scenarios for arc basalt volcanism wherein highly depleted source mantle is infiltrated by a component enriched in Rb, Sr, and Ba or with the hypothesis of *Kelemen et al.* [1990]. T_h of the inclusions are high, ranging from 1470°-1515°C, consistent with their refractory compositions or with the loss of H_2O during decompression and/or measurement.

Trace elements in the KB group reflect the wide variation in the major elements. Cr in olivine-hosted inclusions is moderate (363-451 ppm), but is very low in the cpx-hosted inclusions (41-53 ppm). Sr and K are high in all KB inclusions (Sr = 768-1298 ppm; K_2O = 1.97-2.93 wt%) and Sr increases by ~1.7x from the lowest to the highest concentration samples. HFSE are rather low (Ti = 0.47-0.77 wt%; Zr = 42-65 ppm; Nb = 0.4-2.0 ppm) and plot as large negative anomalies on a spider diagram. REE are elevated relative to the DAN inclusions and are more LREE enriched. In general, incompatible elements are more enriched in the KB inclusions than in the DAN inclusions, consistent with whole rock compositions [Sobolev and Kamenetsky, in preparation; A.V. Sobolev, personal communication, 1990].

The BaO correction to calculate Eu resulted in negative Eu concentrations in one of the analyzed inclusions and a large negative Eu anomaly in the two cpx-hosted inclusions. This is probably a result both of very high Ba concentrations and the existence of significant BaOH, in addition to BaO, molecular ions. Concentrations of other REE are very precise and resemble other arc volcanics.

Similar to DAN inclusions in olivine, inclusions in the KB olivine group are also characterized by pronounced quench crystallization (see Figure 4). Although the quench phase is not known, high MgO in all of the glass inclusions in olivines suggests that the quench crystals may be largely olivine. This is consistent with the observation that calculated K_d's(=$[Fe/Mg]_{ol}/[Fe/Mg]_{glass}$) in these samples are 0.5 - 0.6, compared to

equilibrium values of ~0.3 [*Roeder and Emslie*, 1970; *Takahashi and Kushiro*, 1983]. Incorporation of olivine quench crystals in analyses of the glass inclusions will result in spuriously high MgO concentrations and high apparent K_d values. In addition, Ti in the KB-9 inclusion determined by the ion probe is 2x higher than the value determined by electron probe. Furthermore, Nb in this inclusion is unrealistically high, which leads me to believe that the analyzed composition of this inclusion is far from that of the original liquid. Although the quench phase assemblage cannot be determined by optical inspection, it appears that it is complex and may consist of oxide phase(s) as well as olivine. Microscopic observation of the inclusions in clinopyroxene (KB-38, inclusions L1 and L2) does not reveal quench crystals, consistent with the low MgO and Mg# of the inclusions (Table 1). Although Mg# of the host clinopyroxene is not available, it is felt that the analyzed compositions of the two clinopyroxene-hosted inclusions are liquid compositions, while those of the Kamchatka olivine-hosted inclusions are not. However, the REE patterns of olivine-hosted inclusions are remarkably uniform and are correlated with those of the clinopyroxene-hosted inclusions. A ready explanation for this is not available. However, since the glass is highly enriched in REE relative to the olivine, incorporation of olivine in an analysis will not greatly affect the shape of the glass REE pattern, although absolute concentrations will be diluted.

In summary, it appears that compositions of the Kamchatka olivine-hosted inclusions are significantly affected by quench crystals. Thus, petrogenetic inferences based on absolute elemental concentrations cannot be made, but comparisons between samples based on elemental ratios and rare earth element patterns do suggest differences in inclusion compositions between the two rock samples. Furthermore, similar REE and trace element patterns in olivine- and clinopyroxene-hosted inclusions from sample KB suggests a close compositional relationship between melts trapped by both minerals, in spite of gross major element differences.

Cape Vogel

The inclusions from Cape Vogel are contained in spinel and olivine phenocrysts from a single rock sample, 41F, which also contained clinoenstatite phenocrysts [the sample is described in *Walker and Cameron*, 1983]. The sample is porphyritic, with olivine phenocrysts up to 2 cm long rimmed by groundmass clinoenstatite, clinoenstatite phenocrysts up to 4 cm long, and spinel euhedra up to 2 mm in diameter. The rock is heavily serpentinized, but preserved olivines and clinoenstatites have Mg# = 0.94, and spinels have Cr/(Cr+Al) = 0.94 [*Walker and Cameron*, 1983].

The spinel-hosted inclusion has mottled reflectivity (Figure 15) and very high Cr (13,714 ppm). Thus, I interpret the mottled appearance to be caused by spinel crystals in the inclusion, which have undoubtedly altered the original liquid composition. However, other elemental concentrations are comparable to the olivine-hosted Cape Vogel inclusion. The olivine-hosted inclusion did not have the same textural ambiguity as the spinel-hosted inclusion, and also had fairly high Cr (2549 ppm), very low Ti, Sr, and REE, but rather high Zr and Nb given the other depletions. The inclusion also has extremely low Na_2O and K_2O, CaO, and Al_2O_3 accompanied by high SiO_2 and MgO. Mg# of the inclusions are 0.84-0.86, and Cr in the olivine inclusion is 2549 ppm (0.37 wt% Cr_2O_3), both significantly higher than values reported in the lavas (Mg# $\leq$ 0.82 and $Cr_2O_3 \leq 0.32$ wt%, *Jenner* [1981]; *Walker and Cameron* [1983]). The high MgO and low CaO in the olivine-hosted inclusion may be partly caused by host-phase melting. However, the observed inclusion concentrations are similar to parental magma compositions calculated by *Walker and Cameron* [1983], and are general features of all boninitic lavas [*Meijer*, 1980; *Hickey and Frey*, 1982], although the inclusion compositions are more refractory than the associated lava compositions.

Lavas from Cape Vogel fall into two groups: those with concave up REE patterns, $[La/Yb]_n < 2$, and Zr/Nb $\approx$ 35, and those with light REE enriched patterns, $[La/Yb]_n$ = 3-7, and Zr/Nb $\leq$ 19 [*Jenner*, 1981; *Hickey and Frey*, 1982]. All are characterized by Ti/Zr <

50. The inclusions fall into the second group, the so-called E-group of *Jenner* [1981]. They have geochemical traits clearly related to the E-type lavas, in particular low CaO/Al_2O_3 (0.51-0.53), low Ti/Zr (25-27), chondritic Zr/Nb (16-20), low absolute abundances of CaO, Al_2O_3, TiO_2, alkalis, high MgO and Cr, and high relative Zr and Sr. REE patterns are essentially identical to those reported by *Jenner* [1981], *Hickey and Frey* [1982], and *Cameron et al.* [1983], except that absolute abundances in the inclusions are lower by as much as a factor of 2 (Figure 16). The patterns are not U-shaped, but not all lavas from Cape Vogel are U-shaped either [*Jenner*, 1981; *Hickey and Frey*, 1982]. The essential difference between the inclusions and the lavas is that the inclusions are more refractory and depleted than are the lavas.

Tonga

Three inclusions from Tonga were analyzed; two from olivine N65, and one from olivine N43, both from one rock sample, 26/2, a boninite dredged from the inner wall of the forearc region in the northern Tonga trench at 14°52.2'S, 173°46.7'W (described by *Sharaskin et al.* [1983]). The inclusions are also boninitic in composition, but are significantly different in composition from their host rock (Table 1). It is possible that the bulk analysis of rock sample 26/2 has incorporated cumulus olivine. The inclusion compositions are similar to whole rock compositions of other samples from the same dredge (sample 26/1, Table 1). In general, the trace element concentrations in sample 26/1 are similar to those in the inclusions, but the whole rock is lower in light-middle REE (Figure 17). Pronounced negative Zr and Ti anomalies are observed in spider plots of the inclusions and in the whole rock, but Nb is smooth to only slightly negative (Figure 17). Zr/Nb = 4-5 in the inclusions, which is low for boninites, although a wide variation of this ratio in boninites has been documented [*Cameron et al.*, 1983]. The similarity in pattern shapes for the whole rock and the inclusions implies that they are genetically closely related. However, lower light REE abundances in the whole rock could be a result of 1) crystal dilution of the whole rock analysis, 2) evolution of a liquid represented by the

Figure 15. Reflected light photomicrograph of the Cape Vogel spinel inclusion to show the mottled, heterogeneous appearance of the inclusion. The bright spots inside the inclusion are sputtering craters from the ion beam illustrating the relative size of the heterogeneities and the difficulty avoiding them. Scale bar is shown.

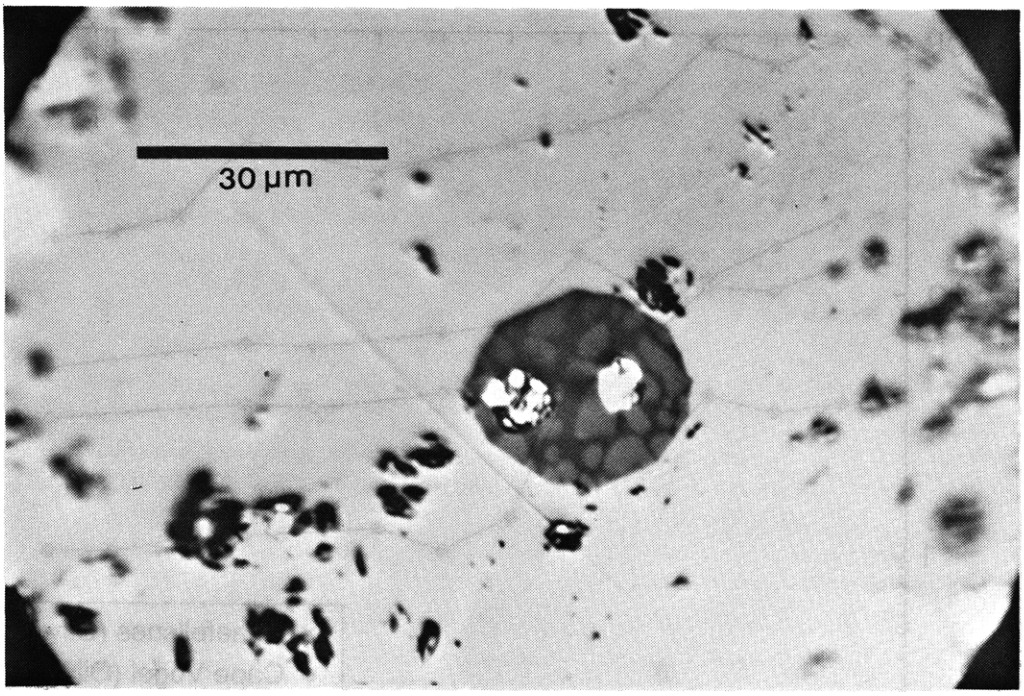
30 µm

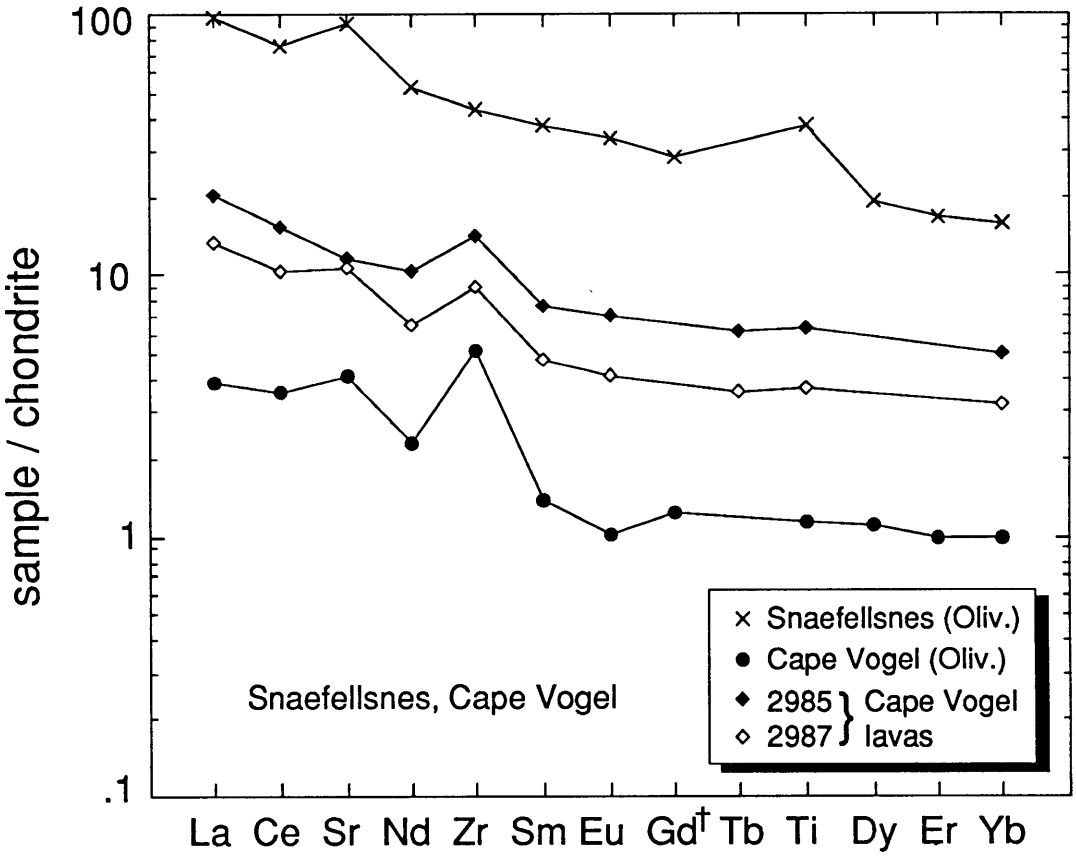

Figure 16. Spider diagrams of Cape Vogel and Snaefellsnes inclusions. Also plotted are two lavas from Cape Vogel, reported by Jenner [1981] for comparison with the inclusion data. The inclusion preserves the general features of the lavas, but is depleted by a factor of 3 to 6.

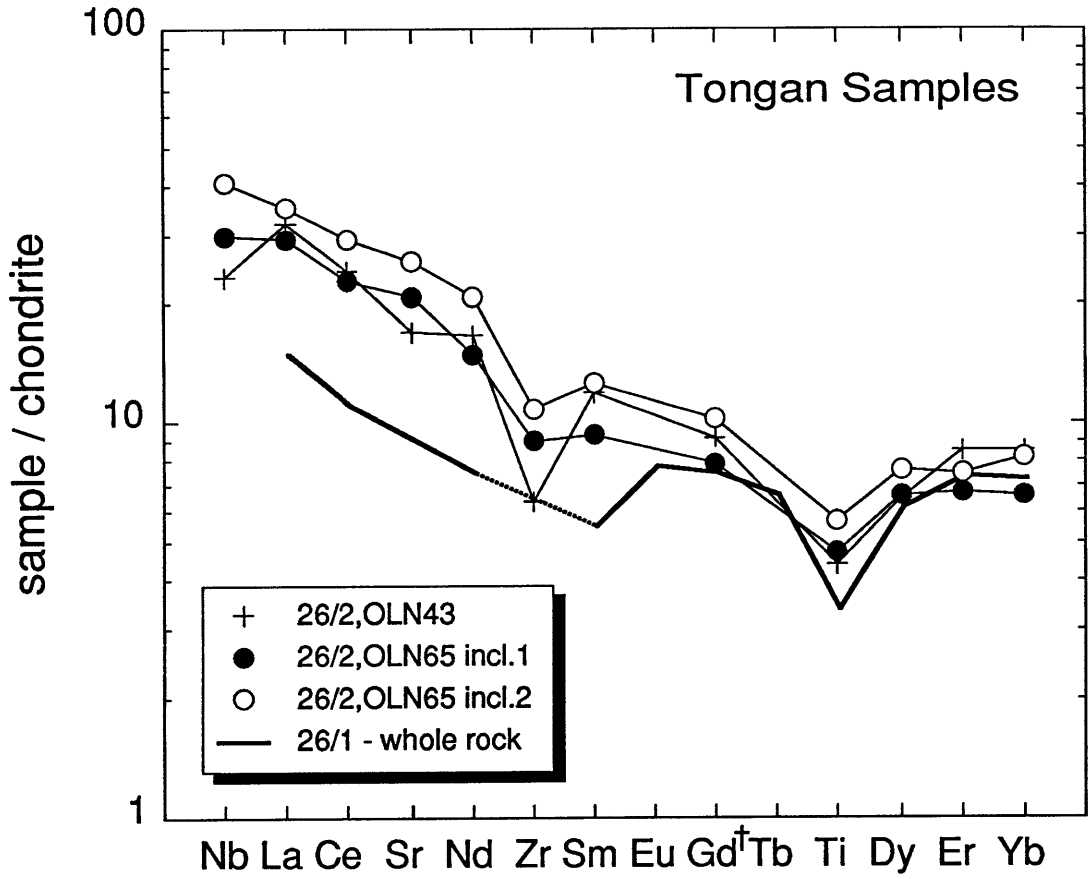

Figure 17. Spider diagram of Tonga inclusions. Also plotted is a whole rock analysis of a boninite collected in the same dredge as the host rock of the inclusions. In this case, the associated lava is more depleted in light REE than the inclusions are, but similar trends are observed in the data. The dashed portion of the whole rock analysis is because no Zr data is available.

whole rock with subsequent trapping by the inclusions, 3) mixing of depleted (arc?) magma with the more light REE enriched forearc magmas.

Trace elements in the Tonga samples reflect their arc setting, except for high concentrations of Nb. Although Nb was not measured in the whole rock [*Sharaskin et al.*, 1983], similarities in the shapes of the trace element patterns of the inclusions and the associated rock suggest that this may be a real chemical trait. Low-K arc tholeiites erupted at the northern end of the Tonga arc at Tafahi and Niuatoputapu [*Ewart and Hawkesworth*, 1987] have flat to light REE depleted patterns with moderate or pronounced Nb anomalies, and show no chemical similarities to the inclusions or the dredged boninites from the forearc. Thus, the sources from these two areas, which are separated by only ~150 km, appear to be distinct.

Troodos

One inclusion, KOL - OLN4, from the Troodos ophiolite upper pillow lavas at Kalavasos, was analyzed. This inclusion is also a boninite and is very depleted in TiO_2 (0.25 wt%) and alkali elements (Na_2O = 0.36 wt%, K_2O = 0.06 wt%). Trace elements are characterized by remarkably low Sr (8 ppm) and Zr (3.4 ppm), and high Ti/Zr (385) and Ti/Sr (160). REE concentrations are very low and are stongly fractionated ($[Ce/Yb]_n$ = 0.12) (Figure 18a). Also plotted in Figure 18 are glasses and whole rocks sampled from the Upper Pillow Lavas and the Arakapas Fault Belt. The Kalavasos area and the Arakapas Fault Belt are characterized by abundant depleted boninitic pillow lavas [*Cameron et al.*, 1983; *Cameron*, 1985]. Figure 18a shows that the light REE enrichment observed in the melt inclusion is a feature shared by the lavas as well. Although sample 9 from the Upper Pillow Lavas [*Cameron et al.*, 1983] and sample 24 from the Arakapas Fault Belt [*Cameron*, 1985] display U-shaped patterns typical of boninites from other localities, a variety of patterns are evident in this area. Sample 10 [*Cameron et al.*, 1983] is similar in shape to the measured inclusion, with almost identical middle and heavy REE and similar valleys at Ce-Nd. Although samples with pronounced U-shaped patterns are lower in

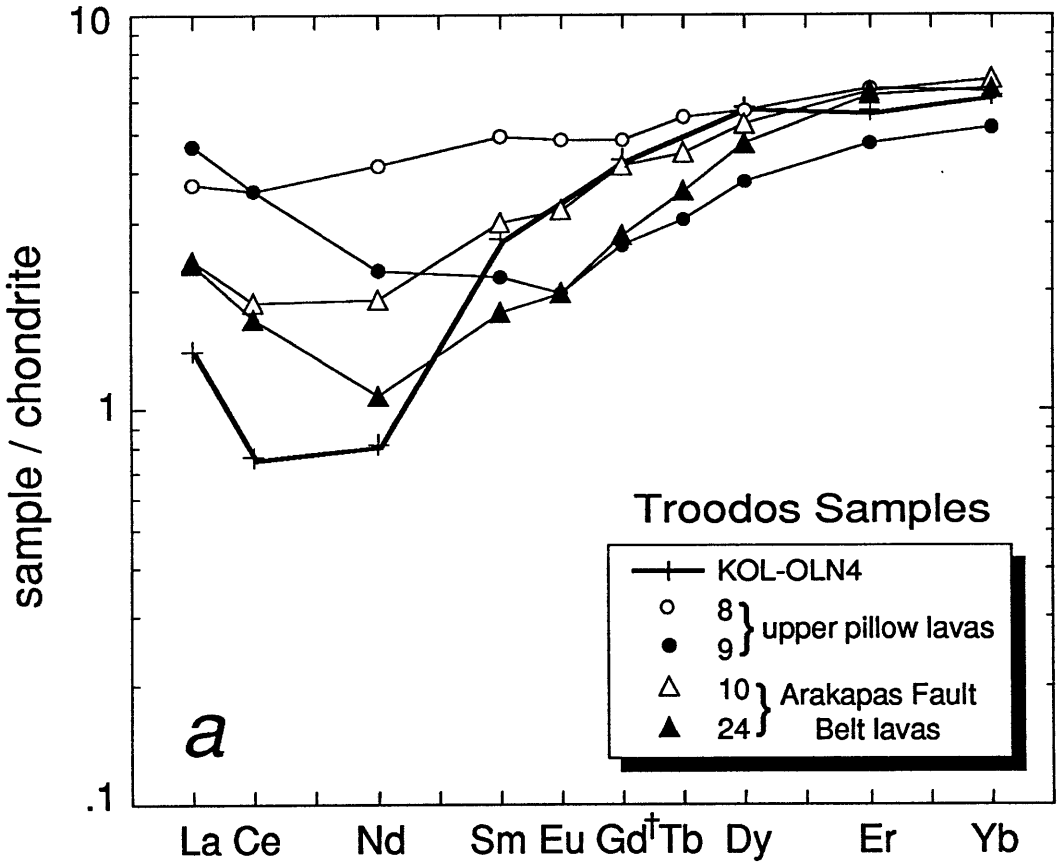

Figure 18. (a). Rare earth element diagram of the analyzed inclusion from the upper pillow lavas at Kalavasos, Troodos ophiolite, Cyprus. Also plotted are lavas from nearby locales. Lavas from the Arakapas Fault Belt resemble the melt inclusion, particularly in the characteristic light REE patterns. (b). Spider diagram of the same samples.

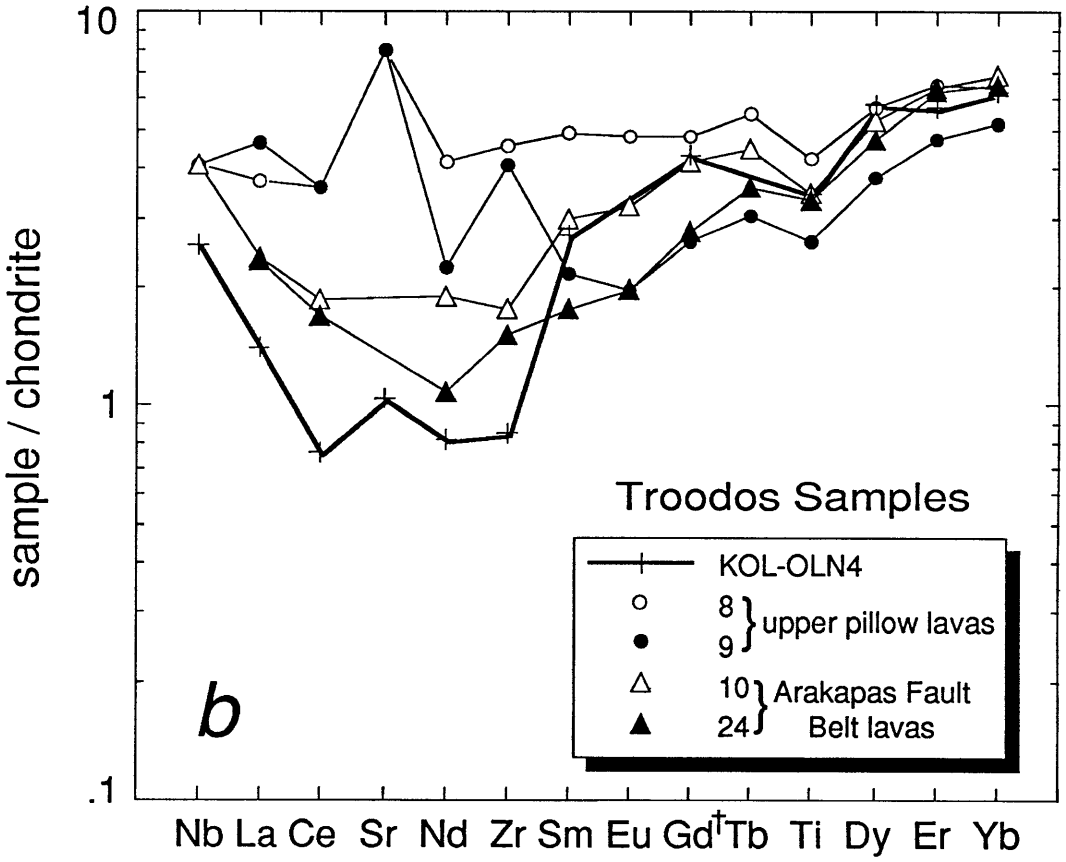
10
1
.1
sample / chondrite
Nb La Ce Sr Nd Zr Sm Eu Gd Tb Ti Dy Er Yb
b
Troodos Samples
KOL-OLN4
8
9
upper pillow lavas
10
24
Arakapas Fault Belt lavas

heavy REE than the inclusion, the latter is lowest in light REE and other incompatible elements, in particular Zr and Nb (Figure 18b). These dissimilarities evince fundamentally different sources for some melts, but similarities between the inclusion and sample 10, for example, support a genetic relationship between these melts. Thus, similar to the Cape Vogel inclusions, the Troodos inclusion is related to some of the lavas, but is more refractory in composition. Thus, these refractory inclusions may be late-stage fractional melts from the same source that produced the lavas. The difference is that the lavas represent mixtures or aggregates of melts produced over a melting interval, whereas the inclusions are subsets of that sum.

Snaefellsnes

Host sample information is not available for this inclusion. The inclusion is contained in olivine. In terms of major elements, the inclusion is of alkalic basalt affinity and contains 3.6 wt% total alkalis and ~3 wt% TiO_2. It is rather primitive (MgO = 9.38 wt%, Mg# = 0.7) and has a T_h = 1250°C. The forsterite content of the host olivine is Fo88, and is consistent with an equilibrium relationship between olivine and inclusion. The sample is strongly light REE enriched ($[La/Yb]_n$ = 6.2, La_n = 97x chondrite) (Figure 16) and is enriched in other incompatible trace elements (Zr = 171, Nb = 51, Sr = 711, Zr/Nb = 3) with chondritic Ti/Zr (111).

DISCUSSION

The following discussion will focus on evaluating possible genetic and evolutionary relationships primarily between the MORB inclusions in Part A since several mineral phases containing inclusions were collected from one rock sample. The data are used to test fractionation, melting, and mixing as potential mechanisms relating the melt compositions. Following the discussion of these mechanisms, the importance of melting on the generation of HFSE anomalies will be discussed.

MORB Samples

Fractional Crystallization

At oceanic crustal pressures, olivine and plagioclase will generally crystallize first, followed by clinopyroxene, from a MORB-type parental magma [e.g., *Miyashiro et al.*, 1970; *Bryan*, 1983]. Crystallization of these phases has predictable effects on the major and trace element composition of residual liquids. For instance, if the melt inclusions were all related by fractional crystallization, then the Mg# and T_h would decrease to the right on Figure 8, while incompatible trace elements would increase. This is not the case for inclusions in olivine and plagioclase, which show increases in Mg# and T_h from left to right (Figure 8) and rather constant or decreasing REE in those same samples (Figure 9). These pieces of information are inconsistent with fractionation of olivine, plagioclase, or clinopyroxene from a parental liquid on the left (PLN47) to produce a derivative daughter liquid on the right (OLN7). However, the host glass and inclusion CPXN2 are not inconsistent with derivation from PLN17 and OLN63 by some amount of olivine ± plagioclase fractionation.

Trace elements can be used as indices of fractionation. In particular, Ti and Zr will increase in basaltic liquids as a result of plagioclase, olivine, and clinopyroxene fractionation. However, the ratio of Ti/Zr in the liquid will not change much with fractionation because of the very low partition coefficients for these elements in those mineral phases. In contrast, Ti versus Sr or Zr versus Sr will show negatively sloping correlations if plagioclase is volumetrically important in the fractionating assemblage of a suite of cogenetic magmas, because $D_{Sr}^{plag} > 1$ and $D_{Ti,Zr}^{plag} \ll 1$. Figure 19 shows Ti versus Zr concentrations in the melt inclusions. Solid vectors show trends the liquid would follow with crystallization of the phases indicated, the dotted vector indicates the trend followed by instantaneous fractional melts, and the dot-dash vector is integrated fractional melts from a 2x chondritic spinel lherzolite source. Clearly, PLN47 cannot be related to the other inclusions by a fractional crystallization process, but PLN17, OLN7, and OLN63 can

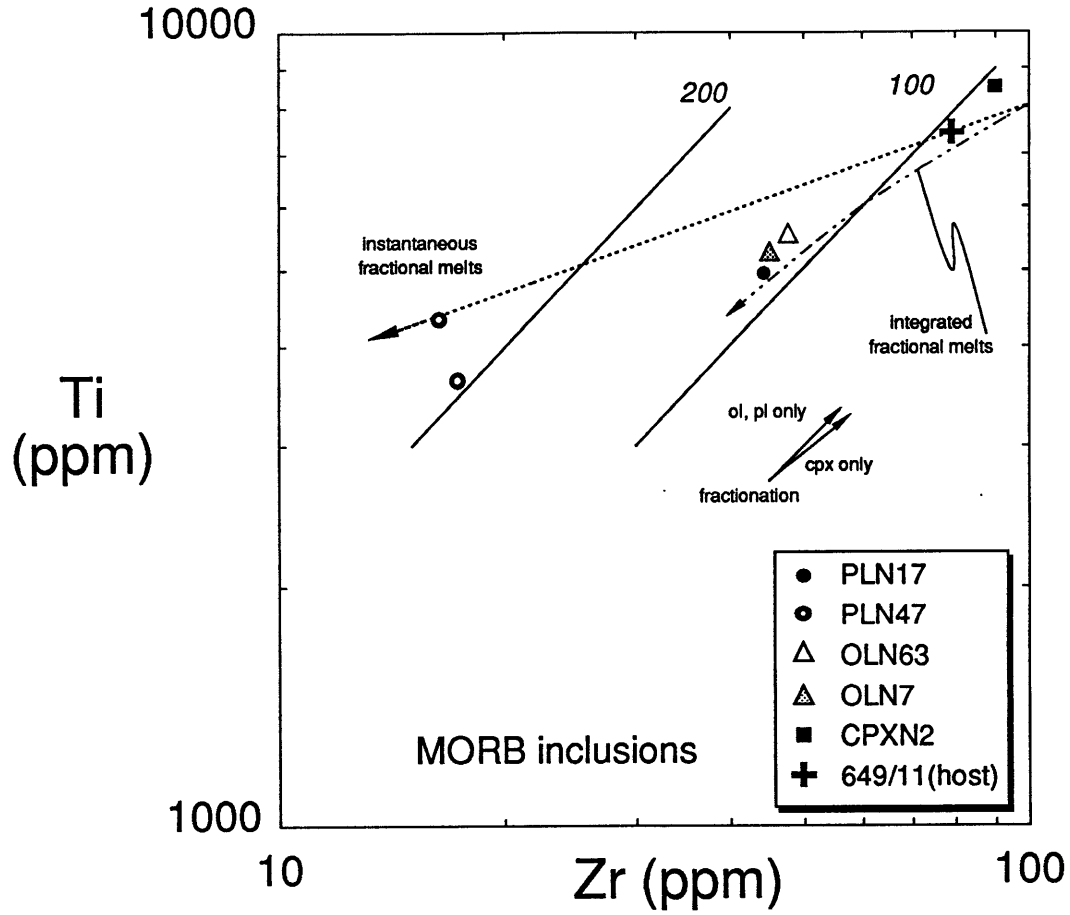

Figure 19. Log-log plot of Zr versus Ti in MORB inclusions with fractional crystallization vectors as well as melting trajectories for integrated fractional (and batch) liquids (dot-dash line) and instantaneous fractional melts (dotted line) from a source with chondritic Ti/Zr. The plot illustrates the inability of fractional crystallization to significantly change the Ti/Zr ratio of the liquid. Ti/Zr ratios of 100 and 200 are shown for reference; chondritic Ti/Zr is ~111 and MORB generally span the range 80-125. In this and subsequent plots, it is possible to derive CPXN2 and 649/11 from OLN7 or PLN17 by olivine + plagioclase fractionation. However, PLN47 is not consistent with a fractionation or melting relationship with the other inclusions (see text). PLN47 inclusion data are matched by instantaneous fractional melting, but not integrated fractional melts or batch melts.

be parental to CPXN2 and 649/11 by olivine ± plagioclase ± clinopyroxene fractionation. The position of PLN47 on this diagram is in the direction expected to be followed by fractional melts.

Figure 20 shows the Zr versus Sr concentration in the inclusions. Because of the nearly opposite directions of the fractionation vectors for plagioclase and for olivine and clinopyroxene, this is a very useful plot for evaluating the relative role of plagioclase in the fractionating assemblage. The data are consistent with derivation of CPXN2 and the host glass (649/11) from PLN17, OLN7, and OLN63 by fractionation of olivine + plagioclase ± clinopyroxene. Moreover, less than 50% of the fractionating assemblage is plagioclase based on the positive slope of the vector connecting these two groups. The lower Mg# and T_h in CPXN2 and 649/11 support this mechanism.

Binary Mixing

Linear arrays of basaltic glass data have been used to infer two-component (binary) mixing in diopside-olivine-silica projections [*Walker et al.*, 1979]. However, binary mixing is not required to explain linear configurations of data. Two-component mixing can be evaluated very effectively using trace elements if care is taken to choose appropriate elements to characterize possible end-member compositions. For example, if samples are related by binary mixing, then ratio-element plots will yield hyperbolae, the mixing end-members plotting at extreme ends of the hyperbolae [*Langmuir et al.*, 1977]. An important requirement is that end-members must be the same in all plots.

If binary mixing were the mechanism responsible for the linear array of inclusion data in Figure 8, then the end-members would be PLN47 and OLN63. However, in that figure intermediate inclusions in the trend have higher Mg#, thus ruling out mixing as a viable explanation for the data. Furthermore, on a plot of Ti/Zr versus Zr, even though the data form a hyperbola (Figure 21), which might be interpreted as a binary mixing trend, the end-members are PLN47 and CPXN2, thus ruling out binary mixing as the singular process relating the inclusions to one another. However, based on the K_d arguments

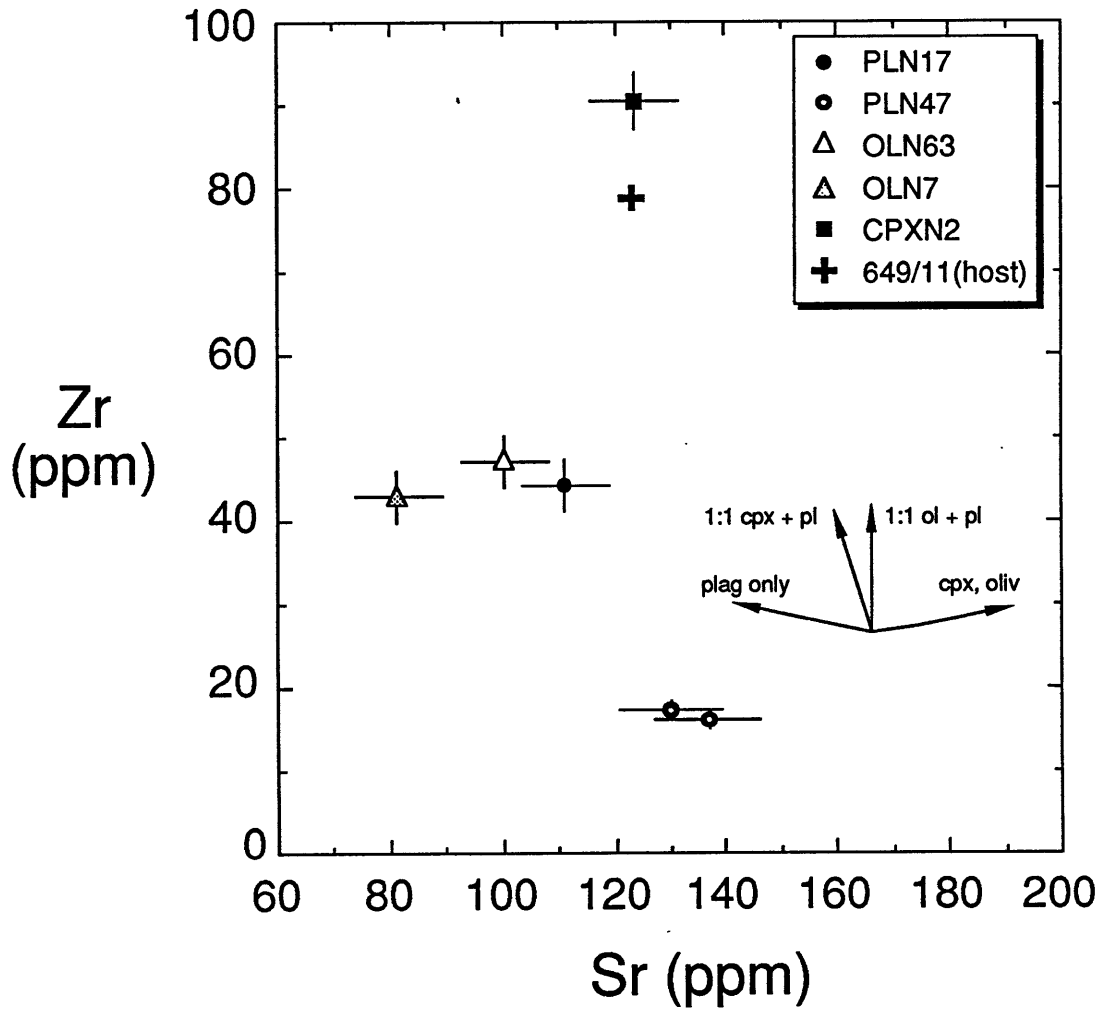

Figure 20. Sr versus Zr in MORB inclusions. Vectors show the direction of compositional change of the liquid with fractionation of the specified phases.

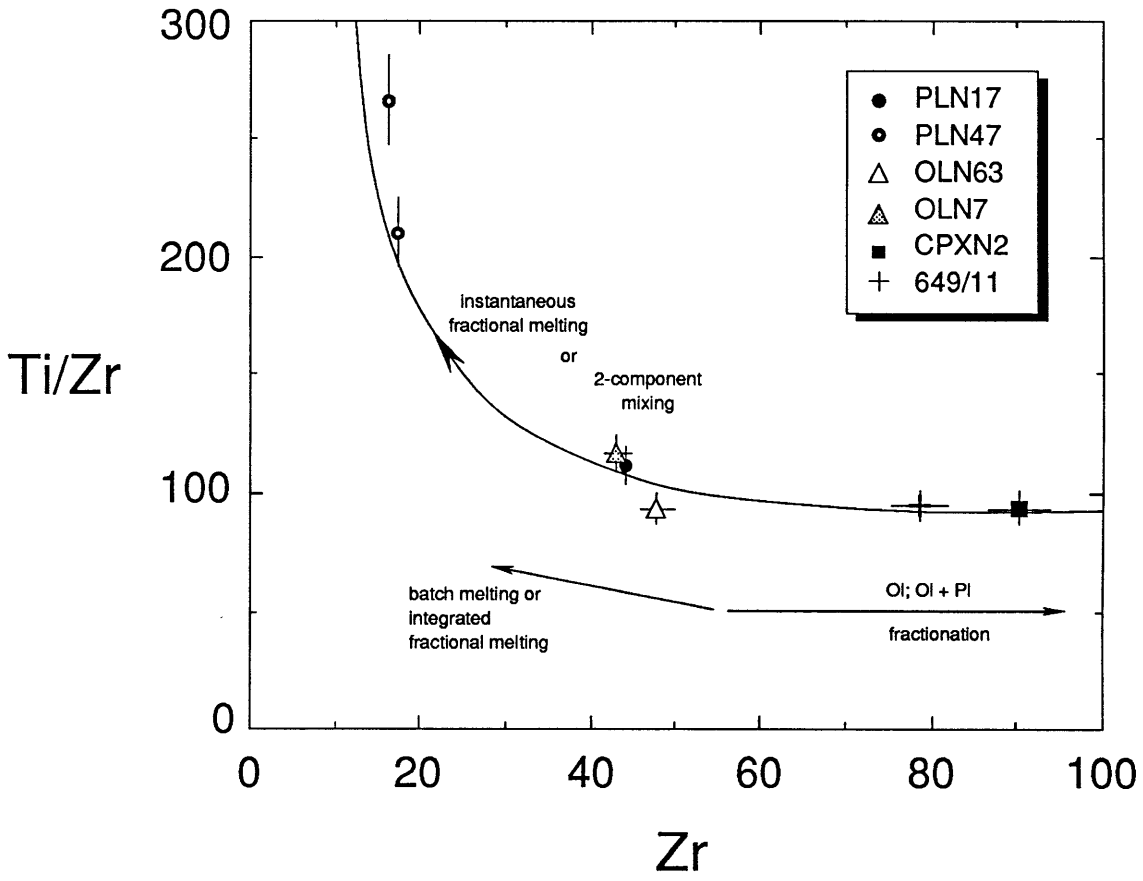

Figure 21. Zr versus Ti/Zr in MORB inclusions. Vectors for the effects of various processes considered in relating the inclusions to one another are shown. Only instantaneous fractional melting or binary mixing between a depleted PLN47-like endmember and an evolved CPXN2-type endmember are capable, in this diagram, of relating all of the inclusions. Figure 23 examines these possibilities further.

above, most of the minerals containing the studied inclusions are xenocrysts in host 649/11. Therefore, the host itself must be a mixture of some sort, the components of which are not all sampled in this study.

Melting

Melting of a peridotite mantle will produce magmas which vary in composition with percent melting as well as with pressure [*Kushiro*, 1969, 1972; *Jaques and Green*, 1980; *Takahashi and Kushiro*, 1983; *Falloon and Green*, 1987]. With increasing pressure, melts become less silica-rich, but conform to pseudocotectic curves in the CMAS projections that are subparallel to each other [*ibid*]. The inclusion data array in Figure 8 is subparallel to experimentally derived pseudocotectics at pressures between 5 and 10 kbar, (dotted lines in Figure 8), which could be viewed as indicating derivation of the suite of inclusions from melting in this pressure range. However, when major elements are considered along with trace elements it can be argued that while melting may be responsible for certain trace element characteristics, relating the inclusions to each other by melting alone is inconsistent with the data.

Many incompatible element depletions in abyssal peridotites are consistent with fractional melting of a light REE-depleted source [*Johnson et al.*, 1990]. The relative uniformity of Ti/Zr in MORB at around chondritic (80-125) is consistent with the model that MORB are integrated increments of near-fractional melting at $\leq$25% total melting of a chondritic source (see Chapter 2). Succesive individual increments of melt, however, will not be constrained to asymptotically approach the Ti/Zr ratio of their source as integrated increments will, but instead will approach infinity. This means that Ti/Zr ratios can increase in melts and residues to greater than the ratio in their source as fractional melting proceeds.

If the upper mantle source for MORB has a roughly chondritic Ti/Zr ratio, then melts with Ti/Zr » chondritic could be produced from a source that has been depleted by varying degrees of fractional melting. Ti/Zr of PLN47 is over twice as large as that of any other

inclusion and cannot be explained by batch melting of the source mantle with a chondritic Ti/Zr. However, Cr and Mg# are not particularly high in PLN47, which either argues against it being a late-stage melt fraction derived from a source with originally chondritic Ti/Zr or indicates host-plagioclase interaction with the inclusion. Since Ti/Zr is not affected by plagioclase dissolution or crystallization, this ratio can be assumed to represent the pre-interaction value.

Plotting Ti/Zr against $(La/Sm)_n$. can be useful in examining the melting process. Figure 22 is a plot of these ratios in melt inclusions from the MORB sample, 649/11, and from several Iceland samples. Also plotted are two dashed model curves. The dot-dash curve is the trajectory that instantaneous fractional primary melts would follow with progressive melting of a source with chondritic Ti/Zr and $(La/Sm)_n \approx 0.5$ (light REE depleted). The initial fraction of melt is far off the right-hand side of the diagram, and the curve is asymptotic to $(La/Sm)_n$ = zero. The shorter dashed curve is the trajectory that integrated fractional melts and batch melts would follow with progressive melting of the same source. Ti/Zr and $(La/Sm)_n$ ratios in the liquids approach those of the source at high degrees of melting, as seen, but cannot exceed them in batch or integrated melts. The vector labeled "melting" indicates the direction that primary liquids will follow with progressive melting. It is clear that batch or integrated fractional melting of a source with the reasonable trace element ratios used in this model can produce the majority of N-type MORB (shaded field in the diagram), but cannot produce the inclusions plotting far outside this field. Inclusions in the MORB olivines and cpx plot in the general MORB field and could be produced in this way. However, inclusion PLN17, while possessing chondritic Ti/Zr, plots well outside the MORB field and to the left of the integrated fractional and batch melt curve. This implies that either it is a batch or integrated fractional melt from a more light REE depleted source, or it is a mixture of late-stage fractional melts that contribute to the MORB field of integrated melts.

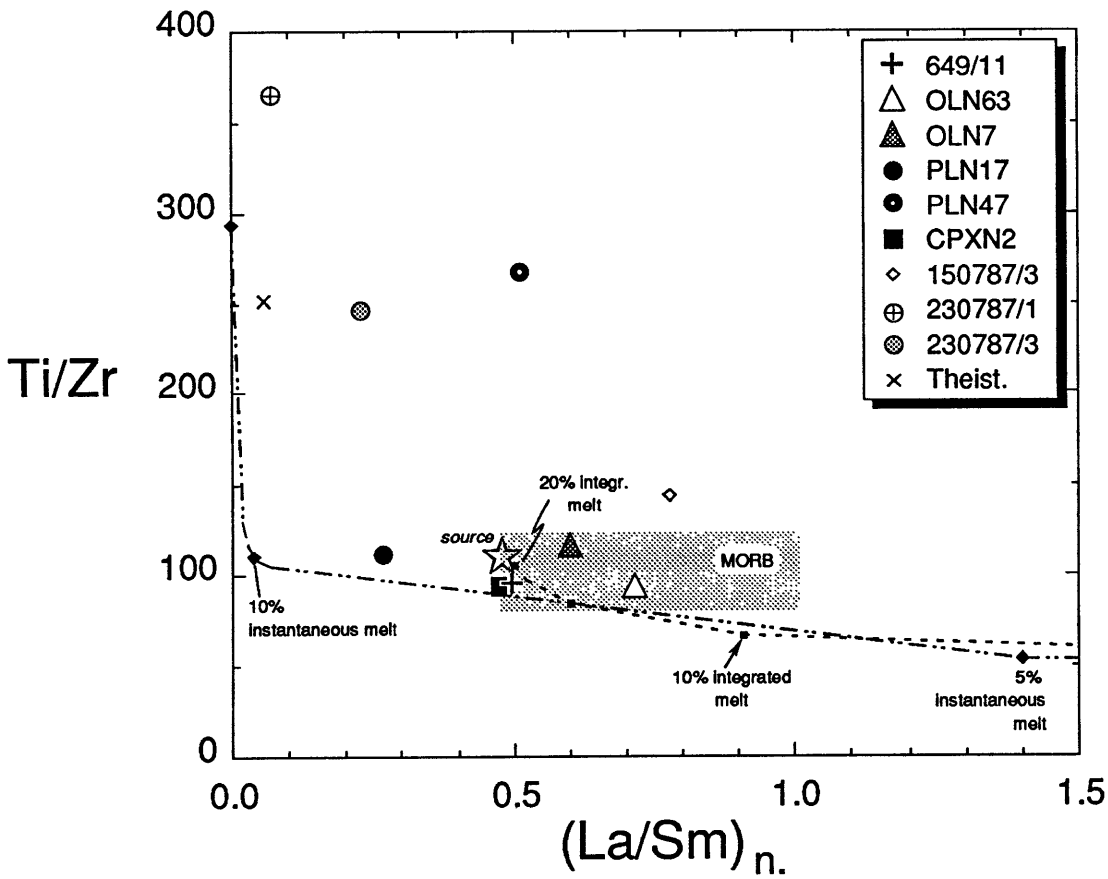

Figure 22. Plot of (La/Sm)n versus Ti/Zr for MORB, Reykjanes, and Theistareykir melt inclusions. Also plotted are model curves for instantaneous (dot-dash lines) and integrated (short dashed lines) fractional melts from a source as shown by the star, and the field for N-type MORB. The curves illustrate the path followed by hypothetical melts and show that some of the inclusions, in particular PLN47 and 230787/3 are inconsistent with derivation by simple fractional melting of the proposed source. Inclusions that plot closer to the curves and within the MORB field may represent fractional melts, but PLN47 and 230787/3 are better explained as mixtures of late-stage melt fractions with more enriched, earlier fractions. The model is not unique, however.

Inclusion PLN47 and Iceland inclusions Reykjanes 230787/1, 230787/3, and Theistareykir 150785/2 plot well outside of the MORB field in Figure 22. Theistareykir and Reykjanes 230787/1 plot close to the theoretical instantaneous melt curve at high Ti/Zr. These two inclusions could represent, in this model, late-stage fractional melts or, more likely, mixtures of late-stage fractional or sequential melts. Inclusions PLN47 and Reykjanes 230787/3, and to a lesser degree Reykjanes 150787/3, plot well off the trajectory of instantaneous fractional melts from the above-mentioned model source. It is not possible, using this plot, to relate them to the other inclusions simply by melting the model source. The Iceland inclusions have low to very low Sr, and high, but variable Cr and Mg# consistent with their being refractory late-stage fractional melts. Although they plot off the hypothetical melting trend, they could be explained as mixtures of refractory liquids with more enriched melts.

The two inclusions analyzed in PLN47 present a more difficult problem. They contain higher Sr than all the other spreading center inclusions, and very low Zr, which is a very unusual liquid by ocean-floor basalt standards. The high Sr inclusions in PLN47 could be explained as either: 1) mixtures of depleted, high Ti/Zr liquids and enriched, high La/Sm, high Sr liquids; 2) artifacts of beam overlap onto plagioclase or post-entrapment interaction with plagioclase, in which case the original liquid was much lower in Sr and somewhat lower in La/Sm. In the latter case the inclusions could be depleted, late-stage fractional melts. However, some amount of plagioclase interaction is suggested since this is the only plagioclase-hosted inclusion analyzed and it has the highest Sr concentration, but this possibility will not affect the Ti/Zr ratio. Thus, even if it is assumed that the Sr concentration, and to a lesser extent the La/Sm ratio, is artificially high, this cannot change the fact that the inclusion plots well above the MORB field in terms of Ti/Zr in Figure 22 and is most readily explained as a mixture of refractory melt fractions and more enriched melts.

HFSE anomalies in the mid-ocean ridge setting

The presence of negative Zr and Ti anomalies in these samples on spider diagrams is important. Most MORB glasses sampled from the world's oceans do not display negative Zr anomalies, though a large number do have small negative Ti anomalies. However, clinopyroxenes in oceanic peridotites, as well as in many mantle xenoliths, invariably display negative Ti and Zr anomalies [*Salters and Shimizu*, 1988; *Johnson et al.*, 1990]. Although the process that causes these anomalies in peridotite clinopyroxenes is not understood well enough to be agreed upon, their absence in MORB has been viewed as an argument against their formation simply by melting a depleted chondritic source. However, Figure 22 has illustrated the possibility that some inclusions represent late-stage melt fractions, which possess unusual trace element characteristics that set them apart from typical MORB. Among the effects of fractional melting, its ability to fractionate elements that have only slight differences in their bulk partition coefficients is important to this discussion. In contrast, batch melting and integrated fractional melting will not yield liquids or residues with pronounced fractionations of such elements. Thus, if the partition coefficients of two elements are slightly different, fractional melting can produce marked separation (fractionation) of these elements in residues and instantaneous melts after only small degrees of total melting.

The role of fractional melting in producing some melt inclusions was suggested in Figure 22. An important question to investigate is whether fractional melting can produce the observed negative Zr and Ti anomalies in the refractory melts and in peridotite clinopyroxenes. From the preceding paragraph it follows that if the true bulk solid and liquid partition coefficients for Zr and Ti are different than coefficients interpolated between Nd and Sm (where Zr is commonly placed in spider diagrams) and between Eu and Dy (where Ti is placed), then anomalies could develop in the residue and in instantaneous melts with progressive fractional melting. This can be investigated by construction of a melting model as outlined below.

First, a simple calculation can rule out host-phase crystallization as the cause for the observed HFSE depletions. Assuming initially smooth spider patterns, host phase crystallization of olivine, plagioclase, or clinopyroxene cannot produce the observed Zr anomalies using the partition coefficients in Table 4. Since the Reykjanes Peninsula host basalts, as well as the inclusions, all exhibit negative HFSE anomalies, there is no need to rationalize their existence in these ways. Thus, I reason that the anomalies in MORB and Iceland inclusions are not secondary phenomena produced by host-phase interaction.

The sequence of plotting elements in spider diagrams is determined by their relative compatibility in MORB, going from least compatible on the left to most compatible on the right of the diagram. [*Sun* , 1980; *Pearce*, 1983; *Thompson et al.*, 1984]. The order of element compatibility is not the same in all mantle and MORB mineral phases, so that placement of incompatible elements among REE differs from one mineral to another. For example, for the order of elements employed in Figure 10, Zr and Ti partition coefficients define positive anomalies relative to REE in olivine and orthopyroxene [*Fujimaki et al.*, 1984; *Dunn*, 1987; P. Kelemen, unpublished data, 1990], while they define slight negative anomalies in clinopyroxene [Chapter 3; *Johnson and Kinzler*, 1989]. The result of this is that over the course of the MORB generation process, the effects of melting, mixing, and fractional crystallization average out the competing influences exerted by different mineral phases in the melting and crystallizing assemblages, leading to rather smooth spider patterns in N-MORB. It was shown, in a rough sense, that integrated fractional melts from a chondritic source are essentially identical to N-MORB in terms of REE and other trace elements (Chapter 2; *Johnson et al.* [1990]).

The magnitude of the anomalies will depend on the relative proportions of mineral phases entering the liquid during melting, the starting chemical and modal composition of the solid, as well as on the partition coefficients for each element in each mineral phase. As long as melting is in the spinel peridotite field, clinopyroxene exerts the most leverage on the incompatible trace element composition of the liquid and residue because of its relatively

TABLE 4. Crystal/Liquid Partition Coefficients Used in Models

	Olivine	Clinopyroxene	Orthopyroxene	Garnet	Spinel	Plagioclase
Ti	0.015	0.36	0.08	0.6	0.10	0.02
Zr	0.007	0.15	0.03	0.5	0.05	0.01
Sr	0.003	0.08	0.01	0.03	0.0001	2.0
Ce	0.0005	0.11	0.005	0.008	0.0006	
Nd	0.0006	0.22	0.01	0.057	0.0008	
Sm	0.0007	0.38	0.02	0.217	0.0009	
Eu	0.0007	0.42	0.03	0.45	0.0009	
Dy	0.001	0.48	0.045	2.0	0.0015	
Er	0.002	0.48	0.06	3.5	0.003	
Yb	0.005	0.49	0.075	7.0	0.0045	

Sources of data: Clinopyroxene: REE, *Irving and Frey* [1984], *Green and Pearson* [1985], *Johnson and Kinzler* [1989]. Ti, Zr, Sr, *McCallum and Charrette* [1978], *Fujimaki et al.* [1984], *Dunn* [1987], *Tormey et al.* [1987], *Johnson and Kinzler* [1989], Chapter 3, this thesis. Olivine, opx: REE, *Stosch* [1982], combined with cpx partition coefficients, *McKay* [1986]. Ti, Zr, Sr, *Fujimaki et al.* [1984], *Weill and McKay* [1975], *McKay and Weill* [1977]. Spinel: REE, *Stosch* [1982], combined with cpx partition coefficients. Ti, Zr, K. Johnson, Ti calculated from electron probe data; Zr estimated from secondary ion counts relative to cpx. Garnet: REE, *Shimizu and Kushiro* [1975], *Nicholls and Harris* [1980], *Fujimaki et al.* [1984]. Ti, Zr,Sr, *Fujimaki et al.* [1984], *Green et al.* [1989]. Plagioclase: Zr, Sr, *Drake and Weill* [1975], *Fujimaki et al.* [1984].

higher partition coefficients for the elements discussed here. Thus, knowledge of clinopyroxene/liquid partition coefficients is critical to the model. This was the main motivation behind the clinopyroxene partitioning study reported in Chapter 3. Using the partition coefficients from that study, and procedures similar to those used in Chapter 2, the following model was constructed to test the effectiveness of fractional melting in producing negative Zr and Ti anomalies. It should be emphasized that the assumption is that the negative HFSE anomalies were generated from a bulk source with an initially smooth, non-anomalous pattern. If the source pattern has negative anomalies to begin with (predicated on some other physical or chemical condition in the mantle), then the solid residues and derived liquids will inherit these anomalies. This will not change the results or conclusions obtained from the following model, but will imply that more complex processes are involved in generating these anomalies.

Using the fractional melting equations of *Shaw* [1970], the derived melting equation for diopside (Chapter 2), measured partition coefficients for clinopyroxene, reported values for other phases, and the same starting compositions, solid, and melt modes as in Chapter 2, negative Zr and Ti anomalies in intermediate stage (10%) fractional melts and in residual clinopyroxene were generated. Figure 23 shows the model results compared to some Reykjanes and Theistareykir, Iceland inclusion data and some residual diopsides from the Vulcan and Atlantis II fracture zones. The agreement between model and data is quite good given the uncertainties in starting composition, melt, and solid modes. Light REE are lower in the model fractional melts than in the data, which could be explained by small amounts of mixing with more evolved melts or by the choice of model parameters. The result is model-dependent, but it is reasonable to say that given the partition coefficients determined in natural and experimental cpx-liquid pairs, negative Zr and Ti anomalies can be produced in fractional residues and instantaneous melts starting with a non-anomalous source. If melting is sequential or if a previously depleted source is remelted, anomalies will be present in the next melt increments. At moderate degrees of melting, element ratios

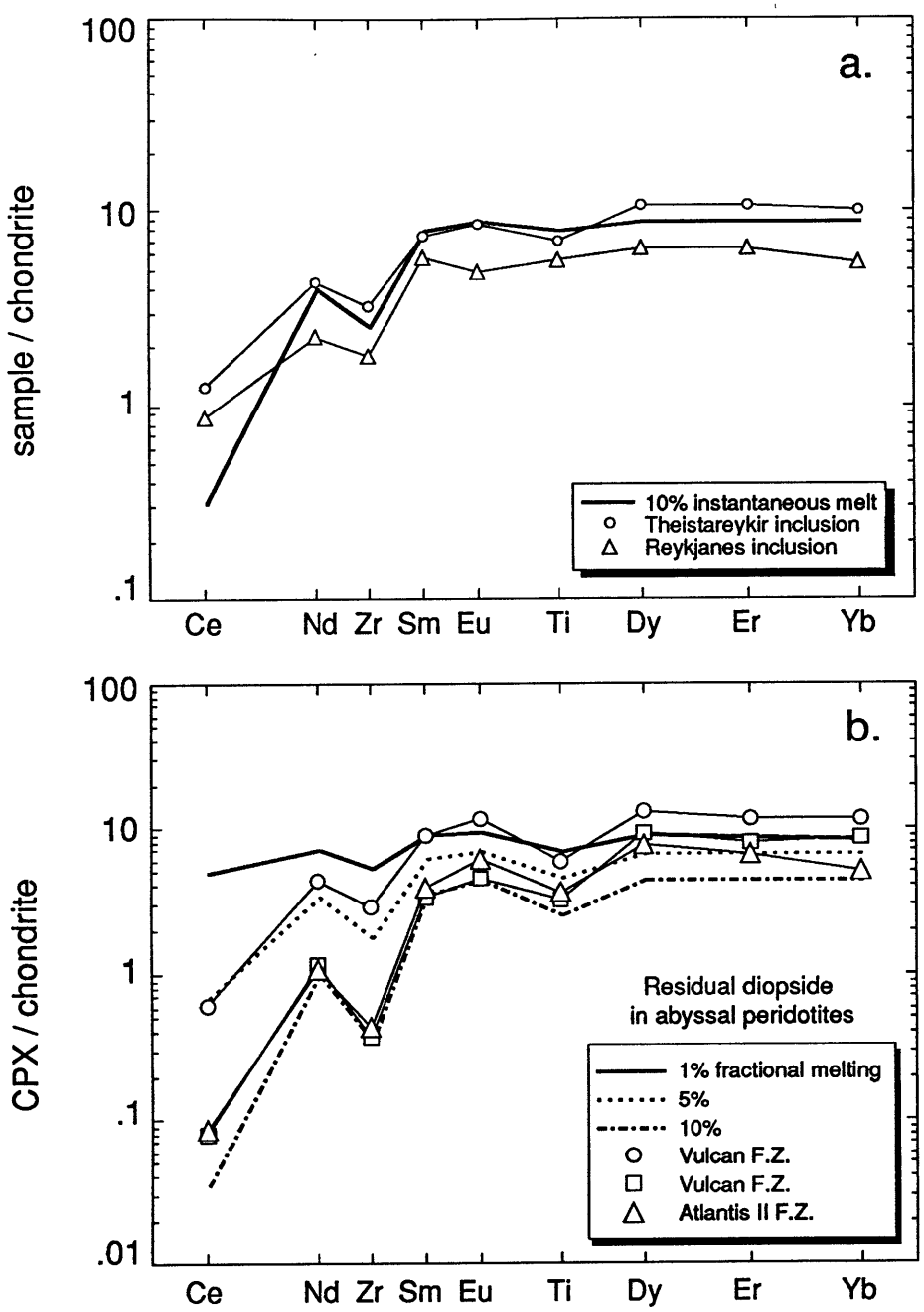

Figure 23. Model spider diagrams of (a) instantaneous melt compositions plotted with Reykjanes and Theistareykir melt inclusions and (b) Residual diopsides plotted with diopsides from abyssal peridotites using partition coefficients reported in the Chapter 3, Table 4, and Johnson and Kinzler [1989] to show the development of HFSE anomalies with fractional melting starting from a non-anomalous source. As discussed in the text, other processes may also contribute to HFSE anomalies, but it appears melting can make a significant contribution as well.

of integrated fractional liquids approach those of the source (e.g. non-anomalous $[Zr/Sm]_n$) and so these anomalies will not be present in integrated fractional melts, possibly explaining the absence of large HFSE anomalies in most MORB. In this scenario, the MORB host glass, 649/11, and CPXN2 could represent integrated or mixed fractional melts, while the other inclusions were trapped by growing phenocrysts at earlier stages, before aggregation and eruption. While rigorous application of this model requires better knowledge of all model parameters, it is useful in showing that HFSE anomalies can increase with increasing degrees of fractional melting, a point made in Chapter 2 based on HFSE anomalies in peridotite diopsides, and that fractional melts from a chondritic source can develop negative Zr and Ti anomalies.

SUMMARY AND CONCLUSIONS

Melt inclusions from a variety of tectonic settings show general compositional similarities with associated erupted lavas. However, in many cases the inclusions are more refractory than the lavas and are characterized, in part, by higher Mg# and lower concentrations of incompatible trace elements. Inclusions from some convergent margins and paleo-back-arc basins (Cape Vogel, Tonga, Kamchatka, and Troodos) have high Mg#, and very low concentrations of incompatible trace elements. These features are consistent with high degrees of melting or remelting of a depleted, refractory residue, the inclusions often representing more depleted and refractory melt fractions than the erupted lavas. The melt fractions represented by the inclusions eventually mix with other evolved and primitive melt increments and may take on "averaged", less strikingly refractory or depleted signatures. As expected in arc settings, melt inclusions often exhibit Zr and Ti negative anomalies (Kamchatka and Tonga), and inclusions from Troodos and Cape Vogel display similar chemical characteristics to lavas from those areas. The inclusions, however, are often more refractory and/or depleted than the lavas.

The results of Chapter 2 led to the prediction that refractory fractional melts, with depletions commensurate with those of their peridotite source, exist in mid-ocean ridge environments. Melt inclusions were targeted as potential representatives of these refractory fractional melts, but the results of this study have not strongly supported this hypothesis. Some observations, however, do lend support to the hypothesis: 1) The presence of Zr and Ti negative anomalies on spider diagrams in some MORB inclusions and in depleted Reykjanes and Theistareykir inclusions, 2) Zr and Ti negative anomalies in Reykjanes host basalts possibly reflecting their formation by (re)melting a highly depleted source. Extreme depletion of the Iceland inclusions is consistent with the observation by several authors that very high degrees of melting in the upper mantle occur near hotspots [*Dick et al.*, 1984; *Michael and Bonatti*, 1985; *Klein and Langmuir*, 1987; *Johnson et al.*,1990] , 3) Ti/Zr ratios in some MORB and Iceland inclusions are more than twice those in host basalts and other "normal" MORB, 4) Absence of pronounced negative anomalies in MORB host basalt, supporting the hypothesis that mixing and melt aggregation may occur and can eliminate the highly depleted, "non-smooth" spider patterns of late-stage melt fractions, and 5) Simple melting models that can partly account for the observed HFSE anomalies in both residual peridotite diopsides and in some melt inclusions.

The data suggest that magma evolution must be a complex process that starts as soon as melts segregate from their source. Mixing between melt increments from different sources can occur in channels, conduits, or veins at any point in the ascending mantle after segregation takes place. Thus, extreme compositions can be trapped as melt inclusions in growing mineral phases before and during homogenization of the diverse melt fractions prior to eruption. Complex magmatic processes undoubtedly occur in the upper mantle and can contribute to the observed anomalies, but some of the observed characteristics can be engendered by fractional melting.

REFERENCES

Ahern, J. L., and D. L. Turcotte, Magma migration beneath an ocean ridge, *Earth Planet. Sci. Lett., 45*, 115-122, 1979.

Anderson, A. T., Magma mixing: Petrological process and volcanological tool, *J. Volcanol. Geotherm. Res., 1,* 3-33, 1976.

Bender, J. F., C. H. Langmuir, and G. N. Hanson, Petrogenesis of basalt glasses from the Tamayo region, East Pacific Rise, *J. Petrol., 25,* 213-254, 1984.

Bryan, W. B., Systematics of modal phenocryst assemblages in submarine basalts: petrologic implications, *Contrib. Mineral. Petrol., 83*, 62-80, 1983.

Bryndzia, L. T., B. J. Wood, and H. J. B. Dick, The oxidation state of the Earth's sub-oceanic mantle from oxygen thermobarometry of abyssal spinel peridotites, *Nature, 341*, 526-527, 1989.

Cameron, W. E., Petrology and origin of primitive lavas from the Troodos ophiolite, Cyprus, *Contrib. Mineral. Petrol., 89*, 239-255, 1985.

Cameron, W. E., M. T. McCulloch, and D. A. Walker, Boninite petrogenesis: chemical and Nd-Sr isotopic constraints, *Earth Planet. Sci. Lett., 65,* 75-89, 1983.

Christie, D. M., I. S. E. Carmichael, and C. H. Langmuir, Oxidation states of mid-ocean ridge basalt glasses, *Earth Planet. Sci. Lett., 79,* 397-411, 1986.

Dick, H. J. B., Partial melting in the Josephine Peridotite, I, the effect on mineral composition and its consequence for geobarometry and geothermometry, *Am. J. Sci., 277*, 801-832, 1977.

Dmitriev, L. V., A. V. Sobolev, M. G. Reisner, and W. G. Melson, Quenched glasses of TOR: petrochemical classification and distribution in Atlantic and Pacific Oceans, Abstracts, International Geological Congress, v. 1, 399-401, Washington, D.C., 1989.

Donaldson, C. H., and R. W. Brown, Refractory megacrysts and magnesium-rich melt inclusions within spinel in oceanic tholeiites: indicators of magma mixing and parental magma composition, *Earth Planet. Sci. Lett., 37,* 81-89, 1977.

Drake, M. J., and D. F. Weill, Partition of Sr, Ba, Ca, Y, Eu^{2+}, Eu^{3+}, and other REE between plagioclase feldspar and magmatic liquid: An experimental study, *Geochim. Cosmochim. Acta, 39,* 689-712, 1975.

Dungan, M. A. and J. M. Rhodes, Residual glasses and melt inclusions in basalts from DSDP legs 45 and 46: Evidence for magma mixing, *Contrib. Mineral. Petrol., 67,* 417-431, 1978.

Dunn, T., Partitioning of Hf, Lu, Ti, and Mn between olivine, clinopyroxene and basaltic liquid, *Contrib. Mineral. Petrol., 96,* 476-484, 1987.

Ewart, A. E., and C. J. Hawkesworth, The Pleistocene-Recent Tonga-Kermadec arc lavas: Interpretation of new isotopic and rare earth data in terms of a depleted mantle source model, *J. Petrol., 28,* 495-530, 1987.

Falloon, T. J. and D. H. Green, Glass inclusions in magnesian olivine phenocrysts from Tonga: evidence for highly refractory parental magmas in the Tongan arc, *Earth Planet. Sci. Lett., 81,* 95-103, 1986.

Falloon, T. J., and D. H. Green, Anhydrous partial melting of MORB pyrolite and other peridotite compositions at 10 kbar: implications for the origin of primitive MORB glasses, *Mineral. and Petrol., 37,* 181-219, 1987.

Falloon, T. J., and D. H. Green, Anhydrous partial melting of peridotite from 8 to 35kb and the petrogenesis of MORB, *J. Petrol., special lithosphere issue,* 379-414,1988a.

Falloon, T. J., and D. H. Green, Anhydrous partial melting of a fertile and depleted peridotite from 2 to 30 kb and application to basalt petrogenesis, *J. Petrol., 29,* 1257-1282, 1988b.

Fujimaki., H., M. Tatsumoto, and K. Aoki, Partition coefficients of Hf, Zr, and REE between phenocrysts and groundmass, *Proc. Lunar Planet. Sci. Conf., 14th, Part 2, J. Geophys. Res., 89,* suppl., B662-B672, 1984.

Green, D. H., W. O. Hibberson, and A. L. Jaques, Petrogenesis of mid-ocean ridge basalts, in *The Earth:Its Origin, Structure, and Evolution*, edited by M. W. McElhinney, pp. 265-299, Academic Press, San Diego, Calif., 1979.

Green, T. H., and N. J. Pearson, Rare earth element partitioning between clinopyroxene and silicate liquid at moderate to high pressure, *Contrib. Mineral. Petrol., 91*, 24-36, 1985.

Green, T. H., S. H. Sie, C. G. Ryan, and D. R. Cousens, Proton microprobe-determined partitioning of Nb, Ta, Zr, Sr, and Y between garnet, clinopyroxene and basaltic magma at high pressure and temperature, *Chem. Geol., 74,* 201-216, 1989.

Grove, T. L. and W. B. Bryan, Fractionation of pyroxene-phyric MORB at low-pressure: an experimental study, *Contrib. Mineral. Petrol., 84*, 293-309, 1983.

Hickey, R. L. and F. A. Frey, Geochemical characteristics of boninite series volcanics: implications for their source, *Geochim. Cosmochim. Acta, 46*, 2099-2115, 1982.

Irving, A. J. and F. A. Frey, Trace element abundances in megacrysts and their host basalts: Constraints on partition coefficients and megacryst genesis, *Geochim. Cosmochim. Acta, 48*, 1201-1221, 1984.

Jaques, A. L., and D. H. Green, Anhydrous melting of peridotite at 0-15 kbar pressure and the genesis of tholeiitic basalts, *Contrib. Mineral. Petrol., 73*, 287-310, 1980.

Jenner, G. A., Geochemistry of high-Mg andesites from Cape Vogel, Papua New Guinea, *Chem. Geol., 33*, 307-332, 1981.

Johnson, K. T. M., and R. J. Kinzler, Partitioning of REE, Ti, Zr, Hf, and Nb between clinopyroxene and basaltic liquid: An ion microprobe study, *Eos Trans. AGU, 70,* 1388, 1989.

Johnson, K. T. M., H. J. B. Dick, and N. Shimizu, Melting in the oceanic upper mantle: an ion microprobe study of diopsides in abyssal peridotites, *J. Geophys. Res.*, 95, 2661-2678, 1990.

Kelemen, P. B., K. T. M. Johnson, R. J. Kinzler and A. J. Irving, High field strength element depletions in arc basalts due to mantle-magma interaction, Nature, in press, 1990.

Kirkpatrick, R. J., Towards a kinetic model for the crystallization of magma bodies, *J. Geophys. Res., 81*, 2565-2571, 1976.

Klein, L. C. and D. R. Uhlmann, The kinetics of lunar glass formation, revisited, *Proc. 7th Lunar Sci. Conf.*, 1113-1121, 1976.

Kushiro, I., The system forsterite-diopside-silica with and without water at high pressures, *Am. J. Sci., 267-A*, 269- 294, 1969.

Kushiro, I., The effect of water on the composition of magmas formed at high pressures, *J. Petrol., 13*, 311-334, 1972.

Langmuir, C. H., R. D. Vocke, G. N. Hanson, and S. R. Hart, A general mixing equation with applications to Icelandic basalts, *Earth Planet. Sci. Lett., 37,* 380-392, 1977a.

Langmuir, C. H., J. F. Bender, A. E. Bence, G. N. Hanson, and S. R. Taylor, Petrogenesis of basalts from the FAMOUS area: Mid-Atlantic Ridge, *Earth Planet. Sci. Lett., 36*, 133-156, 1977b.

McCallum, I. S., and M. P. Charette, Zr and Nb partition coefficients: implications for the genesis of mare basalts, KREEP, and sea floor basalts, *Geochim. Cosmochim. Acta, 42*, 859-869, 1978.

McKay, G. A., Crystal/liquid partitioning of REE in basaltic systems: Extreme fractionation of REE in olivine, *Geochim. Cosmochim. Acta, 50*, 69-79, 1986.

McKay, G. A., and D. F. Weill, KREEP petrogenesis revisited, *Proc. 8th Lunar Sci. Conf.*, 2339-2355, 1977.

McKenzie, D., The extraction of magma from the crust and mantle, *Earth Planet. Sci. Lett., 74,* 81-91, 1985.

McKenzie, D., Some remarks on the movement of small fraction melts in the mantle, *Earth Planet. Sci. Lett., 95,* 53-72, 1989.

McKenzie, D., and M. J. Bickle, The volume and composition of melt generated by extension of the lithosphere, *J. Petrol., 29,* 625-679, 1988.

Meijer, A., Primitive arc volcanism and a boninite series: examples from western Pacific island arcs, in *The Tectonic and Geologic Evolution of Southeast Asian Seas and Islands*, edited by D. E. Hayes, pp. 269-282, Amer. Geophys. Union Monogr. 23, Washington, D. C., 1980.

Miyashiro, A., F. Shido, and M. Ewing, Crystallization and differentiation in abyssal tholeiite and gabbros from mid-ocean ridges, *Earth Planet. Sci. Lett., 7,* 361-365, 1970.

Nicholls, I. A., and K. L. Harris, Experimental rare earth element partition coefficients for garnet, clinopyroxene, and amphibole coexisting with andesitic and baslatic liquids, *Geochim. Cosmochim. Acta, 44,* 287-308, 1980.

Pearce, J. A., The role of sub-continental lithosphere in magma genesis at destructive plate margins, in Continental Basalts and Mantle Xenoliths, edited by C. J. Hawkesworth and M. J. Norry, pp. 230-249, Shiva Press, London, 1983.

Roedder, E., *Fluid Inclusions*, Min. Soc. Amer., Reviews in Mineralogy, v. 12, 644 p., 1984.

Roeder, P. L. and R. F. Emslie, Olivine-liquid equilibrium, *Contrib. Mineral. Petrol., 29,* 275-289, 1970.

Salters, V. J. M., and N. Shimizu, World-wide occurrence of HFSE-depleted mantle, *Geochim. Cosmochim. Acta, 52*, 2177-2182, 1988.

Sharaskin, A. Ya., I. K. Pustchin, S. K. Zlobin, and G. M. Kolesov, Two ophiolite sequences from the basement of the Northern Tonga Arc, *Ofioliti, 8,* 411-430, 1983.

Shaw, D. M., Trace element fractionation during anatexis, *Geochim. Cosmochim. Acta, 34*, 237-243, 1970.

Shimizu, N., and I. Kushiro, The partitioning of rare earth elements between garnet and liquid at high pressures: Preliminary experiments, *Geophys. Res. Lett., 2*, 413-416, 1975.

Sobolev, A. V., and L. V. Dmitriev, Primary melts of tholeiites of oceanic rifts (TOR): Evidence from studies of primitive glasses and melt inclusions in minerals, Abstracts, International Geological Congress, v. 3, 147-148, Washington, D.C., 1989.

Sobolev, A. V. and V. B. Naumov, First direct proof of the presence of water in ultramafic melts and their estimated water content, *Geochem. International*, 102-105, 1985.

Sobolev, A. V., L. V. Dmitriev, V. L. Barsukov, V. N. Nevsorov, and A. B. Slutsky, The formation conditions of high-magnesium olivines from the monomineralic fraction of Luna 24 regolith, *Proc. 11th Lunar Planet. Sci. Conf.*, 105-116, 1980.

Stolper, E., A phase diagram for mid-ocean ridge basalts: Preliminary results and implications for petrogenesis, *Contrib. Mineral. Petrol., 74,* 13-27, 1980.

Stosch, H.-G., Rare earth element partitioning between minerals from anhydrous spinel peridotite xenoliths, *Geochim. Cosmochim. Acta, 46*, 793-811, 1982.

Sun, S.-S., Lead isotopic study of young volcanic rocks from mid-ocean ridges, ocean islands, and island arcs, *Phil. Trans. R. Soc. Lond., A297,* 409-445, 1980.

Takahashi, E., and I. Kushiro, Melting of a dry peridotite at high pressures and basalt magma genesis, *Am. Mineral., 68*, 859-879, 1983.

Thompson, R. N., M. A. Morrison, G. L. Hendry, and S. J. Parry, An assessment of the relative roles of crust and mantle in magma genesis: an elemental approach, *Phil. Trans. R. Soc. Lond., A310,* 549-590, 1984.

Tormey, D. R., T. L. Grove, and W. B. Bryan, Experimental petrology of normal MORB near the Kane Fracture Zone: 22°-25°N, Mid-Atlantic Ridge, *Contrib. Mineral. Petrol., 96*, 121-139, 1987.

Uhlmann, A kinetic treatment of glass formation, *J. Non-Crystalline Solids, 7,* 337-348, 1972.

Walker, D., T. Shibata, and S. E. Delong, Abyssal tholeiites from the Oceanographer Fracture Zone II. Phase equilibria and mixing, *Contrib. Mineral. Petrol., 70,* 111-125, 1979.

Walker, D. A., and W. E. Cameron, Boninite primary magmas: Evidence from the Cape Vogel Peninsula, PNG, *Contrib. Mineral. Petrol., 83,* 150-158, 1983.

Watson, E. B., Glass inclusions as samples of early magmatic liquid: determinative method and application to a South Atlantic basalt, *J. Volcanol. Geotherm. Res., 1,* 73-84, 1976.

Weill, D. F., and G. A. McKay, The partitioning of Mg, Fe, Sr, Ce, Sm, Eu, and Yb in lunar igneous systems and a possible origin of KREEP by equilibrium partial melting, *Proc. 6th Lunar Sci. Conf.*, 1143-1158, 1975.

Yonover, R., Petrological effects of rift failure at the Galapagos Spreading Center near 95.5°W including analyses of glass inclusions by laser mass spectrometry and ion microprobe, PhD thesis, 193 pp., Univ. of Hawaii, May 1989.

CHAPTER 5. TEMPORAL AND SPATIAL VARIATIONS IN CHEMICAL COMPOSITIONS OF PERIDOTITES AND BASALTS FROM THE ATLANTIS II FRACTURE ZONE

CHAPTER 5. TEMPORAL AND SPATIAL VARIATIONS IN CHEMICAL COMPOSITIONS OF PERIDOTITES AND BASALTS FROM THE ATLANTIS II FRACTURE ZONE

INTRODUCTION

Geochemical and geophysical variability along the mid-ocean ridge system has been widely described over the past seventeen years or more. Long wavelength isotopic and chemical variations have been observed in ridge basalts [*Hart et al.*, 1973; *Schilling et al.*, 1983; *Dick et al.*, 1984; *Klein and Langmuir*, 1987], and in abyssal peridotites [*Dick et al.*, 1984; *Michael and Bonatti*, 1985; *Johnson et al.*, 1990]. More recently, the widespread use of multi-narrow beam swath mapping has enabled scientists to see the ridge in much finer detail than was previously possible. This has resulted in the description of new morphologic features along the ridge system, including several orders of non-transform ridge offsets [*Macdonald et al.*, 1984; 1988], that have been shown to represent, along with the more well-known large offset oceanic transform faults, the boundaries of shorter wavelength variability or segmentation of the ocean ridge . These mapping techniques have also enabled the planning and implementation of close-spaced dredging programs that have demonstrated petrologic and geochemical segmentation accompanying the subtle morphologic features [*Langmuir et al.*, 1986; *Batiza et al.*, 1988; *Sinton et al.*, 1990 in preparation].

In some cases, the chemical diversity within individual tectonically or morphologically defined spreading cells is large. Upon closer inspection, it has been revealed that small ridge discontinuities are often boundaries between distinct magmatic units [*Whitehead et al.*, 1984; *Langmuir et al.*, 1986; *Batiza et al.*, 1988]. This implies that boundaries of magmatic cells may impose subtle morphologic signatures to the accreting seafloor, and that tectonic boundaries may impose physical, mechanical, and thermal boundaries to adjacent magmatic centers. The possible effects of tectonic boundaries, such as transform faults, on the chemical evolution and volumes of magmas erupted near them have been

discussed in detail [*Fox and Gallo*, 1984; *Langmuir and Bender*, 1984; *Bender et al.*, 1984], as have the effects of adjacent, multiple magmatic injection centers on the accreting ridge morphology [*Schouten and White*, 1980; *Schouten and Klitgord*, 1982; *Whitehead et al.*, 1984; *Schouten et al.*, 1985; *Langmuir et al.*, 1986; *Macdonald et al.*, 1988]. However, because of the relative scarcity of sufficient quantities of dredged peridotites from a single, well-sampled locale, extrapolation of existing segmentation models to mantle depths has been necessarily speculative.

Spatial and temporal episodicity in seafloor spreading is manifested in different ways. In a study of the Mid-Atlantic Ridge and Kane Fracture Zone, *Pockalny et al.* [1988] interpreted a series of evenly spaced, elongated constructional features running parallel to the ridge as resulting from temporal and spatial oscillations in the magma supply rate. *Karson et al.* [1987] mapped, in detail, an along-axis segment of the slow-spreading Mid-Atlantic Ridge and found evidence for abundant volcanic activity accomodating extension in certain sections of the axis, while in adjacent sections evidence for tectonic extension was observed. Regions of attenuated seismic S-wave arrivals, zones of noticeable absence of microseismicity, and the occurrence of hydrothermal vent fields on the seafloor provide additional evidence for both spatial and temporal variation in magmatism under the Mid-Atlantic Ridge [*Kong*, 1990]. Further support for temporal variations in magmatic supply comes from theoretical work by *Scott and Stevenson* [1989] which shows that a transition from steady-state to episodic crustal formation occurs as the spreading velocity is reduced. In contrast to the predicted episodic nature of magmatism at slow-spreading ridges, along- and off-axis variations in magma supply rate at fast-spreading ridges are less pronounced, as inferred by morphological [*Macdonald et al.*, 1984] and theoretical studies [*Scott and Stevenson* , 1989]. Thus, at slow- and very slow-spreading ridges, one would expect many different, but perhaps fundamentally related, manifestations of episodic magmatism or melting.

In this study, I have analyzed peridotites and basalts dredged from the Atlantis II Fracture Zone, Southwest Indian Ridge on cruise 27-9 of the R/V *Robert Conrad.* These samples are from the western and eastern walls of the transform domain of the fracture zone, the ridge transform intersection inside corner highs, the northern and southern neovolcanic zones of the ridges entering the transform, the rift mountains abutting the northern, non-transform fracture zone trace, and the median tectonic ridge of the transform fault. The objectives of the study are threefold: 1) to describe spatial (and by inference, temporal) variability of the peridotite and basalt compositions along a single transform fault system far from the influence of a hotspot, 2) to compare the long wavelength chemical variations in oceanic peridotite compositions described in Chapter 2 [*Johnson et al.*, 1990] with any variations observed in the Atlantis II Fracture Zone, and 3) to discuss the implications of the results and their impact on current models of ridge segmentation and petrogenesis.

TECTONIC SETTING OF ATLANTIS II FRACTURE ZONE

A detailed description of the tectonic setting and physiography of the fracture zone and the Southwest Indian Ridge in this region is given in *Dick et al.* [1990]. In the following paragraphs, I will describe only the elements that have immediate relevance to the present study.

The Southwest Indian Ridge forms one of the legs of the ridge-ridge-ridge Indian Ocean triple junction. Since 80 Ma, the triple junction has been migrating rapidly to the east, with extension of the Southwest Indian Ridge forming a series of new ridge segments and numerous, relatively long (100-250 km) fracture zones. Because of the characteristically very slow spreading rates along the Southwest Indian Ridge, the seafloor topography is much rougher than that associated with the faster spreading Central and Southeast Indian Ridges [*Tapscott et al.*, 1980; *Sclater et al.*, 1981; *Fisher and Sclater*, 1983]. The spreading rates along the Southwest Indian Ridge are in the range 1.5-1.6

cm/yr (full rate) [*Sclater et al.*, 1976; *Sclater et al.*, 1981; *Fisher and Sclater*, 1983]. Spreading at ridge segments adjoining the Atlantis II Fracture Zone, calculated using the inferred marine paleomagnetic anomalies adjacent to the transform, has been episodic and asymmetric over the duration of identifiable anomalies. The Atlantis II Fracture Zone is a 210 km left lateral offset formed during ridge extension at about 58 (±2) Ma [*Patriat et al.*, 1986]. The spreading rate measured from anomalies east and west of the transform is ~1 cm/yr (half rate). The spreading rate on the eastern wall of the transform determined by magnetic anomaly lineations has been confirmed by a zircon age determination of 11.2 my at ODP site 735B [H. Dick, personal communication from Mattinson, 1989]. Thus, the calculated total spreading rate of 1.6 cm/yr in this region [*Tapscott et al.*, 1980] requires asymmetric spreading at the eastern and western ridges, with rates of 0.6 cm/yr on the plates spreading away from the transform and means that the Atlantis II Fracture Zone is growing at a rate of 0.4 cm/yr with a slip rate of 1.6 cm/yr and an age offset of 21-22 million years (Figure 1).

Based on the small proportion of gabbro in dredge recovery statistics for fracture zones along the Southwest Indian Ridge, *Dick* [1989] inferred that crustal thicknesses at very slow-spreading ridges are lower than those at medium- and fast-spreading ridges. Furthermore, *Dick et al.* [1990] state that high sodium and titanium contents in basalts from the Atlantis II Fracture Zone, and inferred similarities with the very slow-spreading Arctic Ridge reinforce their view that crustal thicknesses here are no more than 4 km. It should be pointed out, however, that the proportion of gabbros recovered in the Atlantis II Fracture Zone is higher than in other transform faults along the Southwest Indian Ridge [*Dick et al.*, 1990] implying that magma production rates and crustal thickness, at least locally, may be greater than they estimate for the Southwest Indian Ridge in general.

A bathymetric map of the Atlantis II Fracture Zone from Seabeam data collected on the R/V *Robert Conrad* is shown in Figure 2. The transform has nearly 6000 meters of relief in one location, but typically about 4500 meters of relief is observed. Transform walls are

Spreading Geometry of the Atlantis II Fracture Zone

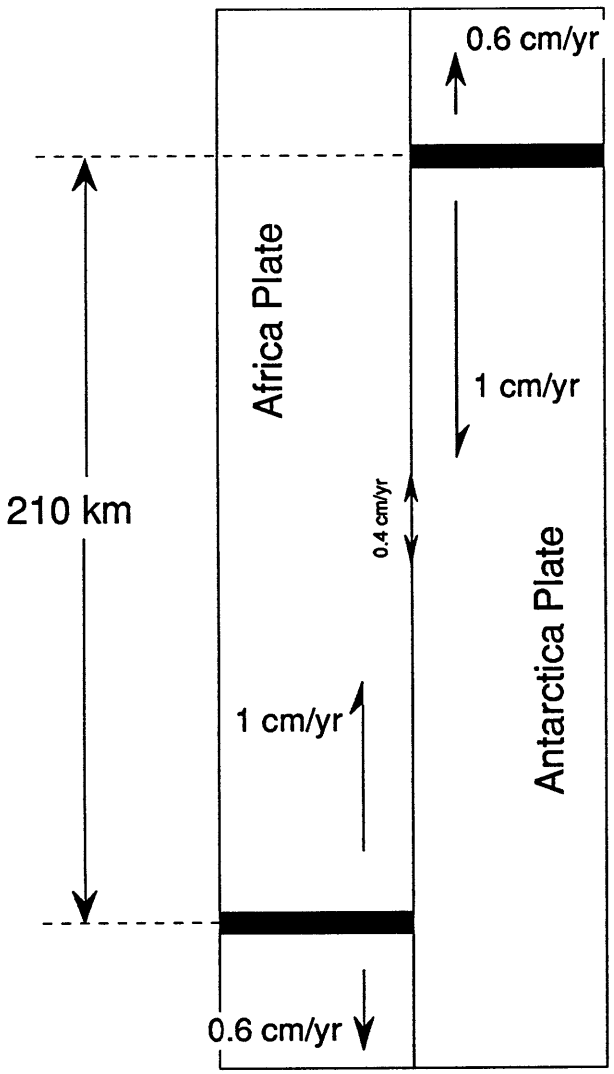

Figure 1. Cartoon depicting the spreading and slip vectors for the Atlantis II Fracture Zone-ridge system.

Figure 2. Bathymetric map of the Atlantis II Fracture Zone from gridded Sea Beam data collected on the R/V *Robert Conrad*. Dredge locations are shown.

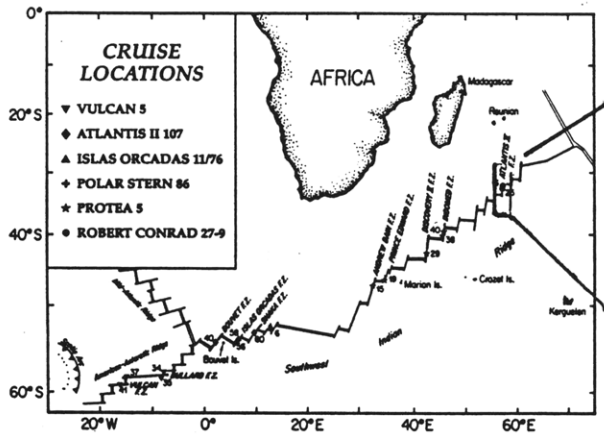
CRUISE LOCATIONS
VULCAN 5
ATLANTIS II 107
ISLAS ORCADAS 11/76
POLAR STERN 86
PROTEA 5
ROBERT CONRAD 27-9
AFRICA
Madagascar
Réunion
Marion Is.
Crozet Is.
Bouvet Is.
Kerguelen
Southwest
Indian
0°
20°S
40°S
60°S
20°W
0°
20°E
40°E
60°E

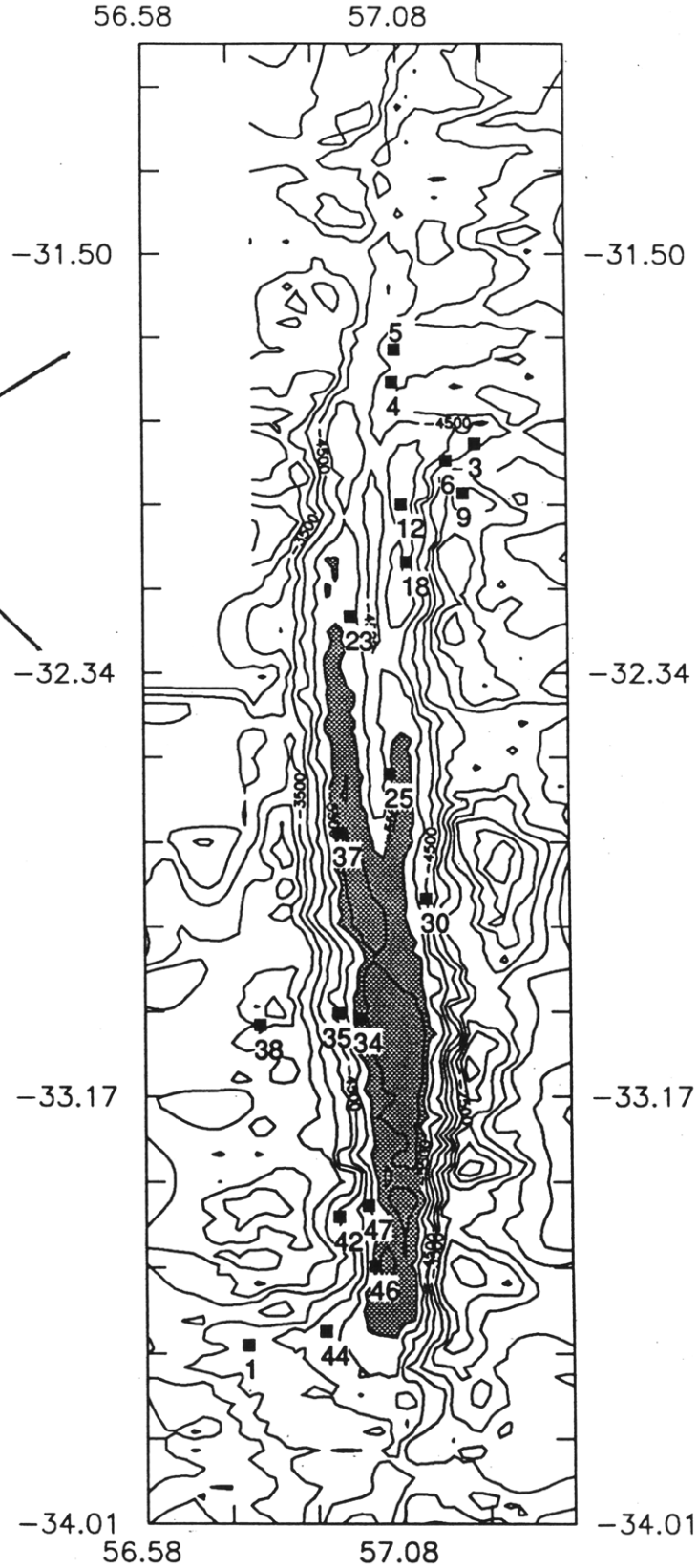
56.58
57.08
-31.50
-32.34
-33.17
-34.01
-4500
-3500
5
4
3
6
9
12
18
23
25
37
30
35
34
38
42
47
46
44
1

extremely steep on both sides, but the eastern wall is generally steeper and higher than the west wall. Slopes on the eastern wall range from 11° to 32°, with an average of 23°, while slopes on the western wall are from 11° to 24°, with an average of about 19°. Nodal basins at both the southern and the northern ridge-transform intersections are the two deepest points in the surveyed area. Crust spreading away from the neovolcanic zone axes toward the transform is uplifted to form steep inside corner walls, while crust spreading away in the opposite directions is uplifted into relatively lower rift mountains. The center of the northern part of the transform is occupied by a 1.5 km high median tectonic ridge. Separating the median ridge from the western transform wall is an elongate depression inferred to be a fossil segment of old transform crust captured by the African Plate due to a spreading direction change [*Dick et al.*, 1990]. This depression joins and becomes the active transform in the southern part of the fracture zone. The inactive trace of the fracture zone to the north strikes approximately N10°E, compared to a nearly due N-S strike of the active transform fault.

SAMPLES AND ANALYTICAL TECHNIQUES

Peridotites

Of 24 dredges in the transform zone, approximately 43% were peridotites [*Dick et al.*, 1990]. They are typical of dredged oceanic residual peridotites from other locations and include protogranular, porphyroclastic, and mylonitic varieties. Protogranular textured peridotites were preferred for analysis because they were inferred to be relatively unaffected by ductile or brittle deformation, compared to the porphyroclastic or mylonitic textured peridotites. The peridotites are extensively altered, from 50% to 100%, by replacement of olivine, orthopyroxene, and clinopyroxene with serpentine or clay minerals. Samples were chosen based on low relative alteration, especially of clinopyroxene. Mineral modal abundances are plotted in Figure 3, for all studied samples, and for dredge averages. Major element compositions of all phases present in a sample were analyzed by electron

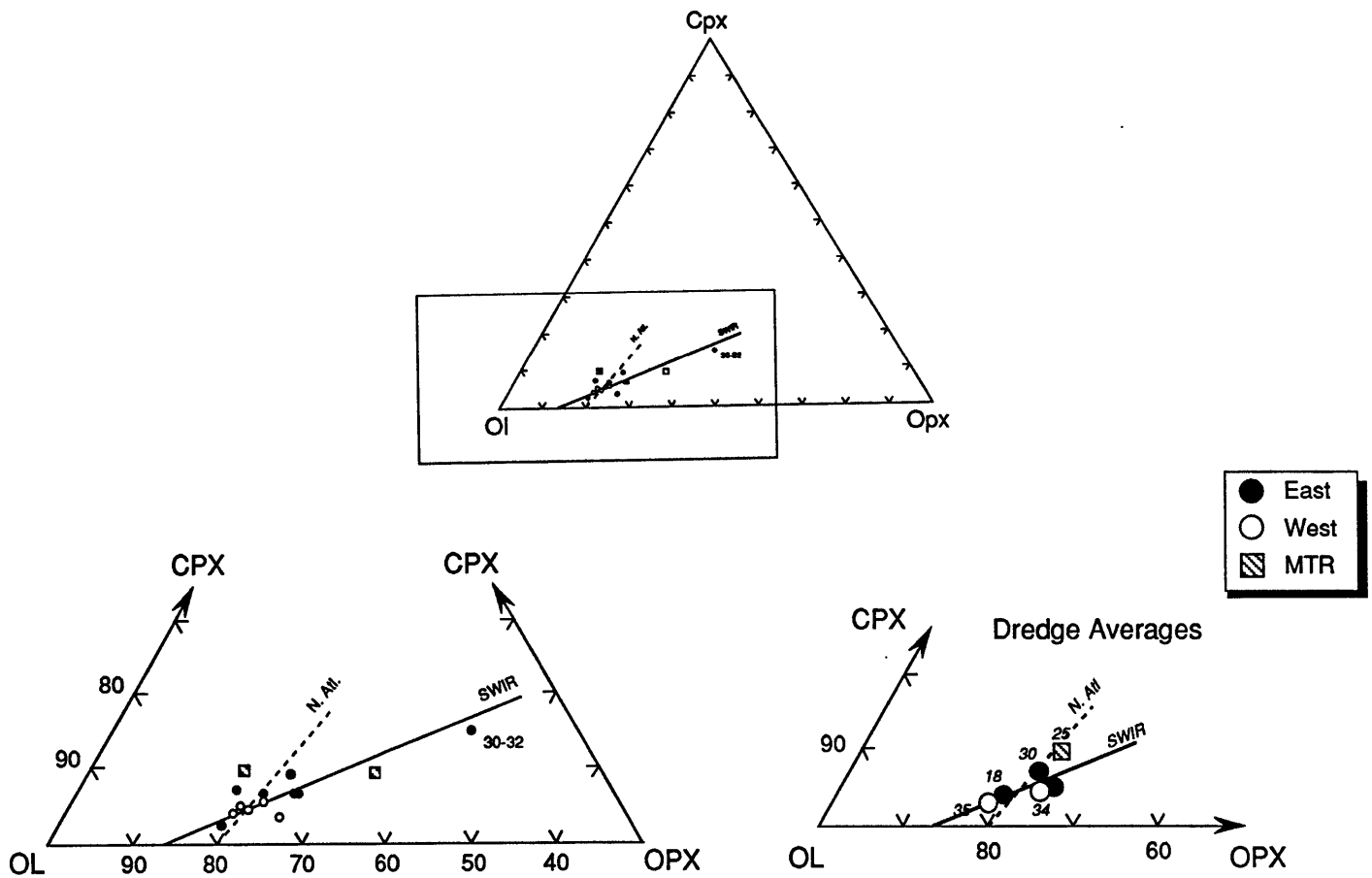

Figure 3. Mineral modes for all samples in this study, and for dredge averages. Also plotted are modal trends for the Southwest Indian Ridge and the North Atlantic, from Dick et al. [1984].

microprobe and are reported in Table 1, and rare earth and other trace element concentrations in clinopyroxenes were analyzed by the ion microprobe following the techniques described in Chapter 2 [*Johnson et al.*, 1990], and are reported in Table 2. A detailed discussion of accuracy and precision of the clinopyroxene analyses is given by *Johnson et al.* [1990], but are approximately ≤±20% for the light REE, ±10-15% for the heavy REE, Sr, and Zr, and ±2-5% for Sc, Ti, V, and Cr.

Basalts

The basalts analyzed in this study are exclusively dredged glasses from the rims of aphyric, plagioclase-phyric, and olivine-phyric pillow basalts, in order of abundance. Major element analyses of the glass chips were done on the electron microprobe at University of Capetown. Rare earth element analyses of some of the glasses were done on the ion microprobe at M.I.T. Rare earth element working curves for basalt glasses were calculated using accurately analyzed basaltic glasses (glasses provided courtesy of John Bender) and energy filtering of -50 Kev and a ±15 volt energy window. The ion probe analytical technique for the glasses is described in detail in Chapter 4. Major and rare earth element analyses for the glasses are presented in Table 3. The accuracy and precision of the rare earth element absolute concentrations is generally ≤15%, but Eu is poorly determined (see Chapter 3). The data were critically analyzed to eliminate any obviously inconsistent analyses for replicate analyses of a given sample, but reanalysis of the glasses is recommended to clarify data inconsistencies in some glass samples between two operators on different occasions. The reported analyses are believed to represent accuracy of ≤±30% for absolute concentrations, but pattern shapes are believed to be accurate and thus ratios of rare earth elements in a given sample are believed to be accurate to ±10%. Dredge locations, depths, and inferred ages are presented in Table 4. Complete dredge recovery statistics are given by *Dick et al.* [1990].

TABLE 1. Electron Microprobe Analyses of Atlantis II Fracture Zone peridotite mineral phases†

Sample	SiO_2	TiO_2	Al_2O_3	FeO	MnO	MgO	CaO	Na_2O	NiO	Cr_2O_3	Total	Ca	Mg	Fe	Mg#	Cr#	MODES ol	opx	cpx	sp
										CLINOPYROXENES										
6-3	51.19	0.22	5.51	2.38	0.00	16.17	22.89	0.412		0.86	99.62	0.485	0.476	0.039	0.923	0.095	67.1	25.6	6.62	0.64
6-3	52.01	0.18	4.41	2.41	0.10	16.38	22.96	0.264		0.79	99.50	0.482	0.479	0.040	0.923	0.107	67.1	25.6	6.62	0.64
6-8	50.30	0.24	6.95	2.67	0.08	14.97	23.20	0.460		1.11	99.98	0.503	0.452	0.045	0.909	0.097	66.6	25.8	6.61	0.8
6-8	50.96	0.27	6.33	2.57	0.08	15.39	23.02	0.398		1.04	100.05	0.496	0.461	0.043	0.914	0.099	66.6	25.8	6.61	0.8
18-23	51.53	0.30	5.66	2.62	0.07	16.35	21.59	0.561		0.97	99.65	0.466	0.490	0.044	0.918	0.103	73.4	18.6	7.18	0.86
18-23	50.43	0.30	7.24	2.58	0.09	15.11	21.74	0.681		1.09	99.26	0.486	0.470	0.044	0.913	0.092	73.4	18.6	7.18	0.86
18-45	51.27	0.31	6.51	2.32	0.07	15.76	21.90	0.600		1.11	99.85	0.480	0.481	0.039	0.924	0.102	77.9	19.4	2.25	0.43
23-1	51.52	0.37	5.29	2.41	0.10	16.30	21.55	0.468		1.16	99.17	0.467	0.492	0.041	0.923	0.128				
25-138	51.16	0.29	6.51	2.65	0.08	15.37	22.10	0.792		0.95	99.90	0.485	0.469	0.045	0.911	0.089	71.08	18.3	9.5	1.13
25-138	51.29	0.39	6.60	2.40	0.05	15.21	22.27	0.822		1.06	100.09	0.491	0.467	0.041	0.918	0.097	71.08	18.3	9.5	1.13
25-138	51.07	0.35	6.64	2.44	0.10	15.31	22.36	0.783		1.03	100.08	0.491	0.468	0.041	0.918	0.095	71.08	18.3	9.5	1.13
25-142	51.95	0.32	5.73	2.56	0.09	16.59	20.44	0.728		0.88	99.29	0.449	0.507	0.044	0.920	0.094	56.1	33.5	8.99	1.46
30-32	51.15	0.28	6.54	2.41	0.10	15.64	22.61	0.694		1.28	100.71	0.489	0.471	0.040	0.920	0.116	42.5	42.1	15.09	0.46
30-33	50.50	0.28	6.85	2.54	0.10	15.39	22.32	0.564		1.14	99.69	0.489	0.468	0.043	0.915	0.101	71.03	21.99	6.31	0.47
30-40	50.53	0.30	6.79	2.45	0.09	14.81	23.09	0.557		1.22	99.84	0.506	0.452	0.042	0.915	0.108	66.3	23.7	9.22	0.75
30-40	50.80	0.27	6.71	2.45	0.10	15.06	23.11	0.534		1.25	100.29	0.502	0.456	0.042	0.916	0.111	66.3	23.7	9.22	0.75
34-58	50.76	0.10	5.25	2.58	0.11	16.36	23.00	0.114		1.22	99.49	0.481	0.477	0.042	0.919	0.134	70.94	25.37	3.31	0.37
34-63	51.38	0.14	4.85	2.67	0.11	16.50	22.80	0.208		1.25	99.92	0.477	0.480	0.043	0.917	0.148	71.06	22.72	5.51	0.71
35-49	50.95	0.07	5.06	2.67	0.10	17.07	21.66	0.071		1.32	98.98	0.456	0.500	0.044	0.919	0.149	75.96	19.53	4.05	0.45
35-49	49.66	0.08	5.40	2.49	0.10	16.15	21.40	0.130		1.40	96.81	0.467	0.491	0.043	0.920	0.148	75.96	19.53	4.05	0.45
35-80	48.90	0.09	5.36	2.24	0.10	15.77	21.49	0.131		1.25	95.33	0.476	0.486	0.039	0.926	0.136	74.52	20.28	5.01	0.19
35-80	49.05	0.10	5.34	2.31	0.08	16.03	20.93	0.138		1.25	95.23	0.465	0.495	0.040	0.925	0.135	74.52	20.28	5.01	0.19
44-1	50.21	0.18	6.64	2.72	0.12	15.52	22.50	0.389		1.32	99.60	0.487	0.467	0.046	0.910	0.118	73.56	21.33	4.64	0.47
46-1	50.54	0.22	6.60	2.60	0.11	15.51	22.70	0.517		1.20	99.99	0.490	0.466	0.044	0.914	0.109				
46-2	50.75	0.25	5.92	2.38	0.11	15.66	23.04	0.529		1.32	99.96	0.494	0.467	0.039	0.922	0.130				

TABLE 1. continued

Sample	SiO_2	TiO_2	Al_2O_3	FeO	MnO	MgO	CaO	Na_2O	NiO	Cr_2O_3	Total	Ca	Mg	Fe	Mg#	Cr#	MODES ol	opx	cpx	sp
ORTHOPYROXENES																				
6-8	54.57	0.085	5.50	6.42	0.15	33.03	1.11	0.016		0.70	101.58	0.022	0.882	0.096	0.901	0.078	66.6	25.8	6.61	0.8
18-23	53.14	0.078	6.11	6.49	0.15	32.98	0.41	0.000		0.76	100.12	0.008	0.894	0.098	0.901	0.077	73.4	18.6	7.18	0.86
18-45	54.96	0.077	4.71	6.23	0.15	34.02	0.57	0.000		0.57	101.29	0.011	0.897	0.092	0.907	0.075	77.9	19.4	2.25	0.43
23-1	54.02	0.105	5.56	6.27	0.15	32.20	0.78	0.000		0.93	100.01	0.016	0.888	0.096	0.902	0.101				
23-1	54.61	0.059	5.47	6.23	0.14	33.48	0.70	0.000		0.80	101.49	0.014	0.894	0.092	0.905	0.089				
25-138	54.28	0.095	5.62	6.27	0.13	32.62	1.22	0.057		0.63	100.93	0.023	0.882	0.095	0.902	0.070	71.08	18.3	9.5	1.13
25-142	53.77	0.097	5.29	6.23	0.14	32.77	1.06	0.041		0.64	100.05	0.021	0.885	0.094	0.904	0.075	56.1	33.5	8.99	1.46
30-32	53.62	0.078	5.27	5.73	0.13	32.97	0.90	0.012		0.86	99.56	0.018	0.896	0.09	0.911	0.099	42.5	42.1	15.09	0.46
30-33	53.40	0.067	5.42	6.08	0.14	32.99	0.66	0.018		0.68	99.47	0.013	0.895	0.092	0.906	0.078	71.03	21.99	6.31	0.47
34-58	53.97	0.040	4.22	5.97	0.17	32.86	1.34	0.008		0.82	99.38	0.026	0.884	0.090	0.907	0.116	70.94	25.37	3.31	0.37
34-63	53.97	0.060	4.42	5.80	0.14	32.27	2.15	0.024		0.97	99.81	0.042	0.871	0.087	0.908	0.129	71.06	22.72	5.51	0.71
35-49	54.34	0.031	4.43	5.76	0.16	32.90	1.52	0.000		0.98	100.12	0.030	0.884	0.086	0.911	0.130	75.96	19.53	4.05	0.45
46-1	54.04	0.061	4.74	6.28	0.14	33.10	0.76	0.024		0.67	99.82	0.015	0.890	0.095	0.904	0.087				
46-2	53.93	0.062	4.99	6.13	0.12	32.88	0.79	0.012		0.86	99.77	0.015	0.891	0.094	0.905	0.103				
OLIVINES																				
6-8	41.10	0.000	0.005	9.55	0.10	50.03	0.03		0.35	0.021	101.18	0.000	0.903	0.097	0.903	0.738	66.6	25.8	6.61	0.8
18-45	40.75	0.042	0.082	9.75	0.11	49.42	0.004		0.36	0.097	100.62	0.000	0.900	0.100	0.900	0.442	77.9	19.4	2.25	0.43
46-1	40.01	0.026	0.011	9.80	0.15	48.90	0.026		0.44	0.051	99.42	0.000	0.899	0.101	0.899	0.757				
46-2	40.49	0.019	0.025	9.48	0.15	49.02	0.056		0.38	0.055	99.67	0.000	0.902	0.097	0.902	0.596				
SPINELS																				
6-8	0.00	0.055	52.40	12.61	0.12	19.27	0.01		0.37	15.54	100.38				0.731	0.166	66.6	25.8	6.61	0.8
18-45	0.72	0.031	54.07	12.42	0.16	18.73	0.01		0.35	13.70	100.20				0.729	0.150	77.9	19.4	2.25	0.43
23-1	0.81	0.082	52.07	11.78	0.16	18.84	0.01		0.36	17.05	101.16				0.740	0.180				
25-138	0.00	0.047	53.99	11.74	0.13	19.44	0.02		0.38	14.19	99.93				0.747	0.150	71.08	18.3	9.5	1.13
25-142	0.72	0.038	54.02	11.24	0.15	19.43	0.01		0.38	14.95	100.95				0.755	0.157	56.1	33.5	8.99	1.46
30-33	0.33	0.000	53.69	12.42	0.13	18.86	0.01		0.34	13.82	99.60				0.730	0.147	71.03	21.99	6.31	0.47
34-58	0.36	0.000	46.00	14.47	0.18	16.98	0.03		0.27	20.90	99.19				0.677	0.234	70.94	25.37	3.31	0.37
34-63	0.35	0.022	43.65	15.02	0.18	16.62	0.02		0.27	22.39	98.52				0.664	0.256	71.06	22.72	5.51	0.71
44-1	0.17	0.029	48.99	12.21	0.16	18.32	0.00		0.30	18.72	98.90				0.728	0.204	73.56	21.33	4.64	0.47

† - each reported analysis is the average of 3-6 points on a given mineral grain.

TABLE 2. Trace element concentrations in peridotite clinopyroxenes† (ppm)

Sample	Sc	Ti	V	Cr	Sr	Zr	Ti/Zr	Ce	Nd	Sm	Eu	Dy	Er	Yb
6-3	58	1639	317	6987	1.25	1.95	842	0.023	0.36	0.52	0.31	1.87	1.17	
6-3	55	1572	329	6402	0.93	1.63	963	0.052	0.50	0.57	0.34	1.88	1.07	0.82
6-3	43	1435	304	7617	0.64	1.25	1151							
6-3	52	1685	341	8018	0.78	1.61	1050	0.036	0.55	0.76	0.35	2.03	1.29	1.25
6-3	57	1565	301	7371	0.97	2.02	775							
6-3	59	1334	265	6224	0.90	1.43	933	0.036	0.40	0.44	0.30	1.00	1.18	1.14
6-3	61	1447	278	6742	2.72	4.97	291	0.052	0.55	0.58	0.36	1.40	1.46	1.49
6-8	62	2283	411	7708	0.93	1.71	1335	0.037	0.60	0.96	0.42	3.25	2.09	2.12
6-8	46	1625	337	7421	0.53	1.47	1105							
6-8	52	1802	361	6919	0.58	1.63	1105	0.029	0.65	0.79	0.40	2.64	1.77	1.70
6-8	42	1503	322	6964	0.47	1.78	844	0.016	0.46	0.55	0.33	2.10	1.31	1.41
6-8	47	1652	323	6722	0.60	1.35	1223							
6-8	42	1746	320	7017	0.50	1.77	986							
6-8	38	1531	320	6985	0.62	2.30	666							
6-8	43	1476	309	5937	0.46	1.69	873							
18-23	61	2134	350	5731	0.94	2.58	827	0.084	0.82	0.89	0.44	2.32	1.47	1.42
18-23	51	1617	303	6088	1.07	2.42	668	0.04	0.67	0.71	0.34	2.11	1.18	1.35
18-45	68	1959	357	4495	1.12	2.73	718							
18-45	60	1702	320	5279	0.95	2.26	753	0.038	0.50	0.59	0.30	2.00	1.16	1.28
18-45	53	1401	325	4918	0.93	1.98	708							
18-45	37	1517	291	5638	0.82	1.95	778							
18-45	44	1951	337	7610	0.85	2.37	823							
18-45	58	2210	335	5765	1.14	3.22	686	0.064	0.74	0.84	0.37	2.36	1.41	1.44
23-1		1657		7898	1.01	2.98	556	0.35	0.72	0.72	0.42	2.00	1.21	1.37
23-1		1876		9641	2.55	3.82	491	0.078	0.77	0.77	0.37	2.23	1.40	1.42
23-1		2141		8204	0.94	4.94	433	0.117	1.09	1.02	0.44	2.96	1.96	1.80
25-138								0.139	0.97	0.91	0.41	2.23	1.37	1.36
25-138								0.133	0.96	0.92	0.40	2.24	1.26	1.34
25-138								0.125	0.99	0.91	0.41	2.22	1.34	1.44
25-138								0.102	0.99	0.77	0.38	1.97	1.18	1.24
25-142	43	1871	310	7570	1.00	3.40	550	0.12	1.12	1.01	0.52	2.53	1.58	1.70
25-142	41	1973	325	7179	1.10	3.30	598	0.094	0.81	0.94	0.47	2.39	1.48	1.60
25-142	37	1813	297	7133	0.70	3.10	585	0.109	0.89	0.88	0.44	2.44	1.57	1.63
25-142	41	1770	302	6064	0.90	2.70	656	0.125	0.93	1.13	0.47	2.30	1.43	1.58
25-142	38	2012	326	8334	2.60	3.40	592	0.125	0.94	0.99	0.55	2.67	1.68	1.87
25-142	29	1621	289	7723	0.80	2.90	559	0.066	0.75	0.6	0.37	2.04	1.27	1.42

TABLE 2. continued

Sample	Sc	Ti	V	Cr	Sr	Zr	Ti/Zr	Ce	Nd	Sm	Eu	Dy	Er	Yb
30-32		1599		8681	3.54	4.18	382	0.166	1.03	0.84	0.41	2.01	1.33	1.20
30-32		1170		8072	2.88	2.99	392	0.237	1.15	0.97	0.45	2.23	1.51	1.46
30-32		1301		9267	3.00	3.67	355	0.197	0.94	0.81	0.39	2.26	1.31	1.21
30-33		1605		6896	2.80	2.85	563							
30-33		1703		7134	1.57	3.20	532							
30-40		1536		7641	1.75	2.48	620	0.097	0.73	0.72	0.38	2.11	1.43	1.20
30-40		1067		7099	1.07	1.73	615	0.077	0.91	0.76	0.40	2.26	1.35	1.28
30-40		2638		8049	1.06	4.97	531	0.139	1.28	1.23	0.52	3.49	2.31	2.28
34-58		500		7829	0.44	0.31	1601	0.015	0.030	0.13	0.070	0.77	0.56	0.61
34-58		513		9427	0.46	0.11	4635	0.013	0.048	0.13	0.065	0.91	0.69	0.66
34-58		598		8814	0.43	0.17	3439	0.018	0.052	0.12	0.058	0.90	0.58	0.64
34-63		613		8719	0.35	0.31	1955	0.01	0.077	0.18	0.088	1.24	0.79	0.85
34-63		761		8824	0.84	0.43	1762	0.016	0.062	0.12	0.079	0.86	0.55	0.59
35-49		615		7790	0.52	0.22	2737	0.019	0.103	0.15	0.088	1.29	0.81	1.03
35-49		598		8721	0.87	0.31	1907	0.014	0.081	0.12	0.063	0.88	0.62	0.61
35-49		602		8841	0.53	0.22	2739							
35-49		578		9082	0.45	0.17	3469	0.012	0.029	0.12	0.077	0.80	0.56	0.60
35-80		495		8705	0.36	0.13	3871	0.014	0.054	0.09	0.072	1.04	0.75	0.68
35-80		606		9681	0.85	0.21	2898	0.011	0.046	0.11	0.060	0.80	0.58	0.63
35-80		614		8637	1.09	0.15	3984	0.017	0.052	0.13	0.068	0.95	0.58	0.66
44-1		1025		8555	3.10	0.56	1840	0.035	0.17	0.28	0.16	1.50	0.88	0.90
44-1		1049		8782	1.54	0.40	2606	0.023	0.16	0.34	0.16	1.65	0.98	1.01
44-1		713		9096	4.02	0.30	2371							
46-1		1697		7919	0.85	1.63	1040	0.026	0.42	0.68	0.30	2.17	1.31	1.40
46-1		1441		7532	0.58	1.14	1263							
46-1		1426		7365	0.70	1.11	1280	0.028	0.44	0.65	0.30	2.52	1.63	1.67
46-2		1114		8502	0.55	1.13	989	0.041	0.40	0.54	0.27	2.12	1.30	1.29
46-2		1156		8289	0.51	1.03	1120	0.021	0.33	0.45	0.20	1.62	1.01	1.01

† - each reported analysis is a separate grain and is an average of 2-3 points.

TABLE 3. Major[1] and Rare Earth Element[2] Analyses of Basaltic Glasses

sample	SiO_2	TiO_2	Al_2O_3	FeO	MnO	MgO	CaO	Na_2O	K_2O	P_2O_5	Total	Mg#	Ca/(Ca+Na)	$Na_{8.0}$	$Fe_{8.0}$	CaO/Al_2O_3	Ce	Nd	Sm	Eu	Dy	Er	Yb
1-1	49.67	1.72	14.75	10.45	0.19	7.37	11.50	3.06	0.09	0.16	98.96	0.562	0.728	2.83	9.40	0.780	19.52	15.88	5.05	1.43	7.38	4.42	4.54
1-2	49.90	1.75	14.76	10.56	0.20	7.27	11.44	2.97	0.09	0.16	99.1	0.556	0.733	2.70	9.34	0.775	21.38	17.03	5.45	1.73	7.58	4.54	4.67
3-17	50.22	2.28	14.63	10.76	0.19	6.44	10.22	3.39	0.21	0.28	98.62	0.521	0.683	2.81	8.16	0.699	22.26	17.83	5.78	1.66	8.17	4.93	4.95
3-25	51.06	2.33	15.25	10.32	0.20	6.33	10.72	2.64	0.18	0.29	99.32	0.527	0.743	2.02	7.54	0.703	22.50	17.95	5.83	1.73	8.41	4.93	5.01
3-28	50.82	2.25	14.93	10.83	0.24	6.37	10.18	3.34	0.20	0.28	99.44	0.517	0.685	2.74	8.12	0.682							
3-29	51.19	2.37	14.90	10.63	0.22	6.53	10.16	3.46	0.23	0.28	99.97	0.528	0.677	2.92	8.18	0.682							
3-32	50.64	2.24	14.72	10.74	0.22	6.53	10.10	3.49	0.22	0.25	99.15	0.525	0.674	2.95	8.29	0.686							
3-53	51.23	2.29	14.92	10.56	0.19	6.35	10.27	3.38	0.21	0.26	99.66	0.522	0.684	2.77	7.81	0.688	24.29	20.18	6.42	1.63	9.19	5.61	5.76
3-58	51.21	2.29	14.97	10.59	0.24	6.58	10.17	3.47	0.25	0.24	100.01	0.531	0.676	2.94	8.23	0.679	23.33	18.82	5.85	1.79	8.69	5.25	5.04
3-59	50.95	2.32	14.83	10.88	0.19	6.44	10.22	3.43	0.23	0.23	99.72	0.518	0.680	2.85	8.28	0.689	21.59	18.04	5.92	1.58	8.30	5.07	5.04
3-63	50.41	2.15	14.54	10.79	0.20	6.31	10.19	3.43	0.22	0.30	98.54	0.515	0.679	2.80	7.98	0.701	22.34	17.86	6.05	1.62	8.71	5.20	5.18
4-6	51.12	1.82	15.57	9.58	0.20	7.46	10.57	3.28	0.19	0.15	99.94	0.586	0.697	3.08	8.68	0.679	14.89	12.45	4.03	1.44	6.19	3.69	3.40
4-10	50.27	2.17	14.82	10.70	0.19	6.76	9.50	3.60	0.27	0.24	98.52	0.535	0.653	3.14	8.64	0.641	19.87	15.67	5.10	1.74	7.52	4.40	4.49
4-14	50.28	2.29	14.68	10.89	0.16	6.70	9.66	3.53	0.25	0.27	98.71	0.528	0.661	3.05	8.73	0.658	20.80	16.35	5.02	2.01	7.42	4.55	4.49
4-20	50.62	2.18	14.86	10.88	0.23	6.36	10.19	3.55	0.23	0.26	99.36	0.515	0.672	2.94	8.15	0.686	19.73	16.92	5.34	1.77	7.99	4.95	4.74
4-23	50.55	2.29	14.81	10.85	0.17	6.26	10.19	3.57	0.23	0.18	99.1	0.512	0.671	2.92	7.95	0.688							
4-27	50.28	2.32	14.71	10.76	0.18	6.29	10.10	3.58	0.24	0.20	98.66	0.515	0.668	2.95	7.91	0.687	22.33	17.91	5.63	2.01	8.46	5.25	5.15
5-3	49.40	1.74	15.95	10.40	0.14	7.13	10.13	3.43	0.18	0.16	98.66	0.555	0.678	3.11	8.95	0.635	16.31	13.86	4.52	1.58	6.56	4.04	3.76
5-56	50.63	2.34	14.82	10.70	0.19	7.29	9.90	3.33	0.22	0.28	99.7	0.553	0.680	3.07	9.52	0.668	20.93	17.98	5.78	1.78	8.74	5.25	4.98
5-4	50.55	3.24	13.93	12.68	0.22	5.09	9.08	3.44	0.36	0.40	98.99	0.422	0.653	2.36	7.84	0.652	34.65	27.48	8.32	2.52	12.38	7.43	7.47
9-9	50.62	1.63	15.83	9.24	0.15	7.15	10.68	3.27	0.19	0.18	98.94	0.585	0.700	2.96	7.82	0.675	15.93	13.28	4.36	1.57	6.71	4.22	4.19
9-17	51.08	2.08	14.88	11.12	0.19	6.47	9.74	3.59	0.26	0.20	99.61	0.514	0.659	3.02	8.57	0.655	19.54	14.96	4.67	1.60	7.04	4.37	4.10
9-35	50.58	1.69	15.85	8.83	0.22	7.15	10.87	3.12	0.19	0.18	98.68	0.596	0.713	2.81	7.41	0.686	18.95	16.22	5.16	1.83	7.47	4.61	4.35
12-6	50.74	1.82	15.57	10.15	0.23	6.78	9.85	3.47	0.25	0.25	99.11	0.549	0.669	3.02	8.12	0.633	19.03	16.72	5.39	1.85	7.88	4.62	4.05
12-8	50.89	1.93	15.75	9.93	0.19	6.79	9.80	3.49	0.24	0.27	99.28	0.554	0.667	3.04	7.92	0.622							
12-10	50.39	2.09	15.59	9.91	0.23	6.83	9.93	3.55	0.26	0.25	99.03	0.556	0.666	3.12	7.96	0.637							
12-12	50.31	2.10	15.58	9.99	0.19	6.68	9.77	3.45	0.26	0.28	98.61	0.549	0.669	2.96	7.79	0.627							
12-16	50.88	1.96	15.65	9.90	0.19	6.70	9.87	3.49	0.23	0.28	99.15	0.552	0.669	3.01	7.74	0.631							
12-18	50.44	1.94	15.57	10.22	0.16	6.78	9.96	3.39	0.27	0.25	98.98	0.547	0.677	2.94	8.19	0.640	26.19	20.29	6.35	1.98	9.32	5.66	5.81
12-21	50.76	2.02	15.75	9.92	0.21	7.01	9.93	3.46	0.24	0.26	99.56	0.562	0.672	3.09	8.27	0.630	22.38	17.05	5.38	1.70	7.88	4.67	4.23
12-23	50.15	1.95	15.66	10.23	0.16	6.89	9.97	3.46	0.25	0.26	98.98	0.551	0.673	3.05	8.38	0.637							
12-28	50.00	1.97	15.62	10.13	0.17	7.02	9.79	3.47	0.25	0.25	98.67	0.558	0.668	3.11	8.50	0.627							
12-36	49.82	1.86	15.63	10.09	0.15	7.09	9.92	3.51	0.24	0.27	98.58	0.561	0.668	3.17	8.57	0.635							
12-39	50.16	1.99	15.56	9.93	0.18	7.12	9.92	3.53	0.24	0.27	98.9	0.566	0.667	3.21	8.46	0.638							
12-45	50.08	1.90	15.63	10.45	0.18	7.23	9.86	3.63	0.27	0.27	99.5	0.557	0.660	3.35	9.17	0.631							
12-41	49.75	1.85	15.45	9.91	0.14	7.11	9.96	3.60	0.25	0.26	98.28	0.566	0.664	3.27	8.43	0.645	21.33	17.35	5.49	1.51	7.84	4.72	4.65
37-57	49.68	2.42	13.97	12.22	0.21	6.55	10.08	3.36	0.23	0.27	98.99	0.494	0.682	2.82	9.81	0.722	21.49	16.21	4.81	1.60	7.49	4.41	4.04
37-60	50.63	2.56	13.46	12.90	0.22	5.78	10.01	3.11	0.25	0.28	99.2	0.449	0.697	2.29	9.20	0.744	18.81	16.79	5.47	1.83	8.51	5.09	4.70
38-19	50.44	2.09	15.38	11.07	0.22	6.87	10.70	3.00	0.14	0.24	100.15	0.530	0.718	2.58	9.19	0.696	13.19	12.31	4.36	1.68	6.73	4.19	3.94
42-2	51.23	1.63	15.27	9.77	0.16	7.66	10.84	2.93	0.16	0.18	99.83	0.588	0.725	2.81	9.20	0.710							
42-4	50.19	1.69	15.94	9.74	0.17	7.91	10.76	2.88	0.11	0.16	99.55	0.596	0.727	2.85	9.59	0.675	12.06	10.63	3.66	1.21	5.70	3.47	3.07

TABLE 3. continued

sample	SiO_2	TiO_2	Al_2O_3	FeO	MnO	MgO	CaO	Na_2O	K_2O	P_2O_5	Total	Mg#	Ca/(Ca+Na)	$Na_{8.0}$	$Fe_{8.0}$	CaO/Al_2O_3	Ce	Nd	Sm	Eu	Dy	Er	Yb
44-3	50.40	1.59	15.75	10.10	0.23	8.06	10.62	2.95	0.12	0.19	100.01	0.592	0.720	2.98	10.20	0.674	12.88	12.81	4.72	1.54	7.26	4.55	4.66
44-4	50.22	1.73	15.70	9.94	0.21	8.16	10.63	2.98	0.10	0.21	99.88	0.599	0.718	3.04	10.21	0.677	15.09	14.76	5.08	1.83	8.09	5.28	5.12
44-5	50.35	1.79	15.89	9.97	0.20	8.20	10.94	2.90	0.09	0.15	100.48	0.599	0.729	2.98	10.30	0.688							
44-7	50.56	2.19	15.36	10.60	0.18	7.61	10.22	3.16	0.16	0.20	100.24	0.566	0.698	3.02	9.95	0.665							
44-9	50.79	2.29	15.44	11.00	0.21	7.19	10.16	3.37	0.12	0.19	100.76	0.543	0.683	3.07	9.65	0.658	16.83	14.92	5.12	1.66	7.87	4.80	4.24
44-10	50.48	2.28	15.17	11.22	0.21	7.05	10.11	3.40	0.12	0.24	100.28	0.533	0.680	3.05	9.64	0.666							
44-11	49.78	1.60	15.74	9.96	0.18	8.44	10.90	3.04	0.10	0.16	99.9	0.606	0.719	3.21	10.69	0.693	12.53	10.99	3.77	1.31	5.97	3.88	3.36
44-12	49.79	2.32	15.01	10.93	0.17	7.05	10.24	3.39	0.13	0.26	99.29	0.540	0.683	3.04	9.35	0.682							
44-13	49.52	1.73	15.70	9.79	0.15	8.28	10.85	2.93	0.11	0.17	99.23	0.606	0.725	3.04	10.25	0.691							
44-14	49.64	1.66	15.80	9.82	0.20	8.19	10.82	2.91	0.11	0.19	99.34	0.603	0.726	2.98	10.14	0.685							
44-16	49.44	1.83	15.58	9.81	0.17	8.18	10.83	2.96	0.12	0.17	99.09	0.603	0.723	3.03	10.11	0.695							
44-18	49.34	1.71	15.84	9.90	0.19	7.08	11.68	2.88	0.09	0.20	98.91	0.565	0.743	2.54	8.37	0.737							
44-20	49.59	1.77	15.45	9.83	0.21	8.36	10.83	2.96	0.09	0.14	99.23	0.607	0.723	3.10	10.43	0.701							
44-21	49.92	1.72	15.50	9.85	0.15	8.22	10.73	2.89	0.10	0.18	99.26	0.603	0.726	2.98	10.22	0.692							
44-25	49.83	1.81	15.56	9.67	0.16	8.25	10.89	2.93	0.11	0.17	99.38	0.608	0.726	3.03	10.09	0.700							
44-26	50.35	2.23	14.54	10.80	0.17	7.79	10.06	3.21	0.14	0.19	99.48	0.567	0.691	3.14	10.45	0.692	12.69	11.43	3.97	1.25	6.04	3.70	3.44
47-1	50.13	1.71	15.74	9.53	0.24	8.33	10.77	2.93	0.09	0.17	99.64	0.614	0.724	3.06	10.08	0.684							
47-2	50.25	1.73	14.65	10.02	0.23	7.60	10.45	3.33	0.09	0.18	98.53	0.580	0.691	3.18	9.35	0.713							
47-3	50.30	2.14	14.63	10.64	0.22	7.09	10.35	3.25	0.15	0.22	98.99	0.548	0.694	2.91	9.12	0.707	12.14	11.13	3.68	1.21	5.85	3.57	3.27
47-4	49.95	2.03	14.57	10.62	0.16	7.82	10.25	3.13	0.13	0.25	98.91	0.573	0.700	3.07	10.32	0.704							
47-5	50.97	1.57	15.72	9.07	0.20	8.09	10.95	3.10	0.08	0.16	99.91	0.619	0.716	3.14	9.22	0.697	11.28	10.23	3.37	1.14	5.45	3.38	3.10
47-6	50.16	1.68	15.43	9.10	0.17	7.88	10.86	3.02	0.09	0.13	98.52	0.612	0.719	2.98	8.90	0.704							
47-7	49.87	1.76	15.26	9.22	0.16	7.94	10.99	3.10	0.09	0.15	98.54	0.610	0.717	3.08	9.12	0.720							
47-8	50.11	1.29	15.53	10.09	0.19	7.91	10.85	3.07	0.07	0.16	99.27	0.588	0.716	3.04	9.94	0.699							
47-9	50.05	1.45	15.30	9.81	0.15	7.82	10.89	2.97	0.07	0.15	98.66	0.592	0.723	2.91	9.51	0.712							
47-17	49.47	1.55	15.25	10.58	0.15	7.51	10.76	3.10	0.13	0.23	98.73	0.564	0.712	2.92	9.76	0.706							
47-28	50.24	1.58	15.51	9.59	0.17	7.97	10.83	3.09	0.08	0.15	99.21	0.602	0.714	3.08	9.54	0.698							
47-32	50.54	1.43	15.54	9.60	0.15	7.88	11.03	3.04	0.09	0.12	99.42	0.599	0.721	3.00	9.40	0.710							
47-33	50.14	1.45	15.41	9.96	0.13	7.85	10.91	3.08	0.10	0.15	99.18	0.589	0.716	3.03	9.71	0.708							

1 - Major element electron microprobe analyses done by F. Beecher Wooding at University of Cape Town
2 - Rare Earth Element ion microprobe analyses done by K. Johnson and P. Meyer at M.I.T.

TABLE 4. Locations, depths, and inferred crustal ages of dredges discussed in text

Dredge	Start Depth (m)	Lat. (S)	Long. (E)	Area	Age (m.y.)[1]
1	3940	33.655	56.781	Axial Volcano S. RV.	0-0.5
3	4250	31.882	57.233	Axial high N. RV.	0-0.5
4	3880	31.760	57.073	Hook R#1 N. FZ ext.	2-3
5	4260	31.695	57.078	Hook R#2 N. FZ ext.	3-4
6	4160	31.915	57.178	Corner N. RTI	0-0.5
9	2023	31.981	57.210	Rift Mtn. Smt. N. Inner Hi	1-2
12	5360	32.003	57.090	N. Trans. Volcano	0-0.5
18	4899	32.118	57.100	E. Wall Trans.	3-4
23	5133	32.226	56.989	W. Wall Med. Tect. R.	?
25	5370	32.537	57.064	E. Wall Med. Tect. R.	?
30	4382	32.782	57.134	Trans. E. Wall	8-10
34	5509	33.019	57.001	Trans. W. Wall	8-9
35	4180	33.009	56.961	Trans. W. Wall	8-9
37	5652	32.653	56.963	Trans. W. Wall	9-10
38	2548	33.032	56.807	Crest Trans. W. Wall	8-9
42	3843	33.406	56.959	Trans. W. Wall	2-3
44	4830	33.628	56.931	Corner S. RTI	0-0.5
46	5675	33.501	57.029	W. Wall S. Nodal Basin	1-2
47	4653	33.383	57.017	Trans. W. Wall	3-4

[1] - Age inferred by combination of magnetic anomalies, latitude, and spreading rate.

RESULTS

Peridotites

Compositional variation within the Atlantis II Fracture Zone

One of the objectives of this study was to determine how much compositional variability exists in peridotites from one well-sampled fracture zone. This question arises from some of the results in Chapter 2 [*Johnson et al.*, 1990] concerning the systematic long wavelength compositional variations observed in oceanic peridotites. It was observed that the degree of melting in residual peridotites, inferred by greater depletions in incompatible trace elements in clinopyroxenes, modal mineralogy, and major element composition,

increases near hotspots and diminishes as a function of distance from the hotspot. Furthermore, rare earth element patterns in clinopyroxenes were observed to change from relatively flat in the middle to heavy rare earth element range in normal peridotites, to characteristic patterns with uninflected, straight slopes from heavy to light rare earth elements in hotspot-proximal peridotite clinopyroxenes. This was interpreted as resulting from deeper, more extensive melting beginning in the garnet stability field and essentially consuming all primary clinopyroxene.

Rare earth element patterns for peridotite clinopyroxenes analyzed in this study are presented in Figure 4. A wide range of compositions exists in the sampled peridotites corresponding to varying degrees of depletion. The heavy line in the figure is a representative pattern from the Bouvet Fracture Zone peridotites reported in Chapter 2 [*Johnson et al.*, 1990]. The clinopyroxenes in Bouvet Fracture Zone peridotites were the most incompatible element and clinopyroxene depleted in the entire Southwest Indian Ridge sample suite, and were inferred to be products of high degrees of melting; Ce concentrations in some of the Atlantis II Fracture Zone peridotite clinopyroxenes are as low as those in the Bouvet Fracture Zone clinopyroxenes. Although the shapes of the Atlantis II patterns are not quite as straight in the middle REE or depleted in the heavy REE, the shapes are closer to those of the Bouvet samples than to those of the less depleted Atlantis II clinopyroxenes. This is illustrated in Figures 5a and b , which are plots of Zr versus $(Nd/Yb)_n$ and $(Sm/Yb)_n$. The characteristic light-middle REE depletion observed in Bouvet F.Z. samples is also observed in dredges 34 and 35, and to a lesser degree, dredge 44. This is somewhat of a surprise since the first six Atlantis II Fracture Zone samples analyzed were in the less depleted group of samples from the eastern wall of the transform, and the values chosen to represent the fracture zone in Chapter 2 were from this rather uniform, less depleted set. It can be seen from Figures 3 and 4, however, that there is no single "representative" composition for the fracture zone, instead there is a wide range of compositions spanning over one order of magnitude in $(Nd/Yb)_n$. A systematic

Figure 4. Rare earth element patterns in peridotite clinopyroxenes. Open symbols are individual samples from the western side of the transform, solid symbols are samples from the eastern wall. The average composition of clinopyroxenes from the Bouvet Fracture Zone [Chapter 2 - *Johnson et al.*, 1990] is shown, for reference, as a heavy line to illustrate the highly depleted compositions of dredge 34 and 35 samples. Also shown as a shaded field is the REE compositional range for all peridotite clinopyroxenes analyzed along the Southwest Indian and American-Antarctic Ridges (data in Chapter 2) to illustrate that the variability observed in the Atlantis II F.Z. peridotites covers nearly the entire range observed in the regional study.

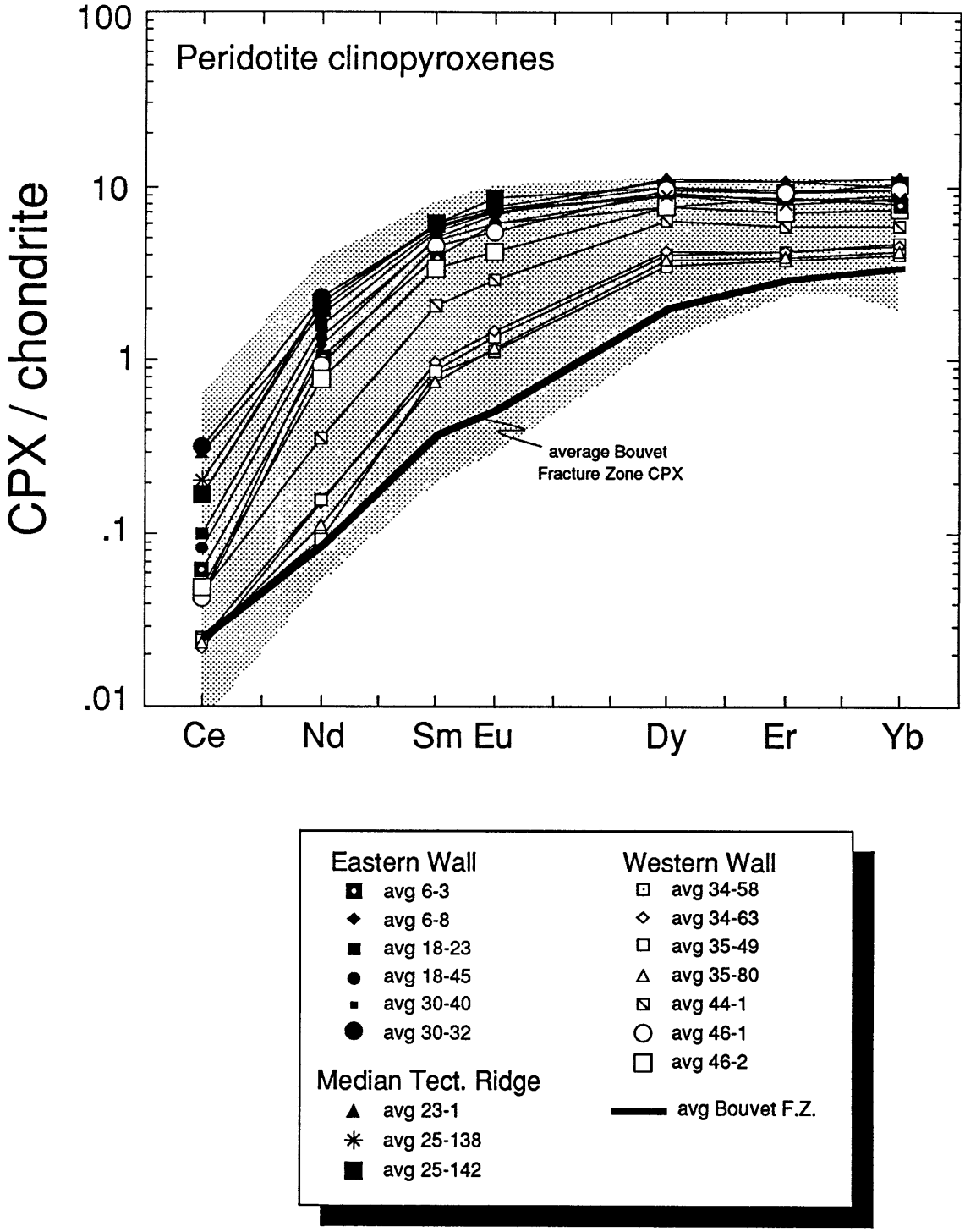
Peridotite clinopyroxenes
CPX / chondrite
100
10
1
.1
.01
Ce
Nd
Sm
Eu
Dy
Er
Yb
average Bouvet
Fracture Zone CPX
Eastern Wall
avg 6-3
avg 6-8
avg 18-23
avg 18-45
avg 30-40
avg 30-32
Median Tect. Ridge
avg 23-1
avg 25-138
avg 25-142
Western Wall
avg 34-58
avg 34-63
avg 35-49
avg 35-80
avg 44-1
avg 46-1
avg 46-2
avg Bouvet F.Z.

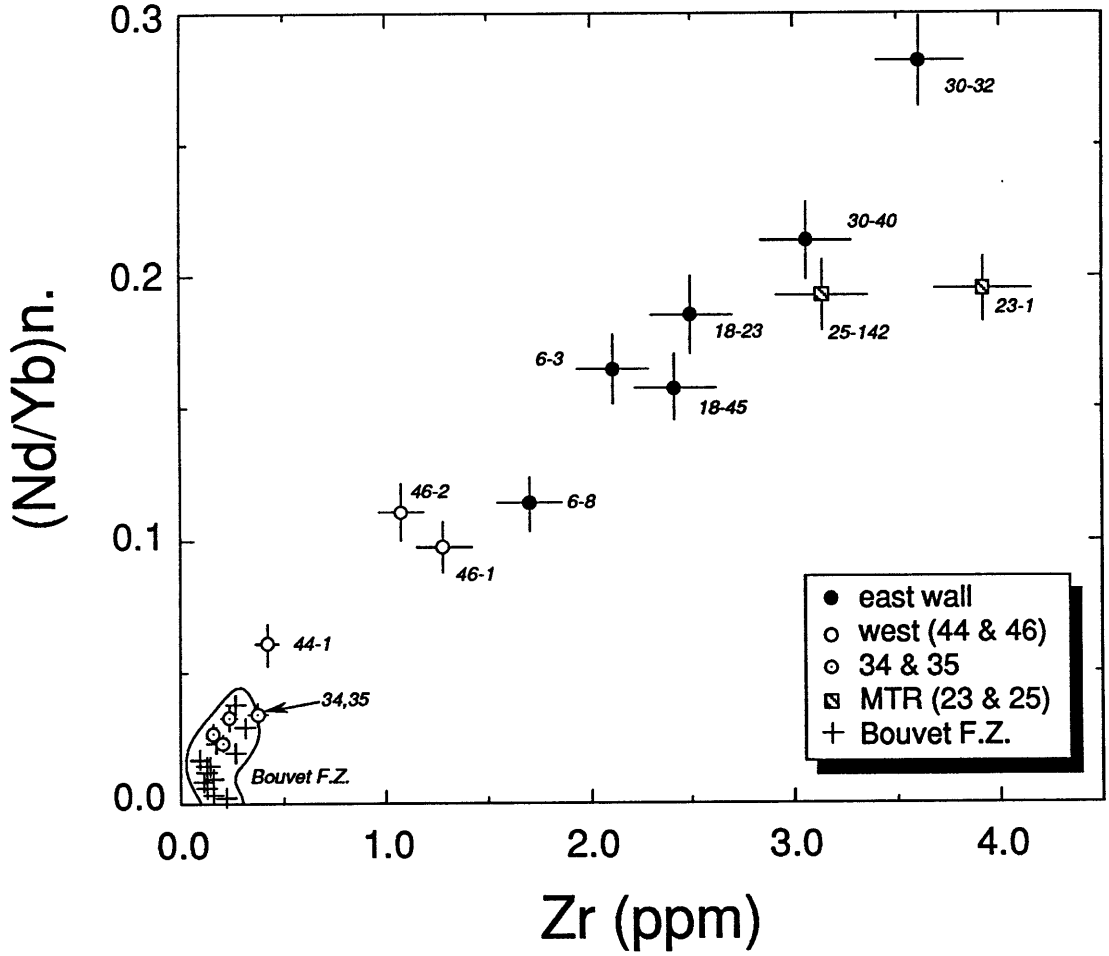

Figure 5. Plots of (a) (Nd/Yb)n and (b) Sm/Yb)n versus Zr in peridotite clinopyroxenes from the Atlantis II Fracture Zone and Bouvet Fracture Zone for comparison. Sample numbers are shown for Atlantis II samples. Samples from the western wall of the transform are open circles and are more depleted in light REE and Zr than samples from the eastern wall (solid circles). Dredges 34 and 35 are similar in their degree of depletion to the Bouvet Fracture Zone samples. Error bars are 2σ analytical precision.

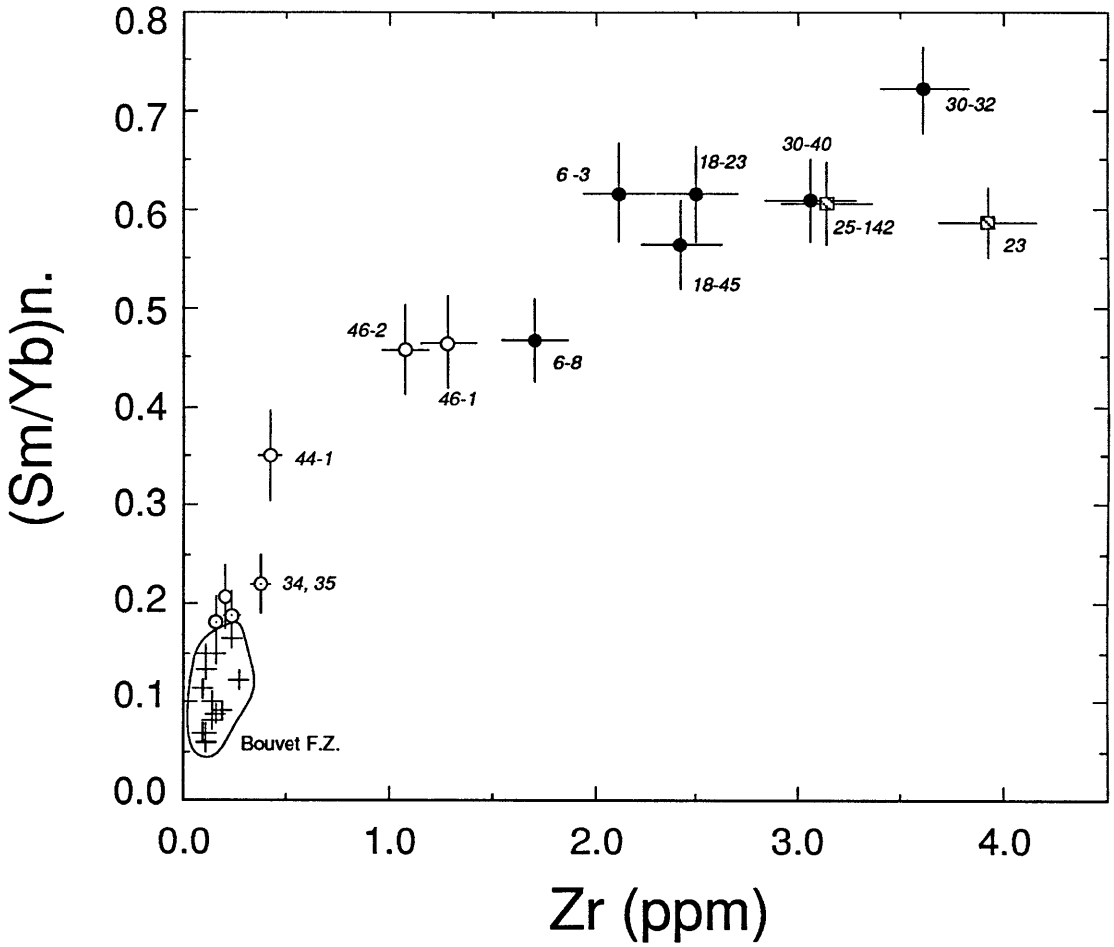
0.8
0.7
0.6
0.5
0.4
0.3
0.2
0.1
0.0
(Sm/Yb)n.
0.0
1.0
2.0
3.0
4.0
Zr (ppm)
30-32
30-40
18-23
6 -3
25-142
23
18-45
46-2
6-8
46-1
44-1
34, 35
Bouvet F.Z.

co-variation is also observed in a plot of modal clinopyroxene versus $(Nd/Yb)_n$ in each sample (Figure 6). Plotted for reference are data from the Bouvet F.Z. at the lower left corner of the diagram, consistent with their highly incompatible element depleted character.

Looking at Figures 5 and 6 in more detail, systematic differences are observed between samples from the eastern and western transform walls. The main difference is that the most depleted samples come from the western wall of the transform (open symbols), in particular dredges 34 and 35. These two succesive dredges cover a depth interval of 2000 meters, starting from near the floor of the transform at 5500 m up to ~4500 m (dredge 34), then from ~4200 m to 3500 m (dredge 35; Figure 2 and Table 4). Thus, the recovery of very depleted samples in both dredges up the transform wall implies that the depleted zone in this area may traverse the entire exposed ultramafic section. Intermediate to dredges 34 and 35 and the group of normally depleted samples is dredge 44, from the inside corner of the southern ridge-transform intersection. Dredge 46, on the transform wall of the inside corner of the southern nodal basin, though close to dredge 44 is more enriched in the middle and heavy REE (Figure 5).

All dredges from the eastern wall of the transform (solid symbols) have similarly shaped REE patterns, although $(Ce/Sm)_n$ systematically decreases by a factor of 8 from dredge 30 to dredge 6. *Johnson et al.* [1990] showed that this can be explained by a ~4-5% difference in fractional melting between the two samples. Dredge 6 is located on the inside corner wall of the northern ridge-transform intersection, and dredges 18 and 30 are located on the eastern transform wall. Dredges 23 and 25 are from the western and eastern walls, respectively, of the median tectonic ridge. Although they are physically located on the western side of the inferred present day slip zone of the transform [*Dick et al.*, 1990], they are chemically similar to the less depleted eastern wall samples. This observation may be helpful in deciphering the tectonic evolution of the transform, as will be discussed below.

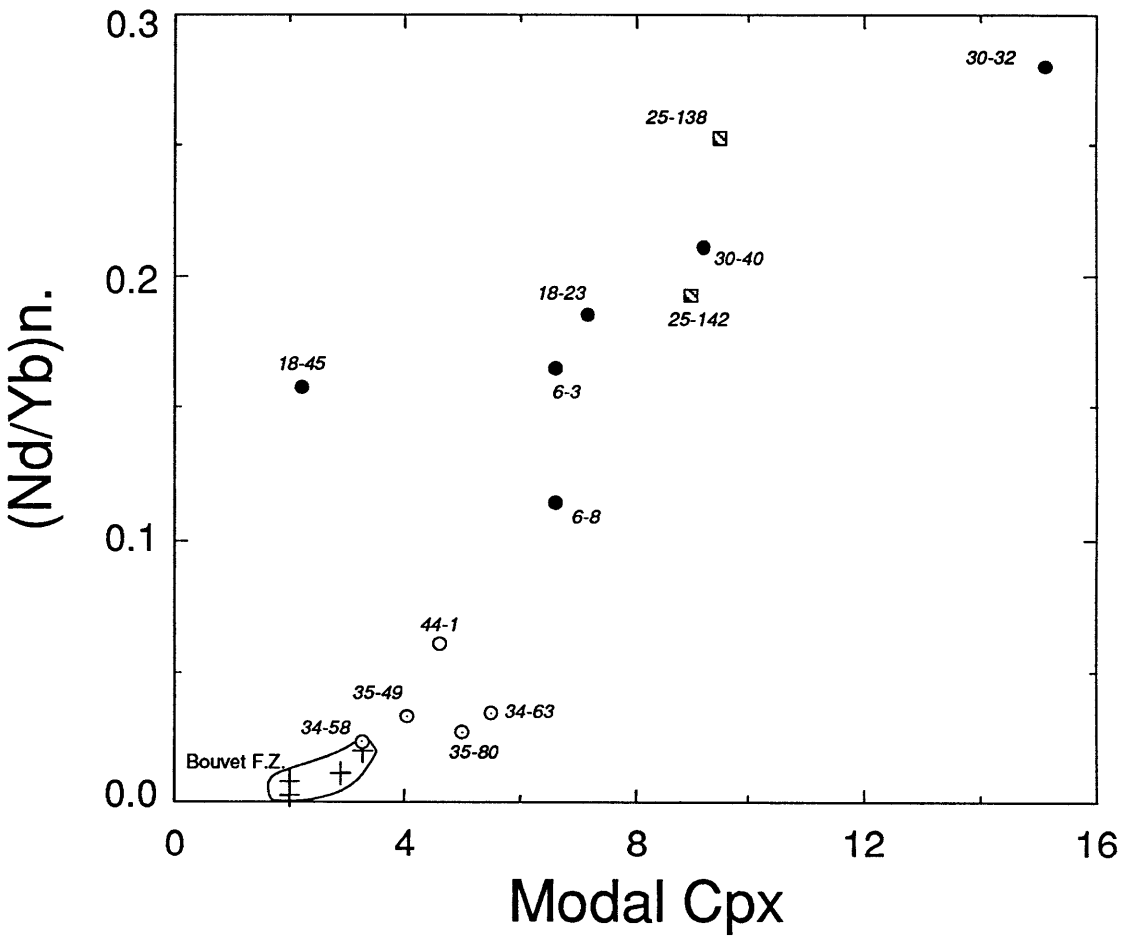

Figure 6. Modal clinopyroxene versus (Nd/Yb)n in peridotite clinopyroxenes from the Atlantis II Fracture Zone showing the trend that is consistent with higher degrees of melting in samples from the western wall of the transform.

The difference in REE between samples from the eastern and western walls is vividly illustrated in a plot of Ti/Zr versus Nd_n (Figure 7). Both the high Ti/Zr ratio and the low Nd concentration in peridotite clinopyroxene are measures of depletion. Thus, it can be seen that the samples from the western side of the transform, particularly dredges 34, 35, and 44, are significantly more depleted than samples from the eastern wall. Also plotted for reference are samples from the Bouvet Fracture Zone. The depletions observed in the dredge 34, 35, and 44 pyroxenes are in the range of those for the highly depleted Bouvet samples.

Returning briefly to the question raised above regarding the representative average composition for the Atlantis II Fracture Zone reported by *Johnson et al.* [1990]. Location averages were used by *Dick et al.* [1984] and *Michael and Bonatti* [1985] to examine regional variations in upper mantle compositions. This approach was used to filter out local "noise" in the data. As is already evident from the present data set, local variations may be very important for evaluating source variability and melting processes at the mid-ocean ridge. This does not necessarily conflict with the concept or validity of using location averages for identifying large-scale mantle variations. Figure 8 plots the mean REE compositions of samples from the eastern and western sides of the fracture zone. These values are really only qualitative in nature, since they depend on the representativeness of the sampling. Clearly, the mean composition of samples from the east side of the transform zone is more enriched than that from the western side of the transform, and is roughly the same as the composition used by *Johnson et al.* [1990]. The error bars represent the standard deviation about the mean value and they overlap the mean REE composition for all of the samples in the fracture zone. The true mean composition for the fracture zone depends on the relative abundances of rocks of a given composition in the fracture zone. Since this is very difficult to establish, the value in Figure 8 is as good as any estimate and probably better than the previous one by *Johnson et al.* [1990] based

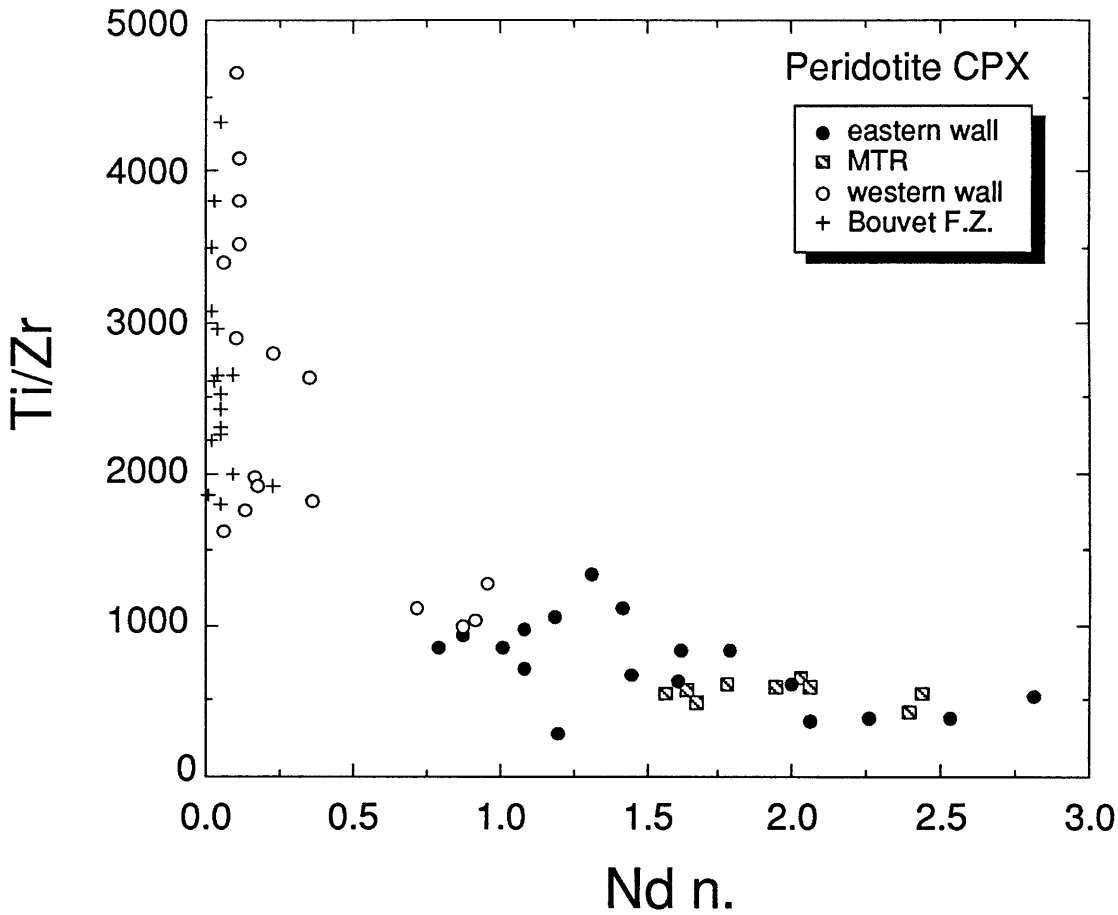

Figure 7. Ti/Zr versus Nd_n in the peridotite clinopyroxenes. Solid symbols are samples from the eastern wall of the transform and open symbols are samples from the western side. All analyses (several for each sample) are plotted along with the mean for each sample (large symbols). The division between eastern and western samples on the basis of their degrees of depletion is very pronounced in this diagram. Also plotted for comparison are samples from the Bouvet Fracture Zone (plus signs) to show the similar levels of depletion as some samples from the western wall of the Atlantis II F.Z.

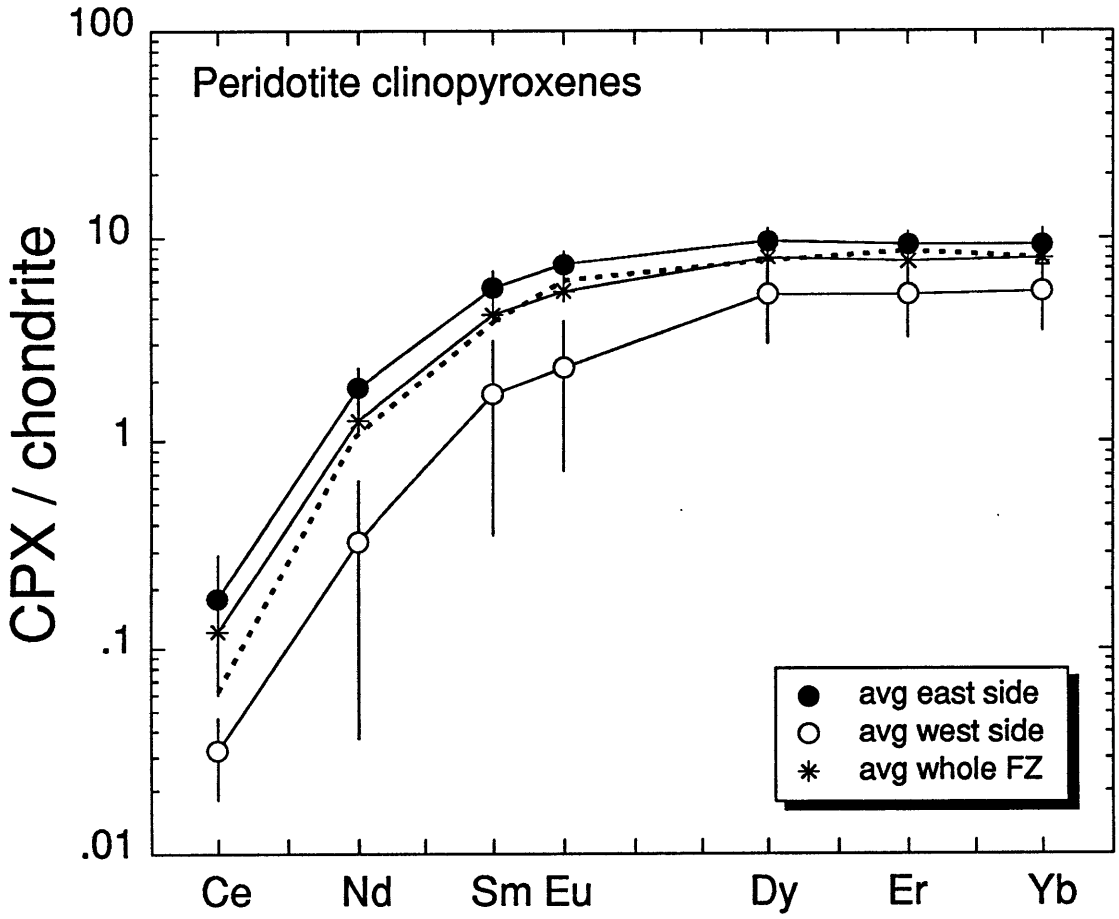

Figure 8. Rare earth element patterns in peridotite clinopyroxenes averaged for both the west and east sides of the transform. Also shown is the mean of 48 analyses on the 17 peridotite samples analyzed in this study to illustrate the similarity of this value to that used in Chapter 2 to represent the Atlantis II Fracture Zone (dashed line).

on one or two dredges alone. The two estimates are, however, identical within the standard deviation of the data.

Chemical variations along mantle flow lines

Now that it has been shown that there is nearly as much variation in peridotite clinopyroxene trace element compositions within the Atlantis II Fracture Zone as there is along the entire length of ridge studied by *Johnson et al.* [1990], it is important to look at the pattern and length scale of variations. Moreover, because mantle flow lines are orientated roughly parallel to the transform fault provides an excellent opportunity to investigate temporal variations in peridotite composition by inference from the spatial separation of samples along the transform walls. In order to evaluate the finer scale chemical variations in the peridotite clinopyroxenes, compositional parameters in the samples have been plotted versus latitude. Since the fracture zone trends due N-S, this representation can be easily converted to kilometers, and knowing the spreading rate, this can be converted to estimated age differences between samples. Since peridotites have undoubtedly had a long melting history on their way from intersection with the solidus to the point at which they last equilibrated with melts, inferring their absolute ages is difficult, and probably not very meaningful. In this case, differences in age of emplacement at the seafloor between peridotite bodies are probably more useful indicators of the longevity of whatever process controlled their compositional differences.

Figure 9a is a plot of dredge latitude versus $(Nd/Yb)_n$ in the peridotite clinopyroxenes. A striking compositional discontinuity across the transform at similar latitude is observed. The greatest depletion is seen in dredges 34 and 35, as expected from Figures 3-5. A pronounced compositional gradient is evident in samples dredged from along the eastern wall and on the median tectonic ridge, going from the least depleted dredge 30, through gradually more depleted dredges 25, 23, 18 and 6. The least depleted peridotite samples are from halfway along the eastern wall of the transform and are inferred to be the oldest

samples from this side, based on their distance from the spreading axis. Thus, a progressive depletion of the mantle is occurring on the eastern wall of the transform, the most depleted peridotites being sampled closest to the northern neovolcanic zone. Assuming that the the 96 km spatial separation between dredge 30 and dredge 6 directly correlates to a difference in age of peridotite emplacement, then the mantle composition has been becoming increasingly depleted in this area over the past 9.6 million years.

In contrast, samples from the western side of the transform show less gradation from strongly depleted dredges 34 and 35 to the least depleted dredge 46. Although there is a suggestion that compositional variation exists along the transform, the sampling density is not great enough to confirm this. However, the distance from most depleted dredges 34 and 35 to the least depleted dredge 46 is 55 km, representing a 5-6 my difference in the time of emplacement. Analogous patterns of depletion are seen in Nd_n (Figure 9b), Zr (Figure 9c), modal clinopyroxene (Figure 9d), and Ca/(Ca+Na) (Figure 9e). Sodium in clinopyroxene is largely held in the jadeite component, and its concentration is therefore a function of pressure. However, it is a minor constituent most abyssal peridotite diopsides and behaves as an incompatible element. Thus, all of the plotted elements reflect, in detail, similar trends in spatial and temporal variability in mantle depletion.

While the modal and compositional data from the eastern wall of the transform fault indicate a progressive depletion of the mantle over the past 9-11 my, data from the western side are too sparse to define trends with confidence. The western side data do display a relative peak in element concentrations at dredge 46 (~33.5°), but paucity of samples along this wall precludes definitive identification of such a peak. However, dredges 34 and 35 are clearly more depleted than any of the other samples from the fracture zone and there is a suggestion of either progressive or episodic mantle depletion along the western side of the transform, as well as along the eastern wall. Although the wavelength of this episodicity cannot be rigorously constrained by the data, the distance between relatively depleted dredge 44 and relatively less depleted dredge 46 is only 15 km, and the distance between

Figure 9. Plots of latitude versus various chemical parameters in peridotite clinopyroxenes illustrating the trends discussed in the text: (a) $(Nd/Yb)_n$, (b) Nd_n, (c) Zr, (d) modal clinopyroxene, and (e) Ca/(Ca+Na). Dashed vertical lines are the positions of the northern and southern ridges, and dredge numbers and plate boundary orientation is depicted in Figure 9a. Large symbols in some plots are dredge averages. On the eastern wall of the transform, the trend of gradually increasing depletion toward the northern ridge-transform intersection at around 31.8°S is clearly represented. The highly depleted compositions of dredges 34 and 35 across the transform from the relatively enriched dredge 30 can be clearly seen at ~33.0°S.

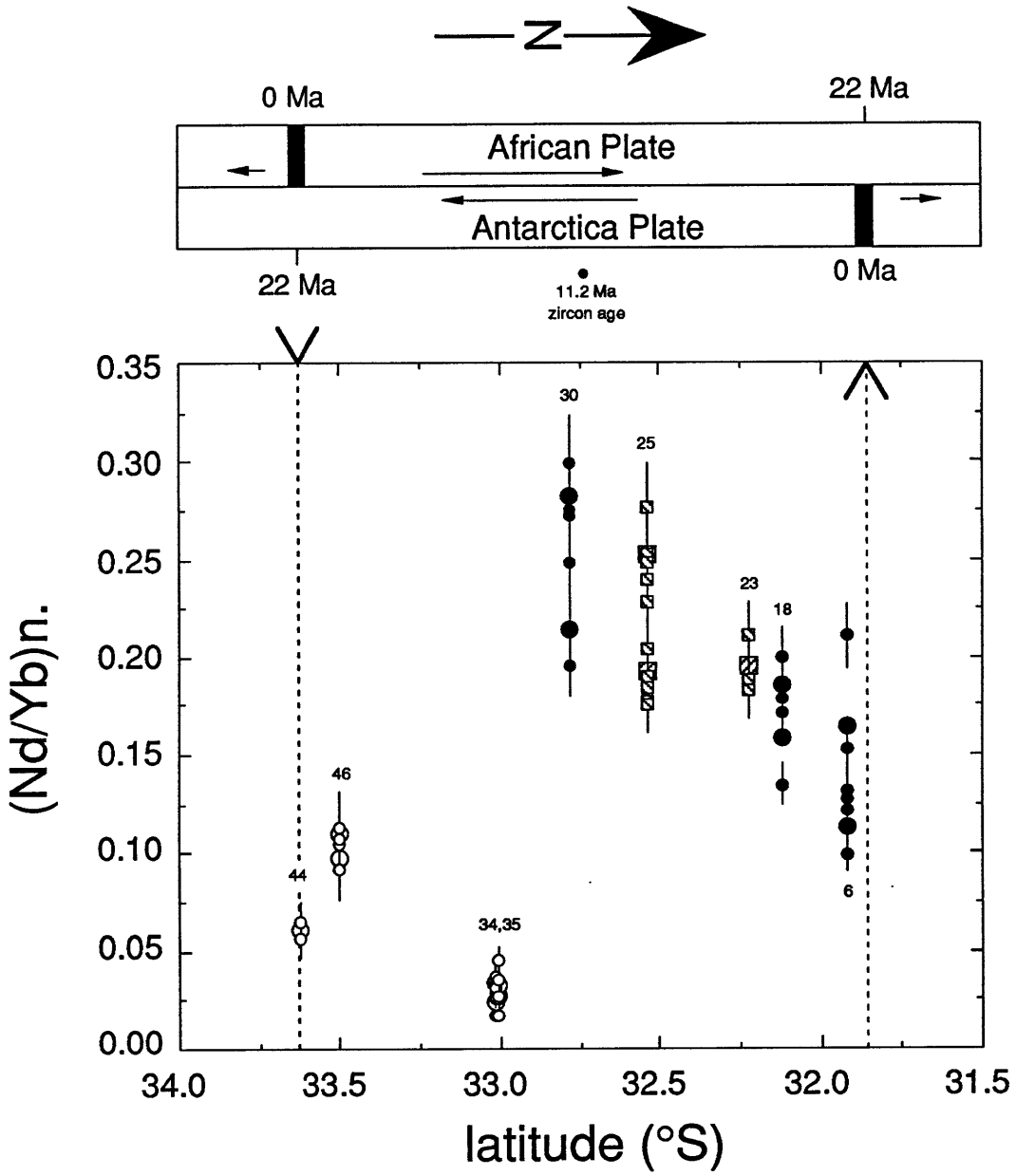
Z
0 Ma
22 Ma
African Plate
Antarctica Plate
22 Ma
0 Ma
11.2 Ma
zircon age
(Nd/Yb)n.
0.35
0.30
0.25
0.20
0.15
0.10
0.05
0.00
30
25
23
18
46
44
34,35
6
34.0
33.5
33.0
32.5
32.0
31.5
latitude (°S)

Figure 9a

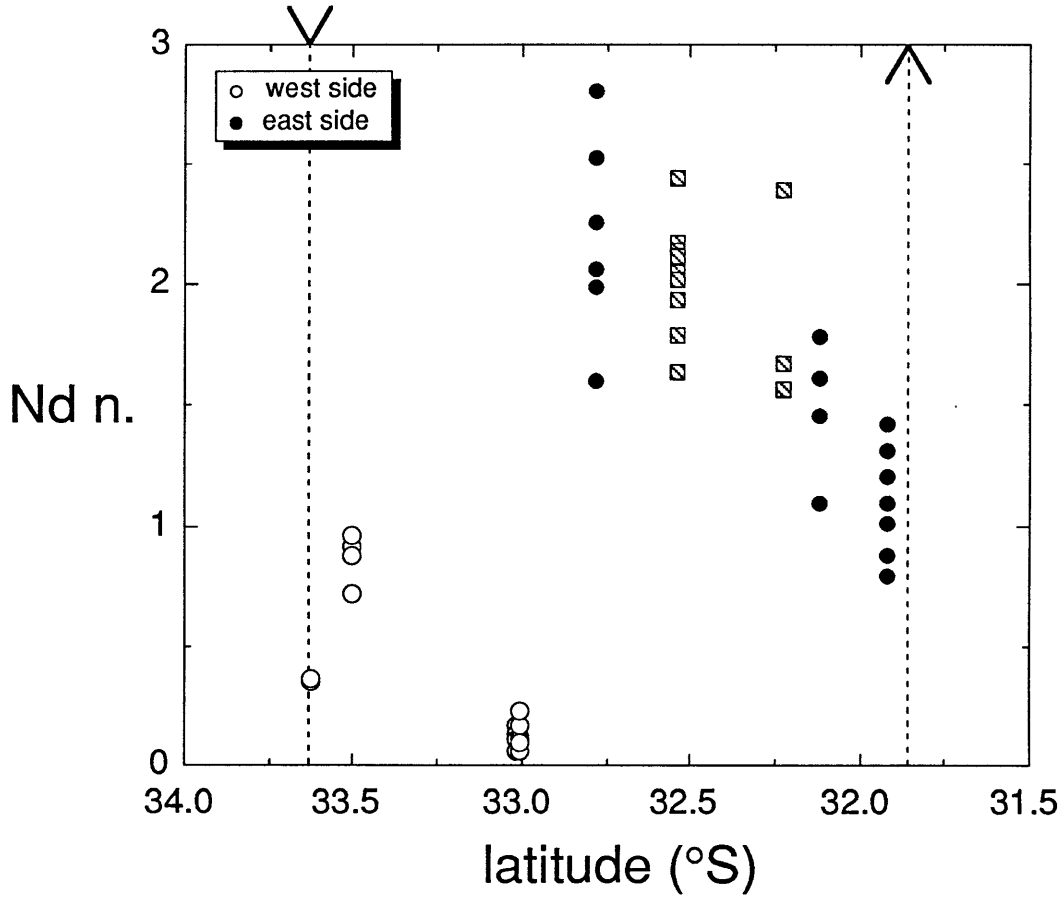
west side
east side
Nd n.
3
2
1
0
34.0
33.5
33.0
32.5
32.0
31.5
latitude (°S)

Figure 9b

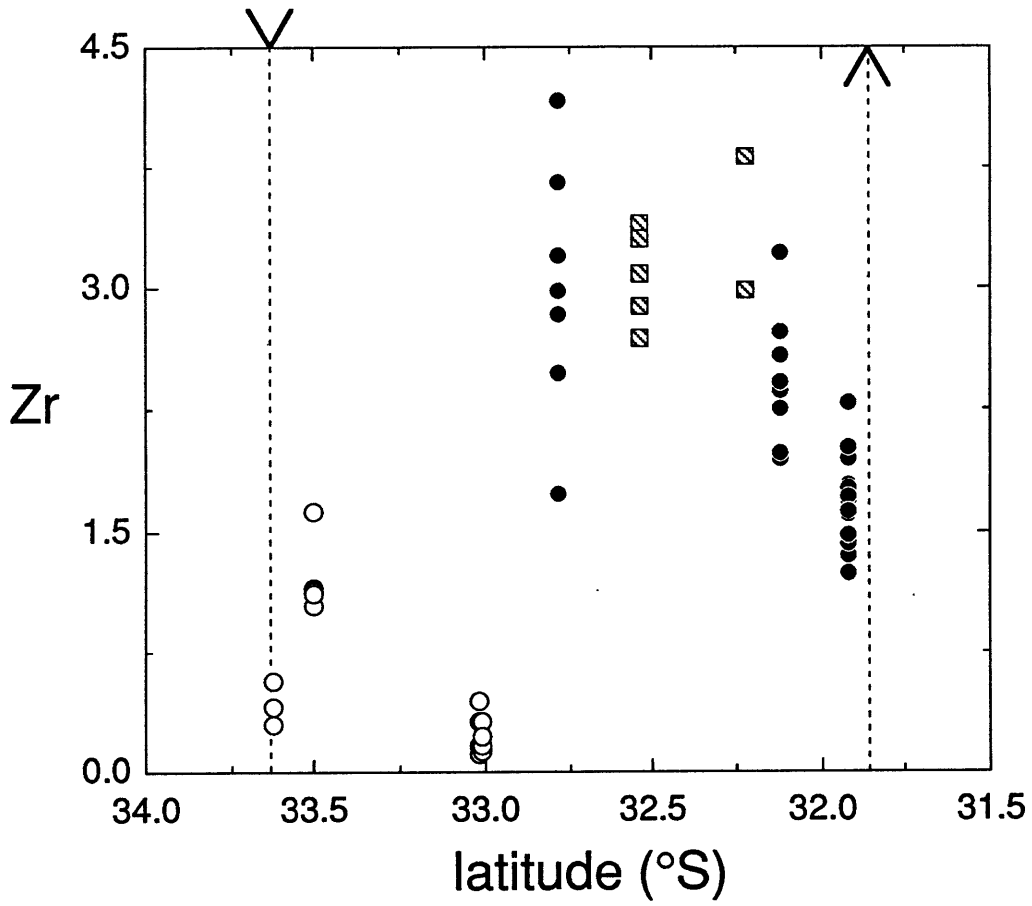

Figure 9c

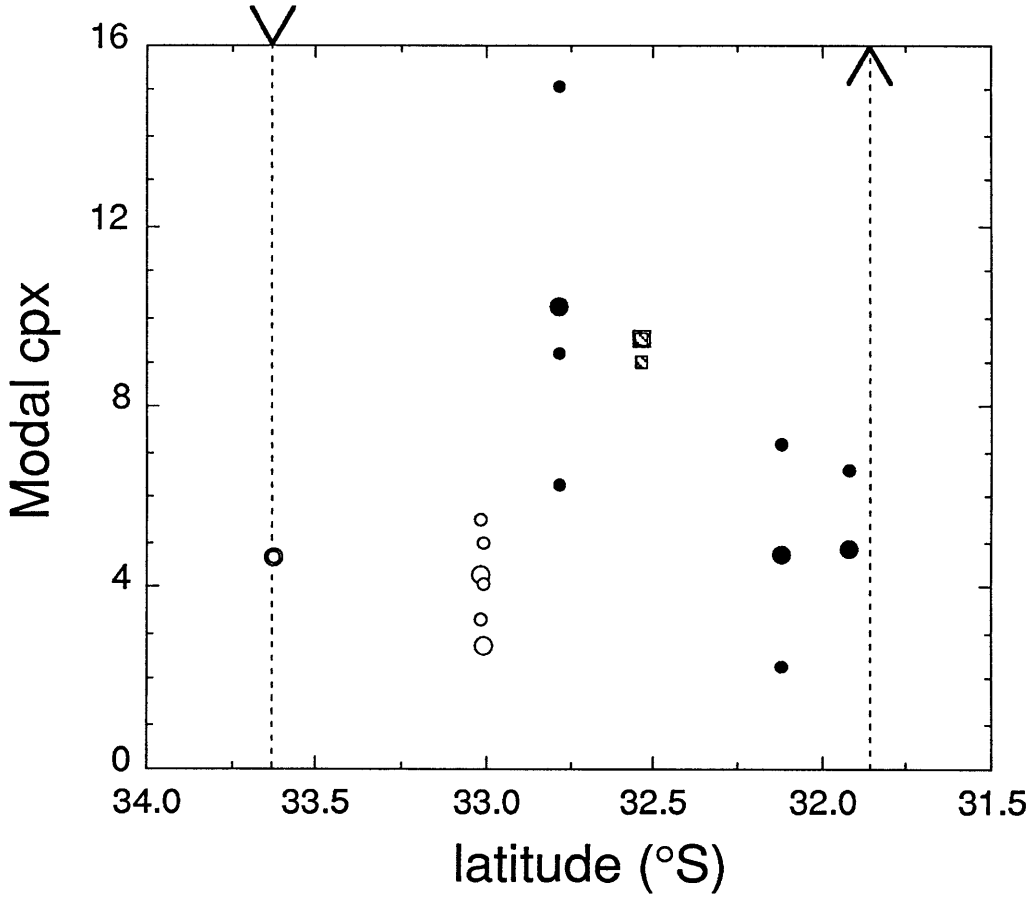

Figure 9d

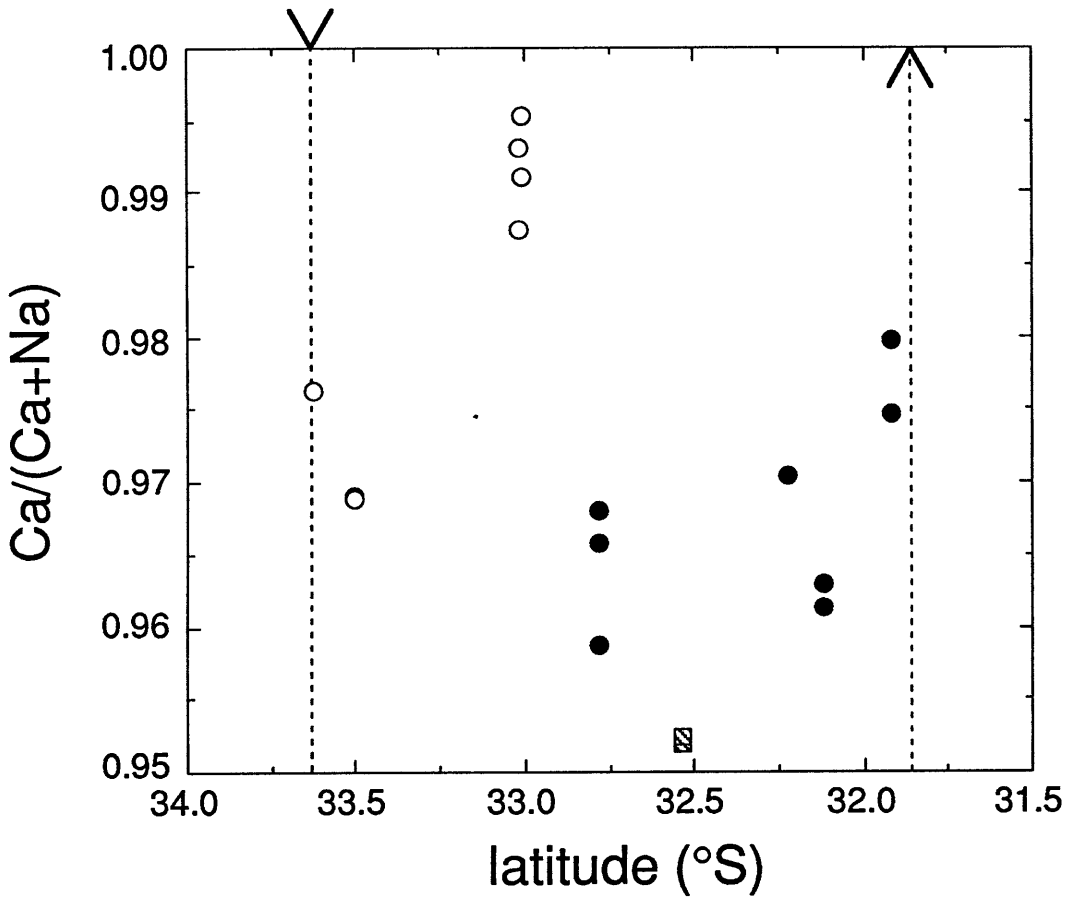
1.00
0.99
0.98
0.97
0.96
0.95
Ca/(Ca+Na)
34.0
33.5
33.0
32.5
32.0
31.5
latitude (°S)

Figure 9e

dredges 34 and 35 and dredge 46 is only 54 km. Thus, the zone of mantle depletion either has a wavelength of ~70 km between the two concentration minima, or the western side of the transform has become progressively less depleted over the past 7 my. More data are needed to constrain these hypotheses, however.

Basaltic Glasses

At first, the data for basalt glasses appear rather uniform and nondescript. When plotted, following *Walker et al.* [1979], on a pseudoternary projection from plagioclase onto the diopside-olivine-silica plane (Figure 10), the glass data all cluster in a narrowly defined field within the general field for mid-ocean ridge basalts. There is some indication of greater silica-undersaturation in the glasses from the eastern side of the transform, but this can result from lower degrees of melting, higher pressure of melting, or a combination of both [*Mysen and Kushiro*, 1977; *Jaques and Green*, 1980; *Takahashi*, 1986; *Fujii and Scarfe*, 1985]. However, in order to evaluate whether basalt compositions show analogous compositional variations across the transform to the peridotites, other discriminants are needed. Inadequate spacing between basalt dredge recoveries on the eastern side of the transform precludes documentation of a similar compositional gradient in basalts as was observed in the peridotites. Furthermore, while dredge spacing on the western side was larger, with a total spread of approximately 110 km (half way along the transform) from dredge 1 in the southern rift valley to dredge 37 on the western wall, very low basalt recovery in dredges 37 and 38 prevent statistically meaningful analysis of along-transform compositional variations. Hence, discussions of the basalts will be limited to documenting compositional differences across the transform. Additional basalt data are required to evaluate compositional variations along the transform similar to those observed in the peridotites.

Various discriminants have been developed to evaluate differences in basalt compositions as a function of degree or depth of melting. In the present situation, given

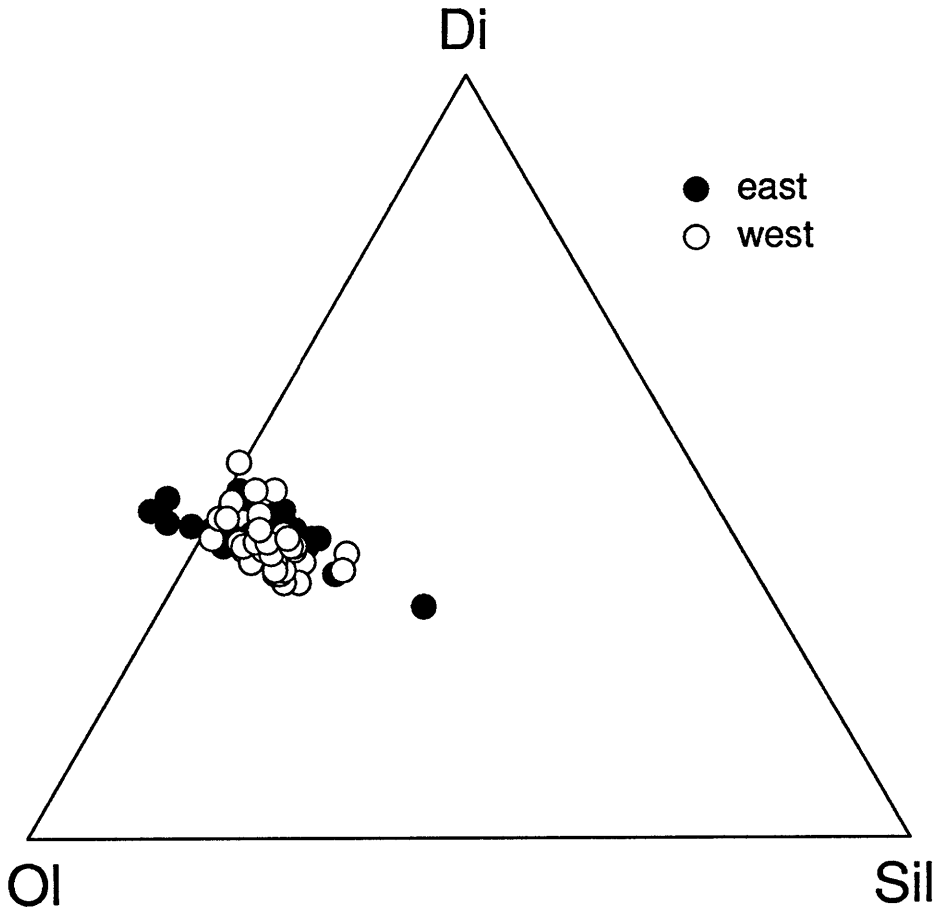

Figure 10. Pseudoternary projection of basalt glass compositions from plagioclase onto the plane diopside-olivine-silica using the plotting algorithm of Walker et al. [1979]. Most of the samples plot at the low silica side of the diagram, consistent with derivation by low degrees of melting.

the observed differences in peridotite compositions across the transform, it would be useful to know if basalts also show fundamental compositional differences that can be ascribed to a process other than fractional crystallization. As mentioned above, documenting compositional gradients in the basalts is more dubious due to sampling deficiencies.

In order to compare major element compositions of basalts from different localities with spatially associated peridotites, *Bryan and Dick* [1982] and *Dick et al.* [1984] used the positions of liquid lines of descent for the basalts in the normative pyroxene-plagioclase-olivine ternary. They found that genetically related basalts plot on a single line in this diagram, and they related this line to the position of the olivine-plagioclase cotectic boundary in the synthetic system albite-anorthite-diopside-forsterite. When compared at a constant normative olivine composition, the Na/Ca ratios are higher in basalts that lie on liquid lines of descent that plot closer to the plagioclase apex, consistent with the migration of the plagioclase-olivine cotectic toward the plagioclase apex with increasing albite content of the melt. The Na/Ca ratio of the melt (i.e. albite/anorthite content) is, in turn, related to the amount of diopside that is melted in the source peridotite since Ca is buffered by diopside and Na though present in diopside as jadeite molecule, behaves incompatibly. Thus, Na/Ca will gradually decrease in the melt with increased melting and consumption of diopside from the peridotite, and the basalt liquidus trend will become more Ca-rich (higher normative An and Di) and will shift to the right toward the pyroxene apex. Thus the position of basalt normative liquid lines of descent and various peridotite compositional indices should correlate in genetically related basalt-peridotite systems. It was noted that modal diopside in spatially associated peridotites does in fact increase as the Na/Ca ratios in basalts increase, consistent with the above argument [*Dick et al.*, 1984].

In order to examine possible basalt compositional differences across the Atlantis II Fracture Zone, and their relation to certain peridotite characteristics, the basalt glasses from the east and west sides of the Atlantis II Fracture Zone were plotted in the normative pyroxene-plagioclase-olivine ternary (Figure 11). Although the basalts plot close to each

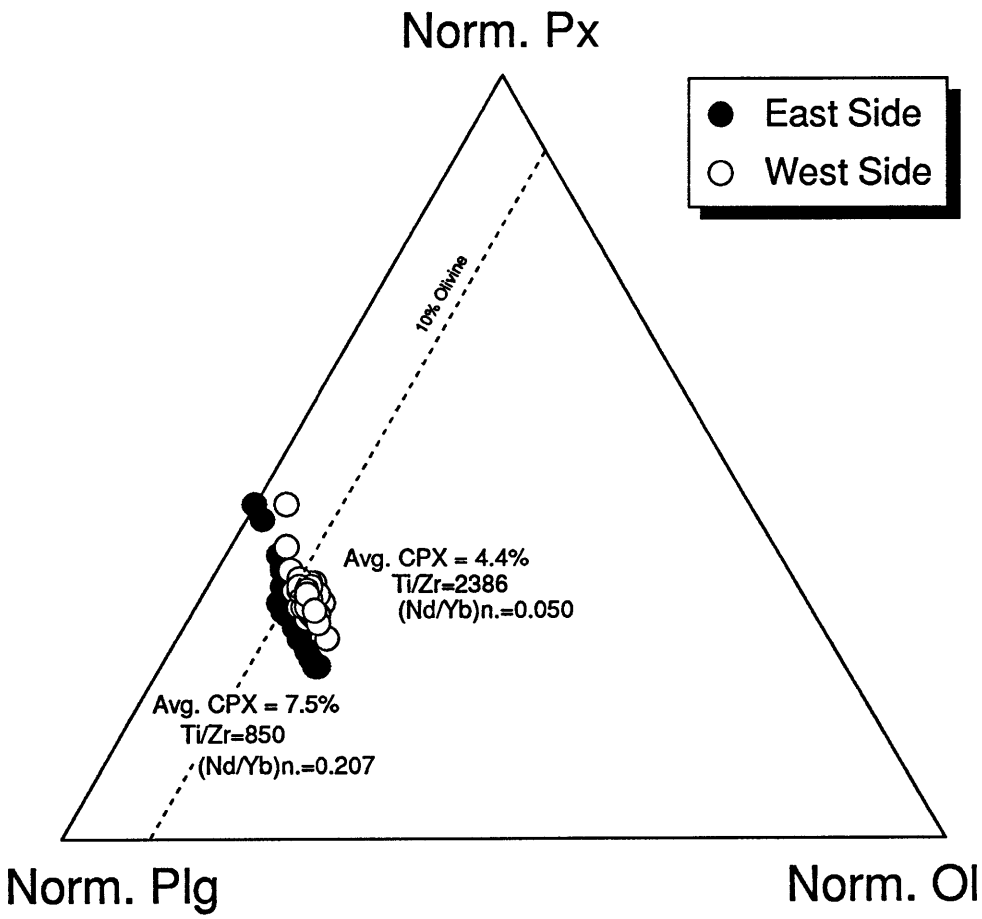

Figure 11. Ternary plot of normative pyroxene-plagioclase-olivine for glasses from the Atlantis II Fracture Zone. Norms are calculated with all iron as FeO. The numbers beside the symbols are average modal clinopyroxene, average Ti/Zr ratio in peridotite clinopyroxenes, and average (Nd/Yb)n in peridotite clinopyroxenes for each side of the transform. Modal clinopyroxene and (Nd/Yb)n are expected to decrease, and Ti/Zr is expected to increase with increased melting. The dashed line is constant 10% normative olivine.

other and in some instances overlap, they appear to define distinct liquid lines of descent. Furthermore, the relative positions of these lines is consistent with basalts from the western side of the transform being formed by generally higher degrees of melting than basalts from the eastern side. This is compatible with the observation that average modal diopside in peridotites from the western side of the transform is lower than that in peridotites from the eastern side (Figures 5 and 8), as annotated in Figure 11 (average modal diopside in all peridotite samples collected, H. Dick, unpublished modal data). Moreover, average Ti/Zr ratios in peridotite diopsides from the western side of the transform are significantly higher, and $(Nd/Yb)_n$ lower than in samples from the eastern side, again consistent with higher degrees of melting on the western side of the transform.

The normative discriminant employed by *Dick et al.* [1984] normalized basalt compositions to 10% normative olivine to account for crystal fractionation. A similar approach was employed by *Klein and Langmuir* [1987] in their study of global basalt correlations. They also looked at Na as a monitor of degree of melting in basalts, calculated liquid lines of descent for suites of basalts in MgO vs. Na_2O, and used these liquid lines of descent to normalize basalt compositions to an arbitrary 8 wt% MgO (referred to as $Na_{8.0}$; cf. 10% normative olivine in *Dick et al.* [1984]), following the conceptual approach of *Dick et al.* [1984] and *Langmuir and Bender* [1984]. In this way, basalt compositions from different locations are corrected for olivine fractionation and compared with each other at the same hypothetical MgO concentration. *Klein and Langmuir* [1987] extended this procedure to evaluate mean relative pressures of melting using $Fe_{8.0}$ as an index, based on experimental evidence that the iron content in primary melts varies as a function of pressure [*Jaques and Green*, 1980].

The Klein and Langmuir approach, though based on the same concepts as the approach presented by *Dick et al.* [1984], is more convenient to use. Equations for liquid lines of descent calculated from the Atlantis II Fracture Zone basalt data are essentially the same as those calculated from global mid-ocean ridge basalt data by *Klein and Langmuir* [1987].

The parameters in the following plot were calculated using *Klein and Langmuir*'s [1987] liquid lines of descent: $Na_{8.0} = Na_2O + 0.373MgO - 2.98$, and $Fe_{8.0} = FeO + 1.664MgO - 13.313$. Figure 12a is a plot of $Na_{8.0}$ versus $Fe_{8.0}$ for the Atlantis II Fracture Zone basalt glasses. Although there is overlap in the $Na_{8.0}$ ranges for basalts from either side of the transform, the two sides are well separated in terms of the $Fe_{8.0}$ parameter. This supports the interpretations above for slightly lower degrees of melting producing melts on the eastern side, but it also indicates that the melting may have occurred at shallower mean depths.

Available REE data for the glasses are also generally consistent with lower degrees of melting on the eastern side. $(Ce/Sm)_n$ is expected to be higher in melts formed by lower degrees of melting, which is roughly observed in eastern lavas (Figure 12b). However, the greater mean depth of melting in western lavas, inferred from their higher $Fe_{8.0}$, apparently does not include large contributions from garnet, since $(Ce/Sm)_n$ is lower in these lavas than in eastern lavas.

PERIDOTITE MELTING MODEL

In the above section on peridotite clinopyroxenes, Figure 7 showed a strong curvature in the data for Ti/Zr versus Nd_n. Since these rocks are all residual after melting, the most likely explanation for this data configuration is that it represents a melting trend starting from a roughly similar source. Since the Atlantis II Fracture Zone is far from any hotspot, assuming a uniform source is not unreasonable, especially given the relative isotopic homogeneity of the basalts [J. Snow, personal communication ,1990]. To test this hypothesis, a fractional melting model was constructed using the equations derived in the appendix of Chapter 2 and the model assumptions listed in Table 5. The results of this model are shown in Figure 13a, which also has the data plotted as in Figure 7. The starting compositions are ~2 times chondritic values reported in *Anders and Grevesse* [1989].

Figure 12. Chemical discriminant plots of basalt glass data. (a) $Na_{8.0}$ versus $Fe_{8.0}$ calculated using the liquid lines of descent presented by [*Klein and Langmuir*, 1987] for their global basalt data set. Calculated liquid lines of descent from the Atlantis II Fracture Zone basalt glasses were essentially identical to those of [*Klein and Langmuir*, 1987], so for uniformity their equations were used. High $Fe_{8.0}$ has been used to infer greater relative mean depths of melting, and high $Na_{8.0}$ has been used to infer lower relative extents of melting to produce a given magma or group of cogenetic magmas [*Klein and Langmuir*, 1987]. By this measure, in general lavas erupted on the eastern side were produced at the shallower levels and by the lower degrees of melting than samples from the western side. (b) $Fe_{8.0}$ versus $(Ce/Sm)_n$, another indication of the degree of melting that produced the glasses. Higher degrees of melting of a given source produces lower values of $(Ce/Sm)_n$, consistent with the major element data.

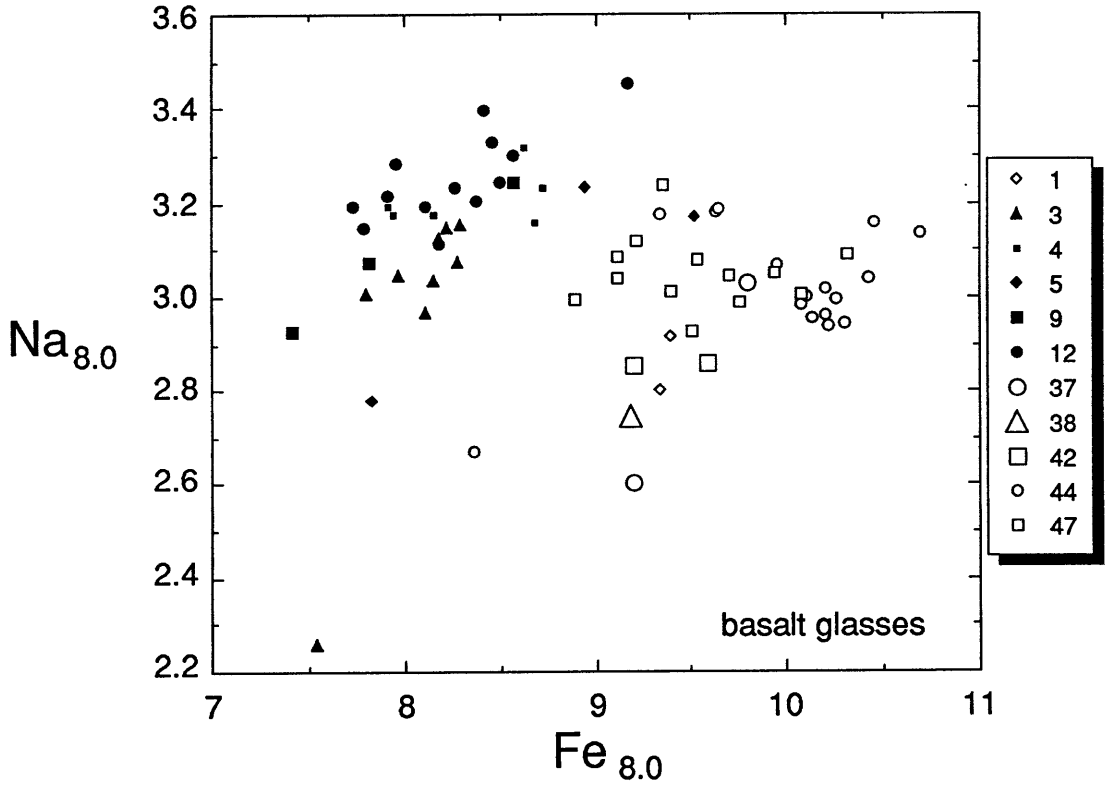
3.6
3.4
3.2
3.0
2.8
2.6
2.4
2.2
Na8.0
7
8
9
10
11
Fe 8.0
basalt glasses
1
3
4
5
9
12
37
38
42
44
47

Figure 12a

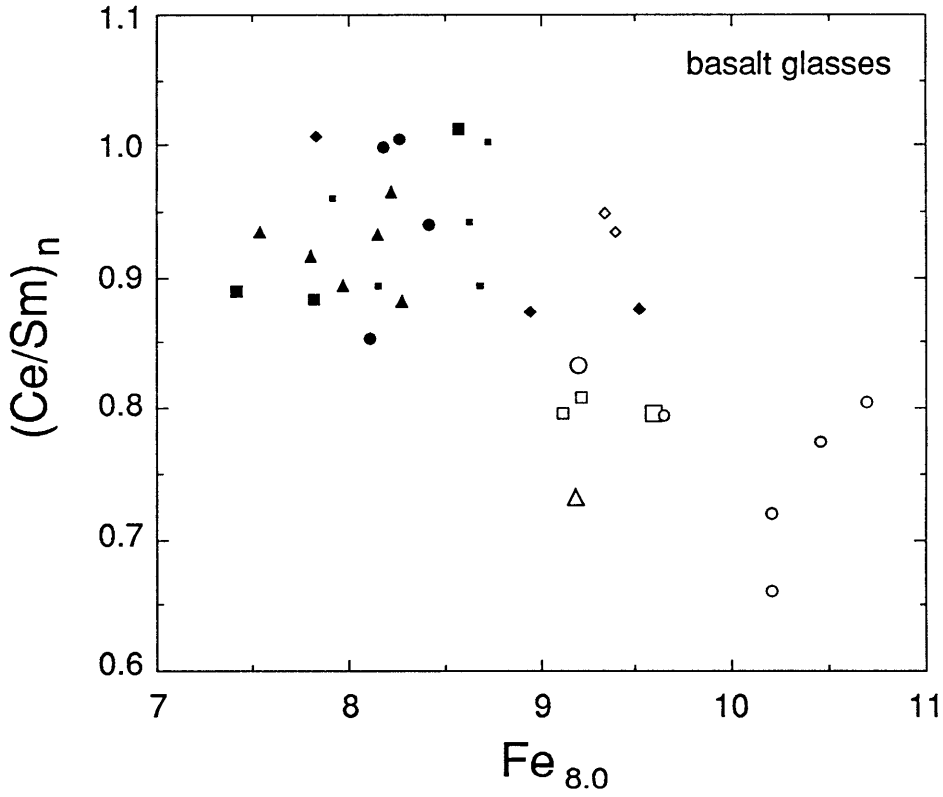

Figure 12b

The data agree very well with the model for melting in the spinel field only, but the more depleted samples could be formed by ~5% initial melting in the presence of residual garnet, with continued melting in the spinel field to a total of 15-17%. There is a gap in the data in the critical range where the model curves bend sharply toward high Ti/Zr, so the need for garnet in the source to explain the data cannot be resolved. In a log-log plot (Figure 13b), the models are better separated. Here, the garnet plus spinel models do not match the depleted Atlantis II data as well as the spinel only model does. However, clinopyroxene data from the Bouvet Fracture Zone, plotted as small plusses, is consistent with low to moderate degrees of melting in the garnet stability field, as was argued in Chapter 2. Subtle differences in the partition coefficients and in the modal proportions of minerals, both in the solid and entering the melt, will change the curvature of the model trends, and small differences in the starting compositions will affect the position of the curves. The parameters listed in Table 5 are well within the accepted range of values for these quantities.

TABLE 5. MODEL PARAMETERS

	Olivine	Orthopyroxene	Clinopyroxene	Spinel	Garnet	C_o
D_{Ti}	0.007	0.08	0.36	0.07	0.6	1000 ppm
D_{Zr}	0.003	0.02	0.16	0.04	0.5	7.5 ppm
D_{Nd}	0.0007	0.015	0.22	0.0008	0.05	2x chond.
$X_{\alpha,sp}$	0.550	0.250	0.180	0.020		
$p_{\alpha,sp}$	0.100	0.200	0.680	0.020		
$X_{\alpha,gt}$	0.570	0.180	0.120		0.130	
$p_{\alpha,gt}$	0.030	0.030	0.440		0.500	

Data sources are listed in Appendix to Chapter 2, except D_{cpx}, which come from Chapter 3.
$X_{\alpha,sp}$ - initial phase proportions (volume %, converted to wt% for calculation) in spinel peridotite.
$p_{\alpha,sp}$ - proportion of phases entering the melt in the spinel stability field.
$X_{\alpha,gt}$ - initial phase proportions in garnet peridotite.
$p_{\alpha,gt}$ - proportion of phases entering the melt in the garnet stability field.

It appears, then, that much of the compositional variation in the Atlantis II Fracture Zone peridotites can be simply explained by varying degrees of melting on a very short

Figure 13. The same plot as Figure 7, but with several calculated melting models superimposed. The method for calculating these melting curves is the same as that used in Chapter 2 and detailed in the Appendix to Chapter 2. a) is a normal plot of the data showing the strong curvature in the data and fractional melting models produced by moderate degrees of melting. The range in degrees of fractional melting needed to account for the clinopyroxene compositions is 5-17%. A model for 5% initial melting in the garnet stability field, followed by the decompression reaction used in Chapter 2 and continued melting in the spinel stability field is shown as the curve with triangles; 5%+5% indicates 5% fractional melting in the garnet stability field, followed by 5% additional melting in the spinel stability field, etc. The presence of garnet produces sharper curvature of the model curve due to the rapid depletion of Nd in the residue. The absence of peridotite data in the critical region of curvature prevents a well-constrained argument for or against the need for garnet in the source. b) a log-log plot of the data and models in a) to better separate the curves. In this representation, the garnet plus spinel models do not match the data as well as the spinel only model, except at higher degrees of melting. Also shown in this diagram are clinopyroxene data from the Bouvet Fracture Zone to illustrate their similarly high Ti/Zr, but lower Nd. In their case, garnet could very likely be required to explain their compositions, as was argued in Chapter 2. Also shown as a dot-dash line is the calculated batch melting trajectory up to 28%, clearly demonstrating that batch melting is inadequate to explain the peridotite compositions.

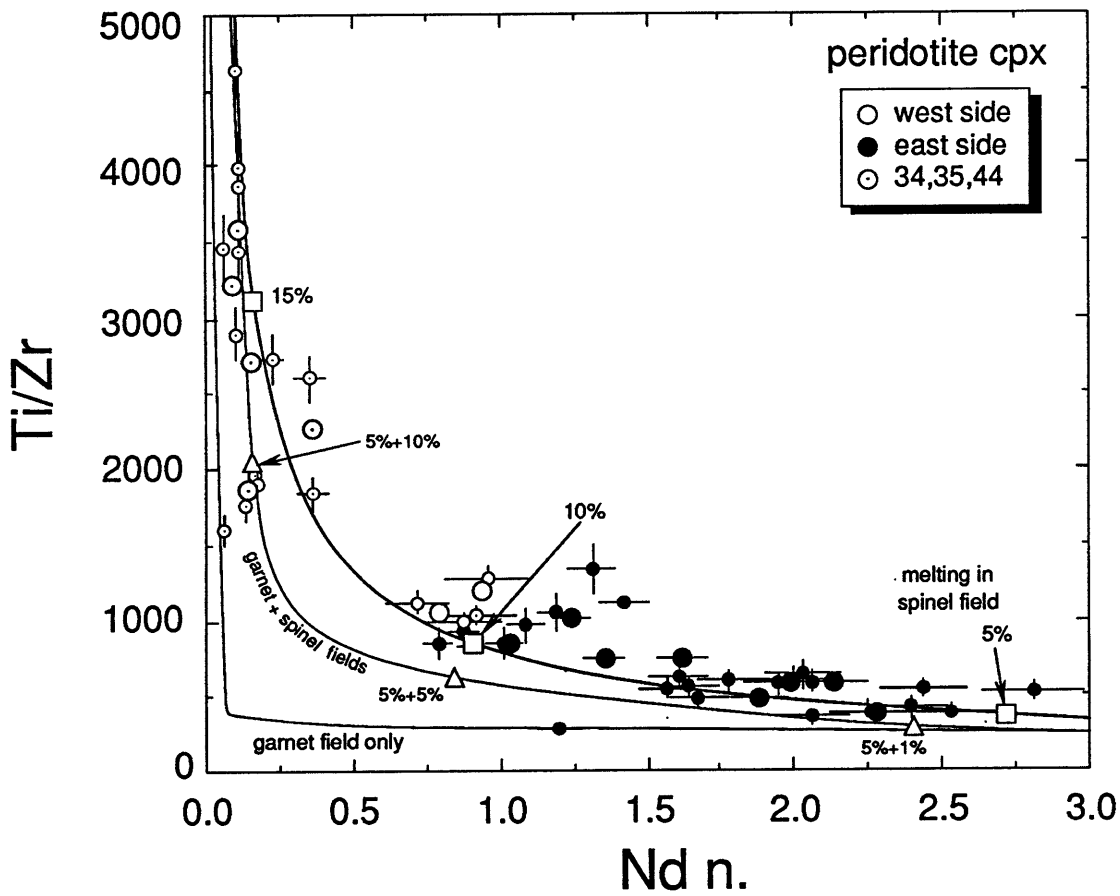
peridotite cpx
west side
east side
34,35,44
15%
5%+10%
10%
melting in
spinel field
5%
garnet + spinel fields
5%+5%
garnet field only
5%+1%
Ti/Zr
Nd n.
5000
4000
3000
2000
1000
0
0.0
0.5
1.0
1.5
2.0
2.5
3.0

Figure 13a.

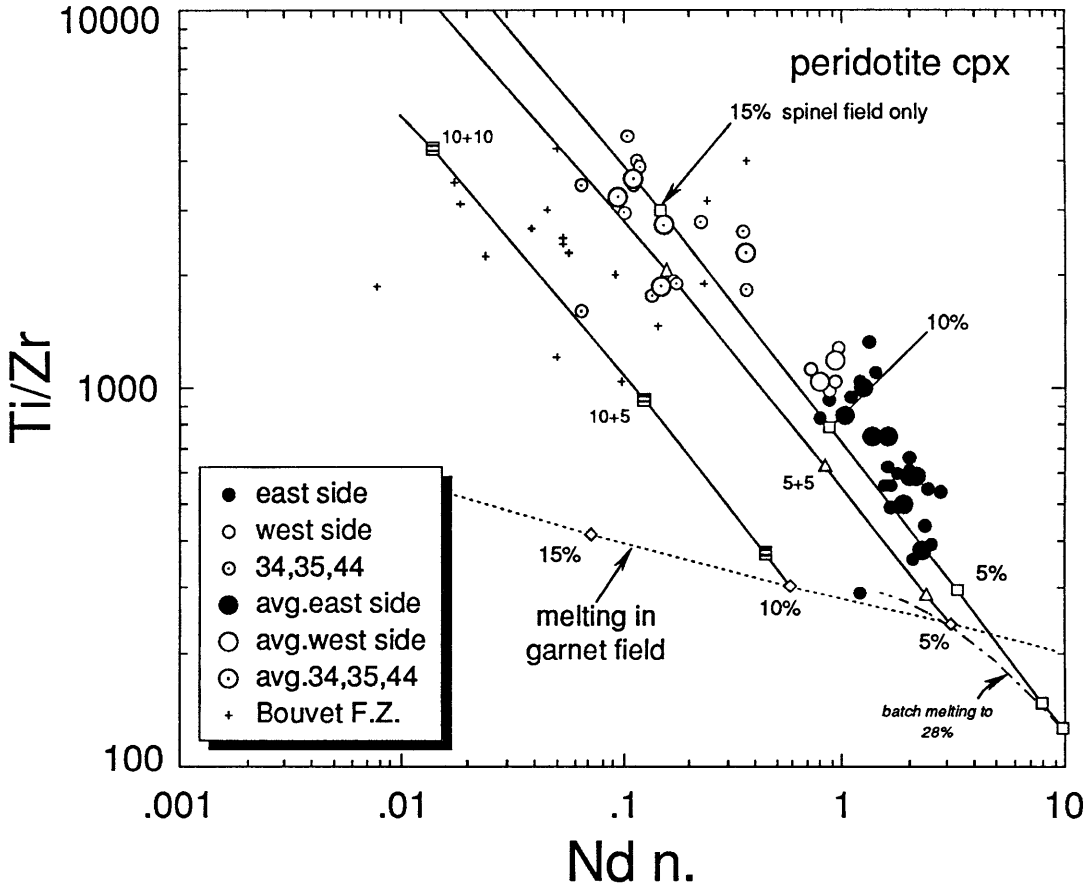
peridotite cpx
15% spinel field only
10+10
10%
10+5
5+5
15%
10%
5%
5%
melting in
garnet field
batch melting to
28%
east side
west side
34,35,44
avg.east side
avg.west side
avg.34,35,44
Bouvet F.Z.
10000
1000
100
Ti/Zr
.001
.01
.1
1
10
Nd n.

Figure 13b

wavelength. The range in degree of melting inferred from the model, from ~5% to ~17%, is nearly as large as the range inferred in the large scale study of the Southwest Indian Ridge [*Johnson et al.*, 1990]. At first, this might seem surprising given that the Atlantis II Fracture Zone is far from the influence of hotspots. However, previous detailed studies of compositional variability in abyssal peridotites observed similar variations within single fracture zones [*Dick et al.*, 1984; *Michael and Bonatti*, 1985]. This was the reason that those authors compared fracture zone averages for many of their discussions. However, the high sampling density in the Atlantis II Fracture Zone affords the opportunity to investigate the systematics of these local variations and implies that high degrees of melting can occur episodically regardless of proximity to an obvious thermal anomaly.

To summarize the results, peridotite clinopyroxene compositions vary both along the strike of the transform fault (along lithospheric flow lines), and on either side of the transform. Systematic, progressive depletion from the center of the eastern wall to the northern ridge axis is observed (approximately 100 km). Peridotites from the western wall are, in general, more depleted than those from the eastern side. The overall depletion can be modeled by fractional melting over the range of 5% to 17%.

Basaltic glasses show gross compositional variations similar to those observed in the peridotite clinopyroxenes. A first order similarity is that the basalts from the western side of the transform are different in composition than those from the eastern side. By various diagnostic chemical ratios and parameters, the basalts from the western side appear to have been generated at higher mean pressures and higher degrees of melting. Furthermore, dredge 12 basalts, from a transform volcano that is located about 10-15 km from the northern ridge-transform intersection, are different from both nearby dredge 3 and dredge 9 basalts in having relatively higher Na at given Mg and Fe concentrations.

DISCUSSION

Most previous studies on ridge segmentation have concentrated on along-axis compositional variability in the basalts, none have looked in detail at the variability along mantle flow lines perpendicular to the ridge axis. The reasons for this are that sampling is more difficult away from the ridge where sediment blankets the lavas. The other obvious places to conduct such a study, along fracture zones, as in the present study, have been largely avoided except to study the effects that the fracture zone has on the evolution of the basalts. Because of the apparent "cold edge" effect of transform faults on the thermal regime and subsequent chemical evolution of mid-ocean ridge magmas erupted near ridge-transform intersections [*Langmuir and Bender*, 1984; *Bender et al.*, 1984], it has been argued that crust produced near transform faults is therefore anomalous in the ocean basins and that crust produced closer to the centers of spreading cells is "normal". This may be true in some cases, but various authors have argued that there are no differences between basalts erupted in fracture zones and ridge segments along the Southwest Indian and American-Antarctica Ridges, except in an isolated case at the Conrad Fracture Zone [*leRoex et al.*, 1983, 1985]. However, abundant evidence shows that slow- and fast-spreading ridges are punctuated by a variety of axial discontinuities that can have subtle morphological expressions, but profound chemical effects [*Bryan et al.*, 1981; *Langmuir et al.*, 1986; *Batiza et al.*, 1988]. This, along with the observation that long (100 - 250 km) transform faults occur every 30 - 100 km along very-slow-spreading ridge systems [*Schouten et al.*, 1985], e.g. the Southwest Indian Ridge, means that most of the lithosphere accreted in very-slow-spreading regions is formed through some influence by transform faults or other ridge discontinuities. For these reasons, crust produced in the vicinity of transform faults should no longer be considered "anomalous", but must be considered "normal" in these and, arguably, in other regions.

Although transform faults may remain distinct for very long periods of time (up to 10^8 yr, *Schouten and Klitgord* [1982]), and thus separate large magmatic cells which have a

characteristic period of activity [*Schouten et al.*, 1985], little is known about the temporal variability or persistence of smaller magmatic segments. Morphological expressions of some of the shorter wavelength, lower order ridge discontinuities are manifested over time scales of 10^3 - 10^6 yr [*Langmuir et al.*, 1986; *Macdonald et al.*, 1988]. It would be useful, then, to know how mantle melting within a cell varies over time along a given mantle flow line, and by how much. Such knowledge could place constraints on the significance of long wavelength zero-age geochemical, morphological, seismic, and potential field variations, as well as providing clues about the nature and scales of mantle upwelling, the fundamental sizes of upwelling cells, and the frequency of melting pulses within individual cells.

Abundant geological and geophysical evidence suggests that accretion at mid-ocean ridges is episodic. Morphologically, the rift valley varies in depth and width along strike [*Francheteau and Ballard*, 1983; *Karson et al.*, 1987; *Kong et al.*, 1988; *Macdonald et al.*, 1988] and is interpreted to be in different stages of activity. At 23°N on the Mid-Atlantic Ridge south of the Kane Fracture Zone Sea MARC I side scan sonar data and SeaBeam bathymetry were used to infer the stages of tectonomagmatic evolution of two *en echelon* spreading cells [*Kong et al.*, 1988]. The northern segment in that study is characterized by a well developed constructional ridge with associated high temperature hydrothermal activity, and is inferred to be in an active magmatic accretionary phase. The southern segment is dominated by a NNE-trending band of small fissured and faulted volcanoes built upon old fissured and sediment-covered lavas, and is inferred to be in a predominantly extensional phase dominated by stretching and normal faulting [*Kong et al.*, 1988]. Further, a coupled seismic refraction experiment and microearthquake study at 26°N on the Mid-Atlantic Ridge correlated variations in hypocentral depths and distribution, crustal velocity structure, and present-day seafloor hydrothermal activity to argue that magmatic activity is temporally variable in that region [*Kong*, 1990]. This is supported by a study by *Solomon et al.* [1988] on the global rate of seismic moment release in which it was

concluded that only 10-20% of seafloor spreading is attributable to seismogenic extension. The inference is that the remainder of the spreading occurs by aseismic processes such as magmatic intrusion at the neovolcanic zone. *Schouten and Klitgord* [1982] have related this volcanic-tectonic cycle to a balance between lithospheric strength, the state of stress in a spreading center segment, and the strain rate in the segment. Thus, spatial variability in magmatic activity along the ridge implies a temporal variability as well.

Additional support for temporal variability in magmatic activity comes from morphological observations made by *Pockalny et al.* [1988] on the Mid-Atlantic Ridge near the Kane Fracture Zone. A series of elongated constructional features that parallel the ridge off-axis were interpreted as manifestations of oscillations in magmatic activity at the neovolcanic zone. Consistent with this interpretation, *Scott and Stevenson* [1989] have shown that mantle upwelling changes from steady-state at high spreading rates, to episodic at low spreading rates, with a period of oscillation that increases with decreasing spreading rate. This results in bursts of rapid decompression, upwelling, and high degrees of melting, punctuated by periods of little or no melting. If this is true, then some aliquots of mantle might show the effects of increased melting, while others wil not. Whether the chemical gradient observed on the eastern side of the transform is part of such a long-period, episodic variation in mantle melting, or is just a gradual increase in degree of melting over the past 10-11 million years cannot be resolved by the present data. Similar studies must be conducted at ridges with higher spreading rates to test the *Scott and Stevenson* [1989] hypothesis.

An increase of 5% fractional melting over a period of ~10 million years is required to explain the compositional range observed in peridotites from the eastern wall (Figure 13). Although the relationship between mantle temperature and degree of fractional melting is not known, estimates of the change in degree of melting with changes in mantle temperature have been made, based on existing experimental data [*McKenzie and Bickle*, 1988]. Using their parameterized temperature function [*McKenzie and Bickle*, 1988, p.

640], a change in potential temperature of 15-20° will cause a 5% increase in melting. Since the parameterization was based on experimental data, which are effectively batch melts, the required change in temperature might be expected to increase if fractional melting is predominant since refractory residues devoid of melt would have higher heats of fusion and thus higher solidus temperatures. Therefore, the observed compositional gradient in the peridotites could correspond to a gradual increase in mantle potential temperature of 2°/my for at least the past 10 my on the eastern side of the transform.

On the western side of the transform, a compositional gradient, though suggested by the data, is poorly constrained. In a rough sense, a similar argument could be made, but more data are needed before significant inferences about compositional and thermal gradients can be made. However, there is a strong suggestion of generally higher degrees of melting experienced by peridotites on the western side. This is coupled with apparently deeper melting to produce basalts on this side of the transform (higher $Fe_{8.0}$), which together suggest an overall higher mantle potential temperature on the western side of the transform, causing the geotherm to intersect the solidus at higher pressures. Alternatively, a single mantle potential temperature could act on different source compositions, producing different extents of melting in each. This scenario is difficult to assess without isotopic data, but it would appear to contradict the coupled basalt and peridotite data. The refractory, depleted mantle on the western side would be expected to melt less, and perhaps shallower, than the less depleted mantle on the eastern side. This would produce basalts with lower $Fe_{8.0}$, and higher $Na_{8.0}$ and $(LREE/MREE)_n$, opposite to what is observed.

The above suggestion that depleted chemical compositions in basalts and peridotites result from temporal variations in the degree of mantle melting implies that crustal thickness must also vary in time. Variations in seismic structure have been linked to non-uniform thinning of layers 2 and 3 along lithospheric flow lines perpendicular to the ridge axis or to the absence of layer 3 altogether [*Sinha and Louden*, 1983; *Purdy and Ewing*, 1986].

Magmatic segmentation across transform faults and other axial discontinuities is commonly observed. The variations in small-scale discontinuities can often be as pronounced as those across major transform offsets [e.g. *Langmuir et al.*, 1986]. The variations across transforms have been attributed to long-lived separations of mantle sources and to cooling edge effects associated with the transform discontinuities [*Bender et al.*, 1984; *Langmuir and Bender*, 1984]. It is now apparent that superimposed on these ridge parallel variations are episodic, deep-seated fluctuations in mantle melting recorded along lithospheric flow lines perpendicular to the ridge. Hence, the 10-50 km small-scale magmatic segmentation observed in basalt compositions along the Mid-Atlantic Ridge and the East Pacific Rise ("devals" and "SNOOS" of *Langmuir et al.* [1986], and fourth-order segmentation of *Macdonald et al.* [1988]), inferred to be caused by crustal differentiation in along-axis magma chambers, may in fact be caused by temporal, as well as spatial, fluctuations in mantle melting.

The peridotite data from dredges 23 and 25 along the northern median tectonic ridge support the model proposed by *Dick et al.* [1990] for the tectonic evolution of the transform fault. Those authors produce a tectonic reconstruction in which the median tectonic ridge is crust transferred across the transform boundary from the Antarctica to the African plate due to plate readjustment in response to a spreading direction change. The inferred present-day slip zone of the transform is along the eastern wall [*Dick et al.*, 1990], but there was a change in spreading direction at 20-22 Ma which put the transform zone into extension. Although the northern extensional basin is now part of the western side of the transform, the peridotites exposed along the median tectonic ridge bear chemical similarities to peridotites from the eastern wall of the transform. Thus, it may be that during the period of transform extension, from 20-22 Ma to 6-7 Ma, the mantle represented in dredges 23 and 25 was beneath the extensional zone and was part of the eastern mantle unit. The migration of the transform would have also caused mylonitization, leading to the observed extreme

serpentinization of the peridotites in dredges 23 and 25 (see *Dick et al.* [1990] for details of the tectonic evolution of this feature).

An hypothesis for the variations in peridotite compositions observed in the Atlantis II Fracture Zone must be integrated with the well documented long-wavelength variations in peridotite and basalt compositions along the mid-ocean ridge system [*Dick et al.*, 1984; *Michael and Bonatti*, 1985; *Klein and Langmuir*, 1987; *Johnson et al.*, 1990]. These studies showed that proximity to hotspots was correlated with depletion in modal pyroxene and incompatible elements in peridotites and with generally higher degrees of melting in associated MORB. *Dick et al.* [1984] and *Michael and Bonatti* [1985] used averages of modal and chemical data for individual locations (e.g. fracture zone) to show that the upper mantle in the vicinity of hotspots was characteristically more depleted in diopside and incompatible elements than that away from hotspots and to argue that this was a direct consequence of higher degrees of melting. When individual dredge averages were plotted, scatter within a fracture zone was much larger. Thus, location averages filtered out local variations so that regional-scale trends could be characterized. Therefore, the important observation in this study is not that significant variations occur within a single fracture zone, but rather that a systematic temporal trend in mantle compositional change can be identified and linked to other ridge processes.

In essence this is a reconnaissance study, since it is the first detailed look at the covariation of peridotite and basalt compositions along and across a transform. The results illustrate the kind of detailed information on mantle variability that can only be garnered from high density sampling along transform faults. Similar studies on other ridge-transform segments near and away from hotspots and at different spreading rates will vastly expand our knowledge on the variability of magma generating processes at spreading centers.

CONCLUSIONS

The results of this study on spatial and temporal variations of peridotite and basalt compositions in the Atlantis II Fracture Zone provide the following conclusions:

1. Significant compositional variability in peridotite clinopyroxenes was found in the Atlantis II Fracture Zone. The range of clinopyroxene compositions in this fracture zone, far removed from the influence of a hotspot, covers approximately three fourths of the range described for 5000 km of the Southwest Indian and American-Antarctic Ridge systems [*Johnson et al.*, 1990; Chapter 2]. However, the mean composition of peridotite clinopyroxenes in the Atlantis II Fracture Zone, which may be more indicative of regional thermal conditions in the mantle, is less depleted than that of hotspot-proximal peridotites.

2. Major offsets in the ridge axis, i.e. transform faults, act as effective boundaries between large spreading cells. This has been demonstrated by a variety of observations that now includes peridotite compositions. Peridotite clinopyroxenes from the western wall of the transform are significantly more depleted in incompatible trace elements than are those from the eastern wall. The depletions in the peridotites are modeled by higher degrees of mantle melting and correlate with compositional differences observed in basaltic glasses from either side of the transform.

In general, major element compositions of glasses from the western side of the transform are distinctly offset from those of glasses from the eastern side. The western glasses are consistent with formation by slightly higher degrees of melting and slightly greater mean depths of melting than the eastern glasses.

3. Superimposed on the across-transform compositional variations are along-transform gradients in peridotite clinopyroxene compositions. These compositional gradients are most pronounced in the peridotites from the eastern side and imply a gradual increase in degree of mantle melting over at least the last 10 my. Whether this is an episodic feature or not cannot be resolved with the present data. A suggestion of similar, possibly shorter

wavelength episodicity on the western side of the transform is poorly constrained by the present dredge recoveries, but deserves further investigation.

REFERENCES

Anders, E., and N. Grevesse, Abundances of the elements: Meteoritic and solar, *Geochim. Cosmochim. Acta, 53*, 197-214, 1989.

Batiza, R., W. G. Melson, and T. O'Hearn, Simple magma supply geometry inferred beneath a segment of the Mid-Atlantic Ridge, *Nature, 335*, 428-431, 1988.

Bender, J. F., C. H. Langmuir, and G. N. Hanson, Petrogenesis of basalt glasses from the Tamayo region, East Pacific Rise, *J. Petrol., 25,* 213-254, 1984.

Bryan, W. B., G. Thompson, and J. N. Ludden, Compositional variation in normal MORB from 22°-25°N: Mid-Atlantic Ridge and Kane Fracture Zone, *J. Geophys. Res., 86*, 11,815-11,836, 1981.

Bryan, W. B., and H. J. B. Dick, Contrasted abyssal basalt liquidus trends: evidence for mantle major element heterogeneity, *Earth Planet. Sci. Lett., 58,* 15-26, 1982.

Dick, H. J. B., Abyssal peridotites, very-slow spreading ridges and ocean ridge magmatism, in *Magmatism in the Ocean Basins,* edited by A. D. Saunders and M. J. Norry, pp. 71-105, Geol. Soc. London Spec. Pub. No. 42, 1989.

Dick, H. J. B., R. L. Fisher, and W. B. Bryan, Mineralogic variability of the uppermost mantle along mid-ocean ridges, *Earth Planet. Sci. Lett., 69,* 88-106, 1984.

Dick, H. J. B., H. Schouten, P. S. Meyer, D. G. Gallo, H. Bergh, R. Tyce, P. Patriat, K. T. M. Johnson, J. Snow, and A. Fisher, Tectonic evolution of the Atlantis II Fracture Zone, Proc. Ocean Drilling Program, v. 118, part B, in preparation, 1990.

Fisher, R. L., and J. G. Sclater, Tectonic evolution of the Southwest Indian Ocean since the mid-Cretaceous: Plate motions and stability of the pole of Antanrctica/Africa for at least 80 m.y., *Geophys. J. R. astron. Soc., 73*, 553-576, 1983.

Fox, P. J., and D. G. Gallo, The tectonics of ridge-transform-ridge intersections, *Tectonophysics, 104*, 204-242, 1984.

Francheteau, J., and R. D. Ballard, The East Pacific Rise near 21°N, 13°N, and 20°S; inferences for along-strike variability of axial processes, *Earth Planet. Sci. Lett., 64,* 93-116, 1983.

Fujii, T., and C. M. Scarfe, Compositions of liquids coexisting with spinel lherzolite at 10 kbar and the genesis of MORBs, *Contrib. Mineral. Petrol., 90*, 18-28, 1985.

Hart, S. R., J.-G. Schilling, and J. L. Powell, Basalts from Iceland and along the Reykjanes Ridge: Sr isotope geochemistry, *Nature Phys. Sci., 246,* 104, 1973.

Jaques, A. L., and D. H. Green, Anhydrous melting of peridotite at 0-15 kbar pressure and the genesis of tholeiitic basalts, *Contrib. Mineral. Petrol., 73*, 287-310, 1980.

Johnson, K. T. M., H. J. B. Dick, and N. Shimizu, Melting in the oceanic upper mantle: an ion microprobe study of diopsides in abyssal peridotites, *J. Geophys. Res.*, 95, 2661-2678, 1990.

Karson, J. A., G. Thompson, S. E. Humphries, J. M. Edmond, W. B. Bryan, J. R. Brown, A. T. Winters, R. A. Pockalny, J. F. Casey, A. C. Campbell, G. Klinkhammer, M. R. Palmer, R. J. Kinzler, and M. M. Sulanowska, Along-axis variations in seafloor spreading in the MARK area, *Nature, 328*, 681-685, 1987.

Klein, E. M., and C. H. Langmuir, Global Correlations of ocean ridge basalt chemistry with axial depth and crustal thickness, *J. Geophys. Res., 92,* 8089-8115, 1987.

Kong, L. S. L., R. Detrick, P. J. Fox, L. A. Mayer, and W. B. F. Ryan, The morphology and tectonics of the MARK area from Sea Beam and Sea MARC I observations (Mid-Atlantic Ridge 23°N), *Marine Geophys. Res., 10*, 59-90, 1988.

Kong, L. S. L., Variations in Structure and Tectonics along the Mid-Atlantic Ridge, 23°N and 26°N, Ph.D. Thesis, M.I.T./W.H.O.I., 1990.

Langmuir, C. H., and J. F. Bender, The geochemistry of oceanic basalts in the vicinity of transform faults: observations and implications, *Earth Planet. Sci. Lett., 69,* 107-127,1984.

Langmuir, C. H., J. F. Bender, and R. Batiza, Petrological and tectonic segementation of the East Pacific Rise, 5°30'-14°30'N, *Nature, 322,* 422-429, 1986.

leRoex, A. P., H. J. B. Dick, A. J. Erlank, A. M. Reid, F. A. Frey, and S. R. Hart, Geochemistry, mineralogy, and petrogenesis, of lavas erupted along the Southwest Indian Ridge between the Bouvet triple junction and 11 degrees east, *J. Petrol., 24,* 267-318, 1983.

leRoex, A. P., H. J. B. Dick, A. J. Erlank, A. M. Reid, F. A. Frey, Erlank, A. J., and S. R. Hart, Petrology and geochemistry of basalts from the American-Antarctic Ridge, Southern Ocean: Implications for the westward influence of the Bouvet mantle plume, *Contrib. Mineral. Petrol., 90,* 367-380, 1985.

Macdonald, K., J.-C. Sempere, and P. J. Fox, East Pacific Rise from Siqueiros to Orozco Fracture Zones: Along-strike continuity of axial neovolcanic zone and structure and evolution of overlapping spreading centers, *J. Geophys. Res., 89,* 6049-6069, 1984.

Macdonald, K. C., P. J. Fox, L. J. Perram, M. F. Eisen, R. M. Haymon, S. P. Miller, S. M. Carbotte, M.-H. Cormier, and A. N. Shor, A new view of the mid-ocan ridge from the behaviour of ridge-axis discontinuities, *Nature, 335,* 217-225, 1988.

McKenzie, D., and M. J. Bickle, The volume and composition of melt generated by extension of the lithosphere, J. Petrol., 29, 625-679, 1988.

Michael, P. J., and E. Bonatti, Peridotite composition from the North Atlantic: Regional and tectonic variations and implications for partial melting, *Earth Planet. Sci. Lett., 73,* 91-104, 1985.

Mysen, B. O., and I. Kushiro, Compositional variations of co-existing phases with degree of melting of peridotite in the upper mantle, *Am. Mineral., 62,* 843-865, 1977.

Pockalny, R. A., R. S. Detrick, and P. J. Fox, Morphology and tectonics of the Kane Transform from Sea Beam bathymetry data, *J. Geophys. Res., 93,* 3179-3193, 1988.

Purdy, G. M., and J. Ewing, Seismic structure of the ocean crust, in *The Geology of North America, volume M, The Western North Atlantic Region*, edited by P. R. Vogt and B. E. Tucholke, pp. 313-330, Geol. Soc. of America, 1986.

Schilling, J.-G., M. Zajac, R. Evans, T. Johnston, W. White, J. D. Devine, and R. Kingsley, Petrologic and geochemical variations along the Mid-Atlantic Ridge from 29°N to 73°N, *Am. J. Sci., 283*, 510-586, 1983.

Schouten, H., and R. S. White, Zero offset fracture zones, *Geology, 8,* 175-179, 1980.

Schouten, H., and K. D. Klitgord, The memory of the accreting plate boundary and the continuity of fracture zones, *Earth Planet. Sci. Lett., 59*, 255-266, 1982.

Schouten, H., K. D. Klitgord, and J. A. Whitehead, Segmentation of mid-ocean ridges, *Nature, 317,* 225-229, 1985.

Sclater, J. G., C. Bowin, R. Hey, H. Haskins, J. Peirce, J. Phillips, and C. Tapscott, The Bouvet Triple Junction, *J. Geophys. Res., 81,* 1857-1869, 1976.

Sclater, J. G., R. L. Fisher, P. Patriat, C. Tapscott, and B. Parsons, Eocene to recent development of the South-west Indian Ridge, a consequence of the evolution of the Indian Ocean triple junction, *Geophys. J. R. astron. Soc., 64,* 587-604, 1981.

Scott, D. R., and D. J. Stevenson, A self-consistent model of melting, magma migration and buoyancy-driven circulation beneath mid-ocean ridges, *J. Geophys. Res., 94,* 2973-2988, 1989.

Sinha, M. C., and K. E. Louden, The Oceanographer Fracture Zone 1. Crustal structure from seismic refraction studies, *Geophys. J. R. astron. Soc., 75,* 713-736, 1983.

Solomon, S. C., P. Y. Huang, and L. Meinke, The seismic moment budget of slowly spreading ridges, *Nature, 334,* 58-60, 1988.

Takahashi, E., Melting of a dry peridotite KLB-1 up to 14 GPa: Implications on the origin of the peridotitic upper mantle, *J. Geophys. Res., 91,* 9367-9382, 1986.

Tapscott, C. R., P. Patriat, R. L. Fisher, J. G. Sclater, H. Hoskins, and B. Parsons, The Indian Ocean triple junction, *J. Geophys. Res., 85,* 4723-4739, 1980.

Walker, D., T. Shibata, and S. E. Delong, Abyssal tholeiites from the Oceanographer Fracture Zone II. Phase equilibria and mixing, *Contrib. Mineral. Petrol., 70,* 111-125, 1979.

Whitehead, J. A., H. J. B. Dick, and H. Schouten, A mechanism for magmatic accretion under spreading centres, *Nature, 312,* 146-148, 1984.

CHAPTER 6. CONCLUSIONS

This thesis has described and discussed geochemical properties of sub-oceanic upper mantle peridotites. The chapters are presented in the order in which they were conceived, roughly a map of the thought processes that the author experienced over the past four years. The goal of all of these chapters, taken together, has been to improve our understanding of the melting process forming magmas parental to mid-ocean ridge basalts. Each project led, more or less, into the next, and they were presented in that order.

The trace element compositions of clinopyroxenes in abyssal peridotites support fractional melting as an important process in the oceanic upper mantle (Chapter 2). This conclusion was reached on the basis of forward modeling using a variant of a non-modal fractional melting equation to desribe the melting behavior of clinopyroxene in the residue. Support for the fractional melting process in the oceanic upper mantle comes from theoretical fluid dynamics [*Ahern and Turcotte*, 1979] as well as geochemical [*McKenzie*, 1985] evidence. In addition, rare earth element compositions of some peridotites close to hotspots were successfully modeled by melting beginning in the garnet stability field and continuing through the spinel field. Thus, these samples appeared to have undergone both deeper and higher degrees of melting.

Major assumptions in the above models include starting mantle composition, proportions of mineral phases in that peridotite and those entering the melt, and partition coefficients for each element used in the model. Studies of meteorites and isotopes in oceanic basalts have provided constraints on MORB source compositions, and experimental petrology has provided an understanding of the phase petrology and melting relations of presumed MORB source rocks. Adding to that body of knowledge was beyond the scope of the thesis, but some addressable questions existed about element partitioning.

Chapter 3 was undertaken to attempt to clarify some uncertainties about both absolute partitioning of elements between clinopyroxene and liquid, and relative partitioning between Zr, Ti, and the rare earth elements (REE). The calculated values for the REE presented in Chapter 3 are slightly higher than 1 atmosphere experimental values (e.g. *Grutzeck et al.* [1974]); Ti and Zr partition coefficients are nearly identical to most other studies. This means that slight negative Zr and Ti partitioning anomalies exist when these elements are plotted together with REE. Thus, partitioning of elements during melting can contribute to the formation of negative Zr and Ti anomalies in residual peridotites. These measurements require further verification, however, before any hard conclusions are made.

Another offshoot of Chapter 2 was the prediction that most N-type MORB are integrated fractional melts. It followed, then, that incompatible element depleted, fractionated, refractory fractional melts must exist somewhere between the mantle and the seafloor. Previous studies on silicate melt inclusions suggested that they might represent liquids of this kind, and a project was initiated with Dr. A. V. Sobolev of the Vernadsky Institute of Geochemistry in Moscow to investigate the trace element compositions of inclusions from a variety of settings. Although the sample suites were not suited for a systematic study of mid-ocean ridge melting, the results of the project suggested that in some cases, unusually depleted, refractory melts are trapped as inclusions. Furthermore, although the MORB suite of inclusions was from one basalt sample, some of the inclusions appeared to be unrelated to others. This implies that in a typical mid-ocean ridge basalt, such as this sample, widely variable, and sometimes unrelated, melts contribute to its formation. Thus, the results provide some support for the fractional melting hypothesis, though a systematic trace element study of melt inclusions in MORB is required to provide firmer documentation.

Finally, Chapter 5 investigated the compositions of peridotites from a single, well-sampled fracture zone in the southwest Indian Ocean. Chapter 2 and two previous studies showed that abyssal peridotite depletion correlates with proximity to hotspots. Therefore,

it seemed important to investigate how peridotite compositions varied in a single fracture zone. The Atlantis II Fracture Zone was extensively sampled during the site survey for ODP Leg 118, and 65 clinopyroxenes in seventeen peridotite samples from nine dredges were selected from that collection for major and trace element analysis.

The results of this study showed that peridotite clinopyroxene compositions in this fracture zone cover nearly the whole range defined in Chapter 2 for the American-Antarctica and Southwest Indian Ridges. The compositions are consistent with a range of ~5-15% fractional melting, the west side of the fracture zone being generally more depleted (more extensively melted) than the eastern side. Superimposed on this broad variation are distinct, systematic compositional gradients. The most striking gradient is displayed by peridotites dredged from the eastern side of the fracture zone. From the middle of the eastern transform wall to the intersection with the northern rift zone, the peridotites beome gradually more depleted in inompatible elements. This corresponds to a gradual increase in the degree of melting experienced by the mantle over the past 10-11 my. A less well-defined, possibly cyclic variation is observed on the western side over a shorter distance. Both gradients occur along a single lithospheric flow line, and thus imply a temporal variation in melting, while the across-transform compositional discontinuity indicates spatial segmentation or heterogeneity in the mantle. The along-axis extent of the temporal variations is an important question which must be answered by more extensive peridotite sampling parallel to ridge axes. The results of such sampling could help to evaluate whether some smaller scales of ridge segmentation, inferred from variations in basalt compositions to be caused by crustal differentiation, may actually be caused by variations in mantle melting.

Incompatible element and modal pyroxene depletions in peridotites corresponding to proximity to hotspots were described in Chapter 2, and previously by *Dick et al.* [1984] and *Michael and Bonatti* [1985]. The chemical depletions seen in some of the Atlantis II Fracture Zone samples were almost as extreme as those observed in Bouvet Fracture Zone

samples. It is believed that the short wavelength intra-fracture zone variations described in Chapter 5 are superimposed on the long wavelength, hotspot-correlated variations described in Chapter 2. The average Atlantis II F.Z. peridotite clinopyroxene composition is typical of other hotspot-distant compositions in Chapter 2. Regional thermal conditions, which are a function, in large part, of proximity to hotspots, may dictate the time-averaged long-wavelength chemical characteristics of the residual upper mantle [*Schilling et al.*, 1983; *Dick et al.*, 1984; *Michael and Bonatti,* 1985; *Klein and Langmuir*, 1987]. On the other hand, the short wavelength variations observed on the segment of very slow spreading ridge cut by the Atlantis II Fracture Zone may be controlled by episodic changes in the rate of mantle upwelling [*Scott and Stevenson*, 1989]. This would result in sections of the upwelling mantle experiencing rapid decompression and excessive melting relative to other nearby mantle sections, in turn leading to local variations in crustal thickness [*Purdy and Ewing*, 1986] and seafloor morphology [*Kong et al.*, 1988; *Pockalny et al.*, 1988] due to temporal variations in melt production.

REFERENCES

Ahern, J. L., and D. L. Turcotte, Magma migration beneath an ocean ridge, *Earth Planet. Sci. Lett., 45,* 115-122, 1979.

Dick, H. J. B., R. L. Fisher, and W. B. Bryan, Mineralogic variability of the uppermost mantle along mid-ocean ridges, *Earth Planet. Sci. Lett., 69,* 88-106, 1984.

Grutzeck, M., S. Kridelbaugh, and D. Weill, The distribution of Sr and REE between diopside and silicate liquid, *Geophys. Res. Lett., 1,* 273-275, 1974.

Klein, E. M., and C. H. Langmuir, Global Correlations of ocean ridge basalt chemistry with axial depth and crustal thickness, *J. Geophys. Res., 92,* 8089-8115, 1987.

Kong, L. S. L., R. Detrick, P. J. Fox, L. A. Mayer, and W. B. F. Ryan, The morphology and tectonics of the MARK area from Sea Beam and Sea MARC I observations (Mid-Atlantic Ridge 23°N), *Marine Geophys. Res., 10*, 59-90, 1988.

McKenzie, D., ^{230}Th-^{238}U disequilibrium and the melting processes beneath ridge axes, *Earth Planet. Sci. Lett., 72*, 149-157, 1985.

Michael, P. J., and E. Bonatti, Peridotite composition from the North Atlantic: Regional and tectonic variations and implications for partial melting, *Earth Planet. Sci. Lett., 73*, 91-104, 1985.

Pockalny, R. A., R. S. Detrick, and P. J. Fox, Morphology and tectonics of the Kane Transform from Sea Beam bathymetry data, *J. Geophys. Res., 93,* 3179-3193, 1988.

Purdy, G. M., and J. Ewing, Seismic structure of the ocean crust, in *The Geology of North America, volume M, The Western North Atlantic Region*, edited by P. R. Vogt and B. E. Tucholke, pp. 313-330, Geol. Soc. of America, 1986.

Schilling, J.-G., M. Zajac, R. Evans, T. Johnston, W. White, J. D. Devine, and R. Kingsley, Petrologic and geochemical variations along the Mid-Atlantic Ridge from 29°N to 73°N, *Am. J. Sci., 283*, 510-586, 1983.

Scott, D. R., and D. J. Stevenson, A self-consistent model of melting, magma migration and buoyancy-driven circulation beneath mid-ocean ridges, *J. Geophys. Res., 94,* 2973-2988, 1989.

APPENDIX A. CONTROLS ON RARE EARTH ELEMENT CONCENTRATIONS IN CLINPYROXENE IN A TWO-STAGE MELTING MODEL WITH MELTING BEGINNING IN THE GARNET STABILITY FIELD

In Chapter 1 a two-stage melting model is presented. The model calculates the composition of residual clinopyroxene in the presence of garnet, accounts for reaction of garnet to pyroxenes and spinel, and then calculates the composition of clinopyroxene with continued melting in the spinel stability field. This model, which utilized non-modal fractional melting equations from *Shaw* [1970] rewritten in terms of clinopyroxene, successfully reproduced rare earth element patterns in clinopyroxenes from the Bullard Fracture Zone (see Chapter 1). The rewritten equation is

$$\frac{C_i^{cpx}}{C_i^{o}} = \left[1 - \frac{PF}{D_i^{o}}\right]^{\frac{1}{P}} \cdot \left[\frac{D_i^{cpx/l}}{D_i^{o} - PF}\right] \qquad (1)$$

The parameters controlling C_i^{cpx} are

$C_i^{o} \equiv$ the original bulk composition of the peridotite,

$P \equiv \sum p_\alpha D_i^{\alpha/liq}$, where p_α = the proportions of mineral phase α entering the liquid and $D_i^{\alpha/liq}$ = partition coefficient of element *i* between phase α and liquid, thus P = the weighted liquid phase partition coefficient,

$D_i^{o} \equiv \sum X_\alpha D_i^{\alpha/liq}$, where X_α = modal proportion of mineral phase α in the starting bulk peridotite, thus D_i^{o} = the weighted starting bulk solid partition coefficient.

$F \equiv$ weight percent melting.

Clearly, many initial assumptions must be made in forward modeling using this equation and care must be taken in constraining these assumptions from available information. In some cases, reasonable approximations must be made. For instance, a rigorous implementation of the equation would require accounting for the change in liquid compositions produced over a melting interval [*Jaques and Green*, 1980; *Takahashi and Kushiro*, 1983; *Fujii and Scarfe*, 1985], and thus the changing proportions of minerals

entering the liquid at different degrees of melting. However, it was found that over the 0-25% range of total melting, the mean composition of liquids produced in the experiments is roughly the same as peritectic compositions [e.g. *Stolper*, 1980], and thus the latter were chosen for computational simplicity. The model parameters are listed below in Table A1.

Table A1. Model Parameters

	Olivine	CPX	OPX	Garnet	C_i^o	D_i^o	P
Ce	0.001†	0.10	0.005	0.008	1.8*	0.020	0.057
Nd	0.002	0.22	0.01	0.057	1.9	0.045	0.138
Sm	0.003	0.39	0.02	0.217	2.0	0.085	0.277
Eu	0.003	0.43	0.03	0.45	2.0	0.104	0.352
Dy	0.012	0.50	0.045	2.0	2.2	0.201	0.767
Er	0.025	0.51	0.06	3.5	2.2	0.316	1.266
Yb	0.059	0.50	0.075	7.0	2.2	0.559	2.334
X_α	0.55	0.20	0.15	0.10			
p_α	0.03	0.44	0.03	0.50			

† - crystal/liquid partition coefficients for individual elements.
* - chondrite normalized values.
Sources of partitioning data: Clinopyroxene: Chapter 3, this thesis. Olivine, opx: *Stosch* [1982], combined with cpx partition coefficients. Garnet: *Shimizu and Kushiro* [1975], *Nicholls and Harris* [1980], *Fujimaki et al.* [1984].

Two important features of the observed Bullard F.Z. clinopyroxene patterns are: 1) high concentrations of heavy rare earth elements with low concentrations of light REE, and 2) a hump in the patterns at dysprosium - erbium. It was found that melting in the garnet stability field was crucial in producing these features. This is illustrated in Figure A1, which shows model clinopyroxene patterns at 1%, 5%, 10%, and 15% fractional melting in the presence of garnet. A very curious phenomenon is that the heavy rare earth elements in clinopyroxene actually *increase* with increasing melting, whereas melting in the spinel field always results in decreasing rare earth element concentrations in clinopyroxene.

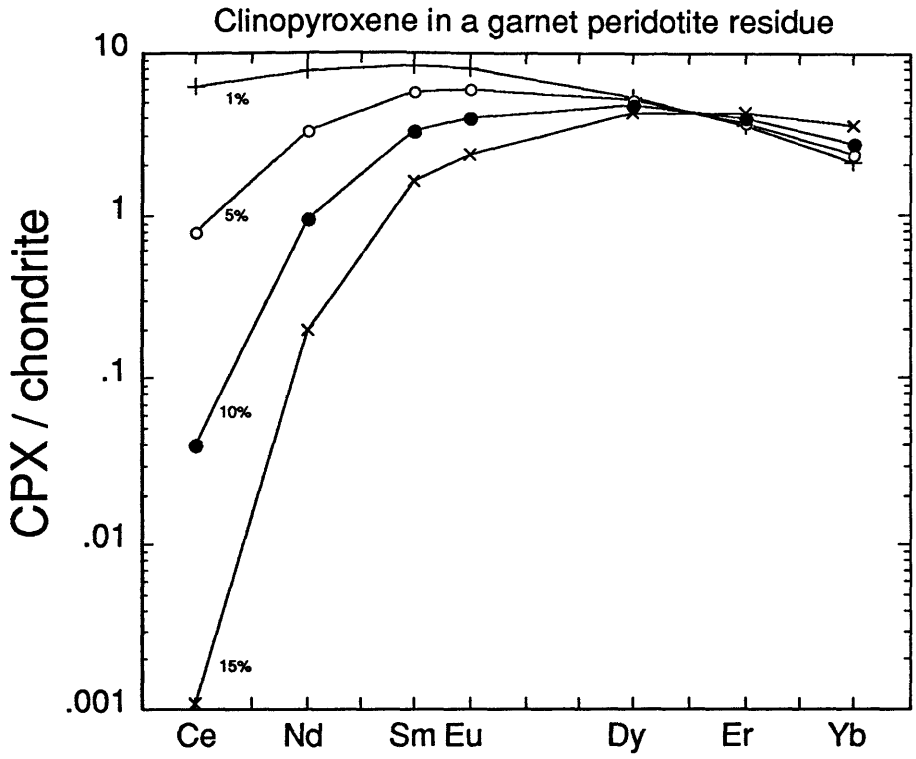

Figure A1. Rare earth element patterns in residual clinopyroxene as a function of different degrees of fractional melting in the garnet stability field using equation (1) and the model parameters given in Table A1. Note the development of a hump between Dy and Er and the increasing concentrations of Er and Yb with melting.

In this appendix, in an attempt to comprehend this unusual behavior, I analyze the parametric controls on the melting equation, specifically in terms of the behavior observed in Figure A1.

It is observed that C_i^{cpx} increases with melting in the heavy REE while decreasing in the light and middle REE. Thus, the problem can be mathematically investigated by taking the derivative of the above melting equation with respect to F. Rearranging equation (1) gives

$$C_i^{cpx} = \left[1 - \frac{PF}{D_i^o}\right]^{\frac{1}{P}} \cdot \left[\frac{C_i^o D_i^{cpx/l}}{D_i^o - PF}\right] \qquad (2)$$

and then taking the derivative with respect to F yields

$$\frac{dC_i^{cpx}}{dF} = \left[1 - \frac{PF}{D_i^o}\right]^{\frac{1}{P}} \cdot C_i^o D_i^{cpx/l}(-1)(D_i^o - PF)^{-2}(-P) + \left[\frac{C_i^o D_i^{cpx/l}}{D_i^o - PF}\right]\left(\frac{1}{P}\right)\left[1 - \frac{PF}{D_i^o}\right]^{\frac{1}{P}-1}\left(\frac{-P}{D_i^o}\right)$$

which can be simplified as follows

$$\frac{dC_i^{cpx}}{dF} = \left[\frac{D_i^o - PF}{D_i^o}\right]^{\frac{1}{P}}\left[\frac{P\,C_i^o D_i^{cpx/l}}{(D_i^o - PF)^2}\right] - \left[\frac{C_i^o D_i^{cpx/l}}{D_i^o(D_i^o - PF)}\right]\left[\frac{D_i^o - PF}{D_i^o}\right]^{\frac{1}{P}-1}$$

$$\frac{dC_i^{cpx}}{dF} = \left[\frac{D_i^o - PF}{D_i^o}\right]^{\frac{1}{P}} C_i^o D_i^{cpx/l}\left[\frac{P}{(D_i^o - PF)^2} - \frac{1}{D_i^o(D_i^o - PF)}\frac{D_i^o}{D_i^o - PF}\right]$$

$$\frac{dC_i^{cpx}}{dF} = \left[\frac{D_i^o - PF}{D_i^o}\right]^{\frac{1}{P}} C_i^o D_i^{cpx/l}\left[\frac{P}{(D_i^o - PF)^2} - \frac{1}{(D_i^o - PF)^2}\right]$$

$$\frac{dC_i^{cpx}}{dF} = \left[\frac{D_i^o - PF}{D_i^o}\right]^{\frac{1}{P}} C_i^o D_i^{cpx/l}\left[\frac{P - 1}{(D_i^o - PF)^2}\right]$$

$$\frac{dC_i^{cpx}}{dF} = \left[\frac{D_i^o - PF}{D_i^o}\right]^{\frac{1}{P}} C_i^o D_i^{cpx/l}\,(P - 1)(D_i^o - PF)^{-2}$$

$$\frac{dC_i^{cpx}}{dF} = \left[(D_i^o - PF)^{1/P - 2}\right] \cdot \left[\frac{(P - 1)C_i^o D_i^{cpx/l}}{D_i^{o(1/P)}}\right] \qquad (3)$$

With this expression, it is possible to evaluate the behavior of C_i^{cpx} as a function of F. In order for the expression to be positive, which is the case for heavy REE in Figure A1, two cases are possible given that all of the parameters are positive: Case 1 - both terms on the right side of equation (3) are positive, or Case 2 - both terms are negative.

In Case 1, if both terms are positive, then $(P - 1)$ in the second term must be positive and P must be greater than 1. Then, in the first term, since $P > 1$, the exponent is negative and the base must be positive since we are dealing with real numbers. Therefore $D_i^o - PF$

> 0, and $D_i^o > PF$. Hence, for Case 1 to be satisfied, only one set of circumstances is possible: $P > 1$ and $D_i^o > PF$. Table A1 shows that this is the situation for Er and Yb when garnet is in the assemblage.

In Case 2, more permutations are possible, but they can be broken down into three subcases. In all of them, the second term is still required to be negative, so $P < 1$.

Subcase a: a special case in which $P = 0.5$. Thus, the exponent in the first term equals zero and the first term = 1. Since the second term is negative, the whole expression is negative and C_i^{cpx} decreases with increased melting.

Subcase b: $0.5 < P < 1$. The first term exponent ranges from -1 to 0, so $(D_i^o - PF)$ must be positive in order to be able to evaluate the term. Thus, the first term is positice and the whole expression is again negative.

Subcase c: $0 < P < 0.5$. The first term exponent ranges from 0 to $+\infty$, and the only way the first term can be negative is if $(D_i^o - PF) < 0$ <u>and</u> the exponent is an odd integer. Thus, $(1/P - 2) = 2n+1$, and $P = 1/(2n + 3)$, where n is any non-negative integer. Hence, the whole expression can be negative only if $P = 1/(2n + 3)$ <u>and</u> $(D_i^o - PF) < 0$. Therefore, D_i^o must be very small (≤ 0.05, if $n = 0$ and $F = 0.15$) and in a lherzolite assemblage this is improbable for the heavy REE. So, by eliminating unreasonable possibilities, Case 1 is the only practical set of conditions in which C_i^{cpx} will increase with melting, and these conditions only occur if garnet is in the assemblage and $P_{HREE} > 1$. Significantly, a similar exercise done on the bulk melting equation

$$\frac{C_i^s}{C_i^o} = \left[\frac{1}{1-F}\right]\left[1 - \frac{PF}{D_i^o}\right]^{\frac{1}{P}}$$

demonstrates that $\frac{dC_i^s}{dF}$ will always be negative.

REFERENCES

Fujii, T., and C. M. Scarfe, Compositions of liquids coexisting with spinel lherzolite at 10 kbar and the genesis of MORBs, *Contrib. Mineral. Petrol., 90*, 18-28, 1985.

Fujimaki., H., M. Tatsumoto, and K. Aoki, Partition coefficients of Hf, Zr, and REE between phenocrysts and groundmass, *Proc. Lunar Planet. Sci. Conf., 14th, Part 2, J. Geophys. Res., 89,* suppl., B662-B672, 1984.

Jaques, A. L., and D. H. Green, Anhydrous melting of peridotite at 0-15 kbar pressure and the genesis of tholeiitic basalts, *Contrib. Mineral. Petrol., 73*, 287-310, 1980.

Nicholls, I. A., and K. L. Harris, Experimental rare earth element partition coefficients for garnet, clinopyroxene, and amphibole coexisting with andesitic and baslatic liquids, *Geochim. Cosmochim. Acta, 44,* 287-308, 1980.

Shaw, D. M., Trace element fractionation during anatexis, *Geochim. Cosmochim. Acta, 34*, 237-243, 1970.

Shimizu, N., and I. Kushiro, The partitioning of rare earth elements between garnet and liquid at high pressures: Preliminary experiments, *Geophys. Res. Lett., 2*, 413-416, 1975.

Stolper, E., A phase diagram for mid-ocean ridge basalts: Preliminary results and implications for petrogenesis, *Contrib. Mineral. Petrol., 74,* 13-27, 1980.

Stosch, H.-G., Rare earth element partitioning between minerals from anhydrous spinel peridotite xenoliths, *Geochim. Cosmochim. Acta, 46*, 793-811, 1982.

Takahashi, E., and I. Kushiro, Melting of a dry peridotite at high pressures and basalt magma genesis, *Am. Mineral., 68*, 859-879, 1983.

APPENDIX B. Ion Microprobe data for all analyzed peridotite clinopyroxenes (ppm)

sample	Sc	Ti	V	Cr	Sr	Zr	Ce	Nd	Sm	Eu	Dy	Er	Yb
Bullard F.Z.													
Vulc 5-34-56	72	827	286	7892	0.64	0.59	0.01	0.08	0.15	0.11	0.98	0.55	0.36
Vulc 5-34-56	66	856	276	7552	0.6	0.62		0.07	0.12	0.07	0.77	0.45	0.3
Vulc 5-34-56	53	706	259	7293	0.61	0.51		0.08	0.18	0.07	0.87	0.47	0.31
Vulc 5-35-1	70	831	297	7536	0.91	0.72	0.02	0.1	0.25	0.12	1.18	0.8	0.49
Vulc 5-35-1	75	830	315	7016	0.83	0.57	0.02	0.1	0.18	0.1	0.91	0.65	0.6
Vulc 5-35-1	61	602	280	6761	0.57	0.38							
Vulc 5-35-1	76		306	7319									
Vulc 5-35-19	56	1893	270	5876	3.1	4.5	0.33	0.61	0.54	0.21	1.7	1.04	1.03
Vulc 5-35-19							0.39	0.74	0.57	0.24	1.9	1.16	0.82
Vulc 5-35-19							0.27	0.49	0.44	0.19	1.51	0.87	0.66
Vulc5-35-22	69	920	286	7026	1.5	0.32	--	0.03	0.1	0.04	0.63	0.5	0.44
Vulc5-35-22	60	865	317	9748	4.6	0.25	0.01	0.04	0.09	0.07	0.68	0.5	0.43
Vulc5-35-22	59	858	276	7965	0.30	0.27	--	0.03	0.12	0.06	0.78	0.59	0.56
Vulc5-35-22	58	903	299	7859	0.87	0.24	--	0.05	0.17	0.11	1.17	0.99	0.85
Vulc5-35-30	64		281	7294			0.01	0.13	0.21	0.08	1.37	0.97	1.06
Vulc5-35-30	58	789	310	8947	3.4	0.26	0.02	0.16	0.21	0.08	1.25	0.85	0.96
Vulc5-35-30	64	856	334	8393	3.0	0.41							
Vulc5-35-30	63	906	350	8260	5.0	0.29	0.01	0.11	0.15	0.08	1.03	0.65	0.82
Vulc 5-37-3	84	1335	367	8275	1.1	3.2	0.05	0.56	0.63	0.31	1.78	1.01	1.06
Vulc 5-37-3							0.05	0.55	0.53	0.31	1.78	1.01	0.76
Vulc 5-37-3							0.04	0.56	0.63	0.3	1.78	0.95	0.79
Vulcan F.Z.													
Vulc5-41-13	51	2602	278	5797	5.9	11							
Vulc5-41-13	55	2596	289	5964	5.3	11	0.46	1.85	1.23	0.56	2.66	1.81	1.52
Vulc5-41-13	50	2616	283	5336	4.8	10	0.25	0.99	0.65	0.29	1.44	0.93	0.83
Vulc5-41-13	47	2655	278	5614	4.7	11	0.53	2.16	1.28	0.66	2.79	2.05	1.89
Vulc5-41-13	45	2606	269	5474	4.9	11							
Vulc5-41-15	55	3606	317	6260	5.9	14							
Vulc5-41-15	42	2801	266	5180	5.2	11							
Vulc5-41-15	46	2789	273	5249	5.6	11	0.51	2.05	1.25	0.61	2.59	1.75	1.66
Vulc5-41-15	48	2772	292	5839	5.4	11	0.42	1.42	1.05	0.48	2.11	1.44	1.33
Vulc5-41-15	42	2950	281	5435	5.6	12	0.58	2.28	1.41	0.62	2.97	2.18	1.84
Vulc5-41-15	57	2712	290	5925	5.1	11	0.36	1.31	0.98	0.39	2.14	1.33	1.35
Vulc5-41-15	58	2909	333	6829	5.6	12	0.39	1.36	0.9	0.43	2.18	1.43	1.33
Vulc5-41-15	47	2491	324	6679	4.8	9.4	0.34	1.44	0.91	0.39	2.05	1.33	1.29
Vulc5-41-29	55	1732	282	8384	0.9	3.0	0.16	0.84	0.95	0.39	2.48	1.39	1.47
Vulc5-41-29	55	1732	282	8384	0.9	3.0	0.07	0.66	0.7	0.32	1.83	1.01	1.11
Vulc5-41-29	54	1933	291	8343	1.2	3.4	0.12	0.68	0.67	0.33	1.72	0.93	1.11
Vulc5-41-29	56	1704	303	8216	1.1	2.7	0.12	0.68	0.67	0.33	1.72	0.93	1.11
Vulc5-41-30	53	1922	318	8414	0.79	2.7							
Vulc5-41-30	53	2250	299	6649	1.6	3.0	0.06	0.67	0.79	0.35	1.81	1.1	1.12
Vulc5-41-30	54	1764	310	7525	0.72	2.2	0.07	0.74	0.77	0.36	2.07	1.35	1.24
Vulc5-41-33	66	1537	291	6866	1.9	5.5	0.11	0.56	0.6	0.29	1.64	1.06	1.1
Vulc5-41-33	51	1464	308	7288	1.9	4.7	0.19	0.59	0.65	0.31	1.72	1.09	1.11
Vulc5-41-33	58	1620	306	6226	2.4	4.6	0.21	0.66	0.85	0.36	1.99	1.28	1.32
Vulc5-41-33	55	1562	291	6020	2.6	5.2							
Vulc5-41-33	47	1558	305	7301	2.0	4.9							
Vulc5-41-33	50	1540	287	6855	1.6	5.0							
Vulc5-41-45	48	1410	306	7272	0.36	1.4	0.05	0.54	0.5	0.26	2.23	1.29	1.37
Vulc5-41-45	51	1468	344	7844	0.55	1.5	0.03	0.28	0.35	0.16	1.4	0.82	0.89
Vulc5-41-45	49		339	7759									
Vulc5-41-45	47	1707	381	8395	1.3	1.6	0.05	0.45	0.41	0.22	1.94	1.2	1.19
Vulc5-41-45	54	1702	401	8372	1.4	1.8							
Vulc5-41-45		1557			0.51	1.5	0.03	0.33	0.39	0.19	1.54	0.91	0.91
Vulc5-41-45		1477			3.0	1.4	0.04	0.38	0.38	0.19	1.66	1.07	1.13
Bouvet F.Z.													
All107-40-6	58	271	356	11017	0.38	0.10	0.01	0.02	0.09	0.02	0.67	0.56	0.71
All107-40-6	47	211	319	10467	0.27	0.09	0.01	0.02	0.03	0.02	0.47	0.39	0.51
All107-40-6	50			9903			--	0.03	0.04	0.02	0.5	0.4	0.46
All107-40-6	48	255	350	10700	1.4	0.11	0.01	0.03	0.03	0.03	0.56	0.47	0.61
All107-40-6	49	240	341	9049	2.9	0.13							
All107-40-8	77	387	264	5185	2.5	2.1							
All107-40-8	74	350	287	6206	1.3	1.8							
All107-40-8	66	362	284	7014	1.7	1.4							
All107-40-8	80	392	286	5442	1.1	2.0							
All107-40-8	61	330	293	6914	2.3	1.5							
All107-40-8	64	358	298	8445	2.1	1.3							
All107-40-11	67	455	257	7397	0.20	0.11	0.01	0.02	0.04	0.02	0.47	0.36	0.46
All107-40-11	54	460	311	8927	0.18	0.09							
All107-40-11	58		296	8992									
All107-40-11	56		269	6733									
All107-40-11	49		281	7964									
All107-40-11	51	432	316	9192	0.5	0.14	0.01	0.01	0.05	0.02	0.48	0.37	0.46
All107-40-11	41	425	312	9795	1.1	0.15							
All107-40-11	56		320	8386									
All107-40-11	53		315	8140									
All107:40-13	63	385	314	8104	1.5	0.13	0.01	0.02	0.07	0.02	0.46	0.41	0.51
All107:40-13	57	384	296	7924	0.64	0.11	0.01	0.01	0.07	0.07	0.5	0.36	0.48
All107:40-13	55	406	289	8296	2.4	0.16	0.01	0.02	0.03	0.02	0.39	0.33	0.38
All107:40-13	43	313	268	9248	0.94	0.14	0.01	0.01	0.04	0.02	0.37	0.32	0.4
All107:40-13	45	353	285	9022	0.68	0.19	0.01	--	0.04	0.02	0.5	0.41	0.52
All107-40-27	92	351	288	6194	0.44	0.24	0.04	0.07	0.08	0.04	0.61	0.57	0.61
All107-40-27	74	291	286	6990	1.4	0.24	0.02	0.02	0.06	0.02	0.38	0.43	0.4
All107-40-27	59	296	252	6556	0.76	0.28	0.02	0.05	0.06	0.03	0.51	0.59	0.55
All107-40-27	69	320	279	6809	0.41	0.16	0.01	0.04	0.07	0.03	0.58	0.51	0.56
All107-40-27	74	372	264	6040	0.96	0.21							
All107-40-35		430		7103	1.5	0.12							
All107-40-35		466		8643	2.1	0.19							

sample	Sc	Ti	V	Cr	Sr	Zr	Ce	Nd	Sm	Eu	Dy	Er	Yb
Islas Orcadas F.Z.													
IO11/76 56-10	50	1428	277	6827	0.51	1.4	0.02	0.40	0.41	0.24	1.76	1.16	1.33
IO11/76 56-10	50	1445	275	6112	0.45	1.4	0.02	0.48	0.44	0.24	2.16	1.65	1.45
IO11/76 56-10	39	1354	274	7252	0.56	1.5	0.02	0.61	0.57	0.35	2.52	1.86	2.05
IO11/76 56-10	42	1468	281	7289	0.56	1.7	0.03	0.52	0.54	0.34	2.12	1.67	1.57
IO11/76 56-10	42	1380	273	6917	0.48	1.4							
IO11/76 56-10	40	1346	279	7229	0.55	1.2	0.01	0.40	0.46	0.30	1.99	1.56	1.53
IO11/76 56-10	48	1474	283	6714	0.68	1.4	0.02	0.43	0.44	0.31	2.20	1.52	1.47
IO11/76 56-10	43	1452	282	7195	0.85	1.4							
IO11/76:56-10	48	1504	281	6712	0.70	1.4							
IO11/76:56-10	41	1347	277	6999	0.38	1.3							
IO11/76:56-54	69	1686	277	7378	1.7	3.0	0.05	0.56	0.55	0.35	2.16	1.47	1.38
IO11/76 56-54	56	1640	297	8633	1.8	2.9	0.07	0.79	0.77	0.39	2.52	1.96	1.84
IO11/76:56-54	53	1564	267	7627	0.98	2.6	0.08	0.54	0.55	0.35	2.05	1.52	1.40
IO11/76 56-54	45	1434	255	8088	0.99	2.4	0.06	0.75	0.56	0.38	2.20	1.64	1.52
IO11/76 56-54	37	1339	248	8231	0.83	2.1	0.05	0.43	0.48	0.33	1.82	1.27	1.23
IO11/76:56-54	35	1204	233	7494	0.90	2.0	0.08	0.51	0.58	0.33	1.89	1.48	1.30
IO11/76:56-54	50	1535	262	7535	1.2	2.8	0.05	0.49	0.67	0.27	1.94	1.35	1.33
IO11/76-56-57	84	1699	315	6299	0.66	2.2							
IO11/76-56-57	78	1683	304	6327	0.54	2.0	0.01	0.40	0.45	0.21	1.48	0.91	0.86
IO11/76-56-57	65	1606	300	6216	0.62	1.9	0.03	0.56	0.75	0.33	2.09	1.42	1.33
IO11/76-56-57	65	1447	285	5326	0.57	2.6							
IO11/76 58-18	37	899	251	7276	0.49	0.50							
IO11/76 58-18	42	1047	262	6828	0.43	0.58							
IO11/76:58-18	42	1094	286	7033	0.67	0.49							
IO11/76-58-34	71	1260	305	6372	20	1.4	1.3	0.54	0.31	0.14	1.16	0.80	0.55
IO11/76-58-34	64	1295	285	5668	22	1.1	1.5	0.58	0.34	0.18	1.66	1.14	0.99
IO11/76-58-34	38	965	260	5655	20	0.97	1.8	0.67	0.38	0.21	1.57	1.10	0.51
IO11/76-58-34	36	934	260	6518	19	0.83							
East of Shaka F.Z.													
PS86-6-37	57	2756	307	7029	5.2	11	0.75	2.37	1.46	0.64	2.82	1.72	1.69
PS86-6-37	50	2635	278	6500	5.4	12							
PS86-6-37	51	2631	295	6958	5.6	11							
Andrew Bain F.Z.													
Prot5-15-90	51	1049	299	10091	0.46	0.45	0.03	0.26	0.47	0.22	1.25	0.75	0.83
Prot5-15-90	44	1129	333	10859	0.6	0.57							
Prot5-15-90	42	1108	288	9697	0.35	0.48	0.04	0.33	0.49	0.21	1.3	0.78	0.83
Prot5-15-90	42	1103	291	9268	0.33	0.57	0.02	0.25	0.37	0.17	1.18	0.66	0.71
Prot5-15-90	40	1021	303	9659	0.41	0.49							
Prot5-15-90	34	1066	263	9508	0.55	0.55							
Prot5-15-90	34		248	8163			0.01	0.14	0.27	0.13	1.01	0.61	0.61
Prot5-15-90	38	1105	293	8448	0.34	0.51	0.01	0.2	0.35	0.18	1.14	0.64	0.73
Prince Edward F.Z.													
Prot5-19-2	81	595	262	8085	8.6	2.3	0.81	0.44	0.18	0.09	0.73	0.66	0.55
Prot5-19-2	74	553	255	6781	8.4	1.9	0.93	0.58	0.19	0.13	0.81	0.79	0.67
Prot5-19-2		583			9.0	2.0	1.07	0.57	0.35	0.14	0.98	0.57	0.52
Prot5-19-2		601			8.2	2.4	1.26	0.69	0.31	0.14	1.14	0.9	0.85
Prot5-19-2		603			8.0	2.0							
Prot5-19-2		603			7.6	2.2	1.18	0.67	0.28	0.13	1.11	0.79	0.68
Prot5-19-2		634			8.1	2.2	1.08	0.61	0.29	0.11	1.04	0.78	0.71
Prot5-19-2		616			6.2	2.2							
Discovery II F.Z.													
Prot5-29-26	113	540	282	7350	1.5	1.2	0.06	0.13	0.12	0.06	0.51	0.57	0.48
Prot5-29-26	84	497	248	6749	1.2	0.99	0.07	0.12	0.13	0.06	0.58	0.53	0.5
Prot5-29-26	72	522	267	7699	1.3	0.76							
Prot5-29-26	59	519	277	7848	1.1	0.88							
Prot5-29-26	62	545	303	8766	1.2	0.89	0.08	0.16	0.14	0.06	0.67	0.63	0.59
Prot5-29-26	56	538	280	8178	1.1	0.85	0.06	0.14	0.16	0.07	0.79	0.65	0.7
Indomed F.Z.													
Prot5-38-1	58	562	296	8296	0.65	0.33	0.04	0.13	0.17	0.08	1.14	0.85	0.63
Prot5-38-1	60	570	299	7676	0.61	0.33	0.03	0.1	0.12	0.06	0.77	0.52	0.35
Prot5-38-1	68	569	251	5398	0.66	0.43	0.04	0.13	0.17	0.08	1.14	0.85	0.63
Atlantis II F.Z.													
RC27-9-6-2							2.11	2.33	1.28	0.49	2	1.33	1.39
RC27-9-6-2	51	1805	302	10357	19	8.8							
RC27-9-6-2		1809		9478	17	7.8							
RC27-9-6-2		1508		9126	24	6.0							
RC27-9-6-2		1678		9634	24	6.9							
RC27-9-6-2		995		9436	54	5.0							
RC27-9-6-2		922		9514	52	4.6							
RC27-9-6-2		1114		9387	39	5.0							
RC27-9-6-2		1037		9321	42	5.0							
RC27-9-6-2	42	1371	287	10691	26	6.5							
RC27-9-6-2	36	1576	322	8139	29	7.3							
RC27-9-6-2							1.76	2.07	1.07	0.43	1.76	0.97	1.12
RC27-9-6-2	42	1371	287	8310	27	6.4							
RC27-9-6-2	38	1342	296	7656	26	6.4							
RC27-9-6-2	36	1366	318	7565	30	7.3							
RC27-9-6-2	33	1223	293	7656	25	5.0							
RC27-9-6-2	47	1901	342	8024	19	7.3							
RC27-9-6-2	37	1340	279	8407	27	6.0							
RC27-9-6-2	36	1298	306	8413	42	5.5	1.8	2.11	0.98	0.34	1.49	0.82	0.97
RC27-9-6-2	44	1410	331	6732	42	6.0	2.34	2.18	1.23	0.45	1.68	1.1	1.18
RC27-9-6-2	35	1194	310	6697	38	5.0							
RC27-9-6-3	58	1639	317	6987	1.2	2.0	0.02	0.36	0.52	0.31	1.87	1.17	--
RC27-9-6-3	55	1572	329	6402	0.93	1.6	0.05	0.5	0.57	0.34	1.88	1.07	0.82
RC27-9-6-3	43	1435	304	7617	0.64	1.2							
RC27-9-6-3	52	1685	341	8018	0.78	1.6	0.04	0.55	0.76	0.35	2.03	1.29	1.25
RC27-9-6-3	57	1565	301	7371	0.97	2.0							
RC27-9-6-3	59	1334	265	6224	0.9	1.4	0.04	0.4	0.44	0.3	1	1.18	1.14
RC27-9-6-3	61	1447	278	6742	2.7	5.0	0.05	0.55	0.58	0.36	1.4	1.46	1.49

sample	Sc	Ti	V	Cr	Sr	Zr	Ce	Nd	Sm	Eu	Dy	Er	Yb
Atlantis II F.Z. (cont'd.)													
RC27-9-6-8	62	2283	411	7708	0.93	1.7	0.04	0.6	0.96	0.42	3.25	2.09	2.12
RC27-9-6-8	46	1625	337	7421	0.53	1.5							
RC27-9-6-8	52	1802	361	6919	0.58	1.6	0.03	0.65	0.79	0.4	2.64	1.77	1.7
RC27-9-6-8	42	1503	322	6964	0.47	1.8	0.02	0.46	0.55	0.33	2.1	1.31	1.41
RC27-9-6-8	47	1652	323	6722	0.6	1.4							
RC27-9-6-8	42	1746	320	7017	0.5	1.8							
RC27-9-6-8	38	1531	320	6985	0.62	2.3							
RC27-9-6-8	43	1476	309	5937	0.46	1.7							
RC27-9-18-23	61	2134	350	5731	0.94	2.6	0.08	0.82	0.89	0.44	2.32	1.47	1.42
RC27-9-18-23	51	1617	303	6088	1.1	2.4	0.04	0.67	0.71	0.34	2.11	1.18	1.35
RC27-9-18-45	68	1959	357	4495	1.1	2.7							
RC27-9-18-45	60	1702	320	5279	0.95	2.3	0.04	0.5	0.59	0.3	2	1.16	1.28
RC27-9-18-45	53	1401	325	4918	0.93	2.0							
RC27-9-18-45	37	1517	291	5638	0.82	2.0							
RC27-9-18-45	44	1951	337	7610	0.85	2.4							
RC27-9-18-45	58	2210	335	5765	1.1	3.2	0.06	0.74	0.84	0.37	2.36	1.41	1.44
RC27-9-23-1		1657		7898	1.0	3.0	0.35	0.72	0.72	0.42	2	1.21	1.37
RC27-9-23-1		1876		9641	2.6	3.8	0.08	0.77	0.77	0.37	2.23	1.4	1.42
RC27-9-23-1		2141		8204	0.9	4.9	0.12	1.09	1.02	0.44	2.96	1.96	1.8
RC27-9-25-138							0.14	0.97	0.91	0.41	2.23	1.37	1.36
RC27-9-25-138							0.13	0.96	0.92	0.4	2.24	1.26	1.34
RC27-9-25-138							0.13	0.99	0.91	0.41	2.22	1.34	1.44
RC27-9-25-138							0.1	0.99	0.77	0.38	1.97	1.18	1.24
RC27-9-25-142	43	1871	310	7570	1	3.4	0.12	1.12	1.01	0.52	2.53	1.58	1.7
RC27-9-25-142	41	1973	325	7179	1.1	3.3	0.09	0.81	0.94	0.47	2.39	1.48	1.6
RC27-9-25-142	37	1813	297	7133	0.7	3.1	0.11	0.89	0.88	0.44	2.44	1.57	1.63
RC27-9-25-142	41	1770	302	6064	0.9	2.7	0.13	0.93	1.13	0.47	2.3	1.43	1.58
RC27-9-25-142	38	2012	326	8334	2.6	3.4	0.13	0.94	0.99	0.55	2.67	1.68	1.87
RC27-9-25-142	29	1621	289	7723	0.8	2.9	0.07	0.75	0.6	0.37	2.04	1.27	1.42
RC27-9-30-32		1599		8681	3.5	4.2	0.17	1.03	0.84	0.41	2.01	1.33	1.2
RC27-9-30-32		1170		8072	2.9	3.0	0.24	1.15	0.97	0.45	2.23	1.51	1.46
RC27-9-30-32		1301		9267	3	3.7	0.2	0.94	0.81	0.39	2.26	1.31	1.21
RC27-9-30-33		1605		6896	2.8	2.8							
RC27-9-30-33		1703		7134	1.6	3.2							
RC27-9-30-40		1536		7641	1.8	2.5	0.1	0.73	0.72	0.38	2.11	1.43	1.2
RC27-9-30-40		1067		7099	1.1	1.7	0.08	0.91	0.76	0.4	2.26	1.35	1.28
RC27-9-30-40		2638		8049	1.1	5.0	0.14	1.28	1.23	0.52	3.49	2.31	2.28
RC27-9-34-58		500		7829	0.44	0.31	0.02	0.03	0.13	0.07	0.77	0.56	0.61
RC27-9-34-58		513		9427	0.46	0.11	0.01	0.05	0.13	0.06	0.91	0.69	0.66
RC27-9-34-58		598		8814	0.43	0.17	0.02	0.05	0.12	0.06	0.9	0.58	0.64
RC27-9-34-63		613		8719	0.35	0.31	0.01	0.08	0.18	0.09	1.24	0.79	0.85
RC27-9-34-63		761		8824	0.84	0.43	0.02	0.06	0.12	0.08	0.86	0.55	0.59
RC27-9-35-49		615		7790	0.52	0.22	0.02	0.1	0.15	0.09	1.29	0.81	1.03
RC27-9-35-49		598		8721	0.87	0.31	0.01	0.08	0.12	0.06	0.88	0.62	0.61
RC27-9-35-49		602		8841	0.53	0.22							
RC27-9-35-49		578		9082	0.45	0.17	0.01	0.03	0.12	0.08	0.8	0.56	0.6
RC27-9-35-80		495		8705	0.36	0.13	0.01	0.05	0.09	0.07	1.04	0.75	0.68
RC27-9-35-80		606		9681	0.85	0.21	0.01	0.05	0.11	0.06	0.8	0.58	0.63
RC27-9-35-80		614		8637	1.09	0.15	0.02	0.05	0.13	0.07	0.95	0.58	0.66
RC27-9-44-1		1025		8555	3.1	0.56	0.04	0.17	0.28	0.16	1.5	0.88	0.9
RC27-9-44-1		1049		8782	1.5	0.4	0.02	0.16	0.34	0.16	1.65	0.98	1.01
RC27-9-44-1		713		9096	4.0	0.3							
RC27-9-46-1		1697		7919	0.85	1.63	0.03	0.42	0.68	0.3	2.17	1.31	1.4
RC27-9-46-1		1441		7532	0.58	1.1							
RC27-9-46-1		1426		7365	0.7	1.1	0.03	0.44	0.65	0.3	2.52	1.63	1.67
RC27-9-46-2		1114		8502	0.55	1.1	0.04	0.4	0.54	0.27	2.12	1.3	1.29
RC27-9-46-2		1156		8289	0.51	1.0	0.02	0.33	0.45	0.2	1.62	1.01	1.01